

PHOTOELECTROCHEMICAL CHARACTERISTICS OF DYE-SENSITIZED SOLAR
CELLS INCORPORATING INNOVATIVE AND INEXPENSIVE MATERIALS

By

Lisa Jean Harlow

A DISSERTATION

Submitted to
Michigan State University
in partial fulfillment of the requirements
for the degree of

Chemistry - Doctor of Philosophy

2014

ABSTRACT

PHOTOELECTROCHEMICAL CHARACTERISTICS OF DYE-SENSITIZED SOLAR CELLS INCORPORATING INNOVATIVE AND INEXPENSIVE MATERIALS

By

Lisa Jean Harlow

The use of energy is going to continue to increase rapidly due to population and economic advances occurring throughout the world. The most widely used energies produce carbon dioxide during their combustion and have finite limits on how much of these resources are available. A strong push to utilizing renewable energy is necessary to keep up with the demand. The only renewable energy that has unlimited supply is solar. Our goal is to find cost-effective alternatives to historically the most extensively used materials in dye-sensitized solar cells. In order to rely on efficiency changes coinciding with the introduction of a new component, a standard baseline of performance is necessary to establish. A reproducible fabrication procedure composed of standard materials was instituted; the efficiency parameters exhibited a less than 10% standard deviation for any set of solar cells. Any modifications to the cell components would be apparent in the change in efficiency.

Our cell modifications focused on economical alternatives to the electrolyte, the counter electrode and the chromophore. Solution-based electrolytes were replaced with a non-volatile ionic liquid, 1-methyl-3-propylimidazolium iodide, and then a poly(imidazole-functionalized) silica nanoparticle. Solid-state electrolytes reduce or prevent leakage and could ease manufacturing in large-scale devices. Platinum has been the counter electrode catalyst primarily used with the iodide/triiodide redox couple, but is a rare metal making it rather costly. We reduce platinum loading by introducing a novel

counter electrode that employs platinum nanoparticles embedded on a graphene nanoplatelet paper. The highly conductive carbon base also negates the use of the expensive conductive substrate necessary for the platinum catalyst, further reducing cost. We also study the differences in transitioning from ruthenium polypyridyls to iron-based chromophores in dye-sensitized solar cells. Iron introduces low-lying ligand field states which the charge-transfer transitions necessary for electron injection deactivate to. We study a series of molecules that converts from a historically well-known ruthenium dye stepwise to an iron-based chromophore that has exhibited photocurrent previously. Converting to iron proves to be complicated and we aim to continue our investigation in order to gain a better understanding of the complexity.

Copyright by
LISA JEAN HARLOW
2014

Dedicated to my parents

ACKNOWLEDGEMENTS

I would like to thank Prof. Jim McCusker, first for entertaining the idea and then accepting me as a transplant student from another area. I find the research I have done and we do in our group incredibly rewarding. I have always appreciated Jim's zest and excitement for science (!) as it has always invigorated us as a group and anyone listening to him talk about what he/we do. He truly enjoys his job and it shows. I am happy and thankful to be a part of the McCusker group alumni. I will remember to never be 'off in deep space', I will always remember to run TLC, and I will always try the Ru(DMSO)₄Cl₂ route, I will never forget to 'just metasthesize and extract into dichloromethane' and that I should just try the ester because it is much easier to purify! But seriously, thanks Jim.

I would next like to thank the McCusker group! I can say I have loved being a part of this evolving group of people as it has changed over the years. Our group is an extreme support system for...everything, and I can't even imagine my graduate career without at least 8 or 10 other people I could talk to at any time. I want to first acknowledge Lindsey, you are my partner in crime, my quiet listener, my cheerleader (yes in two ways) and my fabulous friend. It has been a winding, difficult road but we made the best of it with some bar time :). We made it—I couldn't have done this without you. Richard. I think we are the same person sometimes; we are rebel rousers! I didn't spend much lab time with you, it was more bar time, but I do remember your diligence on letting me know how dirty every surface of the lab is, I have passed that along. Dong! DG! Quietly brilliant and funny. I always have admired and respected your extreme focus and diligence, no one could ever compare. I am SO glad you got your Science paper!

Joel, you are most like my friends back home. I loved that you made time for the things you loved because I am a strong believer in that we shouldn't sacrifice our own life and happiness for work, cause we only live once. Troy. I thoroughly enjoyed riling you up just to hear you yell so I could laugh at how mad you got. I also enjoyed our private gossip talks, rather yours. Kate! Thanks for your spectroscopic and ruthenium-based mind, you have to know you saved me lots of hours. Also my fellow veggie who never failed to bust a move on the dance floor. Alli. Thank you also for your spectroscopic mind, you taught me everything in the beginning and acclimated me to the group and please know that your time and patience teaching an ex-analytical student was much appreciated. You have big dreams and I know you will make them happen. Drew! I feel you are and will always be my little brother, you are hilarious and quirky and I can say my lab life has been much enhanced by your random thoughts, random questions, and random jokes. VT!! Eileen, I admire your quiet compliance :) and then appreciate your true feelings on the matter. Thank you for your organization it has provided me a good focus...I'll be a ghost and still mess up your books, I promise. Larry, thank you for being there to listen and cheer me on and realize my calm the last few months, you are like a little brother to me as well, one I just want to push down and mess with :). Jennie! I truly appreciate your smile and cheery attitude every single day, I literally can't think of a one. You brightened my days! Dani! I feel like you are the closest thing to my successor! Thanks for being patient with my teaching and keeping ruthenium chemistry going in our lab! I was happy to pass along echem and the ns lab, if you couldn't tell :). Annie, thank you for being my super helpful sounding board and connection to the lab and beyond, and thanks for spending your time on acac and hx-bpy :). Monica, Selene and Preston, y'all are doing well, just keep moving forward, try to do something every day, or at least every

week that is *truly* productive in finishing, don't get stuck in tangents that seem important but are really not.

I want to thank my fabulous friends outside of chemistry as well. Kayla! You are always a wonderful listener, I am so so so glad we met, I can't even find the right words. You have become so very important to me and I can't wait for your wedding time!! Brenna :) I miss you terribly my cheerleader extraordinaire! You are great and I hope we can have our chats and time out dancing and what-not like we used to again, I cherish those time sincerely. Erica, I have never had someone I could spend so much time with just doing what I normally do at home by myself. I now know we aren't the same person, but we are darn close, games and drinks and movies oh my. Kim, thank you for being there for me this last year, Booko-sitting, trips to Dublin, GR, Jackson, you are a faithful friend and traveler and I know I can count on you for whatever!

Last I would like to thank my family (includes Booko). Dad, thank you for reminding me of my rational, logical side and talking me through lots and lots of situations and almost-quits and just bad days. Mom, thank you for listening and loving and helping (and my packages!) as much as you could from Nebraska. You really did a lot. And Sal thanks for calling on your drives home and distracting me with anecdotes of Ella or of the day; you fueled our communication while I have been here, maybe I can repay you now. And Booko :) Loyal, patient, loving, forgiving, my best dude forever. I whole-heartedly know I couldn't have done this without each of your love and support. So this is yours too.

TABLE OF CONTENTS

LIST OF TABLES	xii
LIST OF FIGURES	xi
LIST OF SCHEMES	xix
KEY TO SYMBOLS OR ABBREVIATIONS	xx
Chapter 1. Introduction to Dye-Sensitized Solar Cells and the Kinetic Processes that Govern Efficiency	1
1.1 Global Perspective	1
1.2 History of Dye-Sensitized Solar Cells	5
1.3 Solar Cell Efficiency and the Processes that Govern Performance	7
1.4 Advances in Dye-Sensitized Solar Cells	12
<i>Chromophore.</i>	14
<i>Electrolyte.</i>	16
<i>Counter Electrodes.</i>	19
1.5 Contents of Dissertation.....	21
REFERENCES	24
Chapter 2. Method Development and Reproducible Fabrication of Standard Dye-Sensitized Solar Cells	31
2.1 Introduction.....	31
2.2 Experimental.....	32
2.2.1 General	32
2.2.2 Synthesis of 2,2'-Bipyridyl-4,4'-dimethyl (dmb).....	34
2.2.3 Synthesis of 2,2'-Bipyridyl-4,4'-dicarboxylic acid (dcbpy).....	34
2.2.4 Synthesis of <i>cis</i> -Bis(isothiocyanato) bis(2,2'-bipyridyl-4,4'-dicarboxylato)ruthenium(II) (N3).....	36
2.3 General Schematic for a DSSC Device	39
2.3.1 Components of a DSSC.....	39
2.3.2 Favorable Characteristics of DSSC Components.	41
<i>The Semiconductor</i>	41
<i>The Redox Couple and Electrolyte</i>	42
<i>The Counter Electrode</i>	42
<i>External Substrate Materials</i>	43
2.4 Development of a Standard Reproducible Method.....	43
2.4.1 General Fabrication Procedure.	43
2.4.2 Systematic Removal of Sources of Variability to the Fabrication Procedure.	44
2.4.3 Other Notable Improvements.....	56
<i>Active Area</i>	56
<i>Platinum Counter Electrode Preparation</i>	57
<i>Baking Method</i>	59

5.3.2 Platinum Nanoparticles Embedded on Pressed Graphene Nanoplatelet Paper	160
5.3.3 Platinum Nanoparticles Embedded on Pressed Graphene Nanoplatelets with a Polypropylene Binder	164
<i>Synthesis</i>	164
<i>Quantification</i>	165
<i>Catalytic Activity</i>	169
5.4 Dye-Sensitized Solar Cell Fabrication with Platinum Nanoparticles Embedded on Pressed Graphene Nanoplatelets with a Polypropylene Binder as the Counter Electrode	172
<i>DSSC Fabrication</i>	172
<i>DSSC Characterization</i>	175
5.5 Concluding Comments	178
APPENDIX.....	181
REFERENCES	187
Chapter 6. Future Work and Direction	191
APPENDIX.....	200
REFERENCES	217

LIST OF TABLES

Table 2-1	Reaction monitoring of the N3 precursor. Characteristic UV/Vis peak absorbance ratio, in ethanol.	37
Table 2-2.	Efficiency parameters for 5 solar cells fabricated using a one-hole vacuum dessication method to inject electrolyte. N3 dye, electrolyte: 0.3M LiI, 0.03M I ₂ in MeCN, thermalized Pt counter electrode.	46
Table 2-3.	Efficiency Parameters for 9 solar cells fabricated using a two-hole vacuum dessication method to inject electrolyte. N3 dye, electrolyte: 0.3 M LiI, 0.03 M I ₂ in MeCN, thermalized Pt counter electrode.	48
Table 2-4.	Efficiency Parameters for 11 solar cells fabricated using a TBP additive in the electrolyte. N3 dye, electrolyte: 0.3 M LiI, 0.03 M I ₂ , 0.2 M TBP in MeCN, thermalized Pt counter electrode.....	50
Table 2-5.	Efficiency Parameters for a set of 5 solar cells fabricated with 25 μm Surlyn and injection of electrolye with a syringe. Tested on our new solar simulation setup. N3 dye, electrolyte: 0.3 M LiI, 0.03 M I ₂ , 0.2 M TBP in MeCN, thermalized Pt counter electrode.....	53
Table 2-6.	Efficiency parameters for a batch of 4 solar cells fabricated with new syringe injection method of electrolyte, 25 μm Surlyn, tested on new solar setup. N3 dye, electrolyte: 0.3 M LiI, 0.03 M I ₂ , 0.2 M TBP in MeCN, thermalized Pt counter electrode.....	55
Table 3-1.	Efficiency parameters of N3 as a chromophore in a standard clamp cell, with and without a TiO ₂ blocking layer. 0.5 M LiI, 0.05 M I ₂ , 0.2 M TBP in MeCN, thermalized Pt counter electrode.....	98
Table 3-2.	Efficiency parameters of RuCN as a chromophore in a standard clamp cell, with and without a TiO ₂ blocking layer. 0.5 M LiI, 0.05 M I ₂ , 0.2 M TBP in MeCN, thermalized Pt counter electrode.	103
Table 3-3.	Efficiency parameters of FeCN as a chromophore in a standard clamp cell, with and without a TiO ₂ blocking layer. 0.5 M LiI, 0.05 M I ₂ , 0.2 M TBP in MeCN, thermalized Pt counter electrode.....	107
Table 4-1.	Efficiency Parameters for PMII-based DSSCs with and without TBP. N3 dye, 0.2 M I ₂ in PMII for the electrolyte, and a Pt counter electrode sealed in a clamp cell with a 25 μm spacer.....	134

Table 4-2.	Efficiency Parameters for PMII-based DSSCs. N3 dye, 0.2 M I ₂ in PMII for the electrolyte, and a Pt counter electrode sealed in a clamp cell with a 25 μm spacer.	139
Table 4-3.	Efficiency Parameters of a quasi solid-state DSSC. N3 dye, 1-methyl-3-propylimidazolium iodide with 0.2 M iodine as the electrolyte, Pt counter electrode sealed in a clamp cell with 25 μm spacer.	146
Table 4-4.	Efficiency Parameters of a quasi solid-state DSSC. N3 dye, PVBBIT-functionalized silica nanoparticles in 1-methyl-3-propylimidazolium iodide with added 0.2 M iodine as the electrolyte, Pt counter electrode sealed in a clamp cell with 25 μm spacer.	147
Table 4-5.	Efficiency Parameters of a quasi solid-state DSSC. N3 dye, PVBBIT-functionalized silica nanoparticles in 1-methyl-3-propylimidazolium iodide with added 0.2 M iodine as the electrolyte, Pt counter electrode sealed in a clamp cell with 25 μm spacer.	148
Table 5-1.	Efficiency Parameters for 20 μM, 200 μM and 1000 μM H ₂ PtCl ₆ GNP/PP/Pt, control GNP/PP (no Pt), and FTO/Pt counter electrodes. N3 dye, electrolyte: 0.3 M LiI, 0.03 M I ₂ , 0.2 M TBP in acetonitrile.	176

LIST OF FIGURES

Figure 1-1	World Energy Consumption by Fuel Type from 1990 to 2010 and projected use till 2040.....	1
Figure 1-2.	Projected World Energy Electricity Generation by Energy Source.	2
Figure 1-3.	Plot of the J-V curves resulting from both (■) dark and (■) light current. The efficiency parameters are also labeled. Thick dashed lines identify the areas used to calculate fill factor. A line is also drawn at zero current density.....	8
Figure 1-4.	Energy level diagram and schematic of the dye-sensitized solar cell. (■) denotes forward reactions; (■) denotes backward reactions. Rate constants for each process and V_{OC} are also labeled.	10
Figure 1-5.	A J-V curve with arrows showing the effects that series and shunt resistance have on the curve's appearance. A dashed line represents zero current density.....	11
Figure 1-6.	Structures of <i>cis</i> -Bis(isothiocyanato) bis(2,2'-bipyridyl-4,4'-dicarboxylato) ruthenium(II), N3, on the left, and tris(isothiocyanato) (2,2':6',2''-terpyridyl-4,4',4''-tricarboxylato) ruthenium(II) tris(tetrabutylammonium), the black dye, on the right.	13
Figure 1-7.	Lead perovskite dye-sensitized solar cell. J-V curve and efficiency parameters of the best cell	15
Figure 1-8.	Plot of the abundance of the elements in ppm.	16
Figure 2-1.	Components and Layout of a Dye-Sensitized Solar Cell	40
Figure 2-2.	Representative J-V curve for a set of 5 solar cells fabricated using a one-hole vacuum dessication method to inject electrolyte. N3 dye, electrolyte: 0.3 M LiI, 0.03 M I_2 in MeCN, thermalized Pt counter electrode.....	46
Figure 2-3.	Representative J-V curve for a set of 9 solar cells fabricated using a two-hole vacuum dessication method to inject electrolyte. N3 dye, electrolyte: 0.3 M LiI, 0.03 M I_2 in MeCN, thermalized Pt counter electrode.....	48
Figure 2-4.	Representative J-V curve for a set of 11 solar cells fabricated with TBP as an additive in the electrolyte. N3 dye, electrolyte: 0.3 M LiI, 0.03 M I_2 , 0.2 M TBP in MeCN, thermalized Pt counter electrode.....	50

Figure 2-5.	Representative J-V curve of a set of 5 solar cells fabricated with 25 μm Surlyn and injection of electrolyte with a syringe. Tested on our new solar simulation setup. N3 dye, electrolyte: 0.3 M LiI, 0.03 M I_2 , 0.2 M TBP in MeCN, thermalized Pt counter electrode.....	53
Figure 2-6.	Representative J-V curve of a set of 8 solar cells. The TiO_2 slides were pre-heated to 90 $^\circ\text{C}$ before being immersed in dye solution. N3 dye, electrolyte: 0.3 M LiI, 0.03 M I_2 , 0.2 M TBP in MeCN, thermalized Pt counter electrode.....	55
Figure 2-7.	Clean photoanode FTO glass slide overlaid with the 1 cm by 1 cm Scotch tape mask prepped for doctor-blading titanium dioxide paste.....	60
Figure 2-8.	Photoanode slide. Titanium dioxide printed on FTO glass before and after dyeing with the chromophore N3.	62
Figure 2-9.	Side and top view of Pt counter electrodes showing the two holes for electrolyte injection.....	62
Figure 2-10.	Setup for sealing the two electrodes together. Pt counter electrode is face up with epoxied wire in place. The dyed photoanode rests face down on the counter electrode with a Surlyn cutout between them. The leads are attached to the metal clamps that are in contact with the counter electrode. Voltage is applied across the leads to heat and melt the Surlyn.....	64
Figure 2-11.	a) Back view of a completed solar cell displaying the two holes in the counter electrode now sealed with Surlyn and thin microscope cover glass. b) Front view of a complete solar cell, the red area is the dyed titanium dioxide, the yellow area surrounding is the standard electrolyte.....	66
Figure 2-12.	DSSC Characterization Setup. It consists of a light source, a monochromator, a potentiostat, a computer, and the beam path containing a shutter, filters and the solar cell under study.	67
Figure 2-13.	^1H NMR Spectrum of 2,2'-Bipyridyl-4,4'-Dimethyl in d_6 -DMSO.	72
Figure 2-14.	^1H NMR Spectrum of 2,2'-Bipyridyl-4,4'-Dicarboxylic acid in 0.05 M NaOD in D_2O	73
Figure 2-15.	^1H NMR Spectrum of <i>cis</i> -bis(isothiocyanato)bis(2,2'-bipyridyl-4,4'-dicarboxylato)-ruthenium(II) in 0.05 M NaOD in D_2O	74
Figure 2-16.	IR Spectrum of N3.....	75
Figure 2-17.	ESI-MS of N3.....	76

Figure 2-18.	Absorbance Spectrum of N3 in Ethanol	77
Figure 2-19.	IPCE plots. Each curve is IPCE data corresponding to previous Figures. (—) using a 2-hole vacuum desiccation method, data in Figure 2-3; (—) TBP as an additive, data in Figure 2-4; (—) syringe injection, data in Figure 2-5; and (—) the TiO ₂ slides were preheated to 90°C before being immersed in dye solution, data in Figure 2-6., N3 dye, electrolyte: 0.3 M LiI, 0.03 M I ₂ , 0.2 M TBP in MeCN, thermalized Pt counter electrode.....	78
Figure 3-1.	Relative energies of iron and ruthenium excited states with respect to the conduction band of titanium dioxide.	84
Figure 3-2.	Structure of <i>cis</i> -Bis(4,4'-dicarboxyl-2,2'-bipyridine) dicyano iron(II), FeCN.....	84
Figure 3-3.	J-V curve of a DSSC employing FeCN as a chromophore in a DSSC.....	85
Figure 3-4.	Absorbed-Photon-to-Current-Efficiency of the FeCN chromophore in a DSSC and absorbance plot of FeCN in 0.5 M LiI in acetonitrile solution. The lower plot is the APCE for bare TiO ₂ film.....	86
Figure 3-5.	Absorbance of N3 (—) in 1 mM pyridine, 1 mM pyridinium triflate in ethanol solution and (—) adsorbed to TiO ₂	97
Figure 3-6.	Representative J-V curve with N3 as a chromophore in a DSSC clamp cell. (—) Without and (—) with a TiO ₂ blocking layer. 0.5 M LiI, 0.05 M I ₂ , 0.2 M TBP in MeCN, thermalized Pt counter electrode.	98
Figure 3-7.	OCVD plot of N3 as a chromophore in a standard DSSC clamp cell (—) without a blocking layer, (—) with a TiO ₂ blocking layer. 0.5 M LiI, 0.05 M I ₂ , 0.2 M TBP in MeCN, thermalized Pt counter electrode.	100
Figure 3-8.	Structure of <i>cis</i> -Bis(4,4'-dicarboxyl-2,2'-bipyridine) dicyano ruthenium(II), RuCN.	101
Figure 3-9.	Absorbance of RuCN (—) in 1 mM pyridine, 1 mM pyridinium triflate in ethanol solution and (—) adsorbed to TiO ₂ . The absorbance of the undyed TiO ₂ film (—) is also shown.	102
Figure 3-10.	Representative J-V curve for RuCN as a chromophore in DSSCs (—) without and (—) with a TiO ₂ blocking layer. 0.5 M LiI, 0.05 M I ₂ , 0.2 M TBP in MeCN, thermalized Pt counter electrode.	103

- Figure 3-11.** OCVD plot of RuCN as a chromophore in a DSSC clamp cell (—) without and (—■) with a TiO₂ blocking layer. 0.5 M LiI, 0.05 M I₂, 0.2 M TBP in MeCN, thermalized Pt counter electrode.104
- Figure 3-12.** Absorbance of FeCN (—■) in 1 mM pyridine, 1 mM pyridinium triflate in ethanol solution and (—■) adsorbed to TiO₂. The absorbance of the undyed TiO₂ film (—) is also shown.106
- Figure 3-13.** Representative J-V curves for FeCN as a chromophore in DSSCs (—) without and (—■) with a TiO₂ blocking layer. 0.5 M LiI, 0.05 M I₂, 0.2 M TBP in MeCN, thermalized Pt counter electrode.107
- Figure 3-14.** OCVD plot of FeCN as a chromophore in a DSSC clamp cell (—) without and (—■) with a TiO₂ blocking layer. 0.5 M LiI, 0.05 M I₂, 0.2 M TBP in MeCN, thermalized Pt counter electrode.109
- Figure 3-15.** OCVD plots of FeCN and RuCN as chromophores in DSSC clamp cells. FeCN (—) without and (—■) with a TiO₂ blocking layer. RuCN (—) without and (—■) with a TiO₂ blocking layer. 0.5 M LiI, 0.05 M I₂, 0.2 M TBP in MeCN, thermalized Pt counter electrode.....110
- Figure 3-16.** Diagram of the relative redox potentials of N3, RuCN and FeCN with respect to the iodide/triiodide redox couple and the conduction band of TiO₂. The potentials are referenced to NHE.111
- Figure 3-17.** ¹H NMR Spectrum of *cis*-bis(2,2'-bipyridyl-4,4'-dicarboxylato) dicyano iron(II) in 0.05 M NaOD in D₂O.115
- Figure 3-18.** ESI-MS of FeCN.116
- Figure 3-19.** Setup for the reaction of Ru(dcbpy)₂Cl₂ with NaCN to yield RuCN. The system is completely enclosed to ensure HCN containment. Acid addition is performed via a glass fitted separatory funnel attached to the reaction flask with a nitrogen inlet through the condenser and an outlet that bubbles through a basic solution.117
- Figure 3-20.** ¹H NMR Spectrum of *cis*-bis(2,2'-bipyridyl-4,4'-dicarboxylato) dicyano ruthenium(II) in 0.05 M NaOD in D₂O.118
- Figure 3-21.** Representative J-V curve comparison for FeCN (—) without and (—■) with a TiO₂ blocking layer, also RuCN (—) without and (—■) with a TiO₂ blocking layer. The dyes are chromophores in DSSCs. Electrolyte: 0.5 M LiI, 0.05 M I₂, 0.2 M TBP in MeCN, thermalized Pt counter electrode.....119

Figure 3-22.	IPCE plot of N3 as a chromophore in a DSSC () without and () with a TiO ₂ blocking layer. Electrolyte: 0.5 M LiI, 0.05 M I ₂ , 0.2 M TBP in MeCN, thermalized Pt counter electrode.....	120
Figure 3-23.	Cyclic voltammogram of FeCN adsorbed onto TiO ₂ film as the working electrode, Ag/AgCl reference electrode and a carbon rod as the counter electrode in 0.1 M TBAPF ₆ in acetonitrile. E _{1/2} = 0.74 V vs. Ag/AgCl, ΔE = 190 mV.	121
Figure 3-24.	Cyclic voltammogram of RuCN adsorbed onto TiO ₂ film as the working electrode, Ag/AgCl reference electrode and a carbon rod as the counter electrode in 0.1 M TBAPF ₆ in acetonitrile. E _{1/2} = 1.13 V vs. Ag/AgCl, ΔE = 210 mV.	122
Figure 3-25.	Spectroelectrochemistry of FeCN in 0.1 M tetrabutylammonium hexafluorophosphate in acetonitrile. Pt mesh working electrode, Ag/AgCl reference and Pt coil counter. The oxidation potential was set to 1.0 V and an absorption spectrum was taken every 30 seconds.....	123
Figure 4-1.	The complete quasi solid-state DSSC clamp cell based on 1-methyl-3-propylimidazolium iodide and 0.2 M iodine as the electrolyte. N3 is the chromophore and thermalized Pt is the counter electrode.	133
Figure 4-2.	The comparison of the 0.2 M I ₂ in PMII as the electrolyte in quasi solid-state clamp cell DSSCs, () with and () without 0.2 M 4- <i>tert</i> -butylpyridine as an additive. N3 is the chromophore and thermalized Pt is the counter electrode.	135
Figure 4-3.	Structure of the silica nanoparticle and the attached poly(1-(4-vinylbenzyl)-3-butyl imidazolium tetrafluoroborate) polymer electrolyte.....	136
Figure 4-4.	Photographs of (a) PMII, (b) PVBBIT-SiO ₂ /PMII, (c) PVBBIT-SiO ₂ /PMII/I ₂	137
Figure 4-5.	The comparison of the representative curves of each set of 0.2 M I ₂ in PMII as the electrolyte in quasi solid-state DSSCs. () with and () without 0.2 M 4- <i>tert</i> -butylpyridine, () with PVBBIT-functionalized silica nanoparticles as an additive in PMII. N3 is the chromophore and thermalized Pt is the counter electrode.	139
Figure 4-6.	Representative J-V curve of a quasi solid-state DSSC composed of PMII with 0.2 M iodine as the electrolyte.....	145

Figure 4-7.	Representative curve of a quasi solid-state DSSC composed of 0.2 M TBP in PMII with 0.2 M iodine as the electrolyte.	146
Figure 4-8.	Representative curve of a quasi solid-state DSSC composed of PVBBIT-functionalized silica nanoparticles in PMII with 0.2 M iodine as the electrolyte.	147
Figure 5-1.	TEM images of 50 wt% platinum nanoparticles.	154
Figure 5-2.	SEM Images of graphene nanoplatelets a) before and b) after decoration with Pt nanoclusters using microwave radiation.	159
Figure 5-3.	Photographs of graphene nanoplatelets on microscope glass a) before and b) after decoration with Pt nanoclusters using microwave radiation. Breaks in the graphene layer are apparent.	160
Figure 5-4.	Photographs of graphene nanoplatelet paper before and after pressing ..	161
Figure 5-5.	Photographs of graphene nanoplatelet paper before and after Pt enhancement.	161
Figure 5-6.	Photographs of graphene nanoplatelet pressed paper after Pt enhancement. a) 20 μ M and b) 200 μ M H_2PtCl_6 precursor concentrations.	163
Figure 5-7.	Photograph showing the delamination that occurs with GNP pressed paper when Surlyn is used to seal the counter electrode to the photoanode.....	163
Figure 5-8.	Graphene nanoplatelet with polypropylene paper after pressing using a molding procedure. a) Top side, b) rolled up, and c) unrolled again.....	165
Figure 5-9.	SEM images showing Pt nanoparticle coverage on plasma-treated GNP/PP surfaces from microwave heating in three concentrations of H_2PtCl_6 solutions: a) 20 μ M b) 200 μ M and c) 1000 μ M.	166
Figure 5-10.	a) Elemental abundance and b) Pt loading at surface of GNP/PP/PtNP and FTO/Pt samples as measured by XPS.....	167
Figure 5-11.	Quantification of Platinum loading by XPS and ICP-MS.	168
Figure 5-12.	Working electrodes for cyclic voltammetry for a) GNP/PP/Pt and b) FTO/Pt. Close up of c) GNP/PP/Pt and d) FTO/Pt electrode area used for reflected light microscopy to normalize the current.	170
Figure 5-13.	Cyclic voltammograms of GNP/PP/Pt and Pt/FTO samples in the electrolyte composed of 5 mM LiI, 0.5 mM I_2 and 0.1 M $LiClO_4$ in	

	acetonitrile. Ag/AgCl reference. Scan rate was 50 mV/s. The current was corrected for electrode area using reflected light microscopy.....	171
Figure 5-14.	The complete GNP/PP/Pt electrode ready for DSSC assembly.	173
Figure 5-15.	GNP/PP/Pt Clamp cell assembly at electrolyte injection step.....	174
Figure 5-16.	Representative J-V Curves for 20 μM , 200 μM and 1000 μM H_2PtCl_6 GNP/PP/Pt, control GNP/PP (no Pt), and FTO/Pt counter electrodes.....	176
Figure 5-17.	Integrated Current Density for 20 μM , 200 μM and 1000 μM H_2PtCl_6 GNP/PP/Pt, control GNP/PP (no Pt), and FTO/Pt counter electrodes.	178
Figure 5-18.	Particle distribution of 20 μM H_2PtCl_4 GNP paper in three different spots. a), c) and e) are SEM images of each spot. b), d) and f are the size distribution of the nanoparticles.	182
Figure 5-19.	Particle distribution of 200 μM H_2PtCl_4 GNP paper in three different spots. a), c) and e) are SEM images of each spot. b), d) and f are the size distribution of the nanoparticles.	183
Figure 5-20.	Sheet resistance of the different composites and treatments of GNP and GNP with polypropylene. Processed is microwave irradiated and plasma treated.....	184
Figure 5-21.	FESEM images of a) un-pressed GNP paper b) pressed GNP paper and c) pressed GNP with polypropylene paper.	185
Figure 5-22.	Each set of four J-V Curves for 20 μM , 200 μM and 1000 μM H_2PtCl_6 GNP/PP/Pt, control GNP/PP (no Pt), and FTO/Pt counter electrodes.....	186
Figure 6-1.	Structure of 4,4'-hydroxamic acid-2,2'-bipyridine.....	195
Figure 6-2.	^1H NMR Spectrum of tris(4,4'-dicarboxylic acid-2,2'-bipyridine)iron(II) in 0.05 M NaOD in D_2O	202
Figure 6-3.	^1H NMR spectrum of 4,4'-diethylester-2,2'-bipyridine in CDCl_3	204
Figure 6-4.	^{13}C NMR Spectrum of 4,4'-diethylester-2,2'-bipyridine in CDCl_3	205
Figure 6-5.	^1H NMR Spectrum of tris(4,4'-diethylester-2,2'-bipyridine)iron(II) in CDCl_3	207
Figure 6-6.	^1H NMR Spectrum of 4,4'-hydroxamic acid-2,2'-bipyridine in d_6 -DMSO.	

	209
Figure 6-7.	Representative J-V curve of [Fe(dcbpy) ₃](PF ₆) ₂ as a chromophore in DSSC. Electrolyte: 0.5 M LiI, 0.05 M I ₂ , 0.2 M TBP in MeCN, thermalized Pt counter electrode.....	210
Figure 6-8.	¹ H NMR Spectrum of Tris(2,2'-bipyridine)cobalt(II) Hexafluorophosphate in d ⁶ -acetone.....	212
Figure 6-9.	¹ H NMR Spectrum of Tris(2,2'-bipyridine)cobalt(III) Hexafluorophosphate in CD ₃ CN.	213
Figure 6-10.	¹ H NMR Spectrum of Tris(4,4'-di- <i>tert</i> -butyl-2,2'-ipyridine)cobalt(II) Hexafluorophosphate in d ⁶ -acetone.....	215
Figure 6-11.	¹ H NMR Spectrum of Tris(4,4'-di- <i>tert</i> -butyl-2,2'-bipyridine)cobalt(III) Hexafluorophosphate in CD ₃ CN.	216

LIST OF SCHEMES

Scheme 2-1.	Preparation of 2,2'-bipyridyl-4,4'-dicarboxylic acid.....	36
Scheme 2-2.	Preparation of <i>cis</i> -Bis(isothiocyanato)bis(2,2'-bipyridyl-4,4'-dicarboxylato)ruthenium(II)	37
Scheme 4-1.	Synthesis of 1-(4-Vinylbenzyl)-3-butyl imidazolium tetrafluoroborate.....	143
Scheme 4-2.	Synthesis of Poly(1-(4-Vinylbenzyl)-3-butyl imidazolium tetrafluoroborate)functionalized SiO ₂ nanoparticles.	144
Scheme 6-1.	Synthesis of 4,4'-acetylacetonate-2,2'-bipyridyl.....	194

KEY TO SYMBOLS OR ABBREVIATIONS

DSSC	Dye-Sensitized Solar Cell
J-V Curve	Current Density vs. Potential Curve
η	Global Efficiency
J_{SC}	Short-Circuit Current Density
V_{OC}	Open-Circuit Voltage
ff	Fill Factor
P_{IN}	Incident Power Density
J_{ph}	Photocurrent Density
J_0	Interfacial Exchange Current
q	Electron Charge
T	Temperature
γ	Ideality Factor
k	Boltzmann's Constant
k_{CR}	Charge Recombination Rate Constant
k_{BET}	Back Electron Transfer Rate Constant
k_{coll}	Electron Collection Rate Constant
k_{inj}	Electron Injection Rate Constant
k_{reg}	Dye Regeneration Rate Constant
k_{red}	Redox Couple Reduction Rate Constant
IPCE	Incident-Photon-to-Current-Efficiency
α	Absorptance

ϕ_{inj}	quantum yield of injection
η_{coll}	Collection Efficiency of Electrons
%T.....	Percent Transmittance
N3.....	<i>cis</i> -Bis(isothiocyanato) bis(2,2'-bipyridyl-4,4'-dicarboxylato)ruthenium(II)
black dye	tris(isothiocyanato) (2,2':6',2''-terpyridyl-4,4',4''-tricarboxylato)ruthenium(II) tris(tetra-butylammonium)
TBA ⁺	tetrabutylammonium
MLCT	Metal-to-ligand-charge-transfer
LF	Ligand Field
ALD	Atomic Layer Deposition
BL	Blocking Layer
spiro-OMeTAD.....	2,2',7,7'-tetra is (N,N-di- <i>p</i> -methoxyphenyl-amine) 9,9'-spirobifluorene
bpy	2,2'-Bipyridine
dmb	2,2'-Bipyridyl-4,4'-dimethyl
dcbpy.....	2,2'-Bipyridyl-4,4'-dicarboxylic acid
hx-bpy	2,2'-Bipyridyl-4,4'-dihydroxamic acid
deeb.....	2,2'-Bipyridyl-4,4'-diethyl ester
tb-bpy	2,2'-Bipyridyl-4,4'-di- <i>tert</i> -butyl
FTO.....	Fluorine-doped tin oxide
TBP	4- <i>tert</i> -Butylpyridine
HOMO	Highest Occupied Molecular Orbital
LUMO.....	Lowest Unoccupied Molecular Orbital
FeCN.....	<i>cis</i> -Bis(4,4'-dicarboxyl-2,2'-bipyridine) dicyano iron(II)

RuCN*cis*-Bis(4,4'-dicarboxyl-2,2'-bipyridine) dicyano ruthenium(II)
 HTM.....Hole transport medium
 PMII1-Methyl-3-propylimidazolium iodide
 PVBBITPoly(1-(4-vinylbenzyl)-3-butyl imidazolium tetrafluoroborate)
 PVBBIT-SiO₂Poly(1-(4-vinylbenzyl)-3-butyl imidazolium tetrafluoroborate)-
 functionalized silica nanoparticles
 R_{CT}.....Charge-Transfer Resistance
 R.....Gas Constant
 TTemperature
 nMoles of Electrons
 FFaraday's Constant
 J₀Dark Current Density
 OCVDOpen-Circuit-Voltage-Decay
 TCDTransient Current Decay
 AM1.5GAir Mass 1.5 Global
 ND filtersNeutral Density filters
 DIDe-Ionized
 CoVCoefficient of Variance
 FWHMFull-Width-Half-Maximum
 TCOTransparent Conductive Oxide
 ITOIndium Tin Oxide
 GNPGraphene Nanoplatelets
 PEIPoly(ethylenimine)
 PPPolypropylene

PEDOT.....Poly(3,4-ethylenedioxythiophene)

XPS.....X-ray Photoelectron Spectroscopy

ICP-MS.....Inductively Coupled Plasma Mass Spectrometry

FESEM.....Field Emission Scanning Electron Microscopy

Chapter 1. Introduction to Dye-Sensitized Solar Cells and the Kinetic Processes that Govern Efficiency

1.1 Global Perspective

The demands for energy have skyrocketed over the past century in North America and throughout the world. The world's consumption of energy was at a level of 524 quadrillion Btu in 2010 and is projected to be at 820 quadrillion Btu by the year 2040, an increase of 56%, with most of the increase is projected to be as a result of China and India's economic growth.¹ Energy consumption is manifested in various sources: nuclear, liquid fuels, coal, natural gas, hydroelectricity and other renewables, their relative level of use is seen in Figure 1-1.¹ Coal, liquid fuel and natural gas make up 60% of the world's

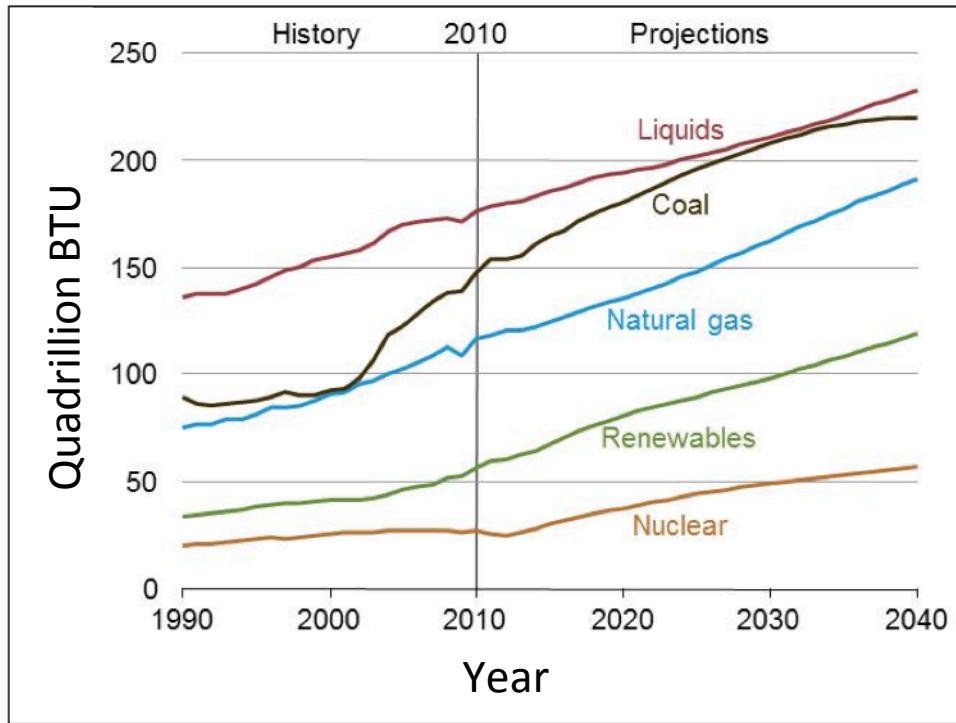


Figure 1-1. World Energy Consumption by Fuel Type from 1990 to 2010 and projected use till 2040.¹ For interpretation of the references to color in this and all other figures, the reader is referred to the electronic version of this dissertation.

energy consumption, all of which have a finite limit to their availability. Stockpiles of coal, oil and natural gas reserves are dwindling; there is a fixed amount of usable fuel in the U. S. and overseas therefore it has become increasingly necessary to rely on energy that comes from renewable sources. This in turn forces the scientific research machine to concentrate on the development of more effective renewable energies; ones that are more efficient, cheaper and can feasibly be put to use.

Globally, the renewable energy capacity for electricity doubled from 2000 to 2012 making up 14% of the installed capacity in 2012. The initiated capacity for electricity production from wind grew 28% and grew 83% for solar in 2012. They are the most rapidly expanding renewable energies for electricity generation.² Figure 1-2 shows each

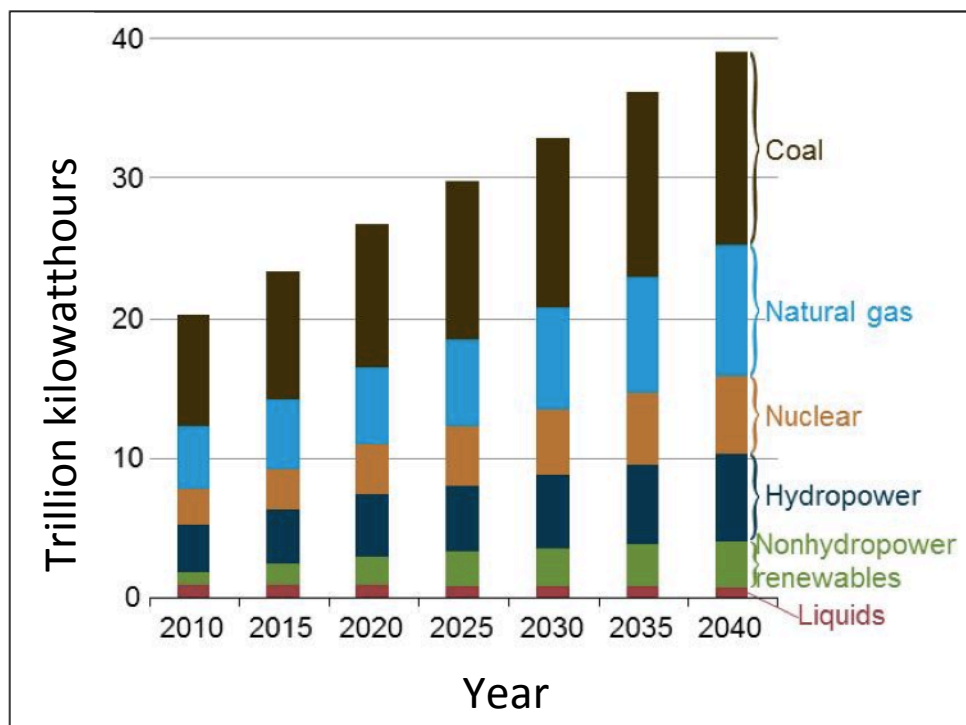


Figure 1-2. Projected World Energy Electricity Generation by Energy Source.¹

energy source and its role in electricity production and the projected growth to the year 2040. All sources grew in use except for liquid fuels, which decreases by 25%. Coal use increases the least whereas the non-hydropower renewables are projected to increase use by over 300%.

In addition to limited availability, and more importantly, there are major environmental impacts to using these fuels that we burn. Carbon-based fuels produce carbon dioxide as part of the combustion process. Increasing concentrations of carbon dioxide has detrimental effects on the environment. More CO₂ in the air means more CO₂ in the ocean, which is known to acidify the water, causing the breakdown of coral reefs, one of the world's oldest ecosystems. Increasing concentrations of CO₂ have also been shown to correlate with a rise in the earth's surface temperatures.³ Warmer temperatures affect global crop and livestock production, causes sea levels to rise, which endangers coastal cities, and also causes more intense storms affecting transportation and energy availability. Higher temps can affect the world's water resources, endanger human health, affect global landmass ecosystems, namely forest areas. These are additional significant reasons to transition to alternative choices as a source of energy.

Alternative options are nuclear, hydrothermal, wind, solar, and biomass. Each alternate has its advantages and disadvantages. In order to effectively use nuclear, there must be enough uranium and power plants to be able to keep up with the demand. Currently, only 5% of the world's energy (20% in the U. S.) comes from nuclear.^{1,4} Disadvantages are the nuclear waste that is produced and the lifetime of each plant is about 40 years on average. In order to keep up with current production we would have to

build a new plant every year for the next 30 years, without considering the plants that need to be decommissioned.⁴

Biomass, energy from plant based materials, has the advantages of being the only liquid transportation fuel usable currently, its use supports U. S. agricultural industries, and it can also be a carbon-neutral source.² Unfortunately biomass is a fuel that must be manufactured in order to use and still produces carbon dioxide when it is utilized.

Geothermal takes advantage of the heat in the earth's deep reservoirs. There is limited use of geothermal; availability is a hindrance as it only occurs in certain regions and there is a finite amount of reserves. Geothermal use doesn't directly manufacture greenhouse gases, but there is the danger of releasing harmful gases when accessing steam within the earth. Also releasing this pressure for use decreases geyser and hot springs activity in these regions, the environmental effects manifest in fallen areas of land causing irrevocable changes to the scenery with undoubtedly affecting biological species in the region as well.⁵

Advantages to using wind energy are that it exists naturally and just needs to be captured/converted into energy, and also produces no detrimental effects once the turbine structure is made. Although there are limits as there is a certain amount wind that can be utilized for energy. Wind is also variable and cannot be relied upon to produce a substantial amount of energy each day.

Dams are a form of hydroelectric energy, their benefit is they can be started and stopped during their use, storing energy for future need. Other environmental benefits result from dams like water that is can be utilized for irrigation, and they produce lakes for recreational use. Also a consideration must be made that concerns the location of the

source of the energy and the necessary transport to where it can be used. A wealth of wind and water is in the middle of the ocean but transport to land is impossible.

Solar energy has a similar advantage to wind as the energy naturally occurs and only needs to be captured and converted. There are no limits to the source of solar energy, the sun; there is essentially an infinite amount of light to be harvested, as it would be impossible to capture all of the photons that hit the earth. The token phrase is ‘there is enough energy that falls on the earth in one day to fuel the world for an entire year’. 120,000 TW of power strike the earth continuously where only about 13 TW of energy are needed.⁶ There is an outrageous amount of light to be converted into electrical energy, and it is never-ending, the scalability is endless in terms of the source. Disadvantages emerge when efficiency, cost and energy storage are discussed. A solar harvester must be efficient enough to balance out the cost of the module. There also must be means to store the energy that is not immediately used since the daily amount of sunlight varies from day to day and obviously doesn’t shine at night.

1.2 History of Dye-Sensitized Solar Cells

In order to efficiently convert solar energy into electrical energy a solar cell must absorb light, charge separation must occur, then the electron must be collected. Edmund Bequerel, using a platinum electrode coated in silver immersed in an electrolyte solution, first observed conversion of light to a detected current in the 1900s. Groups furthered research with use of selenium, copper-copper oxide, lead and thallium in these original photoelectrochemical cells. These were Schottky barrier devices where a metal is in

contact with a semiconductor, the theory was later developed in the 1930s by Walter Schottky and Neville Mott.⁷

P-n junction thin film silicon solar cells were developed in the 1950s performing better than the previous Schottky cells and they are now widely used and commercially available.⁷ The Si solar cell is a small band-gap semiconductor that does both the absorption and the charge separation; the electron is then collected via an external circuit. The p-n junction is composed of a phosphorus-doped Si layer in contact with a sulfur-doped Si layer. Once the n-type layer absorbs the light the opposing p- and n-doped layers draw the electron and the hole away from each other, achieving charge separation. Silicon is a likely choice because of its abundance, yet very pure silicon is necessary for use in photovoltaic devices to rid recombination sites, decreasing the power conversion. The expensive methods used to attain this level of purity are the major disadvantages to the silicon solar cell. Nonetheless the production of it continues as the efficiency has balanced out the cost of the devices.

Due to the expense of high-conversion efficiency silicon solar cells, other methods of light-to-energy conversion have been researched. Dye-sensitized solar cells (DSSCs) originated in the 1960s when Heinz Gerischer and coworkers discovered the sensitization of semiconductors.⁸ Using a monolayer of fluorescein dye on a thin ZnO semiconductor film, a microampere current was seen when the electrode was in contact with electrolyte solution when light was incident on the film. This development introduced a new cell arrangement and changed the processes that govern the function of a solar cell. Here a molecule attached to a surface accomplishes light absorption, not a bulk semiconductor, and the separation of charges happens when the excited electron is

injected into the conduction band of a semiconductor instead of the migration of charges. The electrolyte, not present in the traditional two-layer cells, functions to shuttle electrons to the dye, from the electrode in contact with the external circuit. This design provided a new, innovative direction of solar research vastly different than the previous bi-layer solar cells. The kinetic processes and efficiency of DSSCs will be discussed later in this chapter.

The breakthrough with this cell schematic occurred in 1991 when Michael Gratzel and Brian O'Regan greatly improved the light absorption by introducing a nanocrystalline semiconductor, achieving >7% efficiency.⁹ Instead of a monolayer of dye on the surface of a one-dimensional semiconductor, they developed a 3-D network of nanoparticles with ruthenium polypyridyl-based dye molecules adsorbed throughout. The high-surface area titanium dioxide allowed 46% of the incident light to be harvested, in comparison to the monolayer, which only could absorb 1%.⁹ Their advancement changed the cell's capability and drastically improved the benchmark efficiency of dye cells.

1.3 Solar Cell Efficiency and the Processes that Govern Performance

The efficiency of the solar cell is the measure of how well it can convert the light energy into electrical energy, called the overall power conversion efficiency, η ,

$$\eta = \frac{J_{SC} * V_{OC} * ff}{P_{IN}} \quad (1-1)$$

J_{SC} is the short-circuit current density, V_{OC} is the open-circuit voltage, ff is fill factor and P_{IN} is the incident power density. J_{SC} , V_{OC} , and ff values are obtained by photoelectrochemically testing the solar cell in the range of its function, and P_{IN} is the

power of the light source corrected for area. A J-V curve is produced, which is seen in Figure 1-3, the efficiency parameters are labeled. J_{SC} is the maximum current that is able to flow through the cell under white light illumination, without an externally applied voltage. V_{OC} is the maximum voltage that must be applied to force the current to zero; it is a measure of the voltage the solar cell maintains when current is not allowed to pass through the cell. The product of J_{SC} and V_{OC} gives the larger area enclosed by the dashed lines and the maximum power produced by the cell indicated by, P_{MAX} , is the smaller dashed area. ff is the ratio,

$$ff = \frac{P_{MAX}}{J_{SC} * V_{OC}} \quad (1-2)$$

and is a measure of the fullness of the J-V curve, resistive losses cause the curve to be

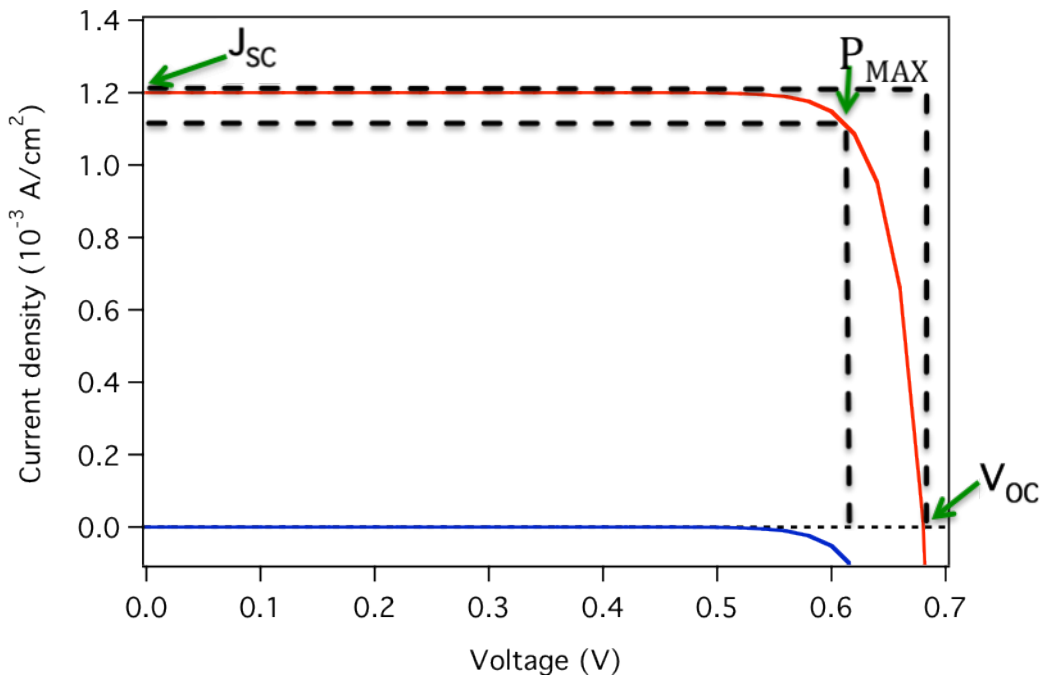


Figure 1-3. Plot of the J-V curves resulting from both (—) dark and (—) light current. The efficiency parameters are also labeled. Thick dashed lines identify the areas used to calculate fill factor. A line is also drawn at zero current density.

less rounded and reduce P_{MAX} . The solar cell, therefore the J-V curve, is governed by the diode equation. After adapted to the solar cell efficiency parameters, the diode equation is

$$J = J_{ph} - J_{dark} = J_{ph} - J_0 * \exp\left(\frac{qV}{\gamma kT} - 1\right) \quad (1-3)$$

J_{ph} is the photocurrent, which is diminished by opposing dark current, J_{dark} . J_0 is the interfacial exchange current, q is the electron charge, V is voltage, γ is the ideality factor, k is Boltzmann's constant, and T is temperature. At zero applied voltage the J_{dark} is zero and $J = J_{SC}$. As V increases from zero, J_{ph} remains constant but J_{dark} increases until $J_{dark} = J_{ph}$ at V_{OC} ,

$$V_{OC} = \frac{\gamma kT}{q} \ln\left(\frac{J_{SC}}{J_0} + 1\right). \quad (1-4)$$

There are many processes that govern the current and potential and therefore efficiency of a solar cell, in our case the DSSC. Cell efficiency is dependent on the competition of rates of each reaction occurring both forward and backward, promoting or hindering function. In Figure 1-4 a diagram shows the relative energy levels of each of the states along with forward and backward reactions labeled with blue and red arrows, respectively. A simple description of the sequence of forward processes is: absorption of light occurs, electron injection into the semiconductor, and then collection at the back contact. The electron travels through the external circuit to reduce the redox species, which has already regenerated, or reduced, the dye. The forward reactions compete with each reaction that opposes it. Electron collection from the TiO_2 competes with back electron transfer and charge recombination. Charge recombination, k_{CR} , competes with

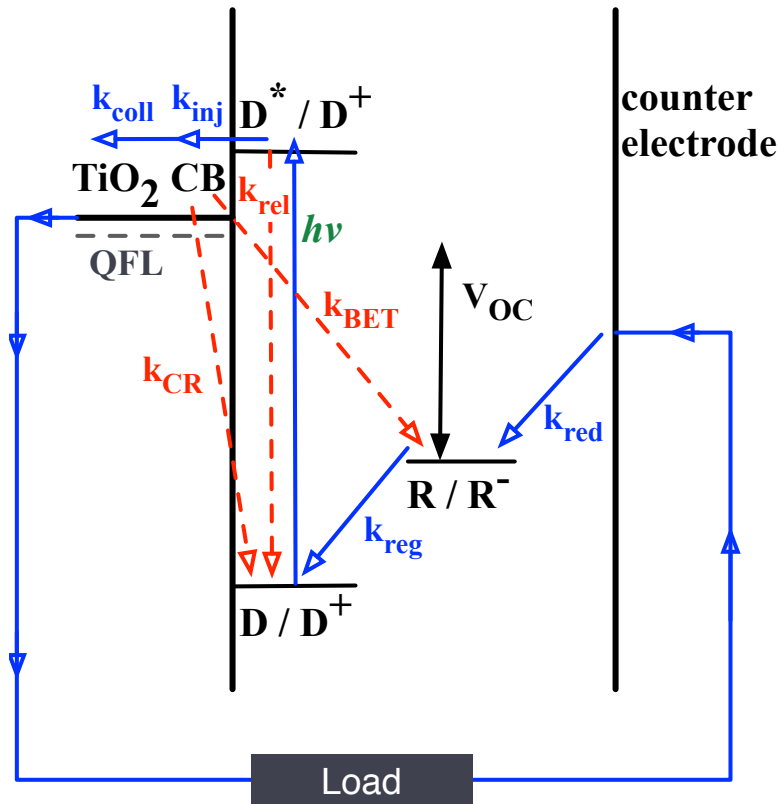


Figure 1-4. Energy level diagram and schematic of the dye-sensitized solar cell. (—) denotes forward reactions; (---) denotes backward reactions. Rate constants for each process and V_{OC} are also labeled.

dye regeneration, k_{reg} and back electron transfer; k_{BET} competes with re-reduction of the redox couple, k_{red} . The relative rates of each of these processes determine which process is predominant, be it the forward or backward process and the predominant process manifests itself in the overall cell efficiency.

Resistive losses must also be discussed since they also have an effect on the cell efficiency via predominantly the fill factor. Series resistance occurs along the path the current takes through the cell. Losses occur at the contacts and the interfaces. Series resistance is exhibited as a reduction in fill factor by a ‘pulling in’ of the curve from the

V_{OC} edge of the J-V curve, seen in Figure 1-5. No other parameters are affected until this resistance is large enough to reduce J_{SC} . Shunt resistance is due to mishaps in cell fabrication. With module defects, current is able to flow via different routes and photocurrent is lost. Shunt resistance exhibited by ‘pulling down’ the current from the top of the curve, also seen in Figure 1-5, and when it is large enough it can cause a decrease in V_{OC} .

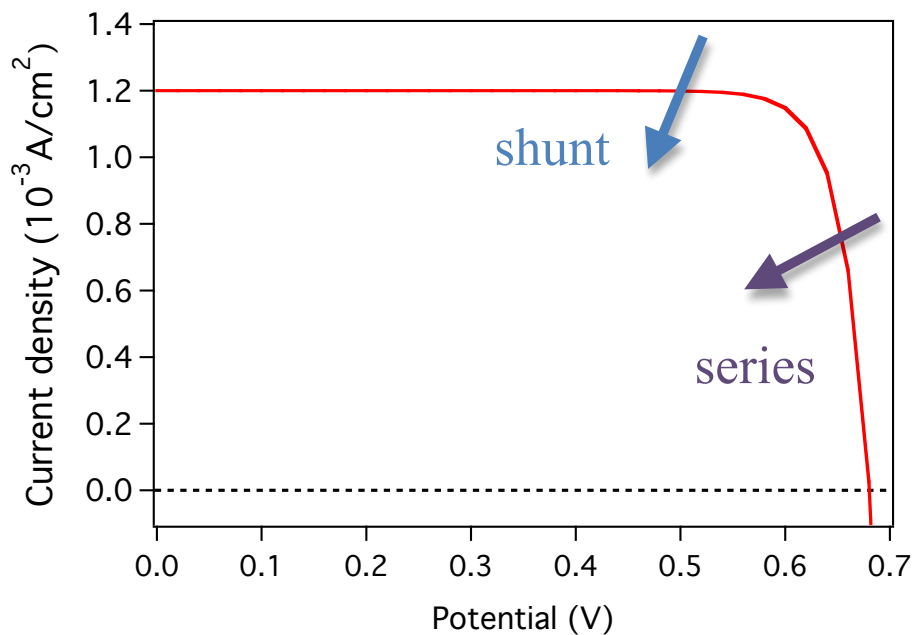


Figure 1-5. A J-V curve with arrows showing the effects that series and shunt resistance have on the curve’s appearance. A dashed line represents zero current density.

Another method of efficiency characterization is by measuring a solar cell’s output of current at each wavelength it absorbs. Incident-photon-to-current-efficiency, or IPCE, measures the number of electrons produced when a monitored number of photons

are incident. The ratio of power out to power in gives an efficiency profile that correlates to the absorption spectrum of the absorbing material. The equation for IPCE is

$$IPCE = \alpha * \phi_{inj} * \eta_{coll} \quad (1-5)$$

where α is absorptance, is the ϕ_{inj} quantum yield of injection and η_{coll} is the efficiency of collection of electrons at the back contact. Absorptance is

$$\alpha = 1 - \frac{\%T}{100} \quad (1-6)$$

where %T is percent transmittance; this term accounts for loss of photons that occur due to the device components. IPCE is useful in finding which photons produce a current and comparing performance between different types of absorbing materials or compounds. The absorptance can be divided out of IPCE to arrive at absorbed-photon-to-current-efficiency, APCE,

$$APCE = \phi_{inj} * \eta_{coll}. \quad (1-7)$$

APCE only reports the percent of absorbed photons that generate a detectable electron. Once a photon is absorbed, an electron is promoted into a higher energy level and the yield of injection and the collection ability are only considered. The losses due to the device materials are removed, including absorption and reflection by substrates not intricate to the workings of the cell. Thus, APCE tends to be higher and is more indicative of the actual cell performance at each wavelength.

1.4 Advances in Dye-Sensitized Solar Cells

The DSSC research has boomed and many advances have been made over the last 30 years. Five ‘dye-sensitized solar cell’ references appear before 1991; since 1991 over

11,600 citations appear. The efficiency has crept upwards with different cell modifications: dyes, additives, blocking layers and general minor and major modifications of aspects of this cell type.

In 1993 a different ruthenium polypyridyl dye, called N3, was reported along with 4-*tert*-butylpyridine, which jumped efficiency to 10.0%, the dye is seen in Figure 1-6.¹⁰ The ‘black dye’, also in Figure 1-6 was first reported in 1997,¹¹ but later, in 2001, this dye was published at an efficiency of 10.4% using the iodide/triiodide redox shuttle.¹² In 2011, a zinc porphyrin chromophore along with a tris bipyridyl Co(II/III) redox shuttle achieved 12.3% efficiency, the first record solar cell without the iodide/triiodide redox couple.¹³ Although a new record was not set, notably in 2012, a group achieved 11.4% with a novel TiO₂ co-adsorbent.¹⁴ Just this year a new maximum 15% efficiency was reached using a perovskite chromophore with a hole-transport medium,¹⁵ also advancing

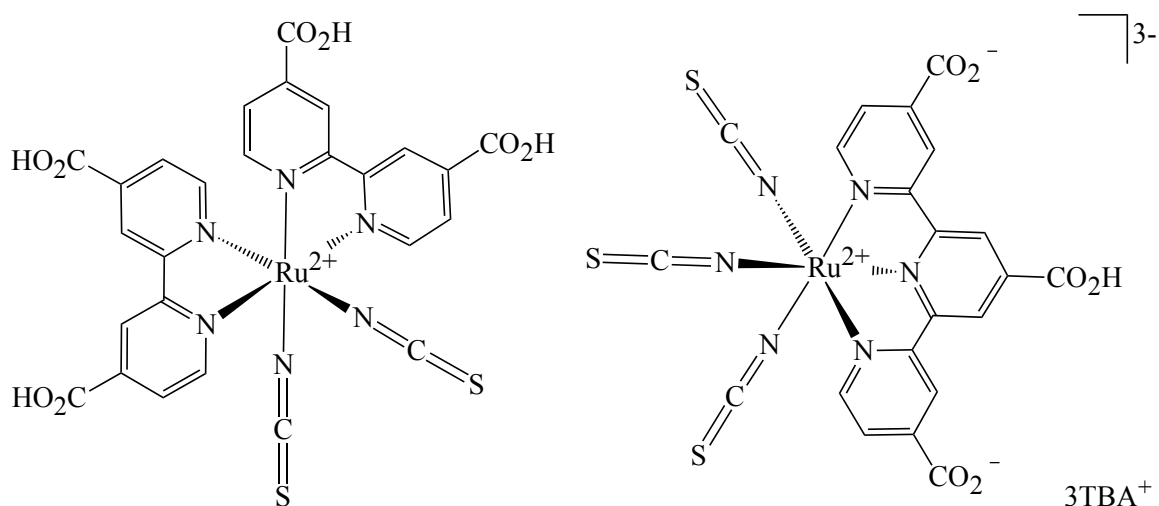


Figure 1-6. Structures of *cis*-Bis(isothiocyanato) bis(2,2'-bipyridyl-4,4'-dicarboxylato) ruthenium(II), N3, on the left, and tris(isothiocyanato) (2,2':6',2''-terpyridyl-4,4',4''-dicarboxylato)ruthenium(II) tris(tetrabutylammonium), the black dye, on the right.

solid-state solar cells, a significant advancement for DSSCs. Some of these pertinent advances are outlined below as they relate to our research.

Chromophore. There have been numerous transition metal complexes, porphyrins, organic small molecule and donor-acceptor compounds employed as dyes in n- and p-type semiconductor DSSCs.¹⁶ Platinum(II), copper(I), osmium(II), rhenium(II), ruthenium(II) are a few of the examples of transition metals used as dyes in DSSCs.^{13,17–27} Compounds have been developed that employ different types, lengths and numbers of linking groups,^{28–33} chromophores with improved optical signature,^{11,12,25,34,35} more widely absorbing extending into the under-utilized red region. Also dyes with extended aliphatic chains have been developed to help intercalation of solid-state electrolytes.³⁴ Ruthenium dyes have been the best performing dyes in these cells^{36–39} until 2001 when a zinc porphyrin along with a cobalt redox shuttle produced similar performance.¹³ This was the first DSSC to produce comparable function to ruthenium or iodide/triodide. In 2009, a group of researchers developed a lead perovskite absorber that produced ~3.5% efficiency with two different halides. Various groups built upon this work and early this year ~15% efficiency was achieved by Gratzel's group, seen in Figure 1-7.

As mentioned, historically ruthenium-based polypyridyl complexes have been the most successful dyes in terms of favorable absorptive properties and fast dye regeneration coupled with slow excited state relaxation and slow charge recombination. Absorption of a photon by the ruthenium chromophore causes a metal-to-ligand charge-transfer, MLCT, a singlet, which delocalizes the electron on the periphery of the ligand. The energy of this

state is above the energy of the conduction band, allowing injection. This state relaxes to the long-lived excited state, a $^3\text{MLCT}$, also high enough in energy to allow injection.

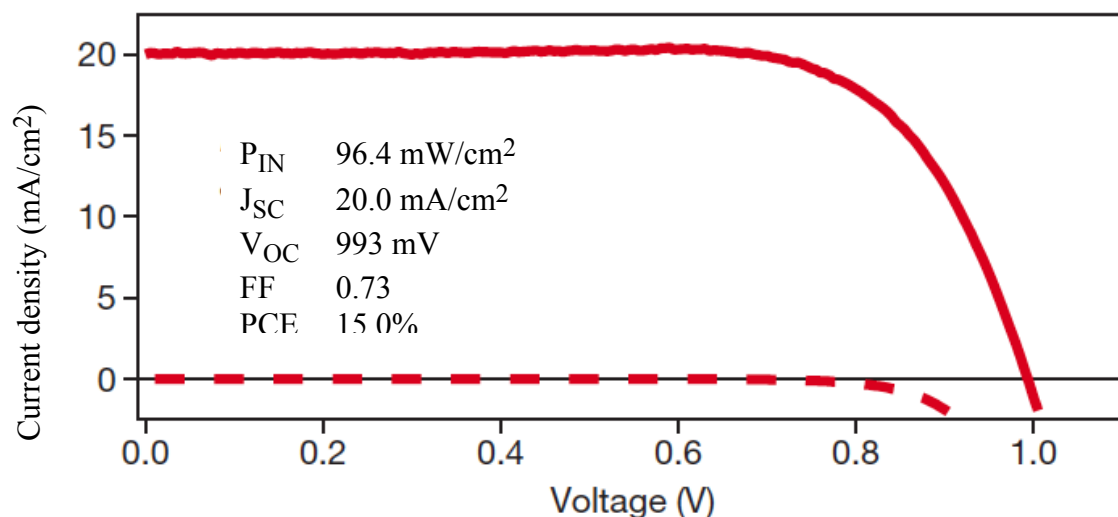


Figure 1-7. Lead perovskite dye-sensitized solar cell. J-V curve and efficiency parameters of the best cell. ¹⁵

We want to build on what is known about ruthenium chromophores and utilize our group's extensive knowledge on iron-based compounds⁴⁰⁻⁴⁵ and simply move from second to first row transition metal compounds for dyes in DSSCs. Iron is about eight orders of magnitude more abundant than ruthenium, seen in Figure 1-8.⁴⁶ Since iron is so abundant, it is much cheaper, along with being much less toxic than ruthenium, so much safer as a material for use commercially.

As mentioned, ruthenium has long-lived MLCT states that are lower in energy than its ligand field states, while the opposite is seen for iron. Iron's long-lived excited states are metal-based ligand field states, which are lower in energy than the MLCT absorptions. Nonetheless photocurrents have been seen from iron-based chromophores

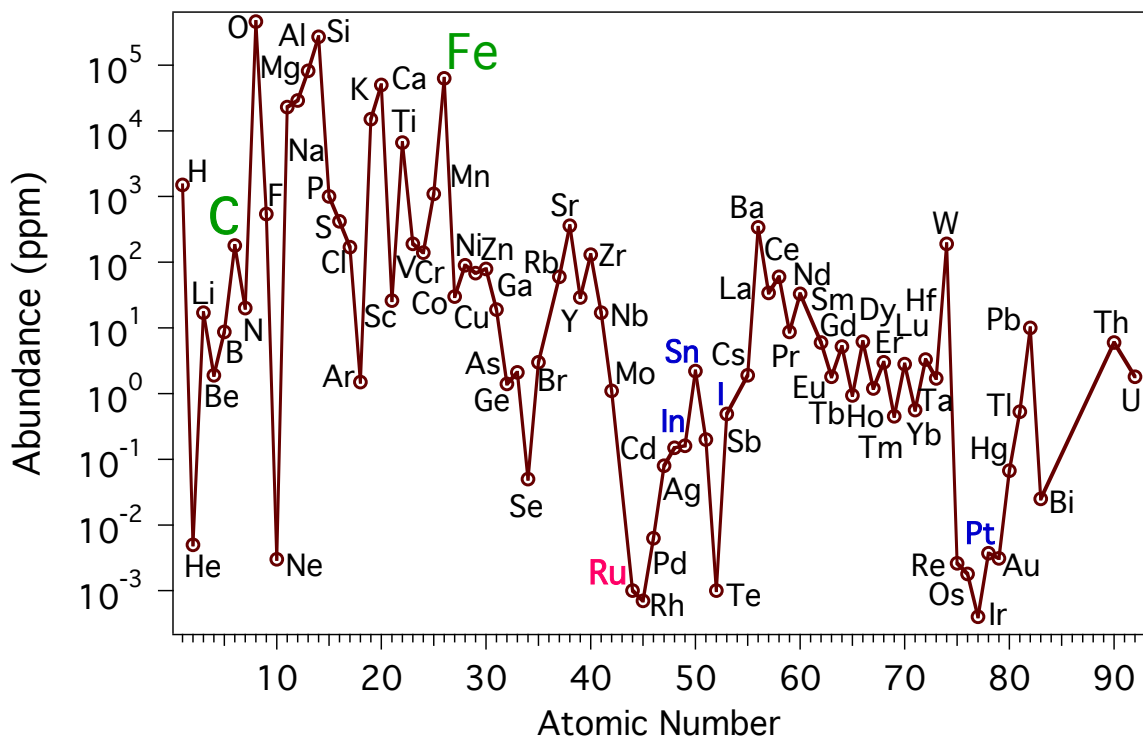


Figure 1-8. Plot of the abundance of the elements in ppm.⁴⁶

but had a much lower current and efficiency than the ruthenium-based chromophores.^{47–49} We set out to elucidate the differences between the two systems by making a ruthenium and iron analog and examine how their performances differ as chromophores in a DSSC.

Electrolyte. Upon extensive research with solution phase electrolytes, it has been realized that in order for stable, consistent use of DSSCs, there is a need for an all solid-state device. Solution electrolytes employ volatile organic solvents, which have the potential to cause issues with leakage through the seals, especially at increased temperatures in direct sunlight. Therefore the lifetime of a solution-based cell is shorter

compared to the widely used silicon cell, which is all solid-state engineering. Transitioning to solid-state electrolyte layer increases versatility and can benefit from different configurations; these layers have the potential to ease small and large-scale manufacturing, making progression to commercial use much more accessible with reduced cost. Also there exists the potential of using cheaper, less harmful materials, making widespread use possible. A solid-state electrolyte material must have high conductivity, low visible absorption, high infiltration into nanocrystalline pores, adequate potential and high reactivity to regenerate the dye, and low affinity for back electron transfer. Often these layers are called hole-transport media.

Solid-state dye-sensitized solar cell research originated in the 1980s with sensitized single crystal semiconductor photoelectrochemical cells constructed with polymer layers for electrolytes exhibited microampere currents.^{50–52} Polymer electrolytes are still widely studied; commonly employed are poly vinyl halides, poly ethylene and propylene oxides, also polymers of acryl groups.⁵³ Dissolved salts can provide the redox activity and conductivity, using predominantly dissolved iodide salts. Plasticizers are often added to increase viscosity and conductivity.^{54,55} Inert particles, such as TiO₂ and SiO₂, with and without functionalization can be added to decrease polymer crystallinity but maintain viscosity.^{56–59} Other additives have been shown to increase charge transport manifesting in higher V_{OC} and J_{SC}.^{10,54,60,61}

n-Type nanocrystalline semiconductor photoanodes with adsorbed dye and deposited p-type CuI as hole transport material was first reported in 1995 by Tennakone and coworkers producing nanoampere currents.⁶² Further development of CuI and CuSCN materials show a milliampere response by the 2000s.^{63–65}

Ionic liquids are quasi solid state compounds that are highly conductive, stable and very viscous.⁶⁶ Nanoparticles and other additives are used to change the physical and electrochemical properties such as increasing conductivity and viscosity. Additives such as imidazolium salts, phosphates, ammonium salts, and functionalized pyridines have all been studied.^{67,68}

A significant finding was the development of 2,2',7,7'-tetrakis(N,N-di-p-methoxyphenyl-amine) 9,9'-spirobifluorene, called spiro-OMeTAD, the first non iodide/triiodide hole transport medium that produced considerable response, at 4% efficiency.⁶⁹ The significant efficiency is due to a similar electron transport of this material compared to traditional solution-phase electrolytes although a higher recombination rate is seen and high resistivity of transport in the material limits the performance.⁷⁰

These quasi solid and solid state electrolytes suffer from lower ion mobility than common solution electrolytes. Our goal is keep mobility on par with the use of a common polymer as the solvent, increase viscosity with dispersed nanoparticles but also introduce communication between them via functional groups that can be polymerized, after application and infiltration into the TiO₂. It is hoped that an increase in conductivity could be seen with the polymerization between particles since they could act as a pipeline of charge transport. We introduce a poly imidazolium-functionalized silica nanoparticle dispersed in 3-methyl-1-propylimidazolium iodide for use as a quasi solid-state electrolyte in dye-sensitized solar cells.

Counter Electrodes. Counter electrodes are another sources of high expense in the dye-sensitized solar cell since platinum metal has been the predominantly used electrode for these cells. Since ruthenium chromophores have been the most efficient dye (up until recently), this requires the use of iodide/triiodide for use as the redox couple since is the best performing shuttle for ruthenium compounds. The use of iodide/triiodide as the redox couple requires the use of platinum metal (until recently, discussed later) for the catalyst to most efficiently re-reduce triiodide to iodide at the counter electrode. Research has been done to look into other catalysts in hopes of finding one that could function efficiently with other electrolyte materials.

Nickel, palladium, tungsten, and molybdenum have been studied as thin films for counter electrodes producing low efficiencies or side reactions with iodide.⁷¹ Gold is suitable for quantum dot use and thin films, exhibiting better efficiency for a cobalt redox shuttle.⁷²

Extensive work in carbon-based materials seems promising as it is so versatile, electrically conductive, chemically and physically stable and its abundance is four magnitudes higher than platinum, so is a much more cost-effective option. Gratzel's group first used carbon black and graphite in a DSSC in 1996 with 6.7% efficiency of conversion.⁷³ Some examples of other carbon materials that afforded minimal success compared to platinum are carbon fibers, carbon particles, mesoporous carbon, activated carbon, etc.⁷¹ Improved performance was seen with work on 3-D carbon nanotubes achieving efficiencies at 8.03% and 10.04%, with two different methods of deposition.⁷⁴

Organic polymers have also been utilized with advantages such as lower cost, transparency and flexibility. Most composites provided lower to similar performance to

Pt, with PEDOT exhibiting superior activity to Pt in their system, at 8% efficiency. Yet these organic films have been shown to be unstable as they tend to make complexes with iodide.⁷⁵

More recently inorganic compounds as counter electrodes have made large advances in DSSC functioning. A breakthrough in 2009 came about with a cobalt sulfide counter electrode, the first electrode to match Pt function while using the iodide/triiodide redox couple.⁷⁶ Also in 2009 a TiN nanotube array as a counter electrode produced similar performance to Pt with an iodide/triiodide redox shuttle.⁷⁷ Carbides, nitrides and sulfides can also perform at the high catalytic activity of Pt.⁷¹

A counter electrode material must be stable, highly catalytic towards the reduction of the redox couple chosen, readily available and low in cost and implementation as an electrode. As research moves away from iodide/triiodide as a redox couple, options open up to create and utilize exciting new efficient counter electrodes for these other materials.

Our research consists of the use of a carbon-based backbone with platinum nanoparticles attached to the surface. We use the knowledge that platinum has been the best electrode for iodide/triiodide to try out a new configuration that our and another lab have been working on but with the intention to reduce the amount of platinum with a change in morphology that accompanies a higher surface area.

Now that the literature scope has been presented, areas of improvement can be identified in regards to the direction of our research interests. The current, most efficient DSSC constitute the emerging perovskite dyes, spiro-OMeTAD as a solid state electrolyte and gold for a counter electrode.¹⁵ The revolutionary perovskite dyes are made of lead and iodine, both fairly non-abundant elements. The same is true for the gold

electrode traditionally used with the spiro-MeOTAD electrolyte, it is a rare, precious metal. The ultimate goal of solar cell development is widespread use so scaling up of materials with cost-effective, low toxicity compounds is necessary. Therefore, more research is needed in this area to find more readily available, less or non-toxic compounds that still produce high efficiency solar cells.

Another main device component, discussed later, that has yet to be replaced due to its expense is the transparent conductive oxide coated materials currently needed for a complete functioning cell. More research is needed in this area to find a different substrate material that provides the conductivity necessary without the loss of light.

A synergy of DSSC components is also necessary. It seems that advances have been made independently within DSSC components (dye, electrolyte, cathode) but a more cohesive integration of the different parts of the cell could help performance, instead of piecing together a mix-match arrangement. A simple, cohesive design is desirable; one in which the needs of a material to yield its best, full operation has been identified and utilized through methodical research.

1.5 Contents of Dissertation

Chapter 2 will cover the necessity for the reproducible fabrication of DSSCs and the path to achievement of a standard fabrication method that produces repeatable cells of the same efficiency parameters. The standard dye-sensitized solar cell procedure will be presented along with the synthesis of the molecular components such as the ligands, the precursors and the eventual chromophores used in the cells.

A few of the disadvantages to solar energy as a renewable energy are the cost, storage and efficiency. We have focused our research on one of these disadvantages: to reduce the overall cost of the solar cell. We aim to reduce the amount or type of material in most aspects of the DSSC to directly lower the value of the materials used in the cell. These ideas are discussed in Chapters 3, 4, and 5.

Chapter 3 illustrates the differences between functionalized heteroleptic ruthenium-based bipyridyl chromophores versus the identical iron-based compounds. Firstly, the complexities of incorporating iron into the standard cell will be presented along with the modifications to the DSSC procedure that was needed to incorporate the iron-based dyes. Also the characteristic performance disparities that occur when iron is the DSSC chromophore; iron differs kinetically from ruthenium, which is observed, and the differences manifest themselves in the efficiency parameters.

Adaptation of the method to incorporate new materials in new designs is also detailed. In Chapter 4, quasi solid state electrolytes are instituted. Both strictly polymer electrolytes and also a composite consisting of a functionalized silica nanoparticle blended with a polymer are introduced and described as electrolytes in these DSSCs. This work is a collaboration, all polymer and composite materials are work done by Dr. Heyi Hu and his thesis outlines the detailed synthesis and characterization of these materials.

In Chapter 5, a series of cells are described that integrate a novel counter electrode, platinum nanoclusters embedded on graphene and graphene paper. This innovative electrode reduces the platinum loading and makes the transparent conductive electrode unnecessary to the design. This research is also a collaboration and all electrode materials were developed and characterized by Dr. Pat Aderhold. The author of this

document guided the research progress to incorporate the new materials and performed all cell fabrication.

Lastly, in Chapter 6, current and future research direction on each of the efforts outlined in this dissertation will be discussed. Ideas on these subjects also various new avenues for investigation with a basis in this research will be presented.

REFERENCES

REFERENCES

- (1) U.S. Energy Information Administration INTERNATIONAL ENERGY OUTLOOK 2013 <http://www.eia.gov> (accessed Nov 7, 2013).
- (2) U.S. Department of Energy 2012 Renewable Energy Data Book <http://www.nrel.gov> (accessed Nov 8, 2013).
- (3) Doney, S. C.; Schimel, D. S. *Annual Review of Environment and Resources* **2007**, *32*, 31–66.
- (4) Nuclear Energy Institute NEW NUCLEAR ENERGY FACILITIES www.nei.org (accessed Nov 8, 2013).
- (5) Stewart, C. Geothermal energy - Effects on the environment <http://www.teara.govt.nz/en/geothermal-energy/page-5> (accessed Nov 11, 2013).
- (6) Crabtree, G. W.; Lewis, N. S. *Physics Today* **2007**, *60*, 37.
- (7) Nelson, J. *The Physics of Solar Cells*; 1st ed.; Imperial College Press: London, 2003.
- (8) Gerischer, H.; Michel-Beyerle, M.; Rebentrost, F.; Tributsch, H. *Electrochimica Acta* **1968**, *13*, 1509–1515.
- (9) O'Regan, B. C.; Grätzel, M. *Nature* **1991**, *353*, 737–740.
- (10) Nazeeruddin, M. K.; Kay, A.; Rodicio, I.; Humphry-Baker, R.; Mueller, E.; Liska, P.; Vlachopoulos, N.; Gratzel, M. *Journal of the American Chemical Society* **1993**, *115*, 6382–6390.
- (11) Nazeeruddin, M. K.; Pechy, P.; Grätzel, M. *Chemical Communications* **1997**, *1*, 1705–1706.
- (12) Nazeeruddin, M. K.; Péchy, P.; Renouard, T.; Zakeeruddin, S. M.; Humphry-Baker, R.; Comte, P.; Liska, P.; Cevey, L.; Costa, E.; Shklover, V.; Spiccia, L.; Deacon, G. B.; Bignozzi, C. A.; Grätzel, M. *Journal of the American Chemical Society* **2001**, *123*, 1613–24.
- (13) Yella, A.; Lee, H.-W.; Tsao, H. N.; Yi, C.; Chandiran, A. K.; Nazeeruddin, M. K.; Diao, E. W.-G.; Yeh, C.-Y.; Zakeeruddin, S. M.; Grätzel, M. *Science* **2011**, *334*, 629–34.

- (14) Han, L.; Islam, A.; Chen, H.; Malapaka, C.; Chiranjeevi, B.; Zhang, S.; Yang, X.; Yanagida, M. *Energy & Environmental Science* **2012**, *5*, 6057.
- (15) Burschka, J.; Pellet, N.; Moon, S.-J.; Humphry-Baker, R.; Gao, P.; Nazeeruddin, M. K.; Grätzel, M. *Nature* **2013**, *499*, 316–9.
- (16) Zhu, H.; Hagfeldt, A.; Boschloo, G. *The Journal of Physical Chemistry C* **2007**, *111*, 17455–17458.
- (17) Bessho, T.; Constable, E. C.; Gratzel, M.; Hernandez Redondo, A.; Housecroft, C. E.; Kylberg, W.; Nazeeruddin, M. K.; Neuburger, M.; Schaffner, S. *Chemical Communications* **2008**, 3717–9.
- (18) Constable, E. C.; Hernandez Redondo, A.; Housecroft, C. E.; Neuburger, M.; Schaffner, S. *Dalton Transactions (Cambridge, England : 2003)* **2009**, 6634–44.
- (19) Polo, A. S.; Itokazu, M. K.; Murakami Iha, N. Y. *Coordination Chemistry Reviews* **2004**, *248*, 1343–1361.
- (20) Sauve, G.; Cass, M. E.; Coia, G.; Doig, S. J.; Lauermann, I.; Pomykal, K. E.; Lewis, N. S. *The Journal of Physical Chemistry B* **2000**, *104*, 6821–6836.
- (21) Miyashita, M.; Sunahara, K.; Nishikawa, T.; Uemura, Y.; Koumura, N.; Hara, K.; Mori, A.; Abe, T.; Suzuki, E.; Mori, S. *Journal of the American Chemical Society* **2008**, *130*, 17874–81.
- (22) Kim, J.-J.; Choi, H.; Lee, J.-W.; Kang, M.-S.; Song, K.; Kang, S. O.; Ko, J. *Journal of Materials Chemistry* **2008**, *18*, 5223–5229.
- (23) Happ, B.; Winter, A.; Hager, M. D.; Schubert, U. S. *Chemical Society Reviews* **2012**, *41*, 2222–55.
- (24) Dabestani, R.; Bard, A. J.; Campion, A.; Fox, M. A.; Mallouk, T. E.; Webber, S. E.; White, J. M. *The Journal of Physical Chemistry* **1988**, *92*, 1872–1878.
- (25) Stromberg, J.; Marton, A.; Kee, H. L.; Kirmaier, C.; Diers, J. R.; Muthiah, C.; Taniguchi, M.; Lindsey, J. S.; Bocian, D. F.; Meyer, G. J.; Holten, D. *The Journal of Physical Chemistry C* **2007**, *111*, 15464–15478.
- (26) Archer, S.; Weinstein, J. a. *Coordination Chemistry Reviews* **2012**, *256*, 2530–2561.
- (27) Wu, Y.; Zhu, W. *Chemical Society Reviews* **2013**, *42*, 2039–58.

- (28) Olivier, J.-H.; Haefele, A.; Retailleau, P.; Ziessel, R. *Organic Letters* **2010**, *12*, 408–11.
- (29) Ferrere, S. *Inorganica Chimica Acta* **2002**, *329*, 79–92.
- (30) Warnan, J.; Guerin, V.-M.; Anne, F. B.; Pellegrin, Y.; Blart, E.; Jacquemin, D.; Pauporté, T.; Odobel, F. *The Journal of Physical Chemistry C* **2013**, *117*, 8652–8660.
- (31) Yang, L.-N.; Sun, Z.-Z.; Chen, S.-L.; Li, Z.-S. *Dyes and Pigments* **2013**, *99*, 29–35.
- (32) Kilså, K.; Mayo, E. I.; Brunschwig, B. S.; Gray, H. B.; Lewis, N. S.; Winkler, J. R. *The Journal of Physical Chemistry B* **2004**, *108*, 15640–15651.
- (33) Heimer, T. A.; D’Arcangelis, S. T.; Farzad, F.; Stipkala, J. M.; Meyer, G. J. *Inorganic Chemistry* **1996**, *35*, 5319–5324.
- (34) Zakeeruddin, S. M.; Nazeeruddin, M. K.; Humphry-Baker, R.; Péchy, P.; Quagliotto, P.; Barolo, C.; Viscardi, G.; Grätzel, M. *Langmuir* **2002**, *18*, 952–954.
- (35) Jang, S.-R.; Yum, J.-H.; Klein, C.; Kim, K.-J.; Wagner, P.; Officer, D.; Gratzel, M.; Nazeeruddin, M. K. *The Journal of Physical Chemistry C* **2009**, *113*, 1998–2003.
- (36) Chiba, Y.; Islam, A.; Watanabe, Y.; Komiya, R.; Koide, N.; Han, L. *Japanese Journal of Applied Physics* **2006**, *45*, L638–L640.
- (37) Yu, Q.; Wang, Y.; Yi, Z.; Zu, N.; Zhang, J.; Zhang, M.; Wang, P. *ACS Nano* **2010**, *4*, 6032–8.
- (38) Chen, C.-Y.; Wang, M.; Li, J.-Y.; Pootrakulchote, N.; Alibabaei, L.; Ngoc-le, C.; Decoppet, J.-D.; Tsai, J.-H.; Gratzel, C.; Wu, C.-G.; Zakeeruddin, S. M.; Grätzel, M. *Acs Nano* **2009**, *3*, 3103–3109.
- (39) Nazeeruddin, M. K.; De Angelis, F.; Fantacci, S.; Selloni, A.; Viscardi, G.; Liska, P.; Ito, S.; Takeru, B.; Grätzel, M. *Journal of the American Chemical Society* **2005**, *127*, 16835–47.
- (40) Jamula, L. L. Design and Synthesis of Iron(II) Terpyridyl Complexes for Application in Dye-Sensitized Solar Cells, Michigan State University, 2010.
- (41) Cho, H.; Strader, M. L.; Hong, K.; Jamula, L.; Gullikson, E. M.; Kim, T. K.; de Groot, F. M. F.; McCusker, J. K.; Schoenlein, R. W.; Huse, N. *Faraday Discussions* **2012**, *157*, 463.

- (42) Huse, N.; Kim, T. K.; Jamula, L.; McCusker, J. K.; de Groot, F. M. F.; Schoenlein, R. W. *Journal of the American Chemical Society* **2010**, *132*, 6809–16.
- (43) Khalil, M.; Marcus, M. A.; Smeigh, A. L.; McCusker, J. K.; Chong, H. H. W.; Schoenlein, R. W. *The Journal of Physical Chemistry A* **2006**, *110*, 38–44.
- (44) Monat, J. E.; McCusker, J. K. *Journal of the American Chemical Society* **2000**, *122*, 4092–4097.
- (45) Smeigh, A. L.; Creelman, M.; Mathies, R. A.; McCusker, J. K. *Journal of the American Chemical Society* **2008**, *130*, 14105–7.
- (46) Haxel, G. B.; Hedrick, J. B.; Orris, G. J. Rare Earth Elements—Critical Resources for High Technology pubs.usgs.gov (accessed May 1, 2009).
- (47) Ferrere, S.; Gregg, B. *Journal of the American Chemical Society* **1998**, *120*, 843–844.
- (48) Ferrere, S. *Chemistry of Materials* **2000**, *12*, 1083–1089.
- (49) Yang, M.; Thompson, D. W.; Meyer, G. J. *Inorganic Chemistry* **2002**, *41*, 1254–1262.
- (50) Cook, R. L.; Sammells, A. F. *Journal of The Electrochemical Society* **1985**, *132*, 2429–2431.
- (51) Sammells, A. F.; Schmidt, S. K. *Journal of The Electrochemical Society* **1985**, *132*, 520–522.
- (52) Hardy, L. C.; Shriver, D. F. *Journal of the American Chemical Society* **1986**, *108*, 2887–2893.
- (53) Ileperuma, O. A. *Materials Technology: Advanced Performance Materials* **2013**, *28*, 65–70.
- (54) Nei de Freitas, J.; Nogueira, A. F.; De Paoli, M.-A. *Journal of Materials Chemistry* **2009**, *19*, 5279.
- (55) Freitas, J. N. De; Gonçalves, A. D. S.; De Paoli, M.-A.; Durrant, J. R.; Nogueira, A. F. *Electrochimica Acta* **2008**, *53*, 7166–7172.
- (56) Ueno, K.; Inaba, A.; Kondoh, M.; Watanabe, M. *Langmuir* **2008**, *24*, 5253–9.
- (57) Stergiopoulos, T.; Arabatzis, I. M.; Katsaros, G.; Falaras, P. *Nano Letters* **2002**, *2*, 1259–1261.

- (58) Kang, M.-S.; Ahn, K.-S.; Lee, J.-W. *Journal of Power Sources* **2008**, *180*, 896–901.
- (59) Shaheerakhtar, M.; Chun, J.; Yang, O. *Electrochemistry Communications* **2007**, *9*, 2833–2837.
- (60) Zhang, X.; Yang, H.; Xiong, H.-M.; Li, F.-Y.; Xia, Y.-Y. *Journal of Power Sources* **2006**, *160*, 1451–1455.
- (61) Ganesan, S.; Muthuraaman, B.; Madhavan, J.; Mathew, V.; Maruthamuthu, P.; Suthanthiraraj, S. A. *Electrochimica Acta* **2008**, *53*, 7903–7907.
- (62) Tennakone, K.; Kumara, G. R. R. A.; Kumarasinghe, A. R.; Wijayantha, K. G. U.; Sirimanne, P. M. *Semiconductor Science and Technology* **1995**, *10*, 1689–1693.
- (63) Tennakone, K.; Kumara, G. R. R. A.; Kottegoda, I. R. M.; Wijayantha, K. G. U. *Semiconductor Science and Technology* **1997**, *12*, 128–132.
- (64) Kumara, G. R. R. A.; Konno, A.; Senadeera, G. K. R.; Jayaweera, P. V. V.; De Silva, D. B. R. A.; Tennakone, K. *Solar Energy Materials and Solar Cells* **2001**, *69*, 195–199.
- (65) Konno, A.; Kitagawa, T.; Kida, H.; Asoka Kumara, G. R.; Tennakone, K. *Current Applied Physics* **2005**, *5*, 149–151.
- (66) Yang, H.; Yu, C.; Song, Q.; Xia, Y.; Li, F.; Chen, Z.; Li, X.; Yi, T.; Huang, C. *Chemistry of Materials* **2006**, *18*, 5173–5177.
- (67) Gorlov, M.; Kloo, L. *Dalton Transactions (Cambridge, England : 2003)* **2008**, 2655–66.
- (68) Wang, P.; Wenger, B.; Humphry-Baker, R.; Moser, J.-E.; Teuscher, J.; Kantlehner, W.; Mezger, J.; Stoyanov, E. V.; Zakeeruddin, S. M.; Grätzel, M. *Journal of the American Chemical Society* **2005**, *127*, 6850–6.
- (69) Bach, U.; Lupo, D.; Comte, P.; Moser, J.-E.; Weissortel, F.; Salbeck, J.; Spreitzer, H.; Grätzel, M. *Nature* **1998**, *395*, 583–585.
- (70) Fabregat-Santiago, F.; Bisquert, J.; Cevey, L.; Chen, P.; Wang, M.; Zakeeruddin, S. M.; Grätzel, M. *Journal of the American Chemical Society* **2009**, *131*, 558–62.
- (71) Wu, M.; Ma, T. *ChemSusChem* **2012**, *5*, 1343–57.
- (72) Sapp, S. A.; Elliott, C. M.; Contado, C.; Caramori, S.; Bignozzi, C. A. *Journal of the American Chemical Society* **2002**, *124*, 11215–22.

- (73) Kay, A.; Grätzel, M. *Solar Energy Materials and Solar Cells* **1996**, *44*, 99–117.
- (74) Nam, J. G.; Park, Y. J.; Kim, B. S.; Lee, J. S. *Scripta Materialia* **2010**, *62*, 148–150.
- (75) Kanciurzevska, A.; Dobruchoska, E.; Baranzahi, A.; Carlegrim, M.; Fahlman, M. *Journal Optoelectronics and Advanced Materials* **2007**, *9*, 1052.
- (76) Wang, M.; Anghel, A. M.; Marsan, B.; Cevey Ha, N.-L.; Pootrakulchote, N.; Zakeeruddin, S. M.; Grätzel, M. *Journal of the American Chemical Society* **2009**, *131*, 15976–7.
- (77) Jiang, Q. W.; Li, G. R.; Gao, X. P. *Chemical Communications* **2009**, 6720–2.

Chapter 2. Method Development and Reproducible Fabrication of Standard Dye-Sensitized Solar Cells

2.1 Introduction

An issue that is rarely addressed in the solar cell community is the ability to produce solar cells reproducibly. Often in the literature it is unknown if a single solar cell produced a J-V curve or if a representative curve of a set of multiple cells is being shown. Also when efficiency parameters are listed it is unbeknownst if they correspond to a single cell or subsist as the average of a number of cells tested. Also rarely seen are standard deviations to show consistency of results. We think it is important to know whether a result was achieved once or multiple times, and with one cell or multiple cells, reproducibly. It is important to be able to achieve a result repeatedly. There have been a couple of reports that have addressed reproducibility of solar cell fabrication, simply by reporting an error, or outlining a reproducible semi-automated manufacturing method.¹⁻⁴

Our goal with this study is two-fold. First, identify and remove variability in DSSC construction and second, build on this method to incorporate new materials. The goal of fabricating solar cells with a consistent performance provides us a standard baseline to compare any future changes to the cells that we make. When varying a component of the cell it is important to know if the modification has improved or worsened the general DSSC function and more specifically, which efficiency parameter(s) it has affected. Through this study, we have established an improved, reproducible standard procedure for the fabrication of solar cells with standard performance metrics. We have developed the set method further to incorporate new compounds and materials. We change a single component of the cell, so any differences

in efficiency are a result of that change, which are easily compared to the standard allowing us to gauge how their addition affects solar cell performance. We systematically identified sources of variability and hindrance to function in the fabrication process and eliminated them. Component by component, enhancements were made through higher quality materials, refined handling, improved and more consistent methods that were acquired through honed techniques and literature advancements. Our goal is not to make the most efficient solar cells, rather cells that are invariable, providing us the necessary baseline to assess the modification and its impact on the overall solar cell efficiency.

The solar cells fabricated at the beginning of this study exhibited extremely low performance; they had low current and voltage and quite significant resistive losses. Through meticulous investigation of the cause of these losses we were able to identify how changes to the cell affect cell function and we were able to achieve a substantial improvement in cell performance.

2.2 Experimental

2.2.1 General. All reagents were used without further purification unless otherwise noted. TEC-15 (15 Ω/mm^2) fluorine-doped tin oxide (FTO) coated glass was purchased from Hartford Glass Co. Transparent titania paste, DSL 18NR-T, was purchased from Dyesol, hydrogen hexachloroplatinate (IV) hydrate (40% Pt) and iodine (resublimed, 99.5%) were purchased from Acros Organics and 4-*tert*-butylpyridine was purchased from TCI America Inc. Anhydrous 2-propanol (99.5%), HPLC grade acetonitrile, lithium iodide were purchased from Sigma Aldrich. Tape for printing mask was 3M Scotch 811, and the silver conductive epoxy (8331G) was purchased from Fulton

Radio Supply Co. Homemade titanium dioxide sol-gel paste and 100 μm heat-sensitive polymer sheets was obtained from Prof. Gerry Meyer's research group at Johns Hopkins University. An electrically heated furnace was purchased from Cress Manufacturing Co.; Model C601/SD Ser. No. 0910. Perkin Elmer Lambda 1050 Spectrophotometer equipped with a 150 mm InGaAs Integrating Sphere was used for all transmittance data on films. 25 μm thick Surllyn was purchased from Solaronix, a Heathkit 30 V 3 A Power Supply provided the voltage source during resistive heating. Microscope cover glass at a thickness of 0.14 mm was from Corning, and a standard wheel carbide glass cutter was purchased from McMaster-Carr. Alconox Powder Detergent was used to wash FTO glass and the tube furnace was homemade.

The solar cell characterization was performed with a 450 W Xenon arc lamp interfaced with a MicroHR dual turret monochromator equipped with a 600 grooves/mm 500 nm blaze diffraction grating and a mirror (in the second position) were purchased from Horiba Jobin Yvon. Arc lamp profile was shaped with a AM0 and AM1.5 filter set purchased from Solar Light Co., and neutral density filters were purchased from Thorlabs, Inc. Photoelectrochemical measurements were conducted with a CH Instruments Inc. 650D Potentiostat equipped with a Dell computer with a Windows XP operating system to run the software. Power was monitored with a 3A-SH-ROHS Power meter from Ophir Optics and Uniblitz VCMD1 shutter and shutter driver from Vincent Associates Inc. was utilized to control the light.

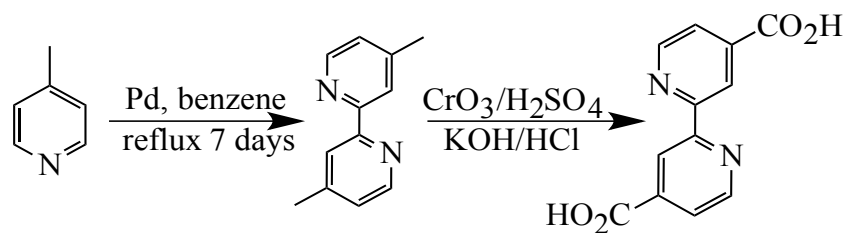
cis-Bis(isothiocyanato)bis(2,2'-bipyridyl-4,4'-dicarboxylato) ruthenium(II) was synthesized as described below. ^1H NMR and were measured with 300 MHz Varian UnityPlus, 500 MHz Varian UnityPlus, and Agilent DDR2 500 MHz spectrometers.

Absorption spectra of dye solutions were obtained on a Varian Cary 50 spectrophotometer. IR spectra were taken on a Mattson Galaxy 5000 FTIR. Elemental analysis was taken by Midwest Microlab, LLC. Electrospray mass spectra (ESI-MS) were obtained from the staff of the Michigan State University Mass Spectrometry Facility. The characterization data of N3 is included in the Appendix at the end of this chapter.

2.2.2 2,2'-Bipyridyl-4,4'-dimethyl (dmb). Dmb was synthesized via a modified literature procedure.⁵ 4-Picoline was dried over 20% by volume of 1:1 activated carbon and sodium or potassium hydroxide for at least two days, filtered, then put over 5 g/L of calcium hydride and let sit over night. It was refluxed over calcium hydride for 2-3 hours then distilled under reduced pressure. 220 mL provides ~200 mL of pure, colorless 4-picoline. 9.5 g of 10% palladium catalyst over carbon was added and refluxed for at least seven days, 75 mL of benzene was added for the last hour of reflux, then let cool. The solid was separated by distillation, then ethyl acetate was added to facilitate filtering on a medium frit. The solid was recrystallized from hot ethyl acetate into white tree-like crystals, and the orange filtrate was left to evaporate creating large single crystals with orange residue, which can be rinsed off with water. ¹H NMR (CDCl₃, 300 MHz): δ 2.41 (s, 6H), 7.11 (dq, J = 5 Hz, 2H), 8.20 (s, 2H), 8.51 (dd, J = 4 Hz, 2H).

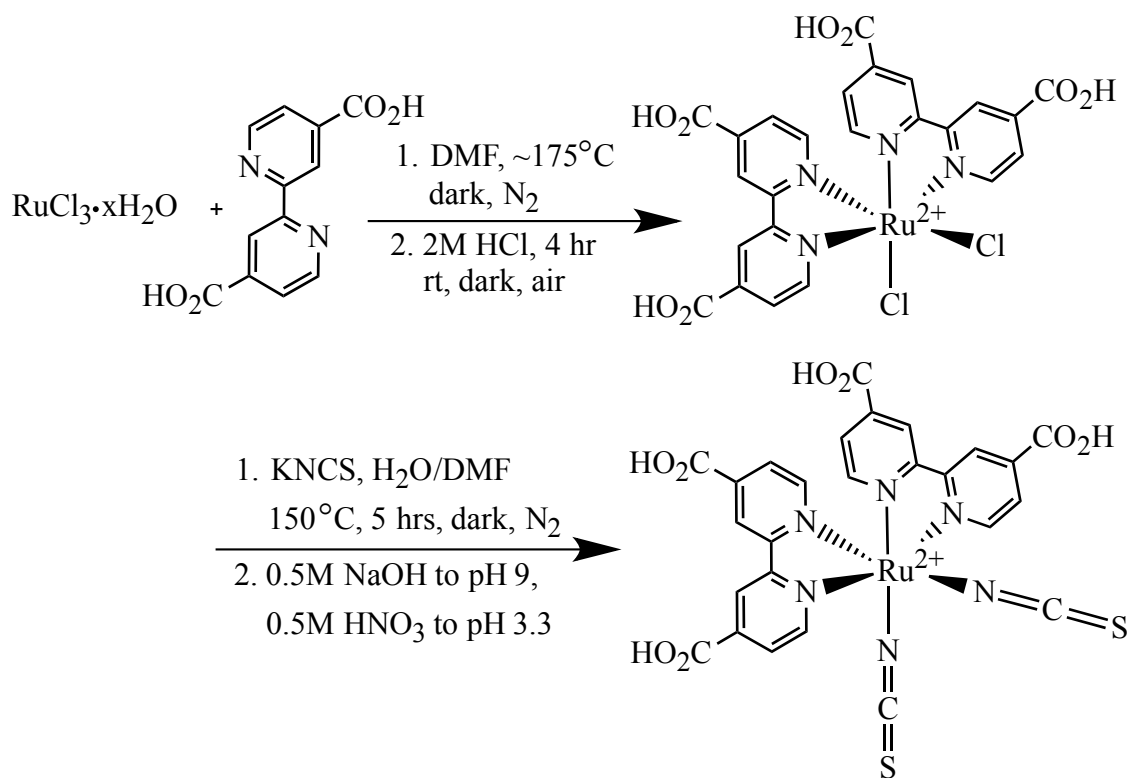
2.2.3 2,2'-Bipyridyl-4,4'-dicarboxylic acid (dcbpy). The full reaction from picoline to dmb to dcbpy is shown in Scheme 2-1. Dcbpy is prepared via a modified literature procedure⁶. 4.26 g (23.2 mmol) of dmb is dissolved into 75 mL of concentrated sulfuric acid while stirring vigorously in a beaker that is cooled to below 0°C with a

salted ice bath. 14.2 g (142 mmol) of crushed chromium (IV) oxide is added very slowly while maintaining a temperature of below 3 °C. As the chromium oxide is added the solution turned from clear tan to a deep green color. Once all the CrO₃ is added the solution is allowed to warm up to less than 50 °C and stir overnight. The mixture was heated at 70-75 °C for an hour. Not all of the chromium oxide dissolves, but it is soluble in water so can be rinsed out in the next step. The deep forest green suspension is then poured over a 2 L beaker of ice wherein a white precipitate forms and the mixture is a bright milky green with red solid flakes of undissolved CrO₃ is seen. The solution is allowed to settle and the excess green water solution is decanted off the top before filtering on a medium porosity frit, a Buchner funnel or separated using a centrifuge. Often the white dcbpy will be colored yellow, pink or gray and can be further purified by converting to the sodium salt, Na₂dcbpy. Water is added to impure dcbpy in a beaker. While stirring, crushed sodium hydroxide is added until all dcbpy is dissolved, therefore deprotonated, the solution is filtered if necessary, then more sodium hydroxide is added until the white Na₂dcbpy precipitate is formed. The solid is then filtered on a medium frit. Often more solid can be recovered from the filtrate with additional sodium hydroxide. The fine needle like white solid is re-dissolved in water and acidified with hydrochloric acid while vigorously stirring, and then the hard plate-like acid is filtered on a medium frit and dried under vacuum. ¹H NMR (NaOD/D₂O, 300 MHz): δ 8.55 (d, J = 6 Hz, 2H), 8.17 (s, 2H), 7.633 (dd, J = 6 Hz, 2H).



Scheme 2-1. Preparation of 2,2'-bipyridyl-4,4'-dicarboxylic acid.

2.2.4 *cis*-Bis(isothiocyanato)bis(2,2'-bipyridyl-4,4'-dicarboxylato) ruthenium(II) (N3). This compound is synthesized using a modified literature procedure⁷ and the full preparation is shown in Scheme 2-2. 0.52 g (2.5 mmol) of Ruthenium (III) chloride hydrate is dissolved in 50 mL of bubble degassed *N,N'*-dimethylformamide while stirring in the dark. 0.94 g (3.9 mmol) of dcbpy is added to the flask and the reaction is submerged into an oil bath that was at 175 °C. The reaction is monitored by UV/Vis as it progresses; absorbance is measured by dilution of the reaction in ethanol. Once the ratios of the absorbance peaks were ~3.33 : 1.05 : 1 the reaction flask is removed from the oil bath. The typical way in which the reaction proceeded via the absorbance of the absorption bands is shown in Table 2-1. The literature published a reaction time of 3 hours, I did not find this amount of time necessary to obtain the desired ratio of the absorbance peaks. I found that the absorbance values approach the desired ratio and then the first peak grows while the other two remain the same, so the reaction can be stopped once the first peak gets to its lowest value or just as it first starts increasing.



Scheme 2-2. Preparation of *cis*-Bis(isothiocyanato)bis(2,2'-bipyridyl-4,4'-dicarboxylato)ruthenium(II).

Time Passed	Abs @ 316nm	Abs @ 414nm	Abs @ 565nm	Ratio
3 mins	1.01	1.48	0.166	6.06 : 8.90 : 1
30 mins	2.87	0.806	0.734	3.90 : 1.10 : 1
40 mins	2.52	0.706	0.664	3.80 : 1.06 : 1
50 mins	3.10	0.959	0.908	3.42 : 1.06 : 1

Table 2-1. Reaction monitoring of the N3 precursor. Characteristic progression of the UV/Vis peak absorbance ratio, in ethanol.

Once cool, the reaction was filtered through a medium porosity frit to rid any remaining solid. The DMF is removed at 44 °C at reduced pressure, it tends to bump, so careful vacuum is added, equilibrated for 30 mins and then slow heating. 10 mL of 2 M hydrochloric acid is added to the flask and stirred for 4 hours in the dark, careful to make sure the entire sticky deep purple red solid is able to react. The solid is filtered on a medium frit and dried under vacuum in a dessicator. This product *cis*-bis(2,2'-bipyridyl-4,4'-dicarboxylato) dichloride ruthenium (II), Ru(dcbpy)₂Cl₂, is not purified and used directly in the next step of the reaction. Typically ~60-70% of impure product is yielded.

2.91 g (30 mmol) of KNCS is dissolved in 10 mL of DI water and 25 mL of DMF is added and the solution is bubble degassed. 0.55 g (9.1 mmol) of Ru(dcbpy)₂Cl₂ was introduced into the flask in the dark along with 25 mL more of degassed DMF. The reaction flask is submerged into an oil bath at 150 °C and maintained at 145-150 °C for 5 hours in the dark and then removed from heat and allowed to cool. The reaction mixture is filtered through a medium frit and the water and DMF are removed under vacuum as before, water is removed at 30 °C and the DMF again at ~45 °C.

This next step is always performed with haste in the dark to reduce ligand substitutions or rearrangements; how long the compound is in solution is recorded in case isolation proves to be an issue to see if there is a correlation to how long the compound is in solution and how difficult it is to purify. The red-purple residue is dissolved in DI water and the product is acid-base recrystallized. The pH is monitored with a calibrated pH meter as the pH is increased to ~9 with 0.5 M NaOH to completely dissolve the product and then it is filtered through a medium frit. The pH of the solution is decreased to 3.3 with 0.5 M HNO₃ to precipitate the product and placed in the fridge overnight. The product is filtered on a medium frit—often gravity then suction filtration works best on

molecules with acid groups—and rinsed with pH 3.5 HNO₃ water. The solid is dried under vacuum. Sometimes a second or third acid-base recrystallization is required if the NMR shows impurities. Yield: 0.42 g (22%). ¹H NMR (0.05 M NaOD/D₂O, 300 MHz): δ 7.24 (dd, J = 6 Hz, 2H), 7.55 (d, J = 6, 2H), 7.91 (dd, J = 6 Hz, 2H), 8.50 (s, 2H), 8.66 (s, 2H), 9.27 (d, J = 6 Hz, 2H). TOF-MS [ESI, *m/z* (rel. int.)]: 352.0 (100) [C₂₆H₁₄N₆O₈RuS₂]⁻², 704.9 (20) [C₂₆H₁₅N₆O₈RuS₂]⁻¹. IR (KBr, cm⁻¹): 3444.2 m, 2453.0 w, 2362.3 w, 2110 br, 2075 m, 1716 s, 1652.7 s, 1405.8 s, 1230.3 s. Elemental Analysis for C₂₆H₁₆N₆O₈RuS₂·4H₂O, Calculated: C, 40.15; H, 3.11; N, 10.81. Found: C, 40.35; H, 2.46; N, 10.74. UV/Vis (EtOH) λ (rel. int.): 315 nm (3.62), 398 nm (1.02), 537 nm (1.00).

2.3 General Schematic for a DSSC Device

2.3.1 Components of a DSSC. In a DSSC, there are five main components, seen in Figure 2-1. The dye that absorbs the light, the nanocrystalline semiconductor that secures the dye in a porous template, the redox couple that regenerates the oxidized dye, the catalyst of the counter electrode that reduces the redox couple and lastly the substrate materials that provide a sturdy construction and complete the circuit.

The first event that must occur in any solar cell is absorption of light. For DSSCs this is done using light-absorbing molecular compounds attached to a small band gap nanocrystalline semiconductor material. In our solar cells we use polypyridyl transition-metal compounds of iron and ruthenium to absorb photons and the semiconductor is nanocrystalline titanium dioxide. When light is absorbed, electrons are promoted into

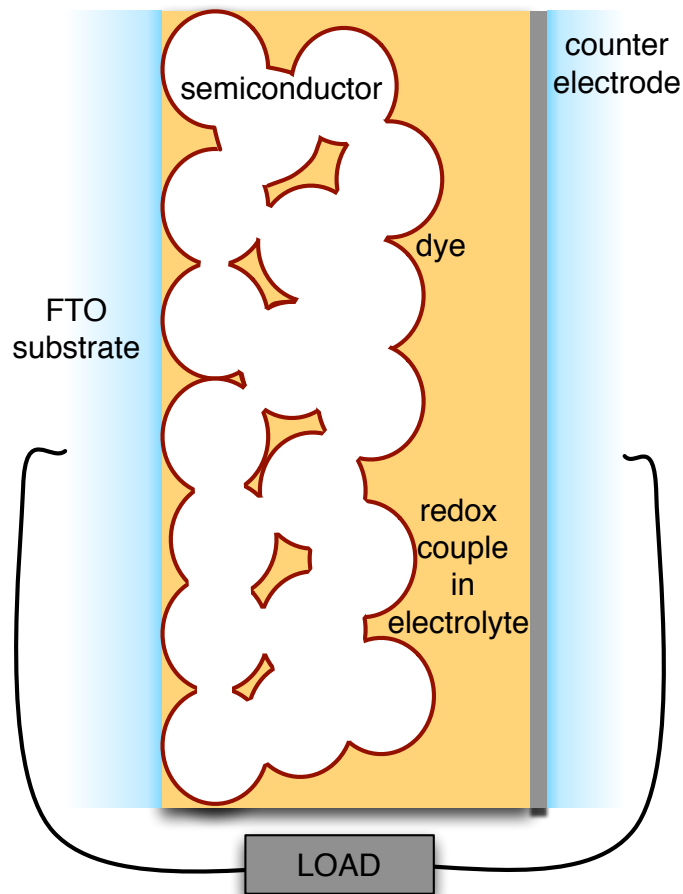


Figure 2-1. Components and Layout of a Dye-Sensitized Solar Cell.

ligand-localized orbitals, leaving a positive charge on the metal. Effective charge separation must be maintained for a productive cell, this occurs with electron injection into the TiO₂. The electrons are collected at the FTO back contact, which is connected to an external circuit. The oxidized dye must be regenerated with a reduction that occurs from a redox shuttle in the electrolyte, in our cells, primarily it is the iodide/triiodide pair dissolved in acetonitrile. The oxidized redox species is in turn reduced by the counter electrode, a platinum catalyst, via movement of current through the external circuit.

2.3.2 Favorable Characteristics of DSSC Components. *The Chromophore.*

Optically, the dye must strongly absorb light in the visible region. The wider its absorption spectrum and the greater the absorption coefficients the more photons can be captured from the solar spectrum. To initiate charge separation, the visible absorptions must be one or more metal-to-ligand charge-transfer (MLCT) bands inherent to transition metal compounds. MLCTs extract an electron from the metal center and promote it to an orbital on the periphery of the ligand. The dye must also be stable, in both oxidation states, and able to be reproducibly converted between the two easily without degradation. The chromophore must have anchoring groups to provide stable attachment to the TiO₂ and also must provide good orbital overlap between the ligand and the semiconductor. The orbital overlap provides a pathway of electronic communication so once an electron is in the ligand-based orbital, electron injection is favorable. Kinetically, the existence of the excited state of the dye, the MLCT state, must be long-lived enough so that injection of the electron into the titanium dioxide semiconductor is allowed to occur.

The Semiconductor. The semiconductor must not absorb much light, if any, in the visible region of the solar spectrum. A semiconductor that absorbs light creates holes in its valence band forming an unfavorable pathway where holes can oxidize the reduced dye. The semiconductor should also be nanocrystalline. The high surface area increases the number of sites for dye adsorption and magnifies the absorption cross section substantially within a given area as compared to a monolayer of dye⁸. The semiconductor should have very few vacancy or trap sites, the more homogeneous and pure a substrate is, the more efficiently electrons can be collected. The semiconductor should be

chemically stable in the reaction conditions the cell will be under. Also, the conduction band edge should rest at a reasonable negative energy to allow MLCT excited state injection.

The Redox Couple and Electrolyte. The redox couple should be completely reversible where each form of the species is stable and efficiently converted between them. The redox couple potential should be sufficiently negative to re-reduce the oxidized dye, negative enough to provide the driving force necessary, as this reaction is predominantly in the Marcus normal region. At the same time, the redox potential should not be so negative as to waste attainable energy. As the potential redox couple moves negative it reduces V_{OC} , which lowers the amount of energy producible by the solar cell. Regenerating the redox mediator should also be facile with a suitable counter electrode material.

The Counter Electrode. The counter electrode should be a robust electrocatalytic material so that overall no chemical reactions occur at the electrode surface. It should have high exchange current density, therefore a low charge-transfer resistance, and a low sheet resistance making it kinetically easy for the passage of electrons to reduce the oxidized redox species. Also the Fermi level of the counter electrode should be negative enough to create the driving force to reduce the redox couple in solution⁹. Benefit also arises from counter electrodes being reflective when illuminating solar cells through the photoanode side.

External Substrate Materials. In our DSSC, the photoanode and the counter electrode need to be laid onto a material for fabrication. In our design, this material needs to be rigid; flexible substrates would alter the integrity of the films we use. The material needs to be highly conductive or have a conductive coating so electrons can be collected and moved along without losses. The material should not absorb visible light nor reflect or scatter much incident light; it should simply pass light through. The material also needs to have a quasi-Fermi level below that of the semiconductor for efficient collection. The attached leads should also be extremely conductive, as well as the epoxy, which also should cure in a relatively short amount of time.

2.4 Development of a Standard Reproducible Method

2.4.1 General Fabrication Procedure. The fabrication of DSSCs was observed at two different laboratories. The first was at Prof. Gerry Meyer's lab at Johns Hopkins University. This observation provided the basis of how standard solar cells are fabricated, the basic methodology, which we developed upon. After a couple of years of experience we have had interactions with Prof. Tom Hamann's lab, here at Michigan State University. Communications with Prof. Hamann's lab have allowed both labs to learn from each other and we have further improved our solar cell design with their aid.

A generic DSSC fabrication procedure follows. FTO glass is cut into each electrode size; a hole is sandblasted into the cathode slide and then the slides are cleaned with soap and acetone. TiO₂ is doctor-bladed onto the conductive side of the FTO glass using a cut-out tape mask and then it is sintered at a temperature profile that ranges from 350 °C to 500 °C. Once cooled to 90 °C it is immersed into ~0.3 mM N3 in ethanol solution and dyed overnight in the dark. The cathode has 5 mM H₂PtCl₆ drop-caste onto

each FTO slide to give a density of platinum of $5 \mu\text{g}/\text{cm}^2$ ¹⁰. The two electrodes are sealed together by melting a heat-sensitive polymer between them, the electrolyte is injected and electrodes are applied. Using this basic methodology, small improvements were made to the procedure throughout the various fabrication steps.

2.4.2 Systematic Removal of Sources of Variability to the Fabrication Procedure. The injection method was the first identifiable source of variance we made changes to. Once the photoanode is dyed and the counter electrode has a wire attached the electrodes are sealed together and injection of the electrolyte occurs. The customary method of injection is via a single drilled hole through the back of the counter electrode. The sealed but empty solar cell is placed cathode side-up inside of a dessicator with a vacuum adapter. A drop or two of the electrolyte is placed on the drilled hole and a vacuum was pulled on the dessicator using a water aspirator. As the pressure in the dessicator decreases, the air from inside of the solar cell bubbles through the electrolyte and the electrolyte is pulled into the cell. I found issues with this method immediately. The performance of cells is dependent on electrolyte; this is why the components of the electrolyte are of certain concentrations. Both iodine and acetonitrile are extremely volatile so the mass and volume that were measured are certainly changing as the vacuum is applied. Also there are time variances between cells on how long the vacuum was administered in order to inject the electrolyte into the cell. This was due to minute differences in the position of the hole with respect to the dyed TiO_2 film, also the differences in the roughness of the sandblasted hole and how large the air bubbles were—how easily an air bubble could emerge from the cell. Also one could rarely get all air out of the cells and the amount of air that remained varied. All of these variances created

uncertainty between the cells, the concentration of electrolyte certainly changed between cells of the same batch and different amounts of electrolyte were in contact with the photoanode.

A batch of five cells were fabricated and tested, a representative curve is seen in Figure 2-2 and average efficiency parameters and their standard deviations are seen in Table 2-2. The curve shown has a linear $V = IR$ component that is overpowering the signal, shifted from zero by the photocurrent. Low efficiency parameters and the shape of the curve indicate strong resistive losses for this set of cells. The cells also have large variances demonstrated in the standard deviations. The coefficient of variance (CoV), or the relative uncertainty, the percentage ratio of the standard deviation to the absolute value of the average is 3% for V_{OC} but 20-45% for J_{SC} , ff and η . Improvements to the method are needed.

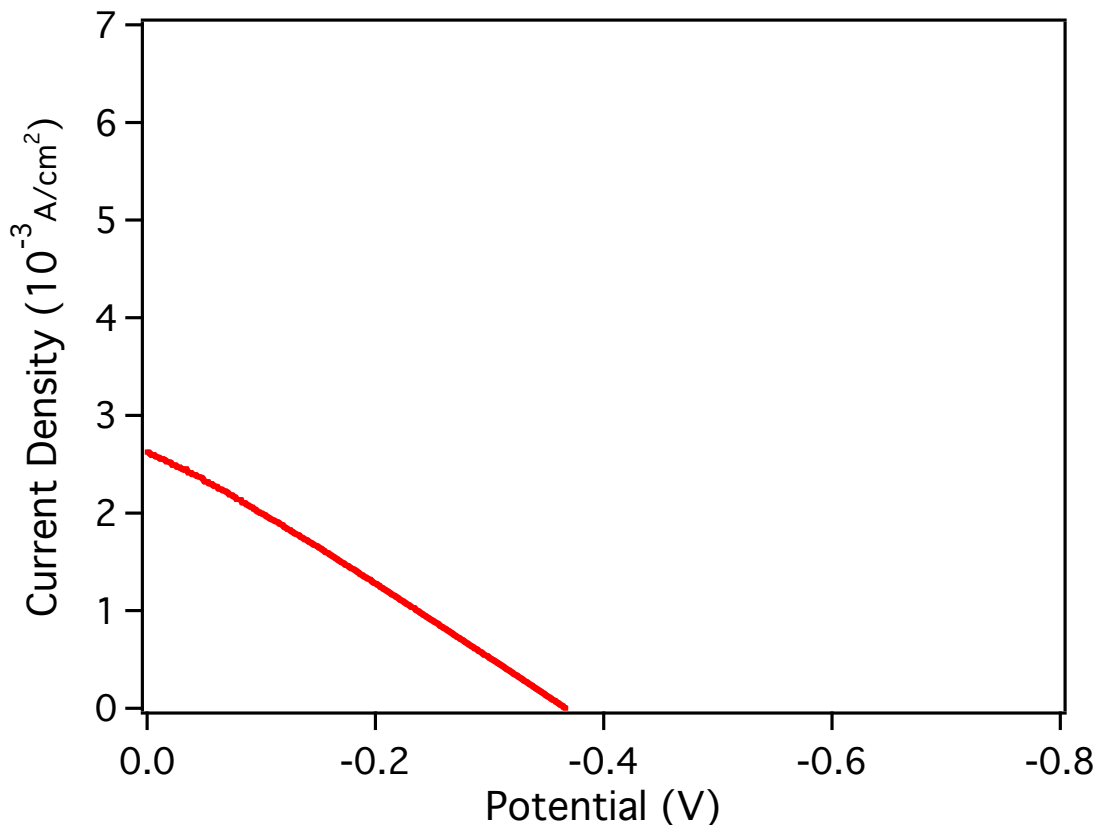


Figure 2-2. Representative J-V curve for a set of 5 solar cells fabricated using a one-hole vacuum desiccation method to inject electrolyte. N3 dye, electrolyte: 0.3 M LiI, 0.03 M I₂ in MeCN, thermalized Pt counter electrode.

	Voc	Jsc	ff	η
Average	-0.383 V	2.48 mA/cm ²	0.29	0.28%
Std Dev ±	0.011 V	0.74 mA/cm ²	0.06	0.13%

Table 2-2. Efficiency parameters for 5 solar cells fabricated using a one-hole vacuum desiccation method to inject electrolyte. N3 dye, electrolyte: 0.3 M LiI, 0.03 M I₂ in MeCN, thermalized Pt counter electrode.

Next I decided to try out a new configuration that used two holes for the injection of electrolyte instead of one. This allows two separate areas of the cell to expunge air and gain electrolyte, hopefully reducing the vacuum time and the number of air bubbles that remained. This change would conceivably decrease variance in the set and improve performance. A batch of cells was fabricated using a two-hole injection method, with all other components remaining the same. Indeed, a shorter vacuum time was needed along with a lower number of air bubbles left inside of the sealed cell. The representative curve is seen in Figure 2-3 and the averages and standard deviations are in Table 2-3.

The J-V plot is now displaying the distinctive curvature showing that its behavior being governed by the diode equation. Based on these results, injection using two holes has improved the method. All parameters increased from the previous data set, except for J_{SC} which is within error. V_{OC} increased by 3%, ff and η both elevated ~20%. Resistive losses have decreased with the method enhancement, which improved the overall efficiency. Relative uncertainty also improved to 3% for the fill factor; the others remained similar to the previous set except for η , which worsened (53%). Therefore the method is becoming more consistent between each cell, especially for V_{OC} , the maximum voltage attainable by the cell, and ff , how ideal the cell is performing.

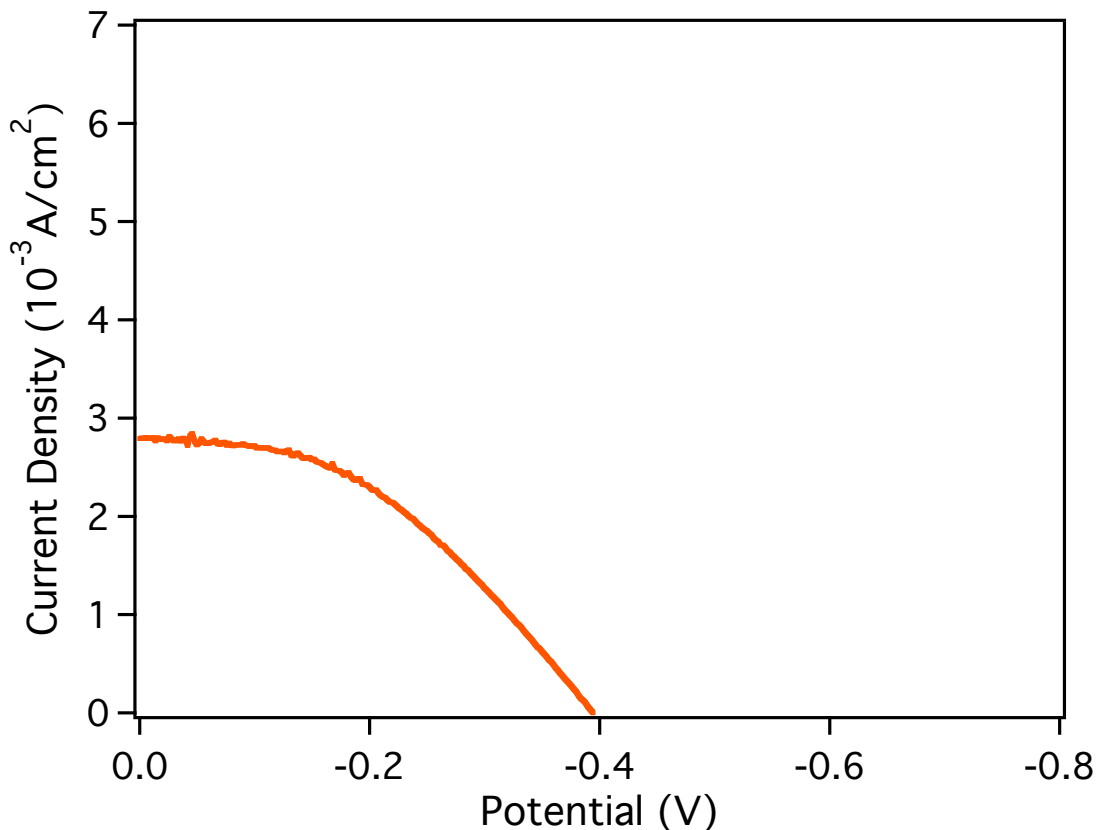


Figure 2-3. Representative J-V curve for a set of 9 solar cells fabricated using a two-hole vacuum dessication method to inject electrolyte. N3 dye, electrolyte: 0.3 M LiI, 0.03 M I₂ in MeCN, thermalized Pt counter electrode.

	Voc	Jsc	ff	η
Average	-0.398 V	2.39 mA/cm ²	0.34	0.34%
Std Dev ±	0.010 V	0.68 mA/cm ²	0.01	0.18%

Table 2-3. Efficiency Parameters for 9 solar cells fabricated using a two-hole vacuum dessication method to inject electrolyte. N3 dye, electrolyte: 0.3 M LiI, 0.03 M I₂ in MeCN, thermalized Pt counter electrode.

In the literature 4-*tert*-butylpyridine (TBP) has been used as an additive in iodide/triiodide-based electrolytes to enhance cell performance¹¹. TBP passivates the TiO₂ active surface sites where dye molecules do not adsorb. It functions to hinder electron recombination that occurs between the TiO₂ and triiodide in solution by blocking triiodide activity at the titania surface^{12,13}. In lithium iodide based electrolytes, TBP also negatively shifts the conduction band edge of the TiO₂ by blocking Li⁺ ions from intercalating the film, because Li⁺ ions positively shifts the band edge¹⁴.

0.2 M TBP was added to the electrolyte for the next batch of cells and a stark improvement of performance was seen as is shown in Figure 2-4 and Table 2-4. The most dramatic change is seen in the open-circuit voltage improving from 0.398 V to 0.679 V. The V_{OC} is a measure of the maximum voltage output of the cell. It is affected by recombination, the dark current, which is the biggest hindrance of solar cell performance. The movement of the conduction band edge and the redox couple potential also affect V_{OC} . So the strong negative shift in V_{OC} is indicative of the TBP both blocking Li⁺ ions and triiodide species at the TiO₂ surface. It is causing a shift of the conduction band edge more negative and also blocking recombination back into the electrolyte.

The fill factor also improved significantly, indicating a decrease in the series resistance within the cell. J_{SC} also increased due to the decrease in recombination, less electrons were captured by triiodide so more current was detected when all electrons are allowed to pass through the cell with no barrier. All of these parameters improved the overall efficiency of the cell, which is also seen, improving from 0.34% to 1.98%.

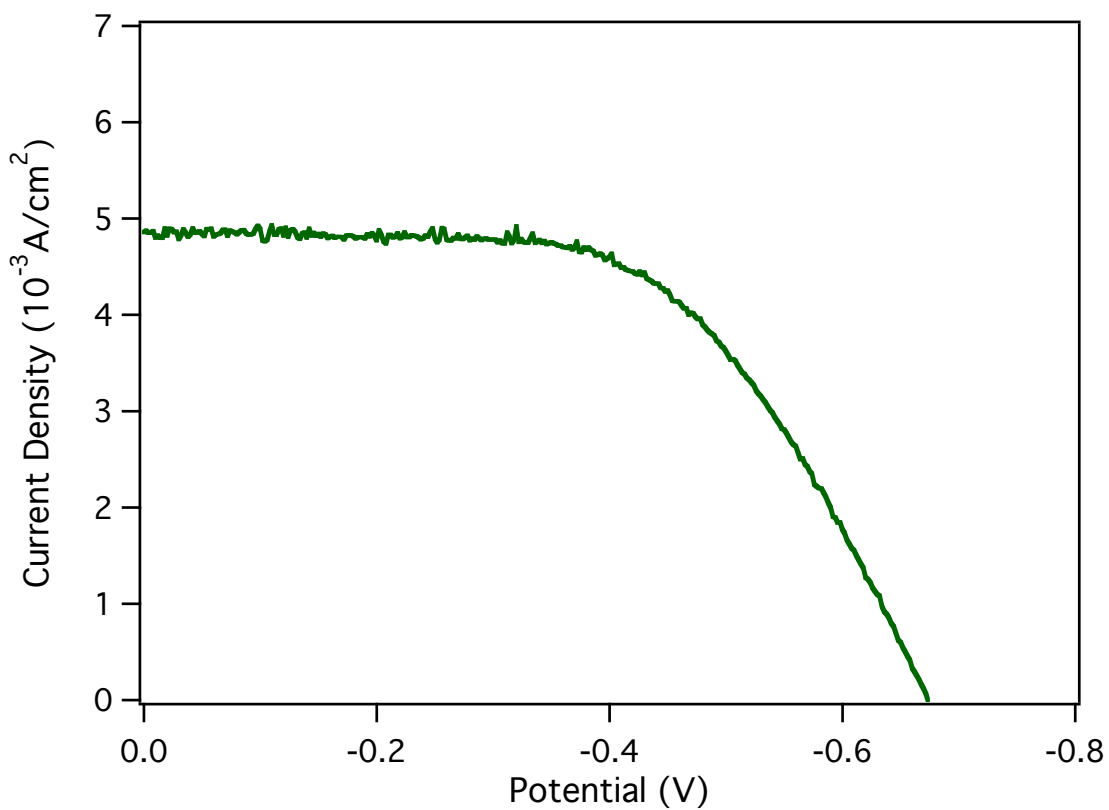


Figure 2-4. Representative J-V curve for a set of 11 solar cells fabricated with TBP as an additive in the electrolyte. N3 dye, electrolyte: 0.3 M LiI, 0.03 M I₂, 0.2 M TBP in MeCN, thermalized Pt counter electrode.

	Voc	Jsc	ff	η
Average	-0.679 V	5.03 mA/cm ²	0.58	1.98%
Std Dev ±	0.016 V	0.46 mA/cm ²	0.06	0.27%

Table 2-4. Efficiency Parameters for 11 solar cells fabricated using a TBP additive in the electrolyte. N3 dye, electrolyte: 0.3 M LiI, 0.03 M I₂, 0.2 M TBP in MeCN, thermalized Pt counter electrode.

Variability between cells has also decreased with the relative uncertainty of each parameter below 15%.

The injection method could also be reasonably improved further as bubbles continued to remain within the cell after injection and the electrolyte concentration, although now under less vacuum with the two-hole method, it was still undoubtedly changing and presumably inconsistent cell to cell. A new method was decided upon using a needle-less syringe. The electrolyte was drawn into the 1mL syringe the small plastic opening was placed around the opening of one of the counter electrode holes and the electrolyte was pushed into the cell. The second hole provides the escape for the air within the sealed cell. Using this method very little to no concentration changes should occur and it was found that very few if any bubbles remained once the electrolyte has been injected. If any bubbles do occur, one can rid them by withdrawing the electrolyte from the cell using the syringe and then simply re-injecting more electrolyte into the cell.

This improvement in electrolyte injection was made at the same time as two other changes to the method so any change in cell performance could be due to all or any one of the three alterations. The second change made in this batch of cells is with the material that seals the cell. A change was made to use Surlyn, the heat-sensitive polymer that the majority of groups utilize in solar cell fabrication. We chose the most widely used thickness of Surlyn, 25 μm . These cells were also the first batch tested on our own new optimized setup, which is described later. Previously, we were gratefully utilizing Prof. Tom Hamann's equipment to test our solar cells. All future batches of cells will be tested on our own setup unless otherwise noted.

This batch of cells' representative curve is shown in Figure 2-5 and efficiency data is seen in Table 2-5. The improvement for this iteration is seen in the short-circuit current density increasing by 27% from 5.03 mA/cm² to 6.4 mA/cm². The fill factor and the open-circuit voltage decrease by 10% but the overall efficiency still increases by 6%. It is not known why these two parameters would decrease. A DSSC is made up of many components, and sometimes it was found that a batch of cells could seem like everything went well, no major indications of a problem and for unknown reasons the metrics on a cell or a group of cells or the entire batch would decrease. Since there was no particular insight to why this would occur, the decreases were assumed to be unseen contaminations along the way in the fabrication process.

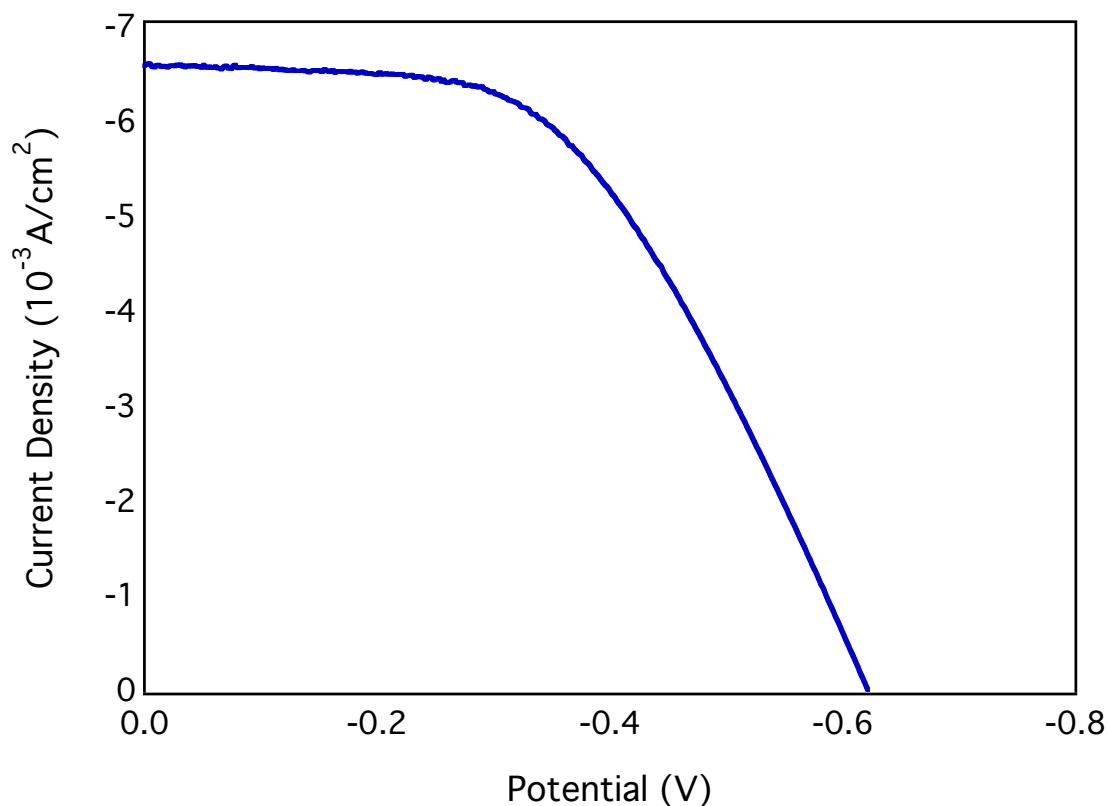


Figure 2-5. Representative J-V curve of a set of 5 solar cells fabricated with 25 μm Surllyn and injection of electrolyte with a syringe. Tested on our new solar simulation setup. N3 dye, electrolyte: 0.3 M LiI, 0.03 M I_2 , 0.2 M TBP in MeCN, thermalized Pt counter electrode.

	Voc	Jsc	ff	η
Average	-0.634 V	6.38 mA/cm ²	0.51	2.09%
Std Dev \pm	0.016 V	0.53 mA/cm ²	0.05	0.17%

Table 2-5. Efficiency Parameters for a set of 5 solar cells fabricated with 25 μm Surllyn and injection of electrolyte with a syringe. Tested on our new solar simulation setup. N3 dye, electrolyte: 0.3 M LiI, 0.03 M I_2 , 0.2 M TBP in MeCN, thermalized Pt counter electrode.

Development of the dyeing procedure was also necessary. Most groups that use N3 as their chromophore use ethanol as their dyeing solvent—N3 is not incredibly soluble so it readily adsorbs to the TiO₂. But since the dye is sparingly soluble we observed that not all weighed solid goes into solution, so the concentration is not what is intended. Sonication was utilized which improved dissolution but it still did not completely disperse. An alteration to the pH of the dye solution but we wanted to remain consistent with the ease of the literature by using a simple solvent. A revision was added to the procedure to grind up the very hard, crusty crystals into a fine powder with a mortar and pestle before dissolving. This seemed to solve the issue with a little sonication for an additional push. At this stage I am also taking care to dye the slides for a set range of time, 20-28 hours, to remain consistent batch to batch.

Also in recent years fabrication procedures in the literature have included a pre-heat step for the slides before they are submerged in dye solution. Typically the printed TiO₂ slide is heated to 90-100 °C and this heat functions to aid in the adsorption process. A batch of solar cells was fabricated with only this change, the results are seen in Figure 2-6 and Table 2-6. All values are within the error of the last batch of cells but the major improvement noticed in this batch is the consistency seen in the standard deviation and the relative uncertainty which decreased to be below 10% for each parameter. A steady honing of the method has continued and it becomes more reproducible with each successive batch of cells.

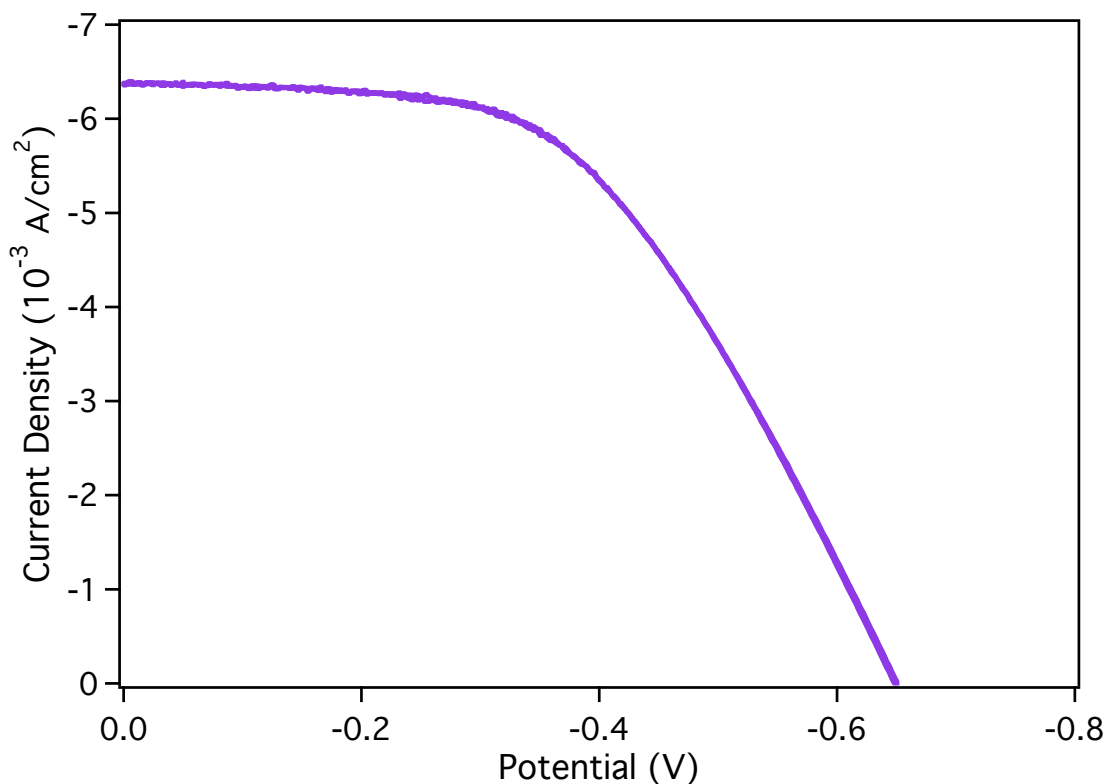


Figure 2-6. Representative J-V curve of a set of 8 solar cells. The TiO₂ slides were pre-heated to 90 °C before being immersed in dye solution. N3 dye, electrolyte: 0.3 M LiI, 0.03 M I₂, 0.2 M TBP in MeCN, thermalized Pt counter electrode.

	Voc	Jsc	ff	η
Average	-0.660 V	6.04 mA/cm ²	0.53	2.11%
Std Dev ±	0.020 V	0.55 mA/cm ²	0.05	0.13%

Table 2-6. Efficiency parameters for a batch of 4 solar cells fabricated with new syringe injection method of electrolyte, 25 μm Surlyn, tested on new solar setup. N3 dye, electrolyte: 0.3 M LiI, 0.03 M I₂, 0.2 M TBP in MeCN, thermalized Pt counter electrode.

2.4.3 Other Notable Improvements. *Electrolyte.* For all previous batches of solar cells, reagent grade acetonitrile was used. Reagent acetonitrile has a purity $\geq 99.50\%$ with a water content $\leq 0.3\%$ and residue on evaporation $\leq 0.005\%$. It was found in the literature that water affects the performance of DSSCs that contain non-aqueous electrolytes. Water actively interacts with the TiO_2 surface displacing TBP and Li^+ ions affecting recombination and conduction band edge position and results in a decrease in the short-circuit current density.¹⁵ Dyed TiO_2 slides exposed to water is shown to cause desorption of N_3 , affect its thiocyanate ligand environment and the position of its HOMO energy with respect to its LUMO, shifting the absorption spectra blue.¹⁶ Water has also been reported to induce degradation in DSSCs.¹⁷

An HPLC grade acetonitrile was purchased; its purity is $\geq 99.93\%$ with a water content $\leq 0.01\%$ and residue on evaporation $\leq 0.0002\%$ which is a magnitude less water content and other residue present. This higher purity acetonitrile is used on all subsequent solar cell electrolytes. A fresh bottle is purchased every month and between uses the bottle is backfilled with nitrogen and Teflon tape and parafilm was used to seal the cap.

Active Area. Our group helped to decide on an area of TiO_2 that would be doctor-bladed on each slide based on the types of experiments we wanted to perform on the cells, so a single method of fabrication could be utilized for all cells. We wanted to be able to perform the standard solar characterization but also be able to perform laser experiments to look at injection times in full cells. Based on the magnitude of the laser energy density in the spot size used for these experiments, the sample cell would need to be translated. So ease and necessity resolved us to decide on a 1 cm by 1 cm square

printed area. Typical areas in the literature are less than 1cm^2 presumably because larger areas introduce more series and shunt resistance but the additional area is necessary for our application. A batch of DSSCs was fabricated with an active area of 0.25 cm^2 and there was no improvement of the characteristic resistance; the fill factor for these cells was within error compared to the 1 cm^2 .

Each tape mask used for each doctor-bladed slide is hand-cut using a razor blade. When a J-V curve is taken, the current detected is converted to current density by dividing by the active illuminated area. Towards the beginning of my cell fabrication procedure I would simply use the entire active area and divide by 1 cm^2 . But later, to omit any minute changes tape mask to tape mask, I began to use a black aluminum disk with a set cut-out in the center of an area equal to 0.3167 cm^2 and divide by this masked area when calculating current density. The mask removed any variances that may have been occurring during this part of the process.

Platinum Counter Electrode Preparation. The counter electrode slides must have holes put through them after they are cut to size in order to inject the electrolyte after sealing. During the first iterations of cells, the bare glass was sand blasted and noticeable scratches in the glass often occurred while sandblasting through the front or the back of the electrode. These scratches mar the FTO surface decreasing its homogeneity and increasing its resistivity, inducing losses in the performance of the cell, and also variances between cells. This method evolved where tape was applied to the glass before it was cut and sandblasted, which protected it from many major defects that could've been added during either process.

During the application of the H_2PtCl_6 solution we have also modified the method to reduce leaking through the holes or off of the edges of the glass. Albeit seemingly rather mundane to mention, I used to hold the glass by its edges and place all of the solution in one area, tilt the glass to spread the solution, then placing the glass slide onto the flat lab bench to dry before firing. The issues with this approach were three-fold. The solution leaked off the edges onto my gloves when the glass was handled by the edges. Also it is difficult to set down the glass without further disturbing the solution. Lastly, the solution, when placed in one area, tended to leak through the holes when tilted especially if a sandblasted hole was especially rough around its edges. The technique is now to rest the slide flat on my gloved hand and apply solution around all areas of the slide and then push the slide carefully off of my hand onto the lab bench to dry. This is a much more effective method to ensure even Pt coverage on the counter electrode slides.

The original publication by Papageorgiou et al. published a procedure for the firing temperature to be $385\text{ }^\circ\text{C}$ for 10 to 15 minutes, and not to exceed this temperature⁵. This is the temperature that all Pt counter electrodes were fired at until a personal communication with a student in Prof. Tom Hamann's group. He advised that not all of the Pt (IV) was shown to be completely converted to Pt (0) when heated at $385\text{ }^\circ\text{C}$, that heating at $400\text{ }^\circ\text{C}$ better reduces the Pt solution to zerovalency. Higher baking temperatures are seen in the literature with no mention of why the change was made or a reference to a previous study.^{18–22} Therefore this improvement to the method was also made to our procedure.

Baking method. The sintering procedure was modified since the very first iterations of solar cells. After the glass was cut and cleaned, the TiO₂ (Meyer lab) was doctor-bladed onto the FTO side of the glass. The glass slides were placed on a long thick glass piece, which was inserted into a tube furnace and fired at 420 °C for 30 minutes²³. The slides emerged after baking and the films were not uniform; they were colorless and transparent in some areas and white in others. At first, it was thought that the method of doctor-blading or the sol-gel paste utilized was causing the inhomogeneity, but after measuring the temperature of the tube furnace at different distances, it was found that there was a ~50 °C temperature gradient from the far end to the middle of the furnace, and another change in temperature from mid-furnace to the open end. Therefore, the slides were being baked at different temperatures. A new programmable furnace was purchased. This furnace allows one to set a series of temperatures that could include a ramp time and soak times at each temperature. So each set of cells is now baked identically to the last at stable set temperatures.

2.5 Standard Procedure for DSSC Fabrication

Batches of cells were either done in a set of four or eight. 20 cm by 20 cm FTO glass sheets were cut into 0.75” by 1” squares for the photoanode. The squares were sonicated in a solution of Alconox in DI water solution for 15 minutes, often this step was done twice depending on how dirty the glass or the resulting sonicated solution appeared. Then the slides are rinsed with DI water and sonicated for 15 minutes in DI water, rinsed and sonicated in acetone, and then rinsed and sonicated in isopropanol, then allowed to air dry or wiped dry with kimwipes.

Once the glass is clean, a ‘mask’ template for the TiO₂ films is constructed; a piece of weigh paper is covered in a piece of Scotch tape and is cut through both layers in a 1 cm by 1 cm square using a razor blade. Another removable piece of tape was overlaid onto the template and cut precisely to the 1 cm by 1 cm square using a sharp razor blade—razor blades are switched out when they no longer cut smoothly. Special care is taken that there are no ridges or bumps in the cutout, this creates ridges when the TiO₂ is doctor-bladed. The tape was applied to the center of the short edge of the conductive side of the FTO glass ~2-3 mm from the bottom edge. The uncovered area of the slide was protected with tape to protect it from being printed during doctor-blading seen in Figure 2-7. A small amount of TiO₂ paste was applied to the bottom edge of the tape mask and it

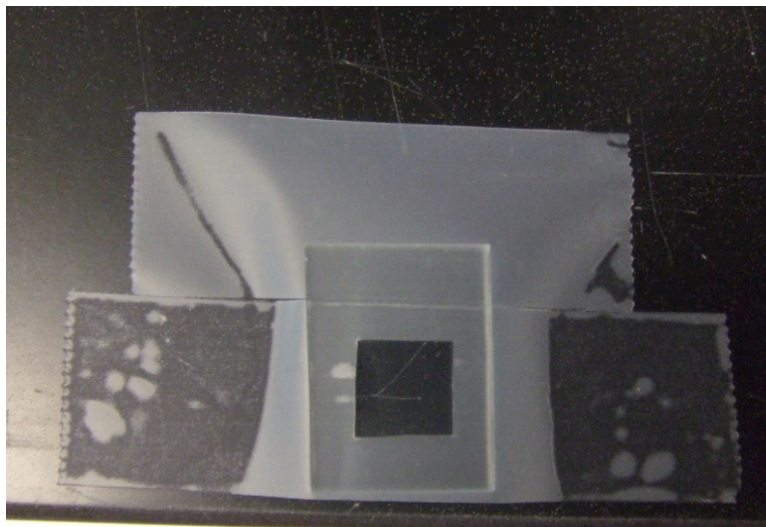


Figure 2-7. Clean photoanode FTO glass slide overlaid with the 1 cm by 1 cm Scotch tape mask prepped for doctor-blading the titanium dioxide paste.

was doctor-bladed across using the edge of a glass pipet that was rinsed with acetone and

wiped dry with a kimwipe, this removes problematic dust. The printed slides were then annealed in air at 375 °C for 5 minutes, 450°C for 5 minutes, 500°C for 5 minutes and then at 550°C for 15 minutes. The temperature profile was decided upon based on conversations with Prof. Hamann's group and is used solely for this titania paste. Once the films have cooled, the transmittance UV/Vis spectrum is taken of each film from 400 nm to 750 nm every 10nm using a black circular mask with an area of 0.3167 cm². The 100%T background was taken with an unprinted area of one of the slides. A sample of the dye is weighed and then ground into a fine powder in a mortar and pestle. It is then transferred to a 10 mL or a 25 mL volumetric flask with aliquots of ethanol until the mortar and pestle surfaces rinse clean. Additional ethanol is quantitatively added and the flask is sonicated; the resulting solution is 0.3 mM N3 in ethanol. The solution is divided up into 10 mL beakers of 5-6 mL of solution each. The printed TiO₂ glass is heated up to 90°C and two slides are placed back to back in each of the beakers of dye solution. The beakers are covered in parafilm and placed in a jar to help prevent evaporation. The slides are dyed for 20-28 hours in the dark. The slides before and after dyeing are seen in Figure 2-8.

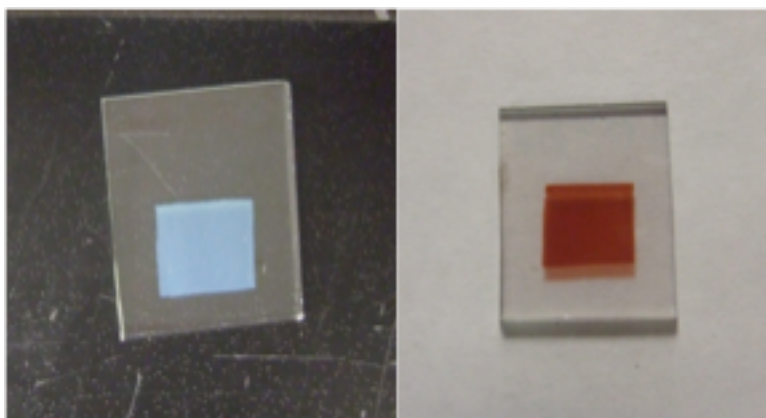


Figure 2-8. Photoanode slide. Titanium dioxide printed on FTO glass before and after dyeing with the chromophore N3.

The dyed slides are removed and rinsed with acetonitrile and dried under nitrogen for 15 minutes and the transmittance of each dyed film was taken once again. The bare and dyed %T spectra are converted to absorbance and subtracted show how the MLCT bands shift when the dye is bound to the TiO₂.

The FTO side of 20 cm by 20 cm glass sheets are covered in tape side for

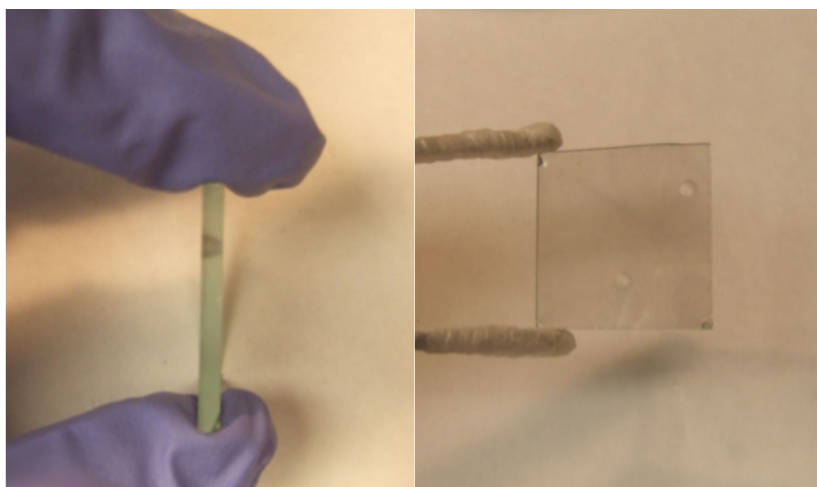


Figure 2-9. Side and top view of Pt counter electrodes showing the two holes for electrolyte injection.

protection and then cut into 1" by 1" squares for the cathode. Two cone-shaped holes are sand-blasted through the taped side of each FTO slide resulting in openings that are approximately 4 mm in diameter on the taped side and 2 mm in diameter on the untaped side. One hole is positioned approximately 3 mm from the bottom edge, 7 mm from the right edge. The other is positioned 1 cm from the bottom edge, 7 mm from the left edge, as seen in Figure 2-9. The tape is removed and the glass is sonicated in a solution of Alconox in DI water for 15 minutes, sometimes twice. Then the slides are rinsed with DI water and sonicated for 15 minutes in DI water, rinsed and subsequently sonicated in 0.1

M hydrochloric acid in ethanol to remove any iron contamination.²⁴ The slides are rinsed with ethanol, then rinsed and sonicated in acetone for 15 minutes, and then rinsed and sonicated in isopropanol, then allowed to air dry or wiped dry with kimwipes. 32.3 μL of a solution of 5 mM H_2PtCl_6 in anhydrous 2-propanol is applied to the conductive side of each square glass slide and tilted to spread the solution; care is taken when solution is around the holes so solution doesn't leak through. The slides are then set on a flat surface to dry for 5 to 10 minutes, and then are fired at 400 $^\circ\text{C}$ for 15 minutes and allowed to cool. Wire electrodes can be applied once cool. 1.5" to 2" copper wires are cut from a spool, the polymer sheathing is removed and the wires are wiped with ethanol to remove any remaining polymer coating. Silver epoxy is prepared and let set till it is sticky and no longer runny, a dollop of epoxy is applied to the wire and the wire is placed on the far side away from the sand-blasted holes in the center of the slide. The epoxy can be cured by baking at 65 $^\circ\text{C}$ for 15 minutes or left at room temperature for five hours.

Pieces of Surlyn are cut 0.75" x 0.5" with the center cut out leaving a 3 mm thick frame. The now platinized counter electrodes were secured to a Teflon block using metal

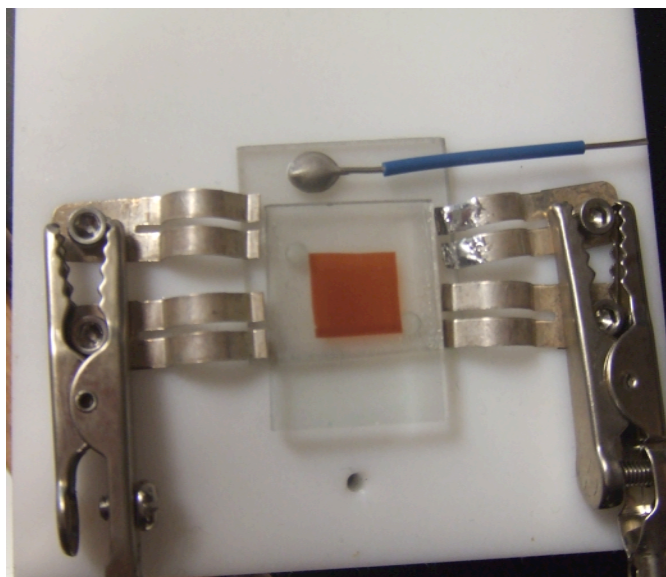


Figure 2-10. Setup for sealing the two electrodes together. Pt counter electrode is face up with epoxied wire in place. The dyed photoanode rests face down on the counter electrode with a Surlyn cutout between them. The leads are attached to the metal clamps that are in contact with the counter electrode. Voltage is applied across the leads to heat and melt the Surlyn.

braces. The Surlyn is placed on the platinized counter electrode around the two holes aligned along the bottom of the electrode and the dyed photoanode is placed on top of the Surlyn ensuring the active area is within the Surlyn area, seen in Figure 2-10. The metal braces are connected to a voltage source and 16V is applied and the braces are adjusted so that a current of about 0.7 to 1.3 A is passed. The resistance of the FTO causes it to heat up, melting the Surlyn, pressure is applied and the photoanode is secured to the counter electrode. As the Surlyn melts it turns more translucent, and the electrodes are adjusted on the metal braces to pass current through sections of the Surlyn that haven't melted yet. This is to ensure that the Surlyn isn't overheated causing it to bubble. Bubbles

in the Surllyn seal increases the chance of electrolyte leaking out of the cell. During the heating process, a wet kimwipe is pressed on top of the photoanode, to help transfer heat away from the dye adsorbed to the TiO_2 , since we have found that the dye changes (desorbs, rearranges) at temperatures above $90\text{ }^\circ\text{C}$. Once all Surllyn is translucent, heating is stopped and the cell is pressed photoanode-side down on a cool wet kimwipe until cool.

The standard electrolyte consists of 0.3 M lithium iodide, 0.03 M iodine, 0.2 M 4-*tert*-butylpyridine in acetonitrile. The lithium iodide is stored in a dessicator as it wets in air and also changes color; it is weighed quickly and rinsed off the weigh paper with acetonitrile into the 1 mL volumetric flask and filled to the line. The solution is minimally sonicated (both iodine and acetonitrile easily vaporize) and put into a tightly capped vial. The cell is placed photoanode-side down and a 1 mL needleless syringe is used to push electrolyte into the hole that is furthest from the edge of the glass until it surfaces out of the opposite hole. Care is taken to not to push air into the sealed cell, this is achieved by having a quarter to a half droplet of electrolyte on the end of the syringe. Also the cells are filled so no air bubbles obstruct the active area, if bubbles are problematic more electrolyte is pushed into the cell or the electrolyte is removed via syringes and filling is retried.

Wipe off the glass *completely* and quickly place a small square piece of Surllyn and a small square piece of cover glass on each hole. Use a soldering iron to melt the Surllyn beneath the cover glass till it is translucent and no longer moves. Often as heating occurs, electrolyte emerges under the Surllyn—it is possible to melt through the layer of electrolyte even if this happens. But sometimes the electrolyte layer will hinder the

Surlyn from melting, re-wipe the glass and try again if this occurs. Once the cell is sealed electrodes are applied to the conductive surface of the photoanode as described before. Be extra careful not to short out the cell by getting epoxy bridged between the two electrodes. The epoxy is cured for five hours in the dark, as the cell can no longer be heated once it is sealed. Once the epoxy is set, the complete solar cell can now be characterized, front and back view of the finished cell is seen in Figure 2-11.

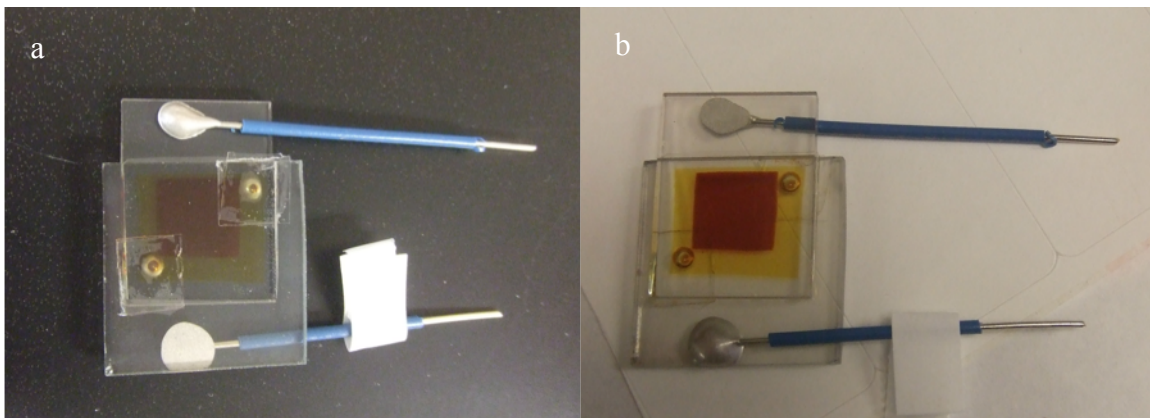


Figure 2-11. a) Back view of a completed solar cell displaying the two holes in the counter electrode now sealed with Surlyn and thin microscope cover glass. b) Front view of a complete solar cell, the red area is the dyed titanium dioxide; the yellow area surrounding is the standard electrolyte.

2.6 DSSC Characterization Setup

Characterization of solar cells requires a solar simulation setup. We chose to build our own using a visible light source, a monochromator, a potentiostat to manipulate and detect voltage and current, a shutter and its associated driver and some select filters to dim and shape the raw light to resemble the solar spectrum. The components of our system are shown in Figure 2-12. A xenon arc lamp produces an intense homogenous

beam of white light, which exits into a monochromator. The monochromator has a dual turret; one position is a simple mirror, reflecting all light through the pathway and out of the housing. The second position is a diffraction grating that separates the white light into its wavelengths for IPCE or single wavelength measurements. At the exit to the monochromator is a driver-controlled shutter.

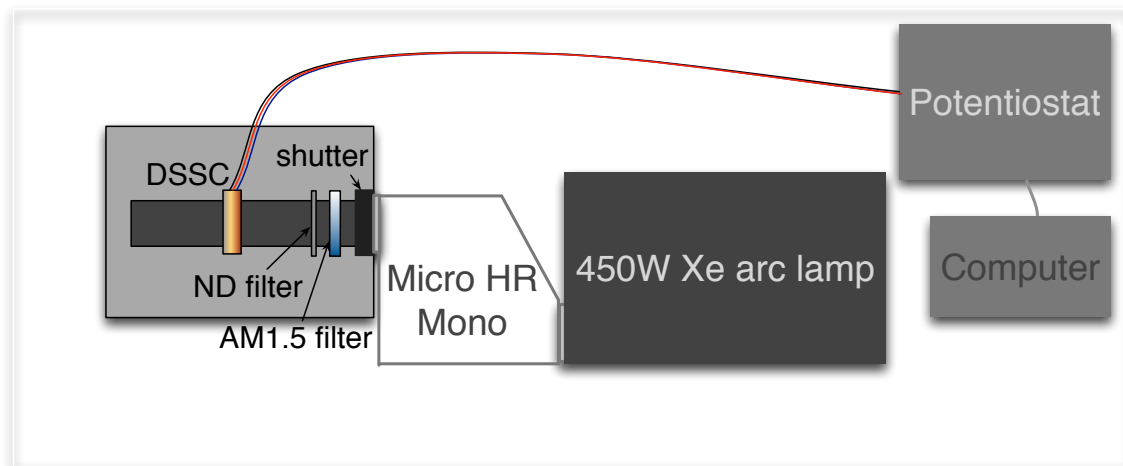


Figure 2-12. DSSC Characterization Setup. It consists of a light source, a monochromator, a potentiostat, a computer, and the beam path containing a shutter, filters and the solar cell under study.

A potentiostat provides the voltage waveforms and detects the current and voltage in all experiments. J-V curves are produced by applying voltage in a two-electrode arrangement; the working electrode lead is the photoanode and the reference and counter electrode leads are placed on the platinum counter electrode side. This setup means the reference is not stationary and any detected voltage is merely a difference in potential not an absolute voltage with respect to a reference.

The shutter with an associated shutter driver is placed after the monochromator for dark current, Open-Circuit Voltage Decay, and Transient Current Decay measurements. OCVD and TCD experiments detect potential or current as the solar simulated light is turned on and off.

An AM 1.5 Global (AM 1.5G) filter is necessary to profile the xenon arc lamp output so the wavelength ratios match the solar spectrum. This filter is formulated to resemble the spectral radiation from the ground's surface, facing south at a 37° tilt; the 'global' designation includes both direct and diffuse sunlight. Neutral density filters uniformly refine the intensity to 1 sun at 100 mW/cm² or any other light intensity desired. The filters were placed immediately after the shutter for ease and so the DSSC could be moved as much as needed.

The solar cell under evaluation is secured onto a post that can be moved up or down to position the active area in the solar-simulated light beam. The post is secured but transferrable forward and backward along a track that is screwed down to a breadboard. This ensures the same positioning for each cell that is tested. During illumination and in the dark, the active area is masked with a black circular disk with an open area of 0.3167 cm². This area is the actual active area and is the value used to convert current (A) into current density (A/cm²). As the beam intensity can change day to day and will change over a few hour period, the power is monitored at the same position as the solar cell and the post is moved forward or backward to maintain the intensity of light that is desired. Most commonly it is 100 mW/cm².

After installation of the system, the Xe arc lamp position was optimized for output using the three screws located under the lamp housing. They are reached via an Allen

wrench carefully placed through each corresponding hole in the housing. The power was monitored while each screw was adjusted to find maximum power output.

The setup was optimized for both white and monochromatic light without the need for much adjustment of equipment. The requirement for white light is that it is strong uniform beam of a certain intensity, while for monochromatic light, which requires these as well, also needs a reasonable FWHM so the cell is illuminated with only one wavelength of interest at a time. The monochromator entrance slit simply allows light from the arc lamp into the monochromator. This slit was adjusted to a value of 1.5 mm so that the light entering just filled the first mirror. Overfilling the mirror introduces stray light within the monochromator, which can be reflected off of surfaces and could go through the exit slit adding a white background illumination during the monochromatic experiment. For the entrance slit I used a spectrometer to visualize each wavelength while measuring the FWHM as I adjusted the slit width. I found that a 750 μm exit slit width gave FWHM in a range of 6 nm to 8.4 nm for 400 nm to 750 nm. The IPCE measures output current of the cell at wavelengths 10 nm apart. This exit width also allows enough white light out to maintain 100 mW/cm^2 at a similar distance, but could be opened to allow more light out for higher intensities.

The computer controls the potentiostat and the monochromator. For IPCE measurements, the monochromator needs to be scanned from 400 nm to 750 nm in increments of 10nm. Unfortunately changing wavelengths is a manual operation with the design of the application that controls the monochromator. A Labview program was written to control the monochromator application for the IPCE experiment where one

could pick the wavelength range and increment and also the time between changing wavelengths.²⁵

2.7 Concluding Comments

The components and the layout of our standard dye-sensitized solar cell have been outlined. The requirements and desired qualities for each component have been described and our choices for the standard cell components have been identified. The first DSSCs were fabricated from a basic procedure giving quite low performance. Method, materials and techniques were improved to increase efficiency parameters to values that would provide enough cushion to be able to gauge how any changes to the cell affected performance. These new methods and materials also proved to, at the same time, remove sources of variability from cell to cell. Standard deviations lower than 10% of the average value of a set of solar cells was obtained. Once the method was developed a standard procedure for the fabrication of our DSSCs was established. Minor changes to the method continue to improve technique. The next step is to utilize this method we have established to incorporate new compounds and materials. Then use the standard solar cell efficiency to compare the new solar cells to see how the incorporation of new materials affected performance.

APPENDIX

APPENDIX

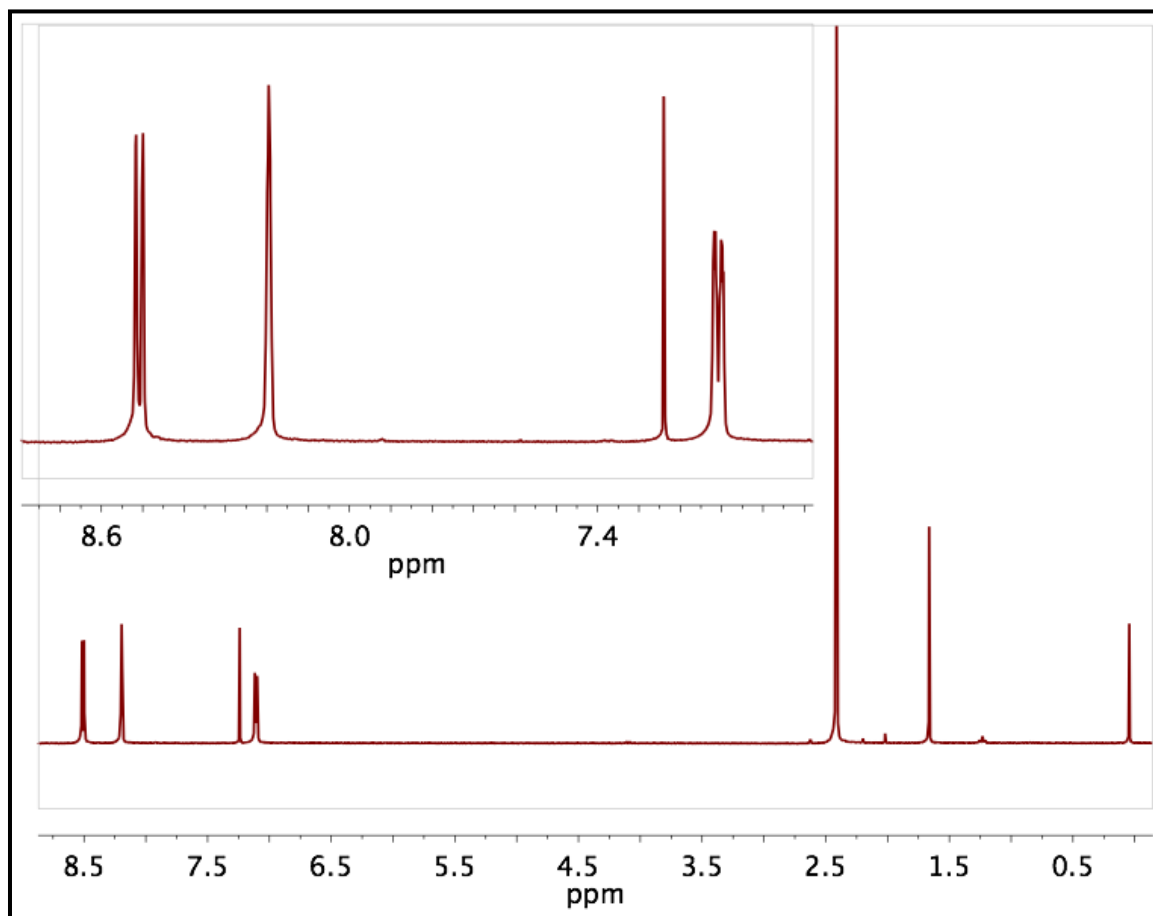


Figure 2-13. ^1H NMR Spectrum of 2,2'-Bipyridyl-4,4'-Dimethyl in d_6 -DMSO.

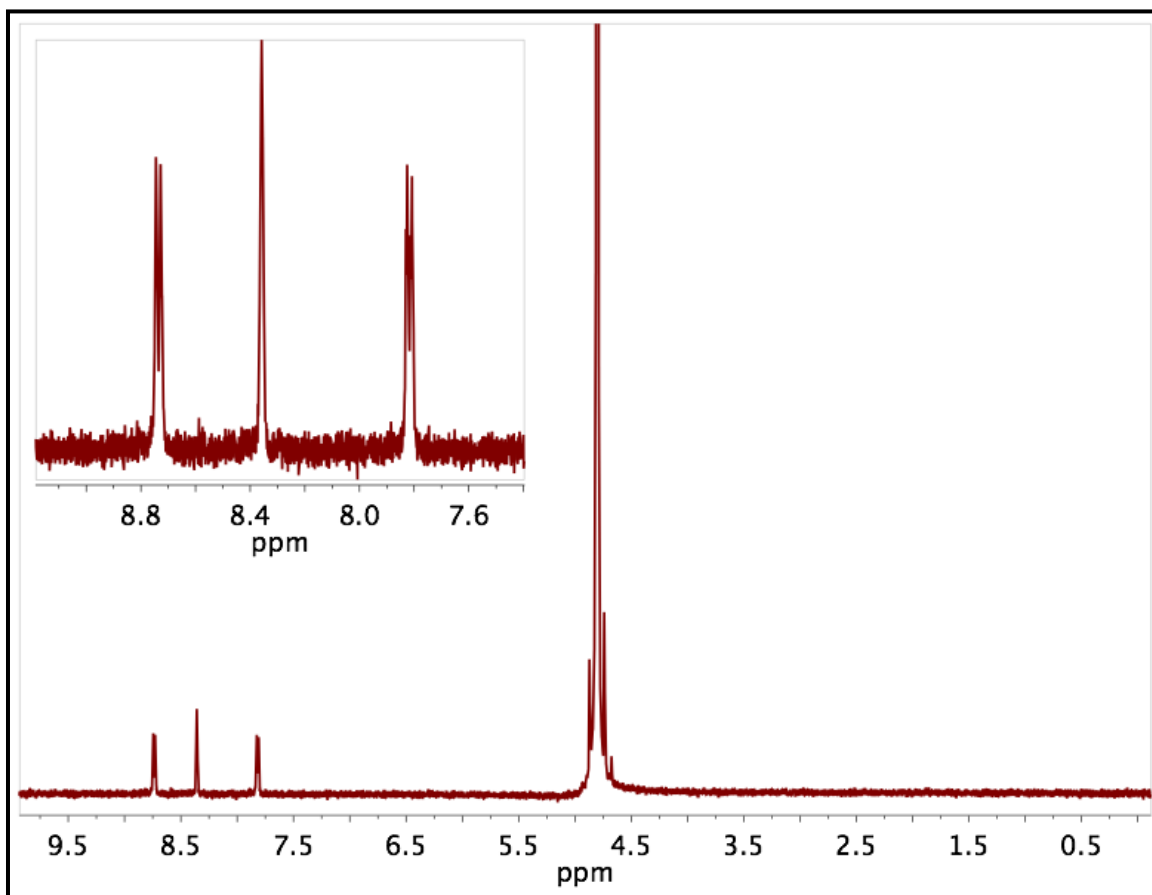


Figure 2-14. ^1H NMR Spectrum of 2,2'-Bipyridyl-4,4'-Dicarboxylic acid in 0.05 M NaOD in D_2O .

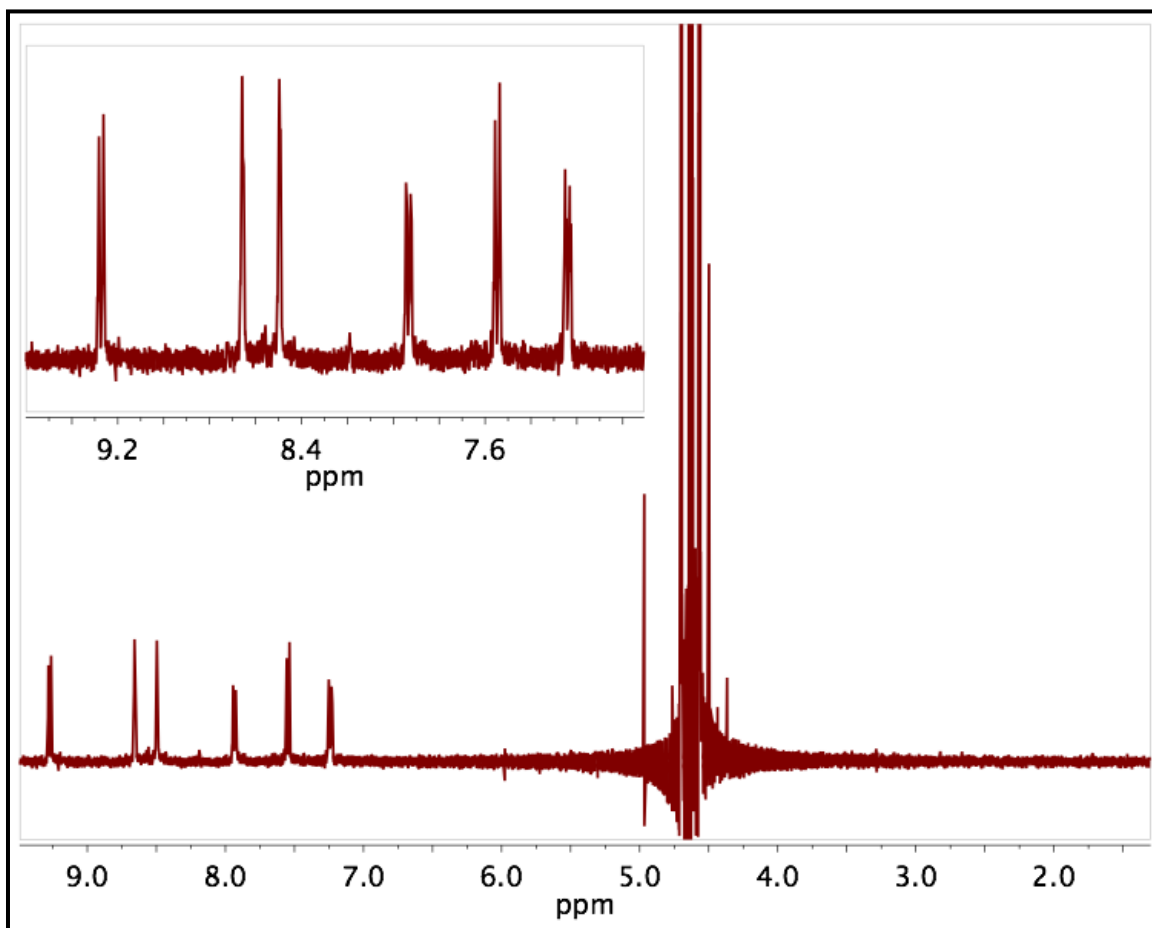


Figure 2-15. ¹H NMR Spectrum of *cis*-Bis(isothiocyanato)bis(2,2'-bipyridyl-4,4'-dicarboxylato)-ruthenium(II) in 0.05 M NaOD in D₂O.

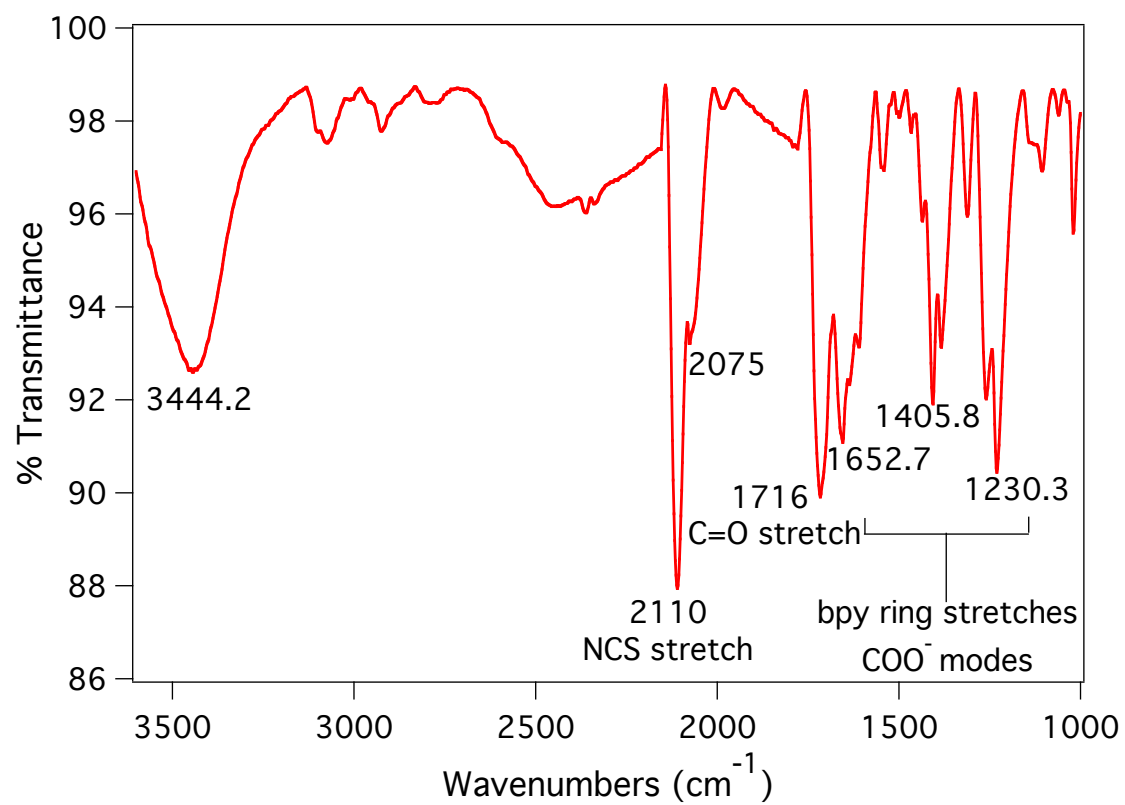


Figure 2-16. IR Spectrum of N3.

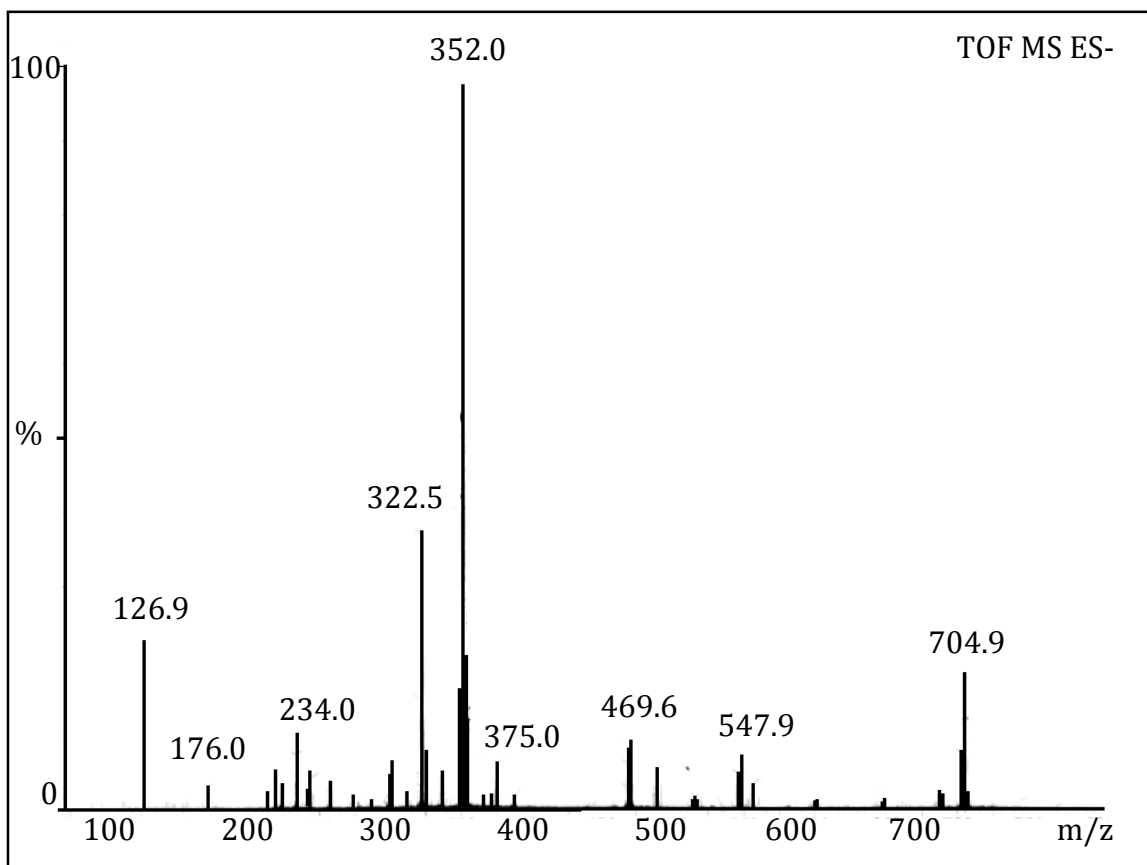


Figure 2-17. ESI-MS of N3.

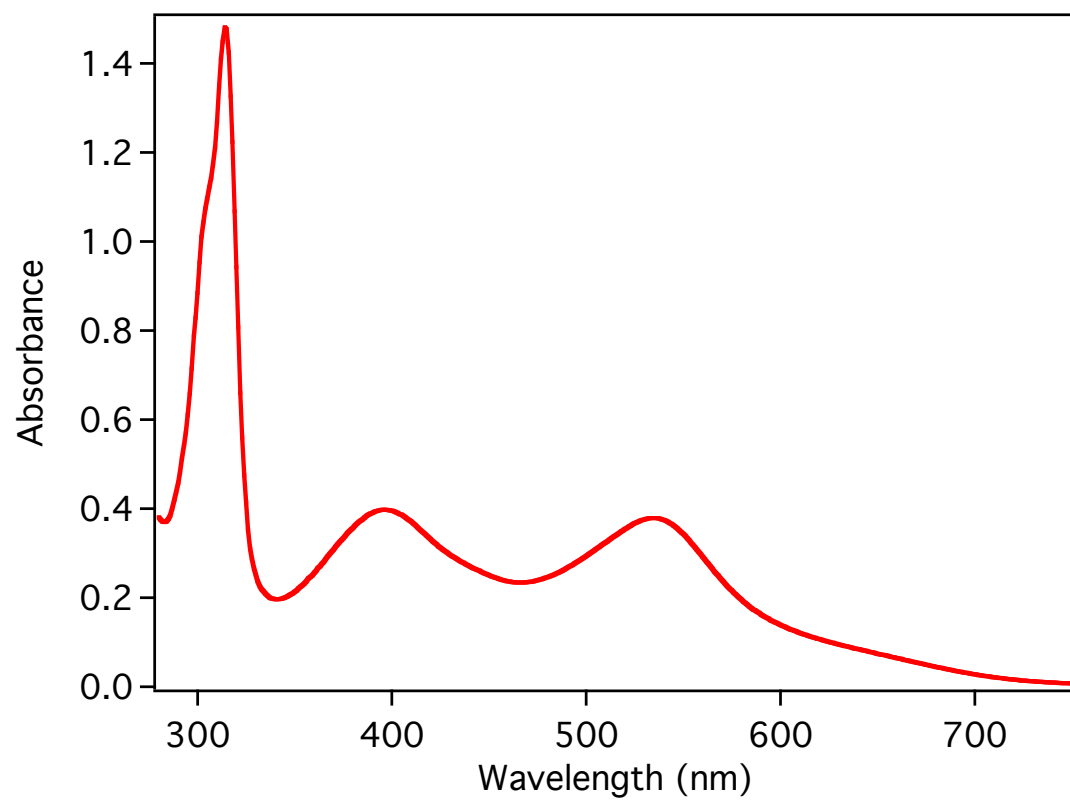


Figure 2-18. Absorbance Spectrum of N3 in Ethanol.

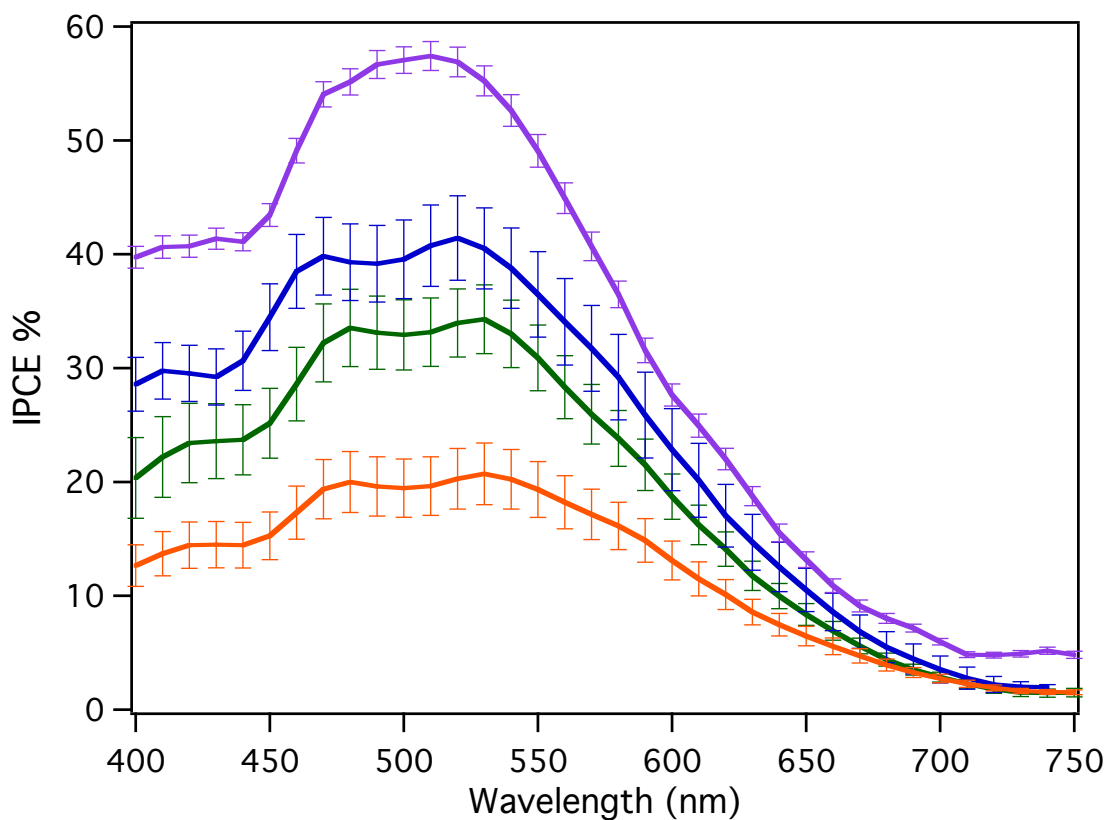


Figure 2-19. IPCE plots. Each curve is IPCE data corresponding to previous Figures. (—) using a 2-hole vacuum desiccation method, data in Figure 2-3; (—) TBP as an additive, data in Figure 2-4; (—) syringe injection, data in Figure 2-5; and (—) the TiO₂ slides were preheated to 90°C before being immersed in dye solution, data in Figure 2-6. N3 dye, electrolyte: 0.3 M LiI, 0.03 M I₂, 0.2 M TBP in MeCN, thermalized Pt counter electrode.

REFERENCES

REFERENCES

- (1) Spath, M.; Sommeling, P. M.; van Roosmalen, J. a. M.; Smit, H. J. P.; van der Burg, N. P. G.; Mahieu, D. R.; Bakker, N. J.; Kroon, J. M. *Progress in Photovoltaics: Research and Applications* **2003**, *11*, 207–220.
- (2) Lepleux, L.; Chavillon, B.; Pellegrin, Y.; Blart, E.; Cario, L.; Jobic, S.; Odobel, F. *Inorganic Chemistry* **2009**, *48*, 8245–50.
- (3) Zhao, Y.; Zhai, J.; He, J.; Chen, X.; Chen, L.; Zhang, L.; Tian, Y.; Jiang, L.; Zhu, D. *Chemistry of Materials* **2008**, *20*, 6022–6028.
- (4) Lee, S.-H. A.; Jackson, A.-M. S.; Hess, A.; Fei, S.-T.; Pursel, S. M.; Basham, J.; Grimes, C. A.; Horn, M. W.; Allcock, H. R.; Mallouk, T. E. *The Journal of Physical Chemistry C* **2010**, *114*, 15234–15242.
- (5) Sprintschnik, G.; Sprintschnik, H. W.; Kirsch, P. P.; Whitten, D. G. *Journal of the American Chemical Society* **1977**, *99*, 4947–4954.
- (6) Garelli, N.; Vierling, P. *The Journal of Organic Chemistry* **1992**, *57*, 3046–3051.
- (7) Gratzel, M.; Nazeeruddin, M. K. *Inorganic Syntheses* **2002**, *33*, 185–189.
- (8) O'Regan, B. C.; Grätzel, M. *Nature* **1991**, *353*, 737–740.
- (9) Papageorgiou, N. *Coordination Chemistry Reviews* **2004**, *248*, 1421–1446.
- (10) Papageorgiou, N.; Maier, W. F.; Gratzel, M. *Journal of The Electrochemical Society* **1997**, *144*, 876.
- (11) Nazeeruddin, M. K.; Kay, A.; Rodicio, I.; Humphry-Baker, R.; Mueller, E.; Liska, P.; Vlachopoulos, N.; Gratzel, M. *Journal of the American Chemical Society* **1993**, *115*, 6382–6390.
- (12) Boschloo, G.; Häggman, L.; Hagfeldt, A. *The Journal of Physical Chemistry B* **2006**, *110*, 13144–50.
- (13) Huang, S. Y.; Schlichthörl, G.; Nozik, A. J.; Grätzel, M.; Frank, A. J. *The Journal of Physical Chemistry B* **1997**, *101*, 2576–2582.
- (14) Schlichthörl, G.; Huang, S. Y.; Sprague, J.; Frank, A. J. *The Journal of Physical Chemistry B* **1997**, *101*, 8141–8155.
- (15) Liu, Y.; Hagfeldt, A.; Xiao, X.; Lindquist, S. *Solar Energy Materials and Solar Cells* **1998**, *55*, 267–281.

- (16) Hahlin, M.; Johansson, E. M. J.; Schölin, R.; Siegbahn, H.; Rensmo, H. *The Journal of Physical Chemistry C* **2011**, *115*, 11996–12004.
- (17) Zakeeruddin, S. M.; Nazeeruddin, M. K.; Humphry-Baker, R.; Péchy, P.; Quagliotto, P.; Barolo, C.; Viscardi, G.; Grätzel, M. *Langmuir* **2002**, *18*, 952–954.
- (18) Daeneke, T.; Kwon, T.-H.; Holmes, A. B.; Duffy, N. W.; Bach, U.; Spiccia, L. *Nature Chemistry* **2011**, *3*, 211–15.
- (19) Hinsch, A.; Kroon, J. M.; Kern, R.; Uhlendorf, I.; Holzbock, J.; Meyer, A.; Ferber, J. *Progress in Photovoltaics: Research and Applications* **2001**, *9*, 425–438.
- (20) Kal, S. H.; Joseph, J.; Lee, J.; Kim, K.-J. *Journal of The Electrochemical Society* **2005**, *152*, A1378.
- (21) Nogueira, A. F.; De Paoli, M.-A.; Montanari, I.; Monkhouse, R.; Nelson, J.; Durrant, J. R. *The Journal of Physical Chemistry B* **2001**, *105*, 7517–7524.
- (22) Katsanaki, A. V.; Tsoukleris, D. S.; Falaras, P.; Karayianni, H. S.; Bernard, M.-C. *Journal of Solar Energy Engineering* **2008**, *130*, 041008.
- (23) Based on Prof. Meyer's group's lab procedure.
- (24) Personal Correspondence with Prof. Tom Hamann's group.
- (25) Labview Program was Written by Ms. Eileen Dixon.

Chapter 3. Iron vs. Ruthenium Chromophores in Dye-Sensitized Solar Cells

3.1 Introduction

Ruthenium-based bipyridyl compounds have historically been the most efficient dyes used in dye-sensitized solar cells, with efficiencies ranging from 7% at its inception¹ to over 11% in more recent years.^{2,3} As outlined in Chapter 2, dyes for application in DSSCs should have a wide absorption spectra, long-lived charge-transfer excited states that lie above the conduction band of TiO₂ (or another wide band gap semiconductor), high injection yield, efficient regeneration, slow recombination, be reversibly able to convert between oxidation states, and stable chemically and physically during use in a DSSC. Ruthenium chromophores possess all of these qualities. But two qualities important for commercial use are abundance of materials and non-toxicity, both of which ruthenium does not have. Our research is interested in replacing ruthenium with iron-based chromophores, and iron is quite abundant (Figure 1-7) and less toxic than its ruthenium counterpart.

The shift to iron is a seemingly simple change for a DSSC chromophore, moving from second row to first row in the same group, since we are maintaining a d⁶ metal. But progressing to the first row reduces spin-orbit coupling and the cascade of metal and ligand-based states reorder. This manifests as *metal*-based long-lived ligand field excited states in iron while they are *ligand*-based in ruthenium, MLCT states. MLCT states are necessary for electron injection because the electron delocalizes on the ligand that is in electronic communication with the TiO₂, required for injection.

Ruthenium-based chromophores are excited into a ¹MLCT, from a metal d-orbital to ligand π^* , and then relax into the long-lived ³MLCT excited state. This state lasts on

the order of nanoseconds, enough time for injection to occur since the timescale for injection is 100 ps or less.⁴ The metal-based ligand field states are higher in energy so do not play a role in the relaxation of ruthenium complexes from the MLCT states accessible by the solar spectrum. Iron bipyridyl compounds have ¹MLCT and ³MLCT states that are attainable and lie above the conduction band of TiO₂. Low-spin iron complexes undergo a vertical transition to a ¹MLCT upon absorption but a fast deactivation occurs to the long-lived ligand field state within ~100 fs.⁵ The pathway is understood to be ¹MLCT → ³MLCT → ⁵T₂.⁶ Our working picture for the difference between iron and ruthenium is qualitatively depicted in Figure 3-1.

Nonetheless, in 1998 a current was observed from an iron polypyridyl compound that is structurally similar to the N3 compound developed by Gratzel.⁷ Photosensitization of TiO₂ by *cis*-bis(2,2'-bipyridyl-4,4'-dicarboxylic acid) dicyano iron(II), Figure 3-2, exhibited a photocurrent on the order of hundreds of microamperes with a photovoltage of 0.360 V. The J-V curve is seen in Figure 3-3. Ferrere's group also measured the absorbed-photon-to-current-efficiency, APCE, and the plot is compared to the absorption of the dye on TiO₂, the result is seen in Figure 3-4. The FeCN molecule displays two features in this region, both MLCT bands, one at ~420 nm and the other at ~600 nm. The APCE plot shows that current results from the higher energy band but not the lower

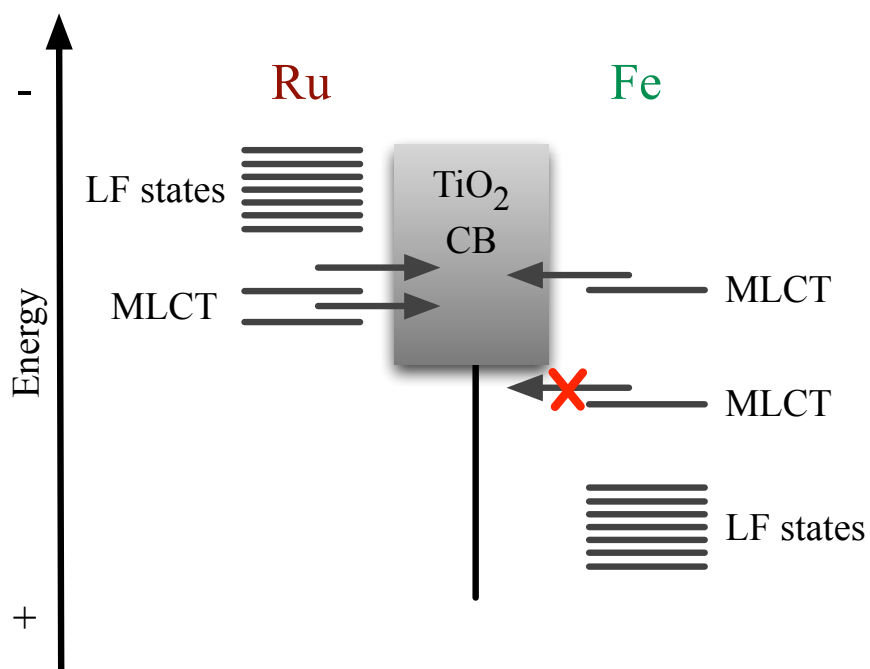


Figure 3-1. Relative energies of iron and ruthenium excited states with respect to the conduction band of titanium dioxide.

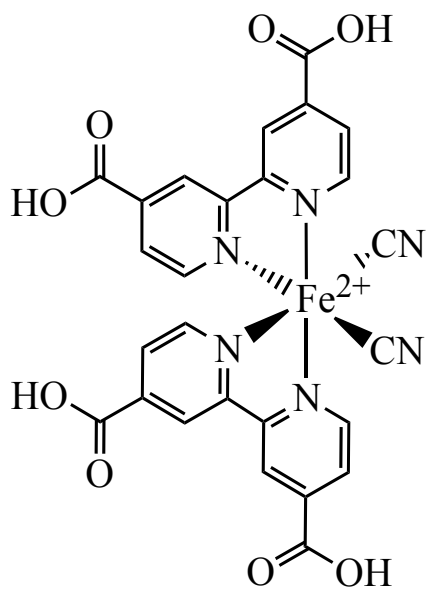


Figure 3-2. Structure of *cis*-Bis(4,4'-dicarboxyl-2,2'-bipyridine) dicyano iron(II), FeCN.

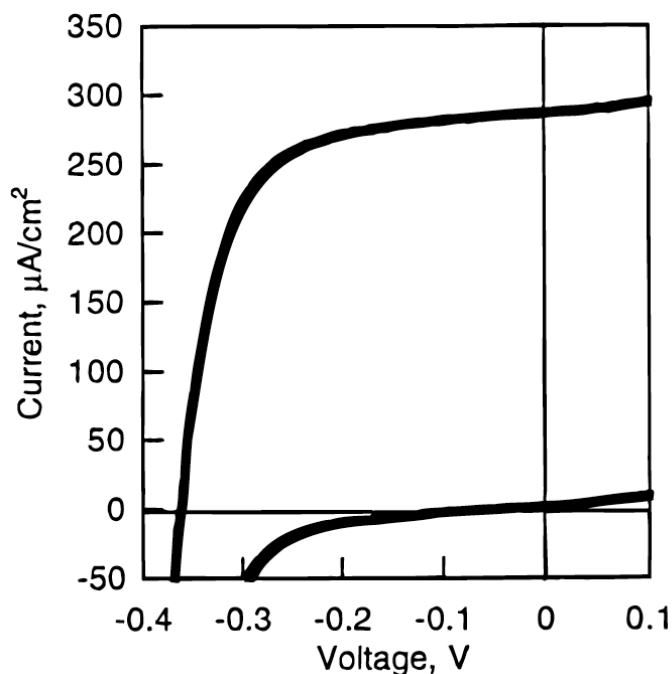


Figure 3-3. J-V curve of a DSSC employing FeCN as a chromophore in a DSSC.⁷

energy band. A likely explanation for this band selectivity is that ‘hot injection’ is occurring. Electron injection is happening from the initial ¹MLCT before it has time to relax, within ~100 fs.⁵ From Figure 3-4, ~10% of the absorbed photons are producing current. This percentage can be described in terms of competing rates; the rate of injection versus the rate of excited state relaxation. In these terms, in order to increase the conversion of photons to electrons, the rate of injection must be accelerated or the rate of relaxation must be slowed. Another avenue of study is modulating the excited states with ligand design to attempt to push the LF states higher in energy while pulling the MLCT states lower in energy. Research in our group has focused on both slowing the rate of

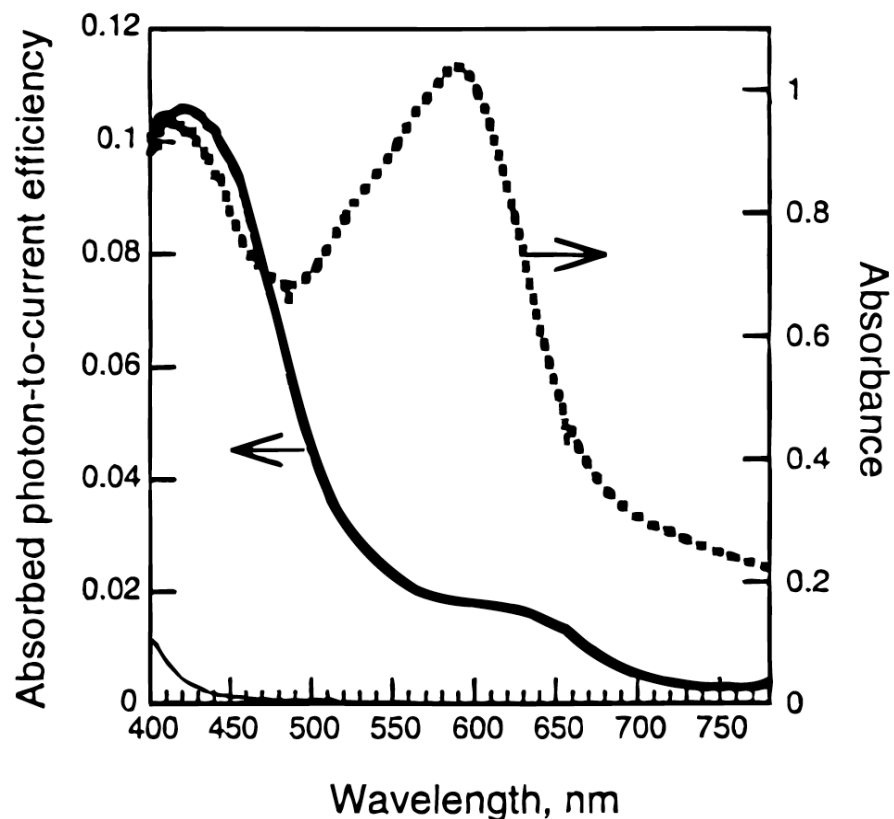


Figure 3-4. Absorbed-Photon-to-Current-Efficiency of the FeCN chromophore in a DSSC and absorbance plot of FeCN in 0.5 M LiI in acetonitrile solution. The lower plot is the APCE for bare TiO₂ film.⁷

relaxation and excited state modulation a dual approach to studying. A group of iron polypyridyls have been developed to elucidate the mechanism for relaxation and conceivably slow the process down.⁸ Another avenue in our group has studied highly symmetric iron chromophores that are intended to adjust the excited state signature and hopefully limit the number of states in LF manifold.^{9,10}

The goal with this study is to take the original Fe compound and compare it to its ruthenium analog to see how the performance and rate of recombination differs, using N3 as a standard for comparison. We construct cells with and without blocking layers of compact TiO₂ to examine if there is a difference in the rate of recombination between two molecules of interest, *cis*-bis(4,4'-dicarboxyl-2,2'-bipyridine) dicyano iron(II), FeCN, and *cis*-bis(4,4'-dicarboxyl-2,2'-bipyridine) dicyano ruthenium(II), RuCN.

3.2 Experimental

3.2.1 Materials and Instrumental Methods. All chemicals were reagent grade and used without further modification or purification unless otherwise noted. All air-sensitive reactions were performed using standard Schlenk techniques. TEC-15 (15 Ω /mm²) fluorine-doped tin oxide (FTO) coated glass was purchased from Hartford Glass Co. Transparent titania paste, Ti-Nanoxide HT/SP and 25 μ m thick Surlyn was purchased from Solaronix. Hydrogen hexachloroplatinate (IV) hydrate (40% Pt) and iodine resublimed (99.5%) were purchased from Acros Organics. 4-*tert*-butylpyridine from TCI America Inc., anhydrous 2-propanol (99.5%), HPLC grade acetonitrile, lithium iodide (99.9%), pyridinium triflate (97%), pyridine (99.8%), 1 M tetrabutylammonium hydroxide in methanol solution were purchased from Sigma Aldrich. Sephadex LH-20 was purchased from GE Healthcare. 1 cm x 1 cm Tape mask is 3M Scotch 811. 790 μ m ethylene propylene diene monomer (EPDM) rubber sheet was purchased from McMaster-Carr. Silver conductive epoxy (8331G) was purchased from Fulton Radio Supply Co., and an electrically heated furnace was from Cress Manufacturing Co. Model C601/SD Ser. No. 0910.

Electrochemistry on dyed films was performed in a homemade electrochemical cell using a three-electrode configuration. The dyed film was the working electrode, a leak-free Ag/AgCl was the reference electrode and a high surface area carbon rod was used as the counter. The electrolyte solution was 0.1 M tetrabutylammonium hexafluorophosphate (Sigma Aldrich, 97%, recrystallized in our lab) in acetonitrile. Cyclic voltammograms were taken on the CHI650D potentiostat at 20 mV/s, and repeated until the plot retraced itself consistently. The Ag/AgCl reference electrode was checked ($E_0 = 0.038$ V vs. SCE) before and after each experiment. The CV are presented in the Appendix.

Transmittance measurements were taken on a Perkin Elmer Lambda 1050 Spectrophotometer equipped with a 150 mm InGaAs Integrating Sphere. A Heathkit 30V 3A Power Supply was used for resistive heating. Solution absorbance measurements were taken on a Cary 50 spectrophotometer. Microscope cover glass thickness 0.14 mm was from Corning, standard 'plain' 1" x 3" x 1.2 mm microscope slides and 0.5 mL and 1 mL syringes (BD Medical) were purchased from MSU Chemistry Stores and 3/4" small nickel-plated binder clips were from ACCO, Alconox brand Powder Detergent was the soap used to clean the glass slides.

DSSCs were characterized on a 450 W Xenon arc lamp, with a MicroHR dual turret monochromator equipped with a 600 g/mm 500 nm blaze diffraction grating and a mirror were purchased from Horiba Jobin Yvon. AM0 and AM1.5 filter set was in place to simulate the solar spectrum, purchased from Solar Light Co., a 385 nm cut-off filter was used to prevent absorption by TiO₂ and neutral density filters were purchased from Thorlabs, Inc. Photoelectrochemical measurements were made with a CH Instruments Inc. 650D Potentiostat equipped with a Dell computer and a Windows XP operating

system was used to run the software. The power was monitored via 3A-SH-ROHS Power meter from Ophir Optics and light was controlled with a Uniblitz VCMD1 shutter and shutter driver from Vincent Associates Inc.

Open-circuit voltage decay measurements were performed using the solar simulation setup. The white light was turned on by opening of the shutter, the photovoltage was allowed to equilibrate, and then the shutter was closed and the photovoltage decay was monitored with time divisions every 0.1 s or 0.0025 s. Voltage decays were repeated three to five times to confirm reproducibility of discharge and recovery.

IPCE plots were measured using the solar simulation setup. The current was averaged over 10 seconds at 10 nm intervals from 400 nm to 700 nm or 750 nm. The 0.3167 cm² mask was employed. The white light was optimized for 100 mW/cm² and then the turret was switched to the diffraction grating. A independent power spectrum was taken for each data set and used to calculate the internal efficiency of conversion. The IPCE plot for N3 is seen in the Appendix. It is ~50% lower than in Chapter 2. The methodology needs to be improved in order to effectively utilize the information attainable from the plots.¹¹ The FeCN IPCE curves still showed band selectivity but exhibited extremely low conversion efficiency (<5%), they are not included in this document. The method needs to be improved and the DSSCs should be repeated in order to obtain efficiencies that have better signal-to-noise.

cis-Bis(isothiocyanato)bis(2,2'-bipyridyl-4,4'-dicarboxylato) ruthenium(II) was synthesized as described in Chapter 2. ¹H NMR and were measured with 300 MHz Varian UnityPlus, 500 MHz Varian UnityPlus, and Agilent DDR2 500 MHz spectrometers. Absorption spectra of dye solutions were obtained on a Varian Cary 50

spectrophotometer. Elemental analysis was taken by Midwest Microlab, LLC. Electrospray mass spectra (ESI-MS) were obtained from the staff of the Michigan State University Mass Spectrometry Facility. The characterization data of the compounds are included in the Appendix at the end of this chapter.

3.2.2 Fabrication Methods. The blocking layers used for our study were prepared by Prof. Hamann's group via atomic layer deposition (ALD). TiO₂ blocking layers were deposited using 1000 ALD cycles of titanium isopropoxide (Sigma Aldrich) and water as precursors with a Savannah 100 instrument (Cambridge Nanotech, Inc.). TiO₂ was grown at 225 °C using reactant exposure times of 0.3 s and 0.015 s for titanium isopropoxide and H₂O, respectively, and nitrogen purge times of 5 s between exposures.¹² TiO₂ paste was applied onto the FTO and blocking layer and sintered as normal. The blocking layer was removed using a file to expose the FTO conductive layer for the attachment of the wire lead.

DSSCs were fabricated as described in Chapter 2 unless otherwise noted. The TiO₂ slides were dyed in ~0.3 mM N3, FeCN or RuCN in ethanol with 1 mM pyridine, and 1 mM pyridinium triflate buffer, to control the protonation state of the dye as it adsorbs to the TiO₂.^{13,14}

The FeCN compound tended to oxidize under standard heated sealing conditions so different methods were attempted. Oxidation and desorption was observed as a discoloration and a hue change from deep forest green to a green-yellow tint. Absorption of the films at the 600 nm absorbance decreased by 75% on average and a peak at 500 nm grew in. Attempting the standard method of resistive heating but with slow and careful

application of the voltage afforded a sealed cell but oxidation and/or desorption of the FeCN dye still occurred. The dye also appeared to recolor with time for all methods although not completely. The dye also appeared to regain color when the electrolyte was injected. It is assumed that a reduction of the dye occurs when the electrolyte comes in contact with the dyed film.

Next, the DSSCs were sealed in an air-free environment to see if the color changes could be prevented. In the first iteration, the photoanode was dyed in air and then placed into a vacuum dessicator, free from light, along with the wired counter electrodes and Surlyn and the dessicator was evacuated for two to three days. The dessicator was then placed into a nitrogen-purged glove bag and then the environment was flushed for >1 hour. Heat to melt the Surlyn was applied using a hot plate inside of the glove bag. Different temperatures were tried. At temperatures up to 90 °C would not completely melt the Surlyn; it is indicated that it melts to seal at 100 °C. At 100 °C and above Surlyn completely melted and the cells were sealed. At all temperatures the dye was observed to discolor and fade to some degree.

Lastly, both the dyeing process and sealing was attempted in an air-free environment. All compounds and materials were evacuated or flushed with nitrogen for several days and the solvents were freeze-pump-thawed. The TiO₂ was prepared as previously described and then placed into a dessicator, along with the counter electrodes and Surlyn, free from light and pumped on for two to three days to remove oxygen. The dessicator was then placed into a glove bag with nitrogen atmosphere and flushed for >1 hour. The dye solution was prepared in the nitrogen atmosphere and the TiO₂ was dyed in the dark under nitrogen overnight. 100 °C was applied using a hot plate to melt the Surlyn under nitrogen yet the dye was observed to discolor and fade to some degree. The

air-free method seemed to make little difference to the dye appearance and also created issues with fabrication. The awkwardness of the glovebag made reproducibility difficult to maintain so air-free methods were abandoned.

Since any method of heating the FeCN dye affected its appearance, a new method was developed that used a cell design that required no heat. A 790 μm rubber spacer was used between the two electrodes, the cell was held together by binder clips. This spacer was used via ease of procuring and the electrolyte was injected at the rubber septa via 27 gauge needles. One syringe held the electrolyte and the plunger was removed from the other syringe to provide the exit for air out of the cell as it is filled. The syringes were placed on the counter electrode side of the septa, at opposite corners of the same edge, as to not risk damage to the dyed photoanode. The empty syringe was placed above the electrolyte-filled syringe and as the electrolyte was pushed into the clamped cell the air bubbles were guided towards the empty syringe. All solar cells in this chapter were fabricated via this clamped cell method. The electrolyte that was employed for these cells was 0.5 M lithium iodide, 0.05 M iodine and 0.2 M TBP in acetonitrile.¹³

3.2.3 Synthesis of Compounds

3.2.3.1 *cis*-Bis(4,4'-dicarboxyl-2,2'-bipyridine) dicyano iron(II). This molecule was synthesized and purified via modified literature procedures. ^{7,15,16} ****EXTREME CAUTION** must be used when performing this reaction as deadly cyanide gas is produced.** The reaction was done within a fully functioning hood, with the sash closed and often the emergency purge operation was utilized. A modification to the acidification step is noted in the procedure to be used if the reaction is attempted again.

Using a two-neck 250 mL round bottom with a vacuum adapter, 0.844 g (3.46 mmol) of dcbpy was added to 50 mL of water. 10 drops of 1 M sodium hydroxide was added and then the flask was heated to 60°C using a stirred oil bath and a hot stir plate. 0.453 g (1.12 mmol) of $(\text{NH}_4)_2\text{FeSO}_4 \cdot 6\text{H}_2\text{O}$ was added once the reaction reached 60°C, the solution turned a deep pink color immediately. 7 mL of water was added and the reaction was stirred at 60°C for 10 minutes. The reaction was then diluted to 70 mL with water, at this point all of the dcbpy solid appeared to be dissolved; the reaction was heated to 90°C. 0.870 g (17.7 mmol) of granule NaCN was added slowly; the solution was allowed to react at 90°C for 8 minutes, then removed from the heat and let cool, while stirring.

The pH was monitored using a freshly calibrated pH electrode while 1.0 M H_2SO_4 was added *extremely slowly and with extreme caution* down to a pH of 4.6, while stirring vigorously. During the addition of the acid the pH moved slowly down to pH 8, fast to pH 5.8, then slowly down to 4.8, then fast...if the pH overshoot the desired pH of 4.6, dilute 0.5 M sodium hydroxide was added to reach pH 4.6. Once the pH was reached, the solution was stirred for 10 minutes to allow equilibration. The pH electrode was always rechecked with the buffer solutions after this step to ensure its accuracy. A modification to the setup will include a nitrogen gas inlet and an outlet that is submerged in a sodium hydroxide solution; the setup is pictured in the following section.

The pink/red solution (~90 mL) was filtered on a fine frit to remove any insoluble impurities; the pH after filtering was ~4.8. H_2SO_4 was added *slowly, dropwise*, down to a pH of 2.5; the solution became a dark blue/green as it precipitated. The dark green/purple solid was filtered using a fine glass frit, a pink filtrate went through, this is indicative of the tris bipyridyl complex. The compound was rinsed on the frit with pH 2.5 H_2SO_4 and

allowed to dry on the frit overnight. Once dry the product appeared violet with iridescent green hues. Yield of unpurified product: 0.490g (74%).

1 M tetrabutylammonium hydroxide in methanol solution was added quantitatively to form the TBA⁺ salt and the product was purified via column chromatography using Sephadex LH-20 with methanol as the eluent. The product eluted as a deep green band first, it was followed by lighter green bands and a pink band, presumably the partially deprotonated/converted and the tris bipyridyl complex, respectively. The methanol was evaporated till the compound was just dissolved and then it was precipitated with a 1:1 ratio of ether and petroleum ether, left overnight in 5-10 °C, and then filtered by gravity on a fine frit. Dried under vacuum on the frit. No overall yield was obtained for this reaction; the pure product was used as it was obtained. ¹H NMR (0.05 M NaOD/D₂O, 300 MHz): δ 7.25 (d, J = 6 Hz, 2H), 7.35 (d, J = 6, 2H), 7.77 (dd, J = 6 Hz, 2H), 8.51 (s, 2H), 8.55 (s, 2H), 9.35 (d, J = 6 Hz, 2H). TOF-MS [ESI, *m/z* (rel. int.)]: 597.1 (100) [C₂₆H₁₇N₆O₈Fe]⁺.

3.2.3.2 *cis*-Bis(4,4'-dicarboxyl-2,2'-bipyridine) dicyano ruthenium(II). The RuCN compound was synthesized and purified using a modified literature procedure.^{13,17} The synthesis of the precursor, *cis*-bis(2,2'-bipyridyl-4,4'-dicarboxylic acid)dichloride ruthenium(II), Ru(dcbpy)₂Cl₂, is described in Chapter 2. ****EXTREME CAUTION** must be used when performing this reaction as deadly cyanide gas is produced.**

The reaction setup is constructed as seen in the Appendix. 0.14 g (0.25 mmol) of Ru(dcbpy)₂Cl₂ is suspended in ~12 mL of water in a 3-neck 50 mL round bottom flask.

While stirring, 0.27 g (5.6 mmol) of NaCN is added and the reaction is completely contained at this point with the separatory funnel (closed) and condenser attached and the septum securing the third neck. The reaction was heated and allowed to reflux at 110°C in the dark for 5 hours. The reaction is allowed to cool overnight. 50 mL of 1.0 M HCl is added to the separatory funnel and sealed and the reaction flask is tilted so the drops from the funnel drip directly into the reaction mixture. A needle fitted with Tygon tubing, is punctured through the septa on the third neck. This tubing is the nitrogen outlet and is bubbled through a 0.5 M KOH solution during and after the acidification step. The KOH solution is also contained under a custom beaker and the exit tubing is directed into the back of the hood. While vigorously stirring, the acid is added drop-wise to precipitate the orange solid product. The reaction flask is purged with nitrogen for a half hour after the addition of acid is ceased to ensure all HCN gas is removed. The solid is separated via centrifugation and is dried under vacuum within the centrifuge tube as the solid is quite sticky due to the acid groups. More product can be obtained from the supernatant by the addition of more HCl. The compound was dissolved in 3-5 mL of methanol and purified via a Sephadex LH-20 column. A light orange band eluted first, then a brown band, which is the product, then a deep red, then a medium orange band. The methanol is evaporated. 1.5 mL of 0.1 NaHCO₃/Na₂CO₃ buffer and 500 μL of 1.0 M HCl was added to precipitate the solid. 1.5 mL of water was added along with one drop of concentrated HCl and the solid was precipitated further overnight in 5-10 °C. The solid was filtered on 0.22 μm filter paper and dried on the paper under vacuum. Small impurities (~2-4%) were apparent in NMR. ¹H NMR (0.05 M NaOD/D₂O, 300 MHz): δ 7.44 (d, J = 6 Hz,

2H), 7.57 (d, J = 6, 2H), 7.90 (dd, J = 6 Hz, 2H), 8.61 (s, 2H), 8.70 (s, 2H), 9.42 (d, J = 6 Hz, 2H). UV/Vis (EtOH) λ (rel. int.): 309 nm (3.37), 362 nm (1.00), 345 nm (1.41).

3.3 Comparing Iron to Ruthenium in Dye-Sensitized Solar Cells

3.3.1 The Standard DSSC Clamp Cell. The structure of N3 is seen in Figure 1-6. The absorbance spectrum of N3 in solution and adsorbed to TiO₂ is seen in Figure 3-5. A 20 nm blue shift is seen for the lowest energy MLCT band when it is bound which is

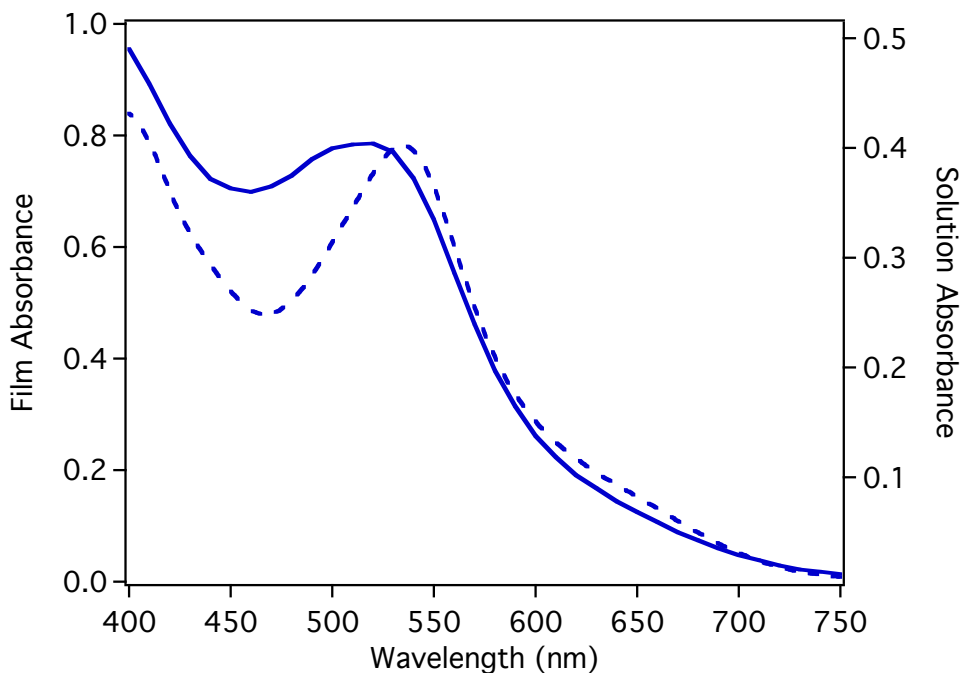


Figure 3-5. Absorbance of N3 (—) in 1 mM pyridine, 1 mM pyridinium triflate in ethanol solution and (---) adsorbed to TiO₂.

an indication of its interaction with the titania.¹⁸ Two sets of three cells were fabricated with N3 as the chromophore; one set without a blocking layer (BL) and another with a TiO₂ BL overlaid onto the FTO. The representative curves are seen in Figure 3-6 and the efficiency parameters are presented in Table 3-1. The curves are similar in shape and

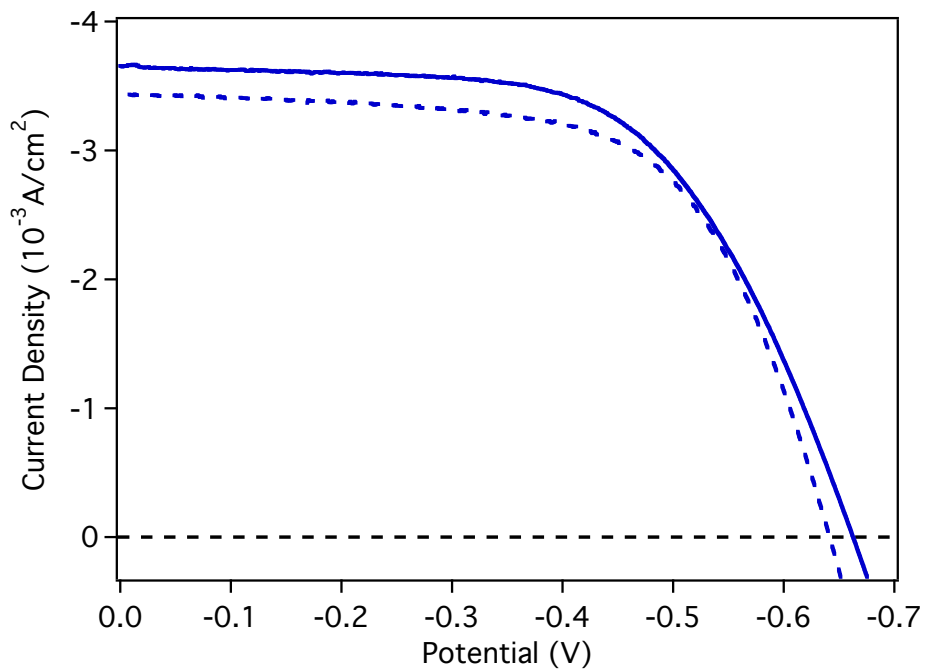


Figure 3-6. Representative J-V curve with N3 as a chromophore in a DSSC clamp cell. (—) Without and (---) with a TiO₂ blocking layer. 0.5 M LiI, 0.05 M I₂, 0.2 M TBP in MeCN, thermalized Pt counter electrode.

	Voc	Jsc	ff	η
<i>N3 no BL</i>	-0.599 V	3.76 mA/cm ²	0.63	1.41%
<i>N3 w/ BL</i>	-0.649 V	3.77 mA/cm ²	0.54	1.31%

Table 3-1. Efficiency parameters of N3 as a chromophore in a standard clamp cell, with and without a TiO₂ blocking layer. 0.5 M LiI, 0.05 M I₂, 0.2 M TBP in MeCN, thermalized Pt counter electrode.

have J_{SC} and V_{OC} values that coincide with each other. These values are lower in magnitude compared to the standard cell values in Chapter 2 presumably due to the larger diffusion distance of the redox couple in the electrolyte due to the rubber septa, as it is 30 times thicker than Surlyn. Each parameter value between the two sets of cells is within error, except for V_{OC} . It is unknown why the BL cells show a smaller fill factor than the cells without a BL. Since only three cells were fabricated for each set it is difficult to ascertain if this is an authentic difference due to the addition of the BL or just an anomaly in the small data set. The solution electrolyte percolates the TiO_2 film since the film is nanocrystalline so the electrolyte will be in contact with the FTO to some degree. It has been shown that an improvement in photovoltage results with the addition of a BL¹⁹ so it is possible that this back reaction process that recombines electrons with the oxidized redox species in solution manifests in a decreased photovoltage. More cells of each set need to be fabricated to determine if the difference in the V_{OC} is substantive. The BL does not seem to substantially affect the N3 cell in regards to the overall conversion efficiency. Next the recombination rate is examined.

Open-circuit-voltage-decay (OCVD) plots are presented in Figure 3-7 for both sets of cells with and without a BL. When the solar-simulated light is on (this section of data is not shown) the voltage jumps to a value close to the open-circuit voltage, 0.6 V, building up electrons in the conduction band of the TiO_2 . Once the light is turned off, the voltages decay, releasing the charge that has built up via the path of least resistance. The plot in Figure 3-7 only shows a single photovoltage decay for each set, after the light has

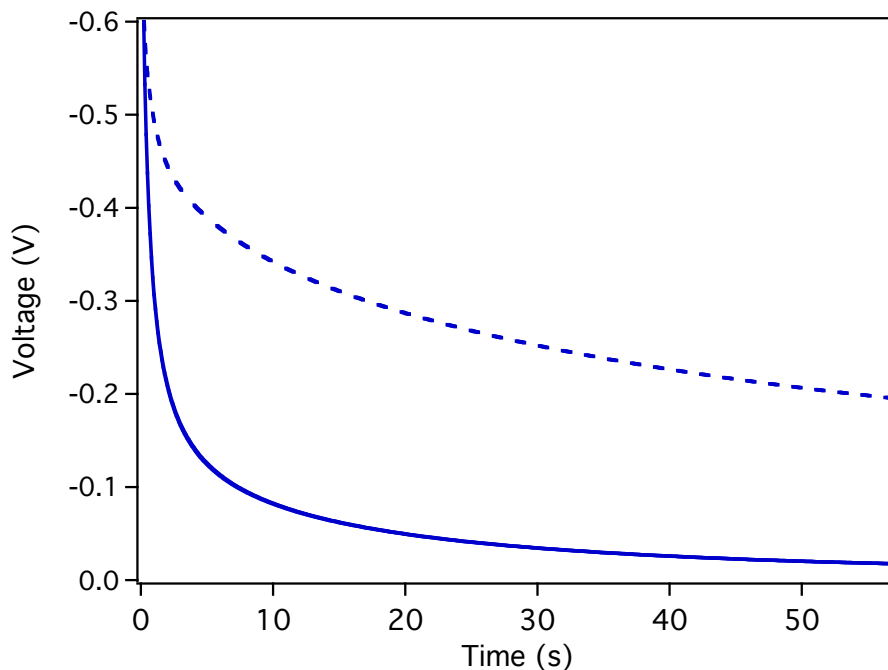


Figure 3-7. OCVD plot of N3 as a chromophore in a standard DSSC clamp cell (—) without a blocking layer, (---) with a TiO₂ blocking layer. 0.5 M LiI, 0.05 M I₂, 0.2 M TBP in MeCN, thermalized Pt counter electrode.

been turned off. In the decay, the electrons recombine with holes in oxidized dye molecules and oxidized molecules in the electrolyte. The rate of discharge is governed by the relative rates of recombination and back electron transfer and possibly the electron transfer from the FTO to the electrolyte. There is increased rate of decrease of photovoltage in the data set without BL, decaying to essentially zero by 60 seconds. The rate of recombination is 17 times slower with a TiO₂ BL than without. Since the only difference between the two sets of cells is the BL, it is presumed that the change in rate of decay is due to the slowing of back contact electron transfer reaction that occurs from the FTO to the electrolyte.¹⁹ The electron lifetimes can be calculated from these data²⁰ but we find that the simple decays are illustrative and clear enough for our interpretations.

Now that a new standard DSSC has been presented using the clamp cell configuration along with the new dyeing method and new electrolyte concentrations, new chromophores can be incorporated and measured against the N3 standard.

3.3.2 *cis*-Bis(4,4'-dicarboxyl-2,2'-bipyridine) dicyano Ruthenium(II) as a Chromophore in DSSCs. Two sets of DSSCs were fabricated using RuCN as the chromophore, one set without a BL present, and one set with a compact TiO₂ under layer. Due to fabrication issues, one cell of each type is represented. In order for a complete study, these data should be repeated.

The structure of the RuCN molecule is seen in Figure 3-8. The absorbance of the

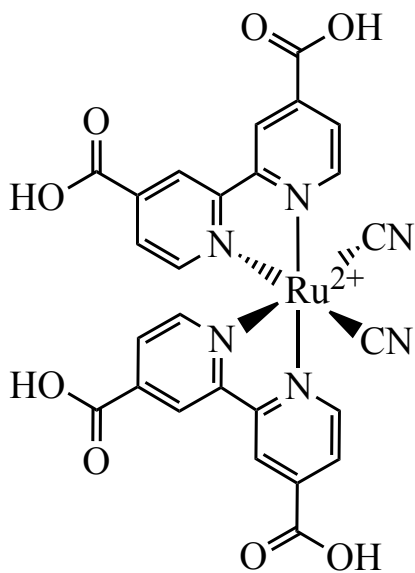


Figure 3-8. Structure of *cis*-bis(4,4'-dicarboxyl-2,2'-bipyridine) dicyano ruthenium(II), RuCN.

RuCN in solution and on TiO₂ film is seen in Figure 3-9, a 65 nm blue shift is seen when the dye is adsorbed to the film. Again the shift is due to the weak interaction of the carboxyl-functionalized ligand interaction with the titania.¹⁸ Also noted is the absorbance

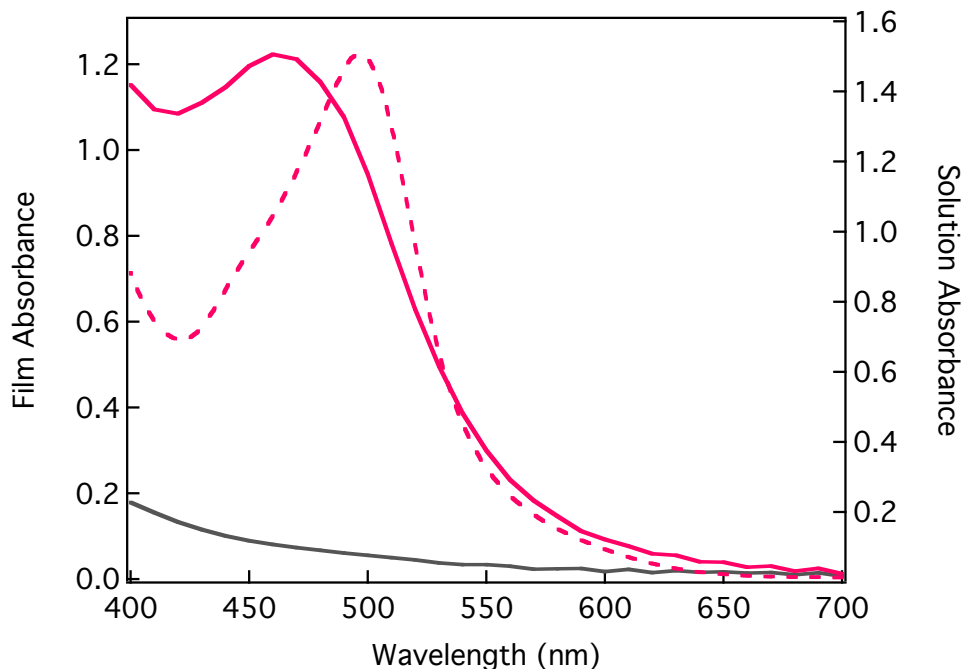


Figure 3-9. Absorbance of RuCN (---) in 1 mM pyridine, 1 mM pyridinium triflate in ethanol solution and (—) adsorbed to TiO₂. The absorbance of the undyed TiO₂ film (—) is also shown.

of 1.2 for the RuCN complex on TiO₂ is quite high when adsorbed from a 0.3 mM solution of the dye.

The J-V curve of each of the cells are seen in Figure 3-10 and the efficiency parameters are in Table 3-2. The two J-V curves show a very similar performance to each

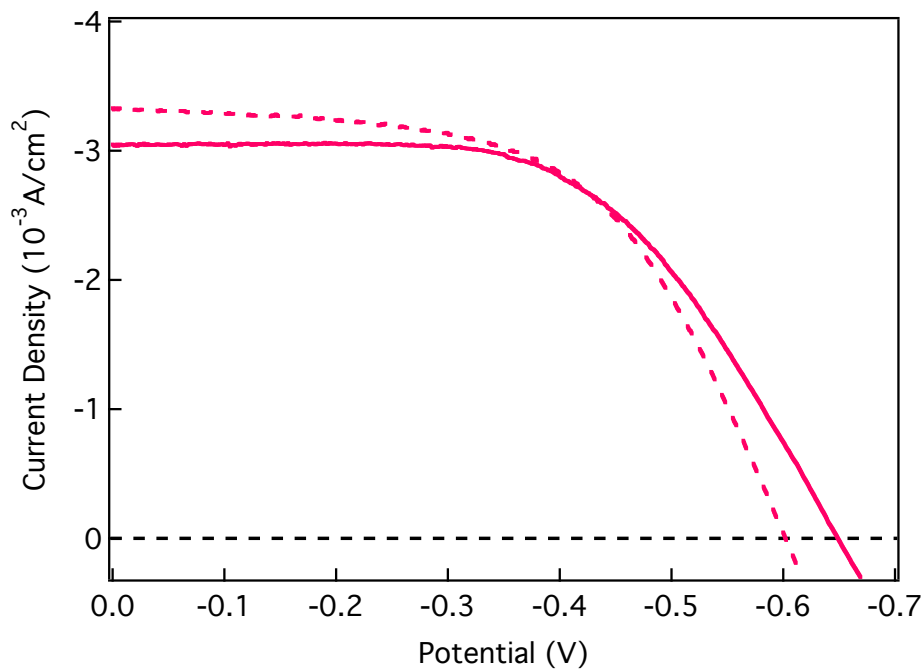


Figure 3-10. Representative J-V curve for RuCN as a chromophore in DSSCs (—) without and (---) with a TiO₂ blocking layer. 0.5 M LiI, 0.05 M I₂, 0.2 M TBP in MeCN, thermalized Pt counter electrode.

	V_{oc}	J_{sc}	ff	η
<i>RuCN no BL</i>	-0.603 V	3.34 mA/cm ²	0.57	1.14%
<i>RuCN w/ BL</i>	-0.649 V	3.04 mA/cm ²	0.58	1.14%

Table 3-2. Efficiency parameters of RuCN as a chromophore in a standard clamp cell, with and without a TiO₂ blocking layer. 0.5 M LiI, 0.05 M I₂, 0.2 M TBP in MeCN, thermalized Pt counter electrode.

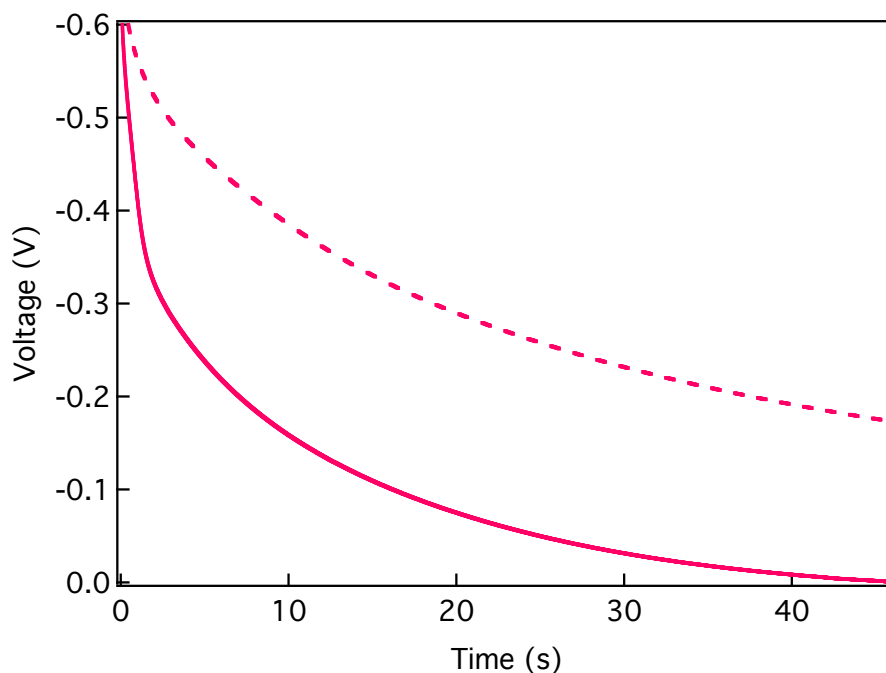


Figure 3-11. OCVD plot of RuCN as a chromophore in a DSSC clamp cell (—) without and (---) with a TiO₂ blocking layer. 0.5 M LiI, 0.05 M I₂, 0.2 M TBP in MeCN, thermalized Pt counter electrode.

other, ff and efficiency are essentially the same, and minimal differences are seen for V_{OC} and J_{SC} . V_{OC} increases by 0.5 V and current decreases 10% for the BL cell.

These data are also quite similar to the N3 data sets. The shape of the J-V curve are fairly similar along with values for V_{OC} and ff . J_{SC} exhibits a bit higher performance for N3 at 3.8 mA/cm², compared to RuCN at ~3 mA/cm². The higher J_{SC} urges the conversion efficiency by ~0.2% higher as well. Higher J_{SC} and efficiency is expected for N3 since it is one of the highest performing ruthenium dyes used in DSSCs.^{21–23} The key here is that the performance of both ruthenium dyes are similar, with N3 performing

slightly better, and the BL does not seem to drastically affect any parameter. A 0.5 V increase in V_{OC} is seen for each dye when a BL is added. Further study is needed to confirm its presence is indeed indicative of a BL effect.

The OCVD curves for the RuCN DSSCs are seen in Figure 3-11, decaying from the V_{OC} value. The cell without a BL discharges 20 times faster and decays to zero within 50 seconds while the BL cell reaches essentially zero after over 400 seconds, 20 times longer. This difference in decay is similar to the N3 cells showing a similar effect the BL has on the discharge of electrons. The BET from the substrate is blocked or slowed, which slows the recombination. Also since the only difference between the cells is the BL, the process that is affected must be the back contact electron transfer from the FTO to the electrolyte. It might be possible the small difference in the decay time is indicative of the better performance of N3. Either a slower back electron transfer to the dye or more likely a more efficient regeneration by the iodide/triiodide redox couple. Next the iron analog is examined.

3.3.3 *cis*-Bis(4,4'-dicarboxyl-2,2'-bipyridine) dicyano Iron(II) as a Chromophore in DSSCs. Two sets of cells were fabricated using FeCN as a chromophore, one with a compact TiO₂ BL and one without. Due to difficulties with construction, one cell was salvaged for each set. Another set of cells without a BL was fabricated as part of another batch where one cell produced an almost identical performance to the first; the other cells also had construction issues. Here the original batch is reported to be consistent since it is composed of both data types.

The structure of the FeCN chromophore is depicted previously in Figure 3-2; the absorption of the dye in solution and adsorbed to TiO₂ is seen in Figure 3-12, a 20 nm

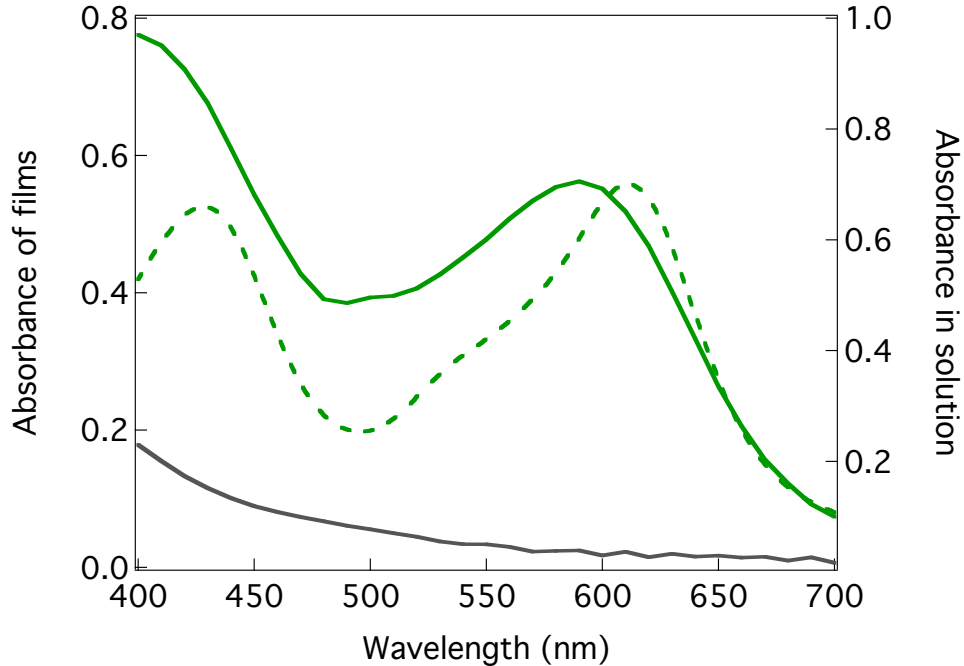


Figure 3-12. Absorbance of FeCN (—) in 1 mM pyridine, 1 mM pyridinium triflate in ethanol solution and (—) adsorbed to TiO₂. The absorbance of the undyed TiO₂ film (—) is also shown.

shift toward the blue is observed when bound, similar to N3. The J-V curves for both of the FeCN cells are presented in Figure 3-13. The J_{SC} increases from 15 μA/cm² to 117 μA/cm² when the BL is added to the cell fabrication, an entire magnitude higher current. The V_{OC} for FeCN is 0.212 V for no BL and 0.39 V with a BL. The increase of these parameter values suggests that with the inclusion of a blocking layer an aspect of dark current is being shut down. From Equations 1-3 and 1-4, a lower J_{dark} increases both the

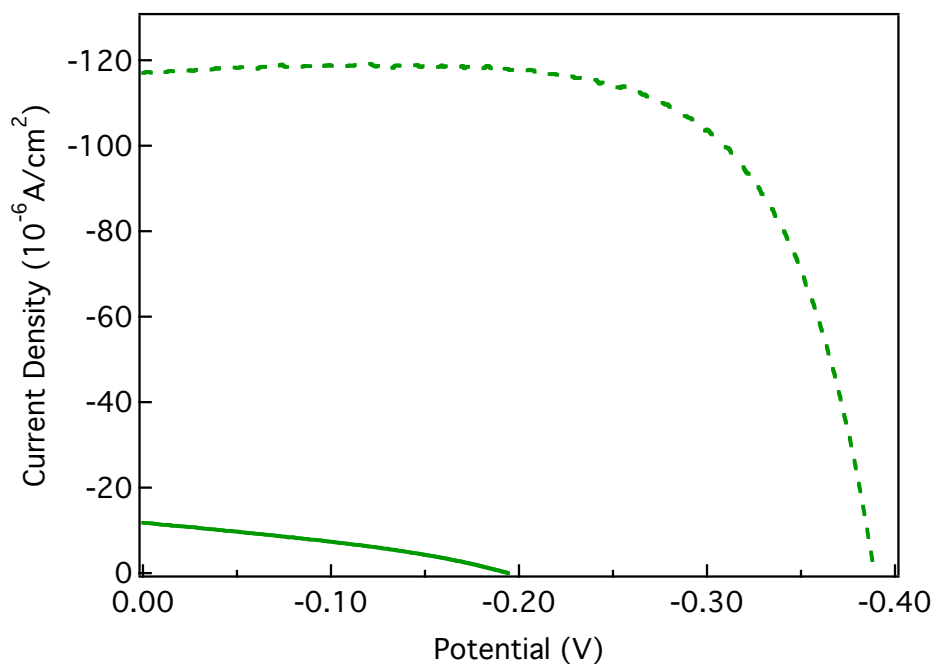


Figure 3-13. Representative J-V curves for FeCN as a chromophore in DSSCs (—) without and (---) with a TiO₂ blocking layer. 0.5 M LiI, 0.05 M I₂, 0.2 M TBP in MeCN, thermalized Pt counter electrode.

	Voc	Jsc	ff	η
<i>FeCN no BL</i>	-0.212 V	15.0 μA/cm ²	0.38	0.0013%
<i>FeCN w/ BL</i>	-0.390 V	117 μA/cm ²	0.68	0.031%

Table 3-3. Efficiency parameters of FeCN as a chromophore in a standard clamp cell, with and without a TiO₂ blocking layer. 0.5 M LiI, 0.05 M I₂, 0.2 M TBP in MeCN, thermalized Pt counter electrode.

photovoltage and the photocurrent. The parameter increase also suggests that this dark current is fast enough to affect the performance of the cell, therefore it's rate is faster than or competitive with another rate. Since the only difference between the two batches of cells is the BL, it follows that the back electron transfer from the substrate is the dark current culprit. This BET process, knowingly, competes with the reduction of the redox couple by the counter electrode, but the counter electrode, redox couple remain the same for these systems. The only other process that could be competing with BET from the substrate but is not ordinarily discussed is the rate of dye regeneration by the redox couple.

FeCN performs worse than RuCN for both with and without the BL data sets. The J_{SC} for FeCN is on the order of microampere, compared to milliampere for the ruthenium compounds. The V_{OC} is also smaller for Fe than Ru, suggesting that there is a backwards process that is more significant for Fe than for Ru. There is also a smaller, 20 nm, absorption shift of the higher energy MLCT band when bound to TiO_2 , compared to RuCN which shifts 65 nm. This could suggest a lower interaction of the Fe molecule with the TiO_2 than the Ru.¹⁸ Yet the shift is similar to the blue shift seen for N3, which performs the better of the three molecules. Peak shifts are normally indicative of differences in protonation with these types of molecules²⁴ but the dyeing process is performed in a buffer solution of pyridine and a pyridinium salt, effectively controlling the level of protonation.

Also concerning the ruthenium analog, there is no significant change when the BL is included. When iron is the chromophore, the BL seems to make a significant difference to the cell performance so there is a distinct difference with the change to iron. It is quite

possible that the regeneration of the dye is slower with FeCN. The BET could be now competing for the regeneration of the dye with performance improving when this process is blocked. Further study is needed to fully understand these processes in iron.

In Figure 3-14, the voltage decays are presented for the FeCN solar cells. The voltage decays from V_{OC} to zero by 20 seconds for the DSSC without a BL. With a BL the decay takes 360 seconds, 18 times longer. This confirms that with a BL a backwards electron transfer process is significantly slowed and it must be a process from the FTO

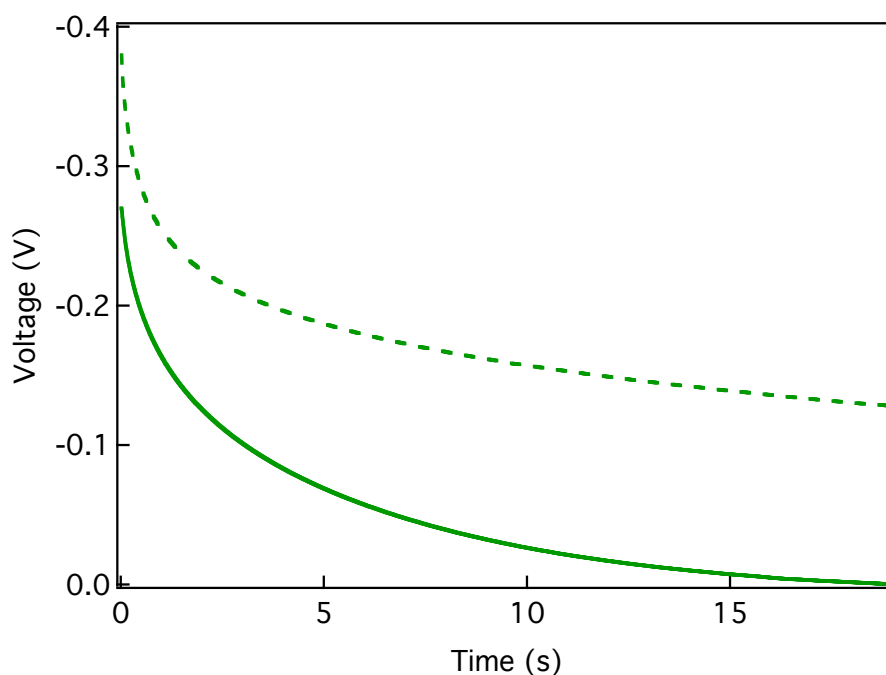


Figure 3-14. OCVD plot of FeCN as a chromophore in a DSSC clamp cell (—) without and (---) with a TiO_2 blocking layer. 0.5 M LiI, 0.05 M I_2 , 0.2 M TBP in MeCN, thermalized Pt counter electrode.

substrate. In Figure 3-15 the OCVD plots are presented for both the FeCN and the RuCN for comparison. For both the Fe and Ru cells the BL causes the increase of the decay by

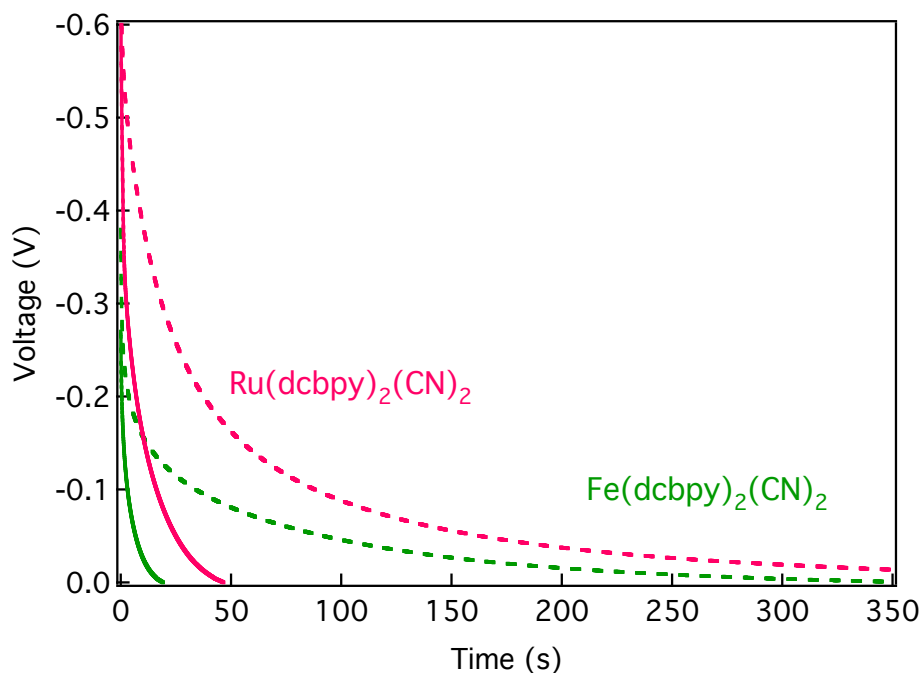


Figure 3-15. OCVD plots of FeCN and RuCN as chromophores in DSSC clamp cells. FeCN (—) without and (---) with a TiO₂ blocking layer. RuCN (—) without and (---) with a TiO₂ blocking layer. 0.5 M LiI, 0.05 M I₂, 0.2 M TBP in MeCN, thermalized Pt counter electrode.

approximately 20 times, demonstrating that BL effect is similar between the two molecules, yet the FeCN DSSC has a faster decay rate for both sets of cells.

The reduction of heteroleptic iron(III) compounds by iodide is in the Marcus Normal region and the rate increases with increased driving force.²⁵ The same is true for the ruthenium(II/III) couple. In Figure 3-16 the redox potentials for N3, RuCN and FeCN are shown relative to the iodide/triiodide redox couple and the conduction band edge for

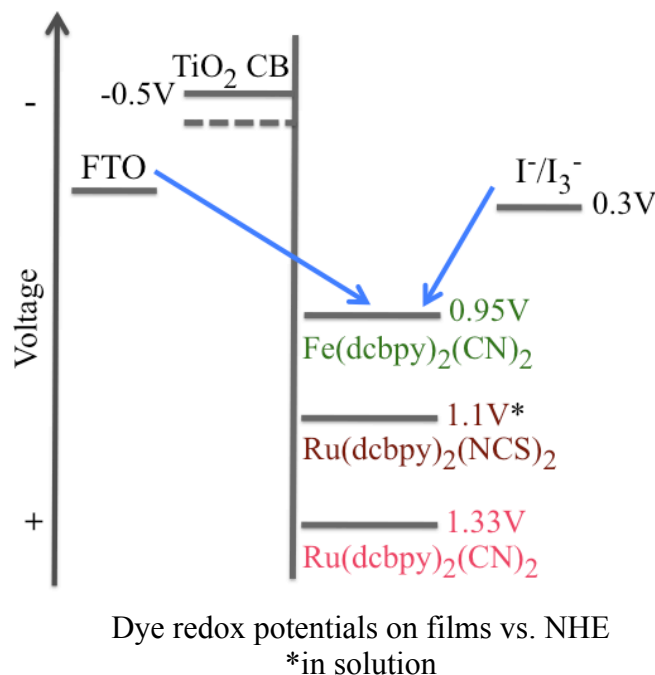


Figure 3-16. Diagram of the relative redox potentials of N3, RuCN and FeCN with respect to the iodide/triiodide redox couple and the conduction band of TiO₂. The potentials are referenced to NHE.

TiO₂. The diagram shows that the driving force for the regeneration of the dye is decreased when moving to FeCN to RuCN by about 400mV. The negative shift of FeCN reduction potential compared to RuCN helps to explain that the overall decreased FeCN DSSC performance is due to the slower rate of dye regeneration by iodide. In a literature example, [Fe(dmbpy)₂(CN)₂]₂NO₃ has a redox potential 100mV more negative than [Fe(bpy)₂(CN)₂]₂NO₃ and the rate of reduction by iodide is substantially slower.²⁵ Yet, it is noticed that N3 performs better than RuCN even with the negative shift of redox potential but N3 has been shown to outperform other ruthenium bipyridyl compounds throughout the literature. The redox potential shift does not explain the change in V_{OC}

and J_{SC} that is seen with FeCN, but not RuCN, when the blocking layer is added. The ‘only’ part of the cell that is changing is the metal center and therefore the redox potential. The only process(es) originate at the FTO. This could mean electrons recombining with oxidized electrolyte but since the rate of regeneration of the FeCN dye is slower than the population of iodide would be higher than in the RuCN cell, this would slow this BET process. Another possibility could be a reduction of the dye by the FTO. A process not ordinarily discussed as a pertinent backwards electron process in DSSCs. Further studies are needed to see if a change in driving force for this possible reduction affects the DSSC performance. Also continued research to investigate the possibility for a correlation between redox potential and the addition of a blocking layer with DSSC performance.

3.4 Concluding Comments

Ruthenium polypyridyls have historically been the most successful dyes in DSSCs until a couple of recent reports.^{26,27} Ruthenium is a rare metal so its commercial scalability is problematic due to cost. Our research group has focused on the development of iron polypyridyls as dye replacement to the ruthenium counterpart due to its substantially increased abundance and therefore its inexpensiveness. Our extensive knowledge provides a good research base to build upon in the examination of iron as a potential dye in DSSCs.

After a modification to the fabrication procedure a new N3 standard cell employing a clamped design was constructed in which to compare changes against. A previously reported Fe dye was incorporated into our DSSC design and its performance

was compared to its Ru analog. The comparison in performance was made using standard J-V curves and OCVD plots for solar cells with and without a compact TiO₂ blocking layer to elucidate a change in back electron transfer differences between the dyes. Further studies are necessary to confirm findings and continue investigation of these systems.

APPENDIX

APPENDIX

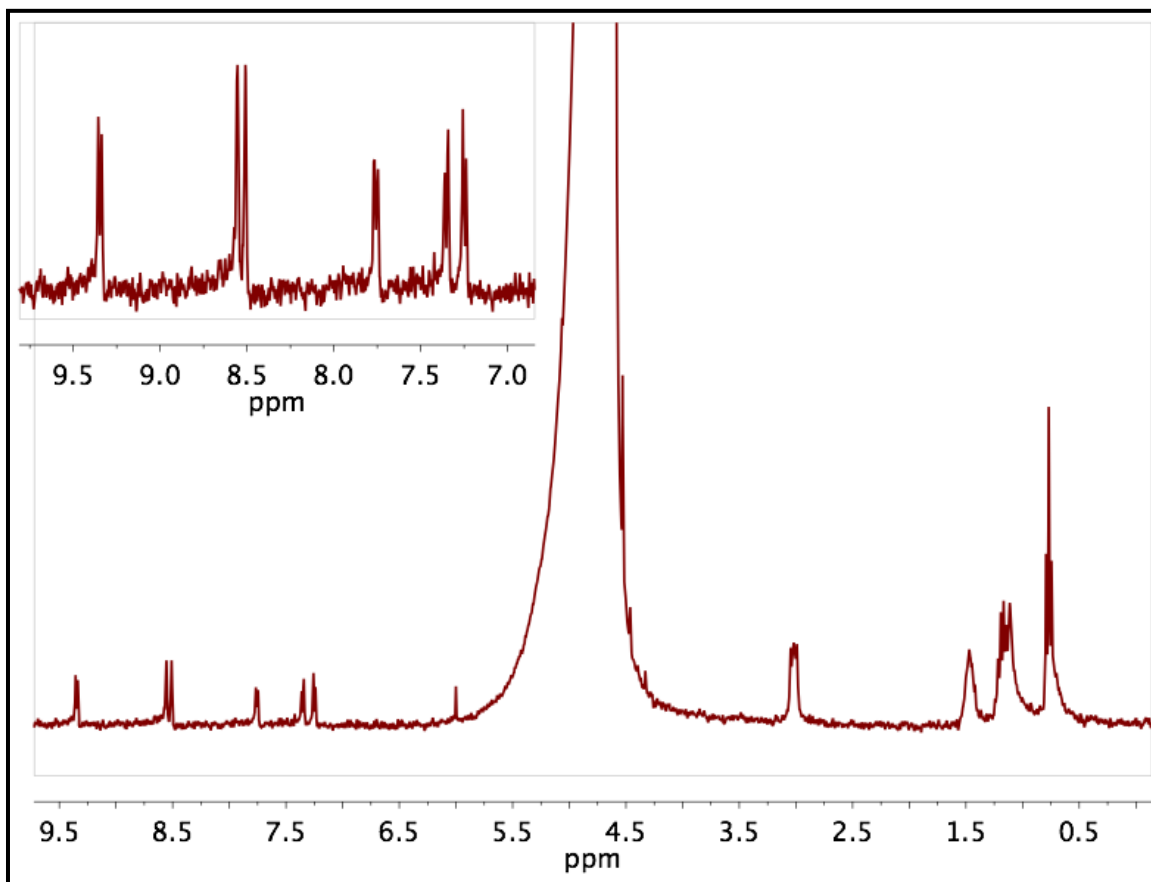


Figure 3-17. ¹H NMR Spectrum of *cis*-bis(2,2'-bipyridyl-4,4'-dicarboxylato) dicyano iron(II) in 0.05 M NaOD in D₂O.

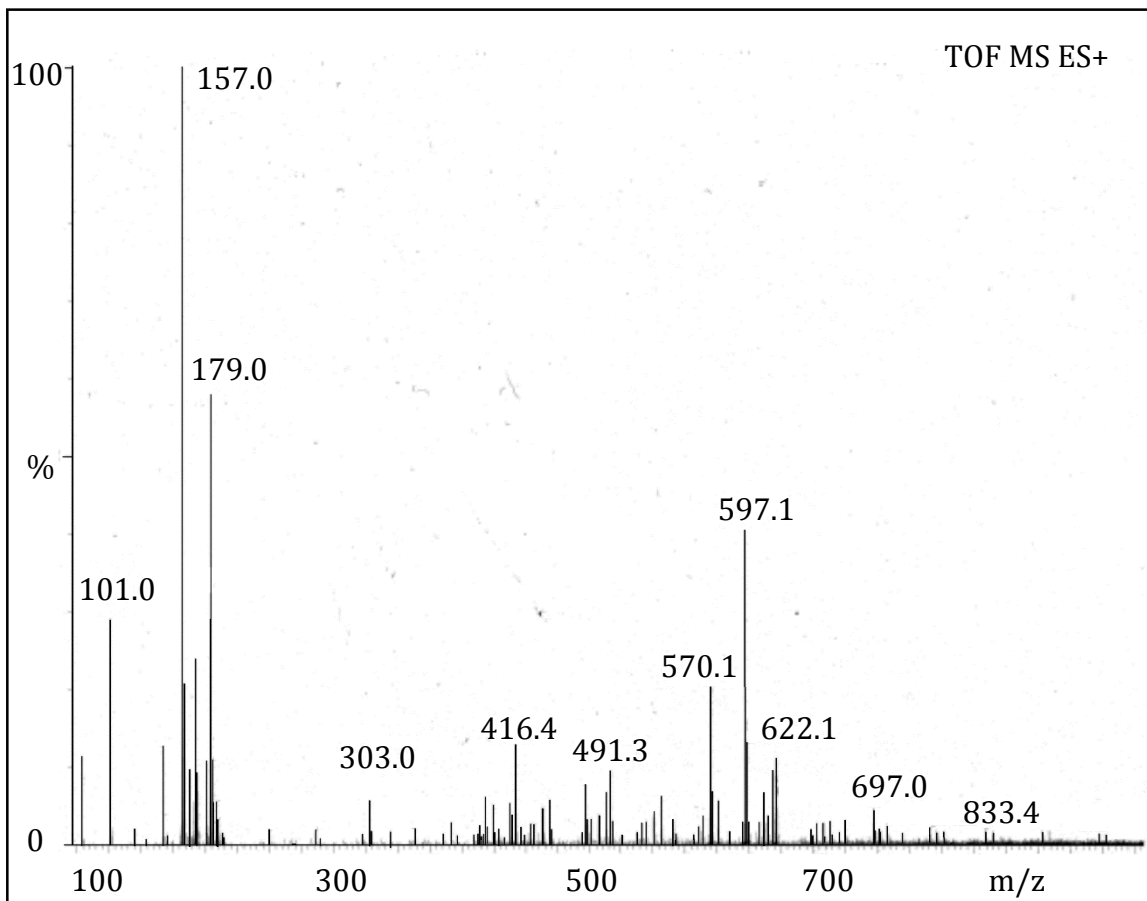


Figure 3-18. ESI-MS of FeCN.



Figure 3-19. Setup for the reaction of $\text{Ru(dcbpy)}_2\text{Cl}_2$ with NaCN to yield RuCN . The system is completely enclosed to ensure HCN containment. Acid addition is performed via a glass fitted separatory funnel attached to the reaction flask with a nitrogen inlet through the condenser and an outlet that bubbles through a basic solution.

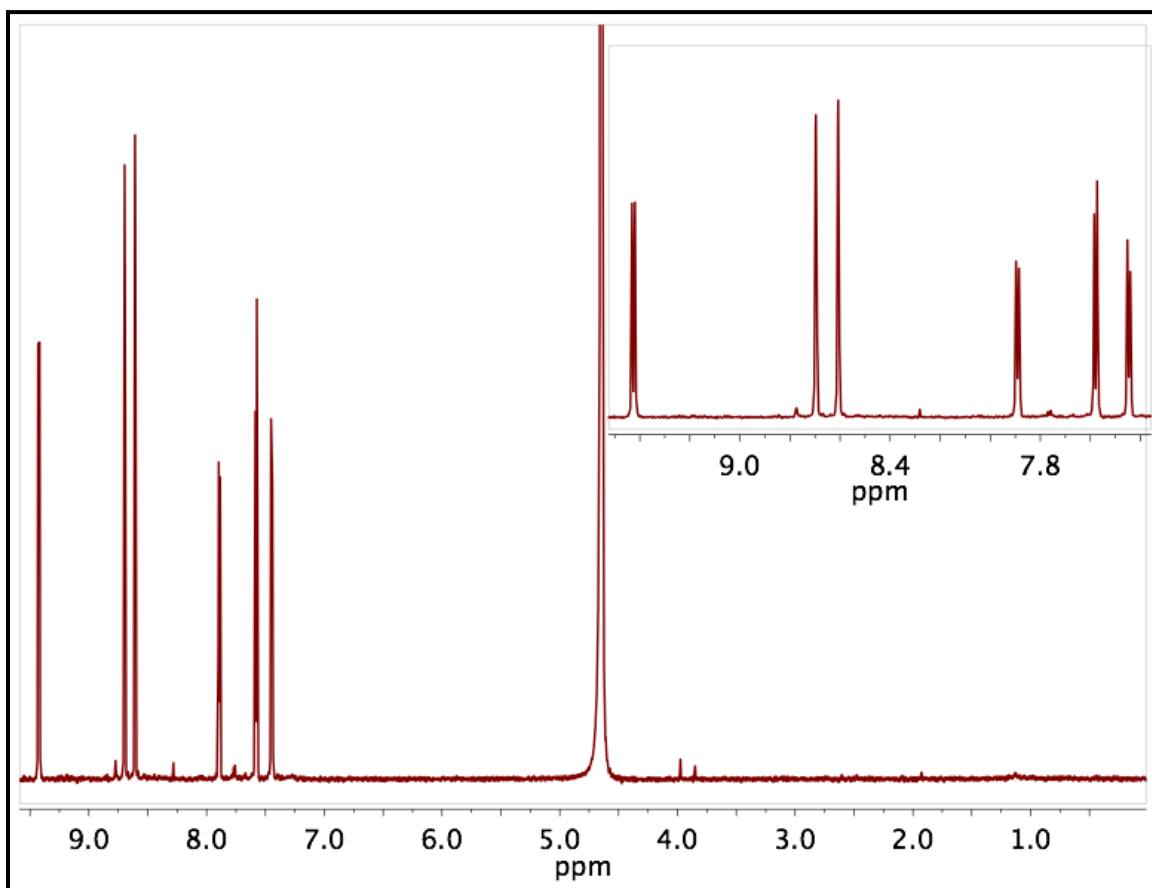


Figure 3-20. ¹H NMR Spectrum of *cis*-bis(2,2'-bipyridyl-4,4'-dicarboxylato) dicyano ruthenium(II) in 0.05 M NaOD in D₂O.

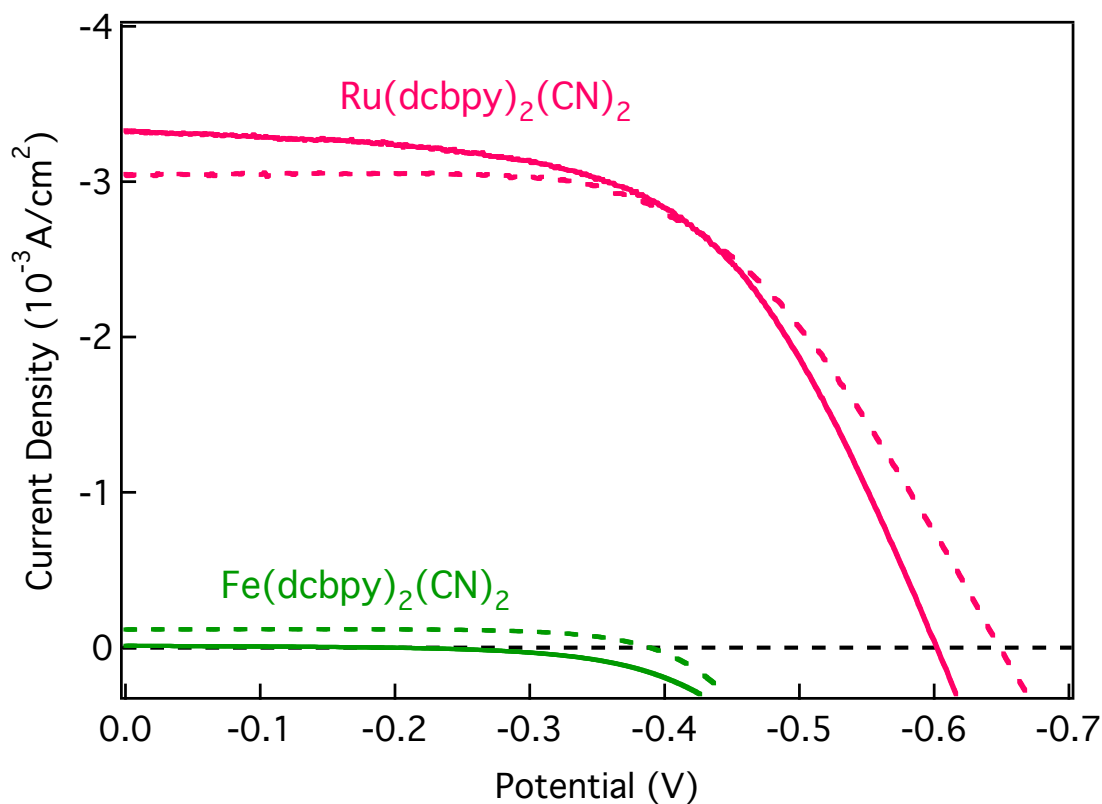


Figure 3-21. Representative J-V curve comparison for FeCN (—) without and (---) with a TiO₂ blocking layer, also RuCN (—) without and (---) with a TiO₂ blocking layer. The dyes are chromophores in DSSCs. Electrolyte: 0.5 M LiI, 0.05 M I₂, 0.2 M TBP in MeCN, thermalized Pt counter electrode.

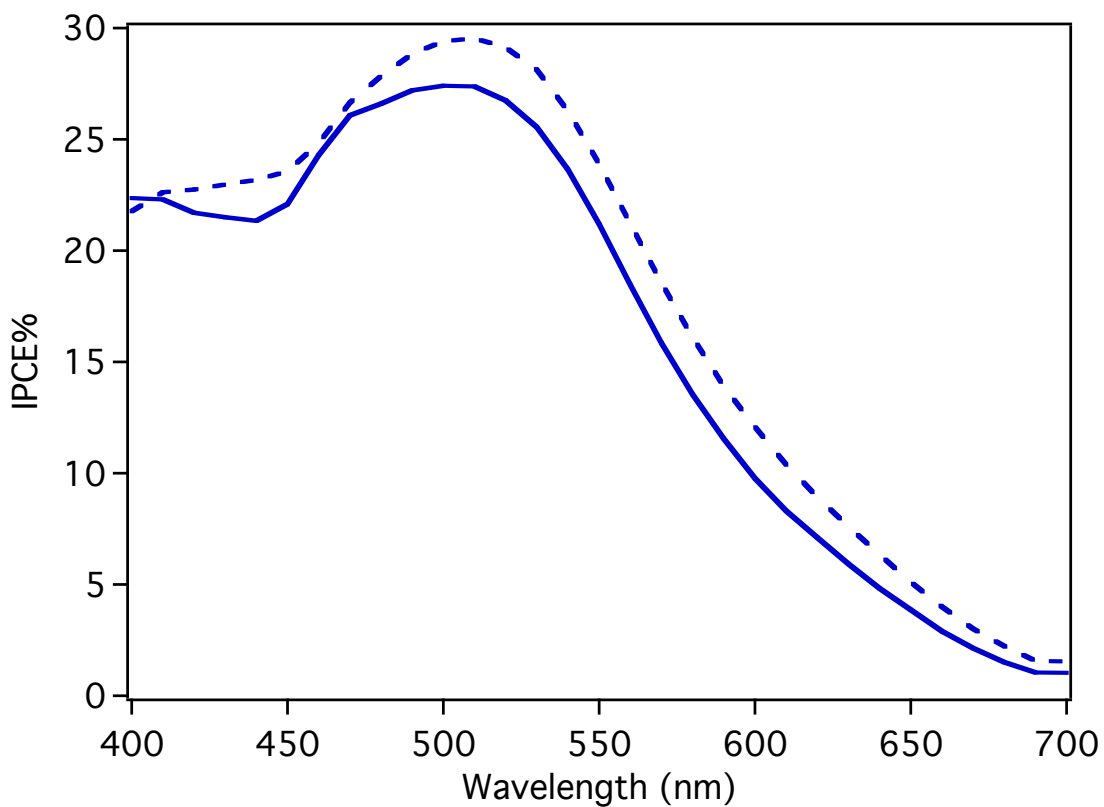


Figure 3-22. IPCE plot of N3 as a chromophore in a DSSC (—) without and (---) with a TiO₂ blocking layer. Electrolyte: 0.5 M LiI, 0.05 M I₂, 0.2 M TBP in MeCN, thermalized Pt counter electrode.

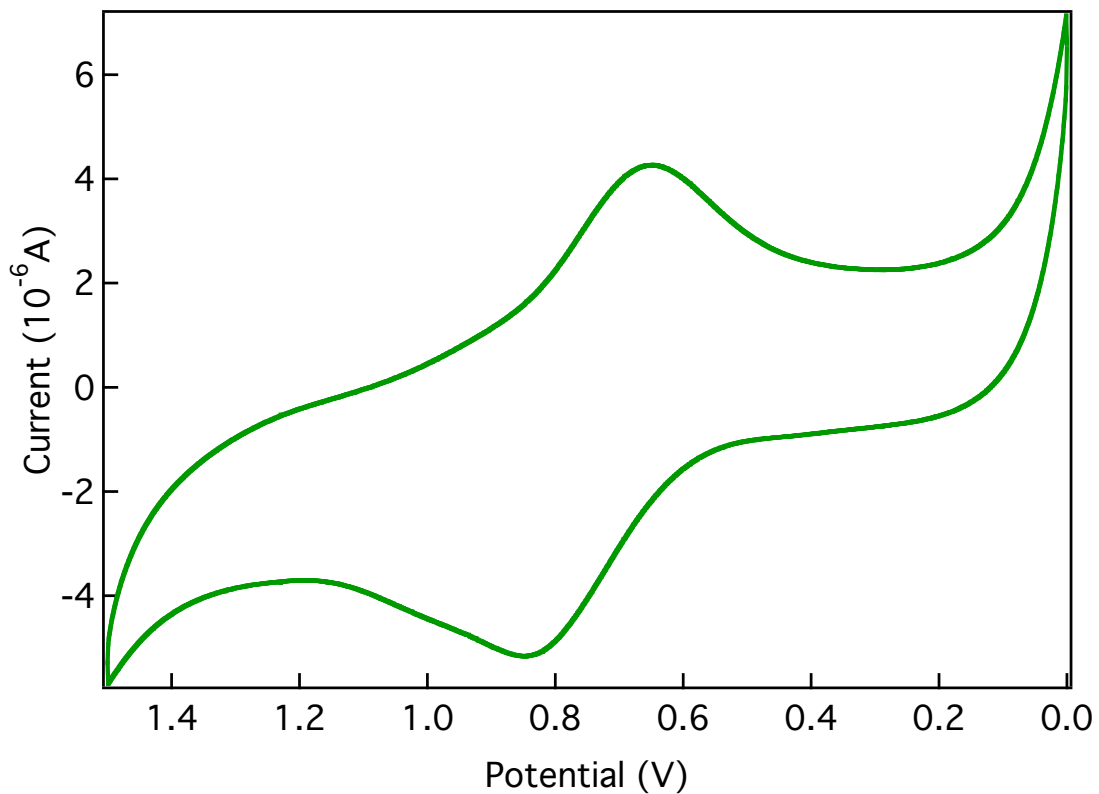


Figure 3-23. Cyclic voltammogram of FeCN adsorbed onto TiO₂ film as the working electrode, Ag/AgCl reference electrode and a carbon rod as the counter electrode in 0.1 M TBAPF₆ in acetonitrile. $E_{1/2} = 0.74$ V vs. Ag/AgCl, $\Delta E = 190$ mV.

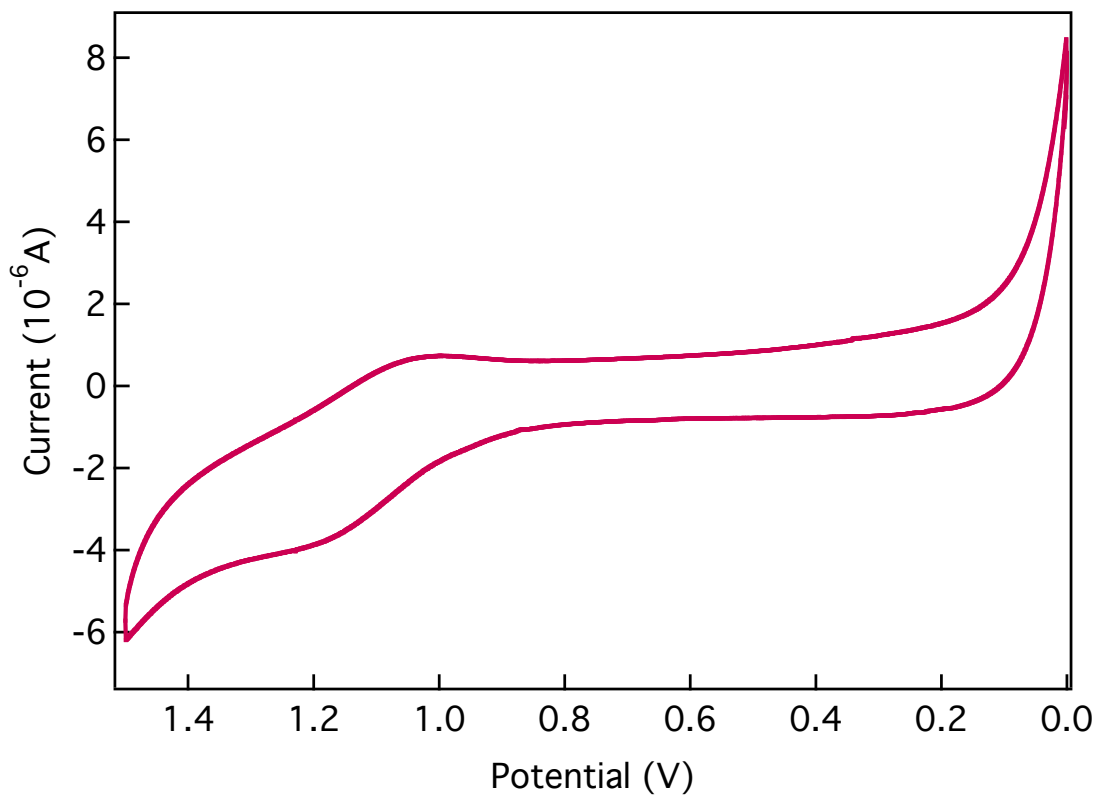


Figure 3-24. Cyclic voltammogram of RuCN adsorbed onto TiO₂ film as the working electrode, Ag/AgCl reference electrode and a carbon rod as the counter electrode in 0.1 M TBAPF₆ in acetonitrile. $E_{1/2} = 1.13$ V vs. Ag/AgCl, $\Delta E = 210$ mV.

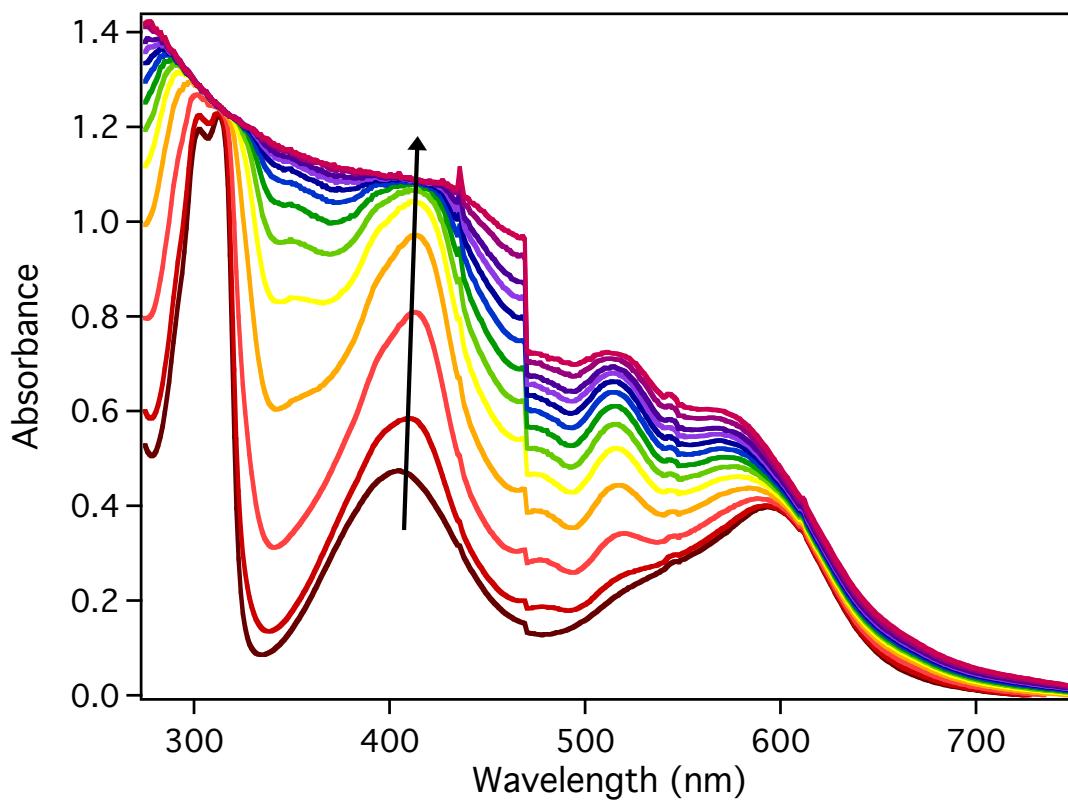


Figure 3-25. Spectroelectrochemistry of FeCN in 0.1 M tetrabutylammonium hexafluorophosphate in acetonitrile. Pt mesh working electrode, Ag/AgCl reference and Pt coil counter. The oxidation potential was set to 1.0 V and an absorption spectrum was taken every 30 seconds.

Freeze-Pump-Thaw Method. The solvent is put into a two or three-neck round bottom flask equipped with a vacuum adapter. A flask is chosen that is large enough so that the flask is two-thirds empty when the solvent is added; the other necks are fastened with septa and then secured with a copper wire. The flask is evacuated and back-filled with nitrogen three to five times. The solvent is put under nitrogen and frozen completely in a bath of liquid nitrogen, freezing from the very bottom of the flask, up to the top. The flask is slowly submerged continuously, or in an up-and-down motion. Once the solvent is frozen, evacuate and pump on the ice under full vacuum for at least 10 minutes. Protected by the sash the vacuum is turned off as the flask could crack or break. Still protected by the sash, the flask is submerged into room temperature water until the ice is melted. Once the ice is freely moving from the glass, vacuum is reapplied and it is pumped on until the solvent is completely liquid. The flask is back-filled with nitrogen. This process is repeated three to five cycles. The solvent is cannula-transferred to the reaction, or storage flask under positive nitrogen pressure.

REFERENCES

REFERENCES

- (1) O'Regan, B. C.; Grätzel, M. *Nature* **1991**, *353*, 737–740.
- (2) Chiba, Y.; Islam, A.; Watanabe, Y.; Komiya, R.; Koide, N.; Han, L. *Japanese Journal of Applied Physics* **2006**, *45*, L638–L640.
- (3) Chen, C.-Y.; Wang, M.; Li, J.-Y.; Pootrakulchote, N.; Alibabaei, L.; Ngoc-le, C.; Decoppet, J.-D.; Tsai, J.-H.; Gratzel, C.; Wu, C.-G.; Zakeeruddin, S. M.; Grätzel, M. *Acs Nano* **2009**, *3*, 3103–3109.
- (4) Koops, S. E.; O'Regan, B. C.; Barnes, P. R. F.; Durrant, J. R. *Journal of the American Chemical Society* **2009**, *131*, 4808–18.
- (5) Asbury, J. B.; Wang, Y.-Q.; Hao, E.; Ghosh, H. N.; Lian, T. *Research on Chemical Intermediates* **2001**, *27*, 393–406.
- (6) Bressler, C.; Milne, C.; Pham, V.-T.; Elnahas, A.; van der Veen, R. M.; Gawelda, W.; Johnson, S.; Beaud, P.; Grolimund, D.; Kaiser, M.; Borca, C. N.; Ingold, G.; Abela, R.; Chergui, M. *Science* **2009**, *323*, 489–92.
- (7) Ferrere, S. *Journal of the American Chemical Society* **1998**, *120*, 843–844.
- (8) Jamula, L. L. Design and Synthesis of Iron(II) Terpyridyl Complexes for Application in Dye-Sensitized Solar Cells, Michigan State University, 2010.
- (9) Jamula, L. L. Exploring Design Strategies to Tune the Electronic Structure and Ultrafast Dynamics of Iron(II) Polypyridyl Chromophores, 2013.
- (10) Brown, A. M. Excited-State Dynamics of Iron(II)-Based Charge-Transfer Chromophores, 2011.
- (11) Personal Correspondence with Prof. Tom Hamann's group.
- (12) Xie, Y.; Hamann, T. W. *The Journal of Physical Chemistry Letters* **2013**, *4*, 328–332.
- (13) Sauve, G.; Cass, M. E.; Coia, G.; Doig, S. J.; Lauermann, I.; Pomykal, K. E.; Lewis, N. S. *The Journal of Physical Chemistry B* **2000**, *104*, 6821–6836.
- (14) *The pyridine—pyridinium triflate buffer holds the pH at 5.25 in water.*
- (15) Ferrere, S. *Chemistry of Materials* **2000**, *12*, 1083–1089.

- (16) Schilt, A. A. *Journal of the American Chemical Society* **1960**, *82*, 3000–3005.
- (17) Sauve, G. Dye Sensitization of nanocrystalline titanium dioxide with osmium and ruthenium polypyridine complexes, California Institute of Technology, 1999.
- (18) Shoute, L. C. T.; Loppnow, G. R. *Journal of the American Chemical Society* **2003**, *125*, 15636–46.
- (19) Cameron, P. J.; Peter, L. M.; Hore, S. *The Journal of Physical Chemistry B* **2005**, *109*, 930–6.
- (20) Zaban, A.; Greenshtein, M.; Bisquert, J. *ChemPhysChem : a European Journal of Chemical Physics and Physical Chemistry* **2003**, *4*, 859–64.
- (21) Ardo, S.; Meyer, G. J. *Chemical Society Reviews* **2009**, *38*, 115–64.
- (22) Nazeeruddin, M. K.; Kay, A.; Rodicio, I.; Humphry-Baker, R.; Mueller, E.; Liska, P.; Vlachopoulos, N.; Grätzel, M. *Journal of the American Chemical Society* **1993**, *115*, 6382–6390.
- (23) Grätzel, M. *Journal of Photochemistry and Photobiology A: Chemistry* **2004**, *164*, 3–14.
- (24) Nazeeruddin, M. K.; Zakeeruddin, S. M.; Humphry-Baker, R.; Jirousek, M.; Liska, P.; Vlachopoulos, N.; Shklover, V.; Fischer, C.; Grätzel, M. *Inorganic Chemistry* **1999**, *38*, 6298–6305.
- (25) Wang, X.; Stanbury, D. M. *Inorganic Chemistry* **2006**, *45*, 3415–23.
- (26) Yella, A.; Lee, H.-W.; Tsao, H. N.; Yi, C.; Chandiran, A. K.; Nazeeruddin, M. K.; Diau, E. W.-G.; Yeh, C.-Y.; Zakeeruddin, S. M.; Grätzel, M. *Science* **2011**, *334*, 629–34.
- (27) Burschka, J.; Pellet, N.; Moon, S.-J.; Humphry-Baker, R.; Gao, P.; Nazeeruddin, M. K.; Grätzel, M. *Nature* **2013**, *499*, 316–9.

Chapter 4. Incorporation of Quasi Solid-State Electrolyte Materials in Dye-Sensitized Solar Cells

4.1 Introduction

The first electrolytes used in dye-sensitized solar cells have been solution-based. Acetonitrile has been the solvent most commonly used; advantages include its wide solvent window, the high solubility of electrolyte components, and also many of the dyes are insoluble reducing chances for desorption from the TiO₂. Solution-based electrolytes in DSSCs pose a significant problem with leakage, especially at the elevated temperatures they are subjected to in direct sunlight. Acetonitrile is extremely volatile, which of course amplifies with increased temperatures. This creates pressure inside of the solar cells when it is heated; causing it to slowly leak through the Surlyn seal or even splits the cell apart.

A move towards solid-state and quasi solid-state electrolytes, or hole-transport media (HTM), in DSSCs has been studied since the 1990s.¹⁻³ They should be more stable in the DSSC under ambient and elevated temperatures lowering the potential for leakage. HTM could also increase the ease of mass production while hopefully reducing cost. Alternative CHNO-based electrolytes, rather than iodine, eliminate the need for platinum counter electrodes along with consisting of cheaper, more abundant elements. In order to compete with solution-based electrolytes, solid-state materials need to have high conductivity, high hole transport from the dye, low rate of recombination from the conduction band of TiO₂ and good penetration into the nanocrystalline film. Different alternatives to solution-based electrolytes that have been used are ionic liquids, polymer electrolytes, molten salts, p-type semiconductors and eutectic melts.⁴ Additives are also

used to help solidify these materials examples include plasticizers, gelling agents, organic and pyridine additives, and inorganic nanoparticles.^{4–10} These new materials have numerous advantages such as low vapor pressure, high conductivity and stability but suffer from lower mobility, lower pore filling and low efficiency than in solution electrolytes. Studies are on going to improve the qualities of the electrolytes.

Ionic liquids are a sub-class of molten salts, existing as a liquid at ambient temperatures. They are not ordered which primarily causes crystallization, but are asymmetric and directional, linked together by hydrogen bonding.¹¹ They are nonvolatile, inflammable, stable chemically, highly conductive, provide a wide electrochemical range, and are greener alternative to many systems they are being increasingly used for.^{11–14} A viscous ionic liquid iodide salt with added iodine can provide a simple system for a quasi solid-state electrolyte. We chose an imidazolium iodide for our base ionic liquid, 1-methyl-3-propylimidazolium iodide. Imidazolium salts can be functionalized or metasthesized to change solubility, viscosity, conductivity and intercalation with the chosen dye.^{11,15}

Inorganic nanoparticles can be used as a gelator to further solidify polymer and ionic liquids, coined ionogels, further reducing DSSC leakage.^{16–19} Nanoparticles are preferred to other gelators because they function without side reactions that is common with some organic additives.¹⁹ Silica nanoparticles have been utilized as a gelator in DSSC electrolytes, solution, polymer and ionic liquid, and a few have been functionalized.^{18–23} The changes in physical properties and effects on stability in ionic liquids as different groups are attached to silica has been studied.^{24,25}

As previously described, we have established a DSSC assembly procedure that produces cells that match each other in design and performance. We would like to continue developing the method to incorporate new materials to aspects of the cell, this time with non-liquid electrolytes. All of our cells up to this point were fabricated with a solution-phase electrolyte that is composed of a dissolved redox shuttle pair. The new electrolytes are both single and multi-component solid-state electrolytes. This chapter covers the modification to the standard procedure to create a solid-state electrolyte composed of functionalized nanoparticles gelled in an ionic liquid solvent with added iodine. In our study, we utilize an ionic liquid, with and without TBP and then replace TBP with a polymerized imidazolium salt attached to a silica nanoparticle. *4-tert-Butylpyridine* has been shown to improve the performance of DSSCs based on ionic liquid electrolytes, so the addition should slow recombination and enhance efficiency.²⁶

4.2 Experimental

General. All chemicals were reagent grade and used without further modification or purification unless otherwise noted. TEC-15 (15 Ω/mm^2) fluorine-doped tin oxide (FTO) coated glass was purchased from Hartford Glass Co. Transparent titania paste, 18NR-T, was purchased from Dyesol, Inc. Hydrogen hexachloroplatinate (IV) hydrate (40% Pt) and iodine resublimed (99.5%) were purchased from Acros Organics. *4-tert-butylpyridine* from TCI America Inc., anhydrous 2-propanol (99.5%), HPLC grade acetonitrile, lithium iodide and 1-methyl-3-propylimidazolium iodide were purchased from Sigma Aldrich. 1 cm x 1 cm Tape mask is 3M Scotch 811. Silver conductive epoxy (8331G) was purchased from Fulton Radio Supply Co., and an electrically heated furnace

was from Cress Manufacturing Co. Model C601/SD Ser. No. 0910. Perkin Elmer Lambda 1050 Spectrophotometer equipped with a 150 mm InGaAs Integrating Sphere. 25 μm thick Surllyn was purchased from Solaronix, Heathkit 30V 3A Power Supply was used for resistive heating. Microscope cover glass thickness 0.14 mm was from Corning, standard 'Plain' 1" x 3" x 1.2 mm microscope slides purchased from MSU Chemistry Stores and 3/4" small nickel-plated binder clips were from ACCO, Alconox brand Powder Detergent was the soap used to clean the glass slides.

DSSCs were characterized on a 450 W Xenon arc lamp, with a MicroHR dual turret monochromator equipped with a 600 g/mm 500 nm blaze diffraction grating and a mirror were purchased from Horiba Jobin Yvon. AM0 and AM1.5 filter set was in place to simulate the solar spectrum, purchased from Solar Light Co. and neutral density filters were purchased from Thorlabs, Inc. Photoelectrochemical measurements were made with a CH Instruments Inc. 650D Potentiostat equipped with a Dell computer and a Windows XP operating system was used to run the software. The power was monitored via 3A-SH-ROHS Power meter from Ophir Optics and light was controlled with a Uniblitz VCMD1 shutter and shutter driver from Vincent Associates Inc.

The ionic conductivities of the PMII electrolytes were measured with an AC impedance analyzer HP 4192A over the frequency range from 5 Hz to 13 MHz in a homemade cell. Conductivities were taken at room temperature and at 90 °C. The electrolyte's resistance was determined from Nyquist plots, and the conductivity was calculated using the area and distance of the cell.²⁷

cis-Bis(isothiocyanato)bis(2,2'-bipyridyl-4,4'-dicarboxylato) ruthenium(II) was synthesized as described in Chapter 2. The DSSCs were fabricated as described in

Chapter 2 unless otherwise noted. New ionic liquid electrolyte materials and functionalized polymer silica nanoparticles were purchased and synthesized by Dr. Heyi Hu.²⁷

4.3 Electrolyte Composed of 1-Methyl-3-Propylimidazolium iodide (PMII)

4.3.1 With Iodine.

The platinum slides were prepared as previously described in Chapter 2, the TiO₂ slides were printed and sintered, heated and then dyed overnight, rinsed and dried under nitrogen. A calculation was performed to introduce enough iodine to the PMII to give a 0.2 molarity a concentration often seen in the literature.^{13,28,29} The measured sample of iodine was added to the PMII in a vial and the system was stirred for a half hour to dissolve; it was stirred inside of a beaker filled with desiccant and covered since PMII is hygroscopic and iodine sublimates. PMII is extremely viscous and doesn't move as a typical solvent, it flows slowly when tipped within a vial. It also does not drop out of a regular pipet ending, rather it sputters. Therefore, a glass pipet was scored to make a larger-ended dropper and two drops of the PMII/I₂ electrolyte was drop-caste onto the dyed TiO₂ slides to completely cover the 1 cm x 1 cm area of TiO₂. The slides were then heated to approximately 40°C for an hour to soften the PMII to induce infiltration into the porous TiO₂ network. The Surlyn was placed onto the platinum counter electrode surrounding an area of the electrode that had no drilled holes. The counter was then carefully placed onto the PMII-covered photoanode and then the two sides were sealed and clamped together using small binder clips, the extra electrolyte was pressed out along the edges and was cleaned up with kimwipes. The final wire lead was set with epoxy to

the photoanode side and cured for 5 hours, then tested. The complete PMII/I₂-based DSSC is seen in Figure 4-1, just before testing.

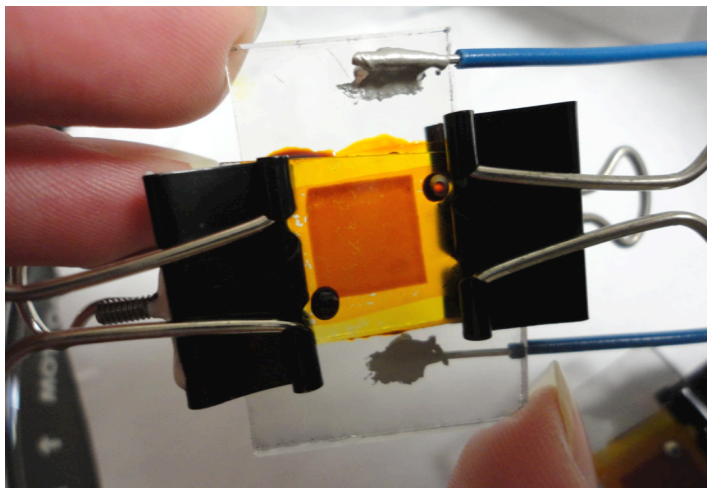


Figure 4-1. The complete quasi solid-state DSSC clamp cell based on 1-methyl-3-propylimidazolium iodide and 0.2 M iodine as the electrolyte. N3 is the chromophore and thermalized Pt is the counter electrode.

4.3.2 With Iodine and 4-*tert*-Butylpyridine. Another set of cells was prepared in a similar manner as before but this time with the addition of TBP to the electrolyte to see if it would produce the proposed improvement to performance.²⁶ A calculation was performed to ensure 0.2 M TBP and 0.2 M iodine was added to the PMII. Once added, the solution was stirred inside the vial inside of a desiccant-filled beaker while covered. A glass pipet was scored and ~1.5 mL of the viscous quasi-solid electrolyte was drop-cast onto the dyed TiO₂ and heated to approximately 40°C for one hour to improve infiltration into the film pores. Each platinum counter electrode was clamped to the photoanode with Surlyn as the seal and spacer. All extra electrolyte was wiped clean off the edges and the other wire was applied. The cells were tested after the epoxy cured for

5 hours. The J-V curves for both with and without TBP for the PMII/I₂ solar cells are seen in Figure 4-2 and their efficiency parameters are listed in Table 4-1. Both batches of cells, with and without TBP, are showing a good consistency within the group; cells without TBP have relative errors at 30% or less; with TBP show better reproducibility at 12% or less relative error. Adding TBP to the electrolyte improves all parameters with the most drastic enhancement occurring with the V_{OC} which manifests as an 80% increase in overall efficiency, combining with the other parameter improvements. It is apparent that TBP amends the performance of our quasi solid-state electrolytes as described. We see a larger change in V_{OC} and a smaller change in J_{SC} than Zhao et al., although a strict comparison

	Voc	Jsc	ff	η
W/out TBP	-0.376 V ± 0.035 V	2.51 mA/cm ² ± 0.38 mA/cm ²	0.43 ± 0.08	0.41% ± 0.12%
With TBP	-0.531 V ± 0.020 V	2.85 mA/cm ² ± 0.32 mA/cm ²	0.49 ± 0.01	0.74% ± 0.09%

Table 4-1. Efficiency Parameters for PMII-based DSSCs with and without TBP. N3 dye, 0.2 M I₂ in PMII for the electrolyte, and a Pt counter electrode sealed in a clamp cell with a 25 μm spacer.

to their results is not possible as a different system is used.²⁶ As discussed in Chapter 2, TBPs effect is to passivate the TiO₂ surface, hindering electrolyte intercalation and slowing the back-recombination of electrons in the conduction band with holes in the electrolyte, this effect is seemingly occurring with its addition to our quasi solid-state electrolyte. There are no lithium ions in our electrolyte so the effect of TBP shifting the conduction band edge by hindering Li⁺ ions from entering the spaces in the TiO₂ will not

be seen. Yet there should be a small effect on the conduction band edge from TBP now at the TiO₂ surface. But it is unclear whether the TBP is indeed making any impact on V_{OC} and J_{SC} via band edge movement or if it is solely the hindrance of recombination that is enhancing signal.

4.3.3 With Iodine and Poly(1-(4-Vinylbenzyl)-3-Butyl Imidazolium Tetrafluoroborate) Functionalized Silica Nanoparticles. The final set of cells were prepared as the other PMMI cells are outlined, but with a novel electrolyte composition. The electrolyte was composed of PMII and interdispersed SiO₂ nanoparticles that are purposed with a polymer imidazolium salt, poly(1-(4-vinylbenzyl)-3-butyl imidazolium

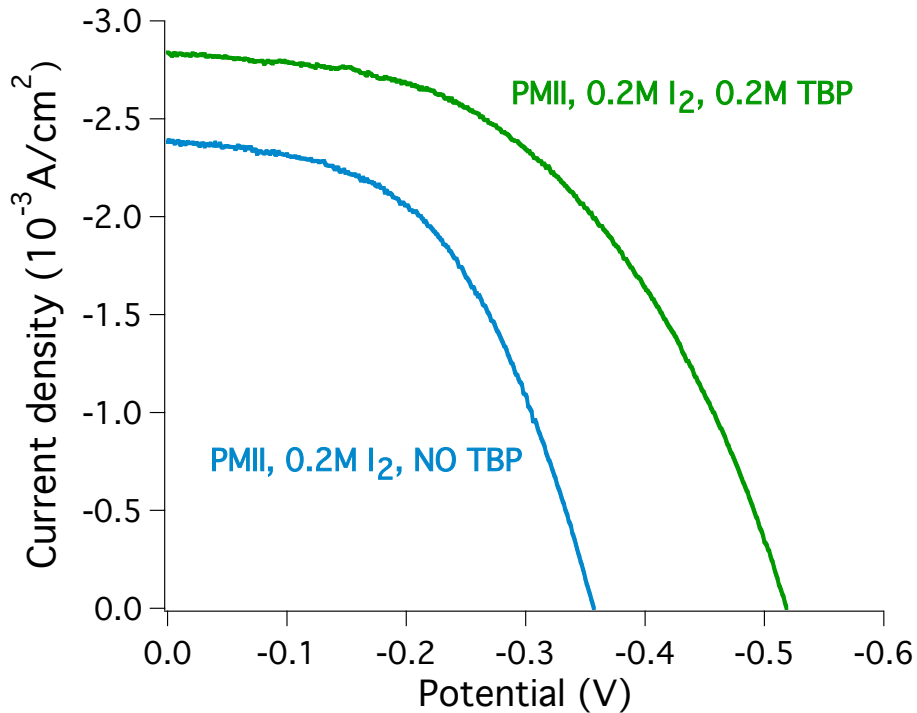


Figure 4-2. The comparison of the 0.2 M I₂ in PMII as the electrolyte in quasi solid-state clamp cell DSSCs, (—) with and (—) without 0.2 M 4-*tert*-butylpyridine as an additive. N3 is the chromophore and thermalized Pt is the counter electrode.

tetrafluoroborate), the structure is seen in Figure 4-3. 20 wt% of PVBBIT-SiO₂ nanocomposite suspended in 2.38 mmol PMII was obtained and 0.238 mmol iodine was added to the suspension in a vial and stirred for a half hour inside of a covered beaker containing desiccant. In Figure 4-4 the PMII is pictured with no additives, with PVBBIT-SiO₂ suspended and lastly with I₂ added. The molar ratio of iodide to iodine was chosen to be 10:1 due to the typical concentrations in standard cells, no optimization of the composition was performed.

A cut glass pipet was used to transfer one drop of the composite to the dyed films. Due to its high viscosity, the drops did not flow as the PMII/I₂ electrolytes did when the slides were tilted. Since the composite wouldn't flow, the electrolyte was 'pulled' around with the glass pipet edge to spread using its intermolecular forces; extra care was taken to

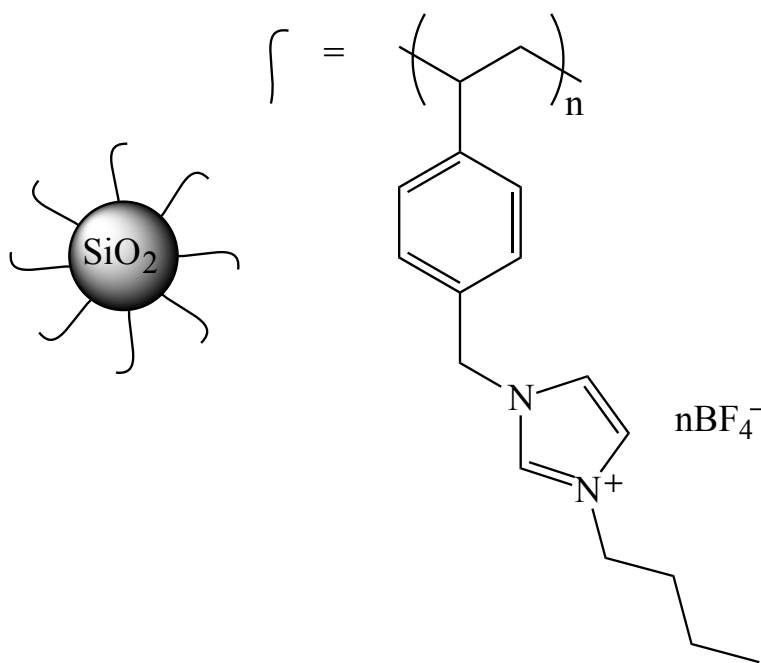


Figure 4-3. Structure of the silica nanoparticle and the attached poly(1-(4-vinylbenzyl)-3-butyl imidazolium tetrafluoroborate) polymer electrolyte.

protect the underlying film and no pressure was applied. A separation of phases occurred; a white precipitation of the silica appeared which was not uniform. The slides were let set for 15 minutes to allow penetration of the electrolyte into the nanocrystalline pores.

In order to gel the electrolyte and cause entanglement of the branched-polymer between silica particles, the electrolyte needs to be heated. For these composites, gelation

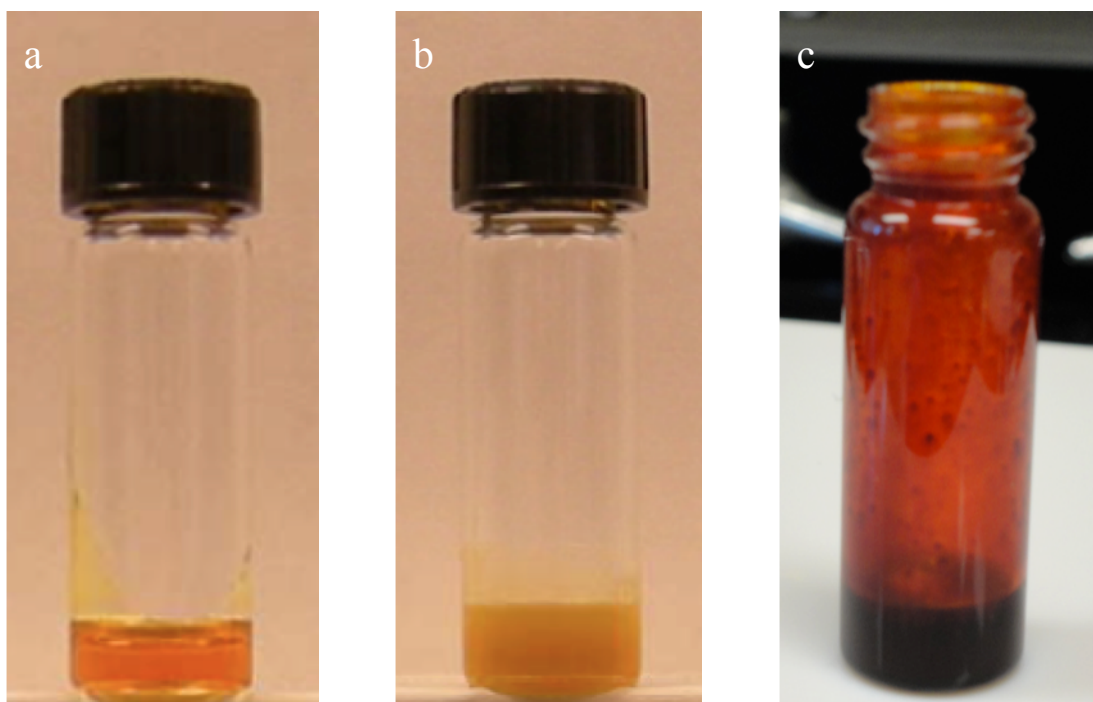


Figure 4-4. Photographs of (a) PMII, (b) PVBBIT-SiO₂/PMII, (c) PVBBIT-SiO₂/PMII/I₂.

had previously been achieved at 60 °C for 3 hours or at 90 °C for 16 hours.²⁷ Since our studies discovered that the dye is known to desorb at increased temperatures (>90°C) the slides were baked at 90 °C for 1 hour, a thickening and further separation of the phases was observed, but a complete gelation wasn't recognized.²⁷ Once cooled, the photoanodes were clamped together with the Pt counter and 25 µm Surlyn spacer. The

wire lead was set with epoxy and allowed to cure 4 hours, and then the cells were tested. The J-V curve is seen in Figure 4-5 compared to PMII/I₂ and PMII/I₂/TBP J-V curves and the efficiency parameters are in Table 4-2. The J-V curve is generally comparable to the other two curves yet smaller J_{SC} and ff resulting in lower efficiency. The lower performance can be accounted for a lower conductivity of PVBBIT-SiO₂ than PMII. Ungelled PVBBIT-SiO₂ is 0.8 mS/cm at room temperature and 14.7 mS/cm at 90 °C, lower than PMII with 1.1 mS/cm at room temperature and 34.6 mS/cm at 90 °C.²⁷ Typical conductivity of the standard LiI/I₂/MeCN solution is approximately 41 mS/cm at room temperature;⁵ a direct comparison is difficult because the conductivity of the PVBBIT-SiO₂ was taken ungelled and the conductivity should increase when the functionalized silica nanoparticles are interacting with each other.

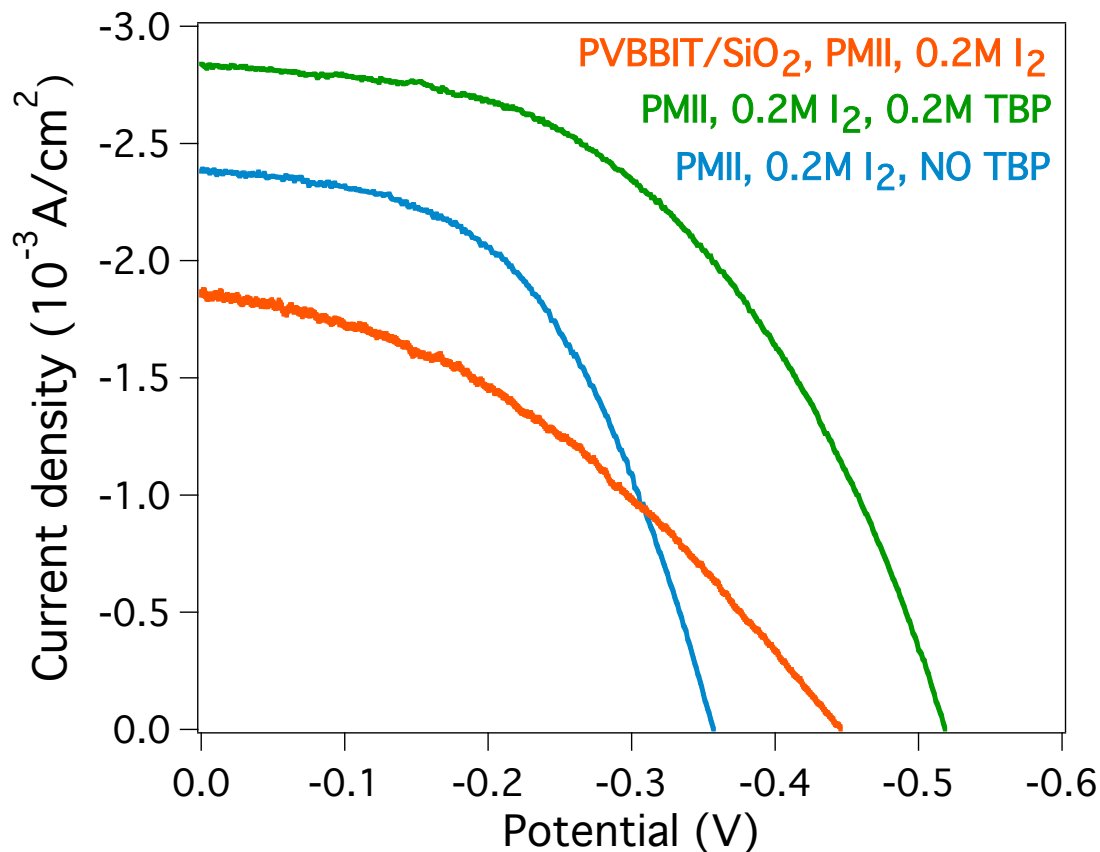


Figure 4-5. The comparison of the representative curves of each set of 0.2 M I₂ in PMII as the electrolyte in quasi solid-state DSSCs. (—) with and (—) without 0.2 M 4-*tert*-butylpyridine, (—) with PVBBIT-functionalized silica nanoparticles as an additive in PMII. N3 is the chromophore and thermalized Pt is the counter electrode.

	Voc	Jsc	ff	η
Without TBP	-0.376 V	2.51 mA/cm²	0.43	0.41%
With TBP	-0.531 V	2.85 mA/cm²	0.49	0.74%
PVBBIT-SiO₂	-0.381 V	1.83 mA/cm²	0.45	0.31%

Table 4-2. Efficiency Parameters for PMII-based DSSCs. N3 dye, 0.2 M I₂ in PMII for the electrolyte, and a Pt counter electrode sealed in a clamp cell with a 25 μm spacer.

There are a few ways in which this system could be improved. One could optimize the iodide concentration within the imidazolium/silica network. Addition of TBP to the PMII-I₂-PVBBIT-SiO₂ would most likely enhance performance as well. Also a complete gelation of the PVBBIT-SiO₂ to improve conductivity would benefit. So developing a different imidazolium functional group to attach to the silica nanoparticle that would gel at a lower temperature, one in which the dye would not have a chance of desorption. The counter electrode and the choice of dye could also be sources of improvement. Chromophores with aliphatic chains could allow a higher degree of permeation of the polymerized electrolyte into the dyed film and allow more of the solar spectrum to be absorbed.^{30,31} There have also been reports on carbon materials for use in quasi solid-state DSSCs that have produced beneficial results.^{32,33}

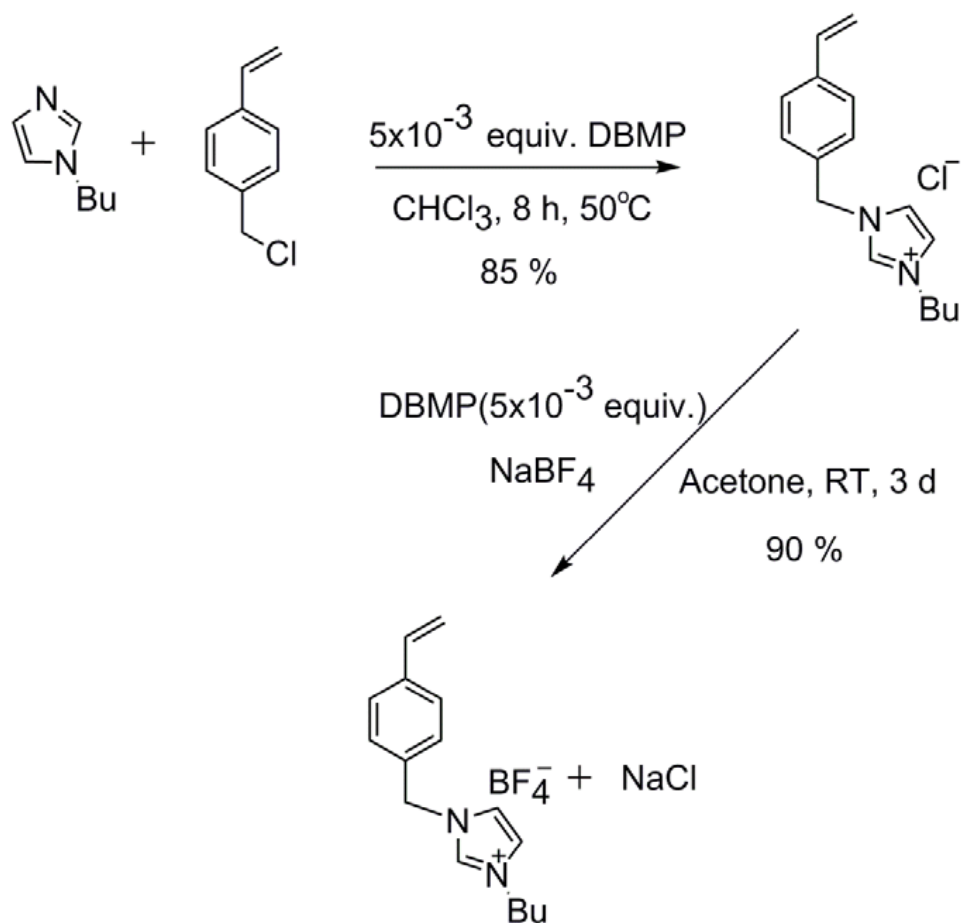
4.4 Concluding Remarks

Liquid phase electrolytes pose serious problems with leaking so a move to solid-state electrolytes is beneficial. It is necessary to modify our reproducible DSSC procedure to institute these electrolytes; their difference in properties will change the method of construction. The standard fabrication method has been adapted to the introduction of quasi solid-state electrolytes composed of 1-methyl-3-propylimidazolium iodide. Small losses in reproducibility were seen but with further development and practice, lower than 10% relative error should be able to be achieved. PMII as an electrolyte is viscous causing lower infiltration into the porous TiO₂ network and has reduced conductivity as compared to the LiI/I₂/MeCN standard which can account for the lower overall performance of these cells. 4-*tert*-Butylpyridine improves performance by

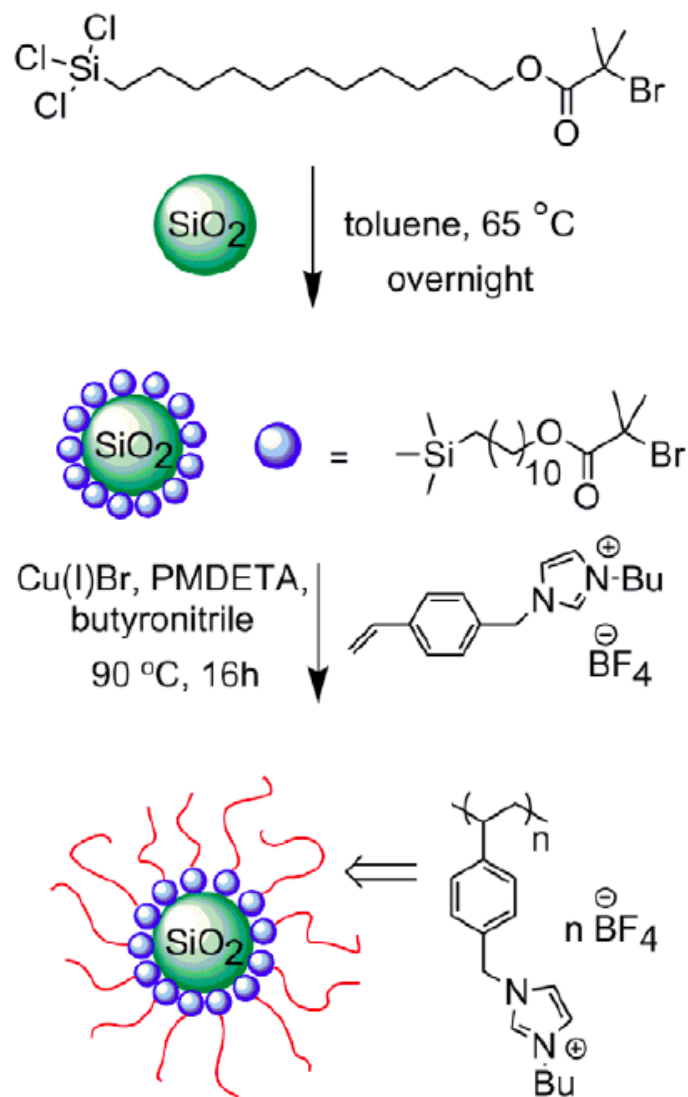
blocking recombination of TiO_2 electrons with holes in the PMII electrolyte, and possibly by shifting the conduction band edge slightly. PVBBIT- SiO_2 is effective as a hole transport medium in DSSCs, although less efficient than PMII as an electrolyte. Improvements can be made to enhance performance: better conductivity, gelling conditions, introducing additives, design of new chromophores and also counter electrode choice

APPENDIX

APPENDIX



Scheme 4-1. Synthesis of 1-(4-Vinylbenzyl)-3-butyl imidazolium tetrafluoroborate.²⁷



Scheme 4-2. Synthesis of Poly(1-(4-Vinylbenzyl)-3-butyl imidazolium tetrafluoroborate) functionalized SiO_2 nanoparticles.²⁷

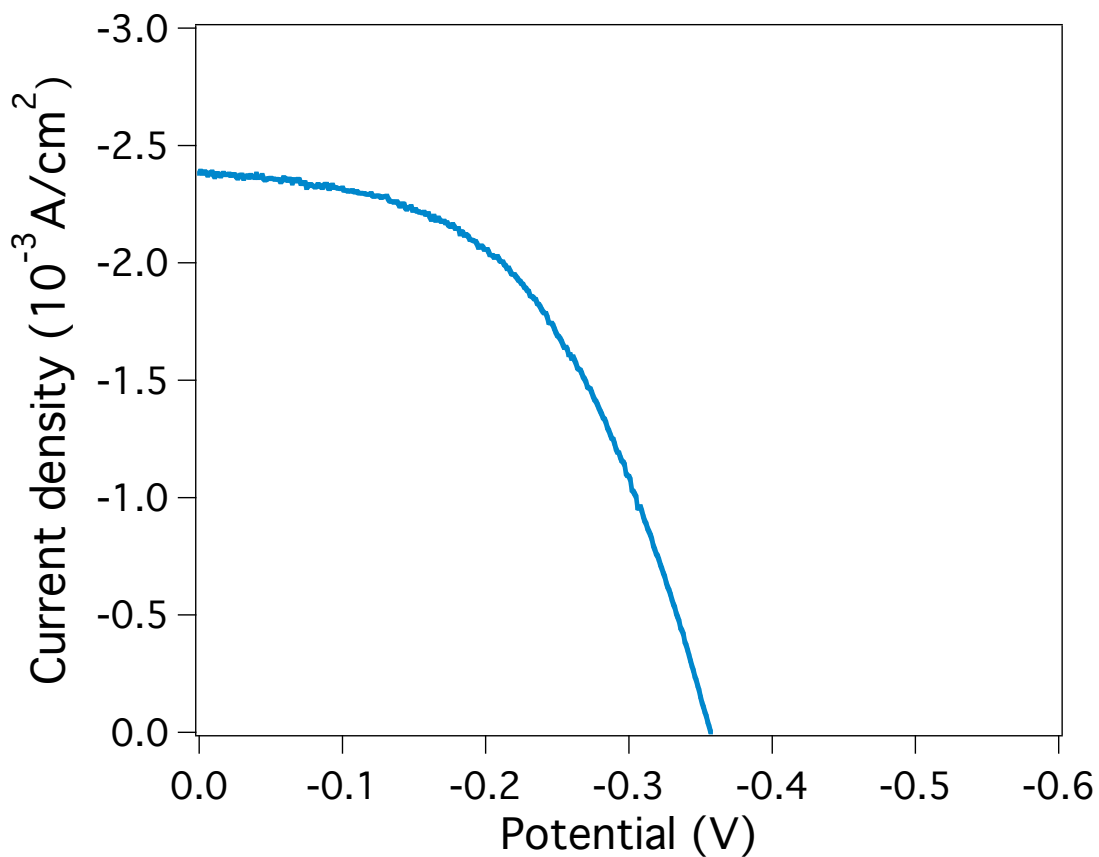


Figure 4-6. Representative J-V curve of a quasi solid-state DSSC composed of PMII with 0.2 M iodine as the electrolyte.

	Voc	Jsc	ff	η
Average	-0.376 V	2.51 mA/cm ²	0.43	0.41%
Std Dev \pm	0.035 V	0.38 mA/cm ²	0.08	0.12%

Table 4-3. Efficiency Parameters of a quasi solid-state DSSC. N3 dye, 1-methyl-3-propylimidazolium iodide with 0.2 M iodine as the electrolyte, Pt counter electrode sealed in a clamp cell with 25 μ m spacer.

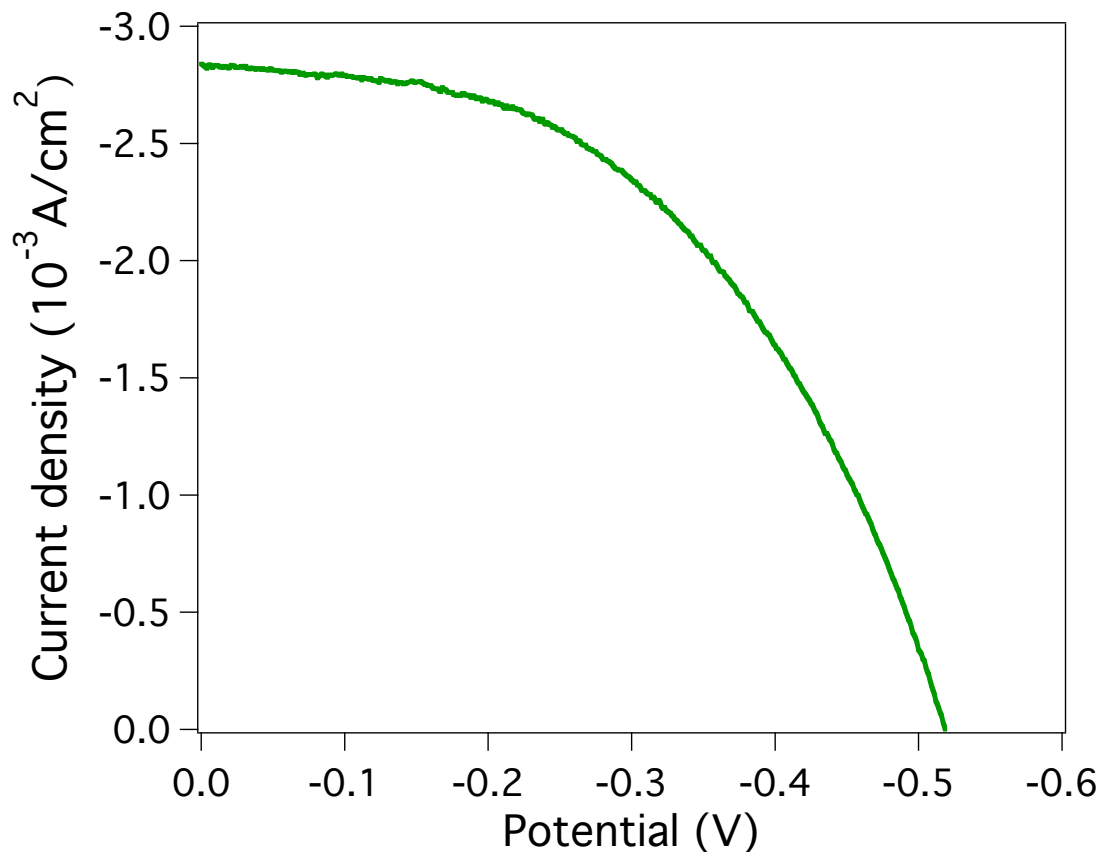


Figure 4-7. Representative curve of a quasi solid-state DSSC composed of 0.2 M TBP in PMII with 0.2 M iodine as the electrolyte.

	Voc	Jsc	ff	η
Average	-0.531 V	2.85 mA/cm ²	0.49	0.74%
Std Dev ±	0.020 V	0.32 mA/cm ²	0.01	0.09%

Table 4-4. Efficiency Parameters of a quasi solid-state DSSC. N3 dye, PVBBIT-functionalized silica nanoparticles in 1-methyl-3-propylimidazolium iodide with added 0.2 M iodine as the electrolyte, Pt counter electrode sealed in a clamp cell with 25 μm spacer.

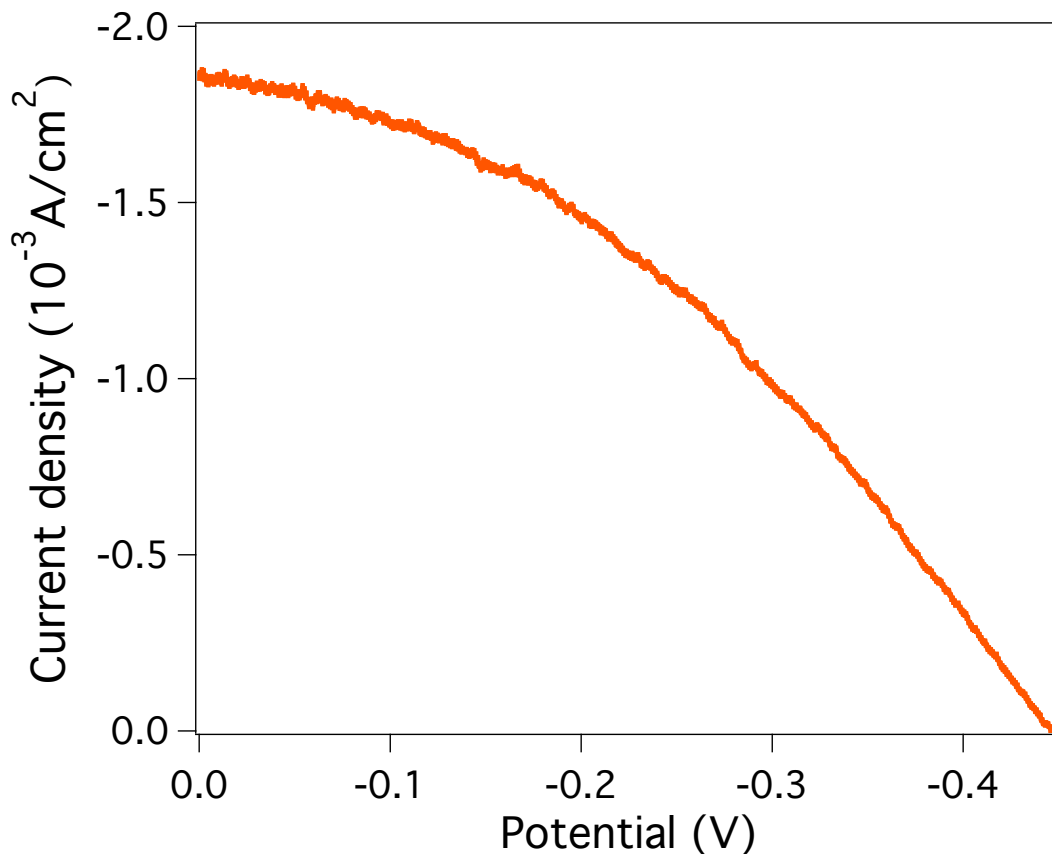


Figure 4-8. Representative curve of a quasi solid-state DSSC composed of PVBBIT-functionalized silica nanoparticles in PMII with 0.2 M iodine as the electrolyte.

	Voc	Jsc	ff	η
Average	-0.381 V	1.83 mA/cm ²	0.45	0.31%
Std Dev \pm	0.056 V	0.11 mA/cm ²	0.05	0.02%

Table 4-5. Efficiency Parameters of a quasi solid-state DSSC. N3 dye, PVBBIT-functionalized silica nanoparticles in 1-methyl-3-propylimidazolium iodide with added 0.2 M iodine as the electrolyte, Pt counter electrode sealed in a clamp cell with 25 μ m spacer.

REFERENCES

REFERENCES

- (1) Cao, F.; Oskam, G.; Searson, P. C. *The Journal of Physical Chemistry* **1995**, *99*, 17071–17073.
- (2) Matsumoto, M.; Miyazaki, H.; Matsuhira, K. *Solid State Ionics* **1996**, *89*, 263–267.
- (3) Papageorgiou, N.; Athanassov, Y. *Journal of The Electrochemical Society* **1996**, *143*, 3099–3108.
- (4) Wang, Z.-S.; Sayama, K.; Sugihara, H. *The Journal of Physical Chemistry B* **2005**, *109*, 22449–55.
- (5) Kontos, A. G.; Fardis, M.; Prodromidis, M. I.; Stergiopoulos, T.; Chatzivasiloglou, E.; Papavassiliou, G.; Falaras, P. *Physical Chemistry Chemical Physics* **2006**, *8*, 767–76.
- (6) Wu, J.; Hao, S.; Lan, Z.; Lin, J.; Huang, M.; Huang, Y.; Li, P.; Yin, S.; Sato, T. *Journal of the American Chemical Society* **2008**, *130*, 11568–9.
- (7) Wang, P.; Zakeeruddin, S. M.; Moser, J. E.; Nazeeruddin, M. K.; Sekiguchi, T.; Grätzel, M. *Nature Materials* **2003**, *2*, 402–7.
- (8) Huang, X.; Qin, D.; Zhang, X.; Luo, Y.; Huang, S.; Li, D.; Meng, Q. *RSC Advances* **2013**, *3*, 6922.
- (9) Bai, Y.; Cao, Y.; Zhang, J.; Wang, M.; Li, R.; Wang, P.; Zakeeruddin, S. M.; Grätzel, M. *Nature Materials* **2008**, *7*, 626–30.
- (10) Wang, P.; Zakeeruddin, S. M.; Moser, J.-E.; Grätzel, M. *The Journal of Physical Chemistry B* **2003**, *107*, 13280–13285.
- (11) Dupont, J. *Accounts of Chemical Research* **2011**, *44*, 1223–31.
- (12) Gorlov, M.; Pettersson, H.; Hagfeldt, A.; Kloo, L. *Inorganic Chemistry* **2007**, *46*, 3566–75.
- (13) Kuang, D.; Klein, C.; Zhang, Z.; Ito, S.; Moser, J.-E.; Zakeeruddin, S. M.; Grätzel, M. *Small* **2007**, *3*, 2094–102.
- (14) Wang, P.; Zakeeruddin, S. M.; Moser, J.-E.; Humphry-Baker, R.; Grätzel, M. *Journal of the American Chemical Society* **2004**, *126*, 7164–5.

- (15) Mazille, F.; Fei, Z.; Kuang, D.; Zhao, D.; Zakeeruddin, S. M.; Grätzel, M.; Dyson, P. J. *Inorganic Chemistry* **2006**, *45*, 1585–90.
- (16) Wang, P.; Zakeeruddin, S. M.; Comte, P.; Exnar, I.; Grätzel, M. *Journal of the American Chemical Society* **2003**, *125*, 1166–7.
- (17) Zhang, X.; Yang, H.; Xiong, H.-M.; Li, F.-Y.; Xia, Y.-Y. *Journal of Power Sources* **2006**, *160*, 1451–1455.
- (18) Chen, X.; Li, Q.; Zhao, J.; Qiu, L.; Zhang, Y.; Sun, B.; Yan, F. *Journal of Power Sources* **2012**, *207*, 216–221.
- (19) Le Bideau, J.; Viau, L.; Vioux, A. *Chemical Society Reviews* **2011**, *40*, 907–925.
- (20) Moganty, S. S.; Srivastava, S.; Lu, Y.; Schaefer, J. L.; Rizvi, S. A.; Archer, L. a. *Chemistry of Materials* **2012**, *24*, 1386–1392.
- (21) Etgar, L.; Schuchardt, G.; Costenaro, D.; Carniato, F.; Bisio, C.; Zakeeruddin, S. M.; Nazeeruddin, M. K.; Marchese, L.; Gratzel, M. *Journal of Materials Chemistry A* **2013**, *1*, 10142.
- (22) Stergiopoulos, T.; Bidikoudi, M.; Likodimos, V.; Falaras, P. *Journal of Materials Chemistry* **2012**, *22*, 24430.
- (23) Huang, S.; Wang, X.; Wong, C. C. *Nanoscience and Nanotechnology Letters* **2013**, *5*, 542–545.
- (24) Ueno, K.; Inaba, A.; Kondoh, M.; Watanabe, M. *Langmuir* **2008**, *24*, 5253–9.
- (25) Ueno, K.; Imaizumi, S.; Hata, K.; Watanabe, M. *Langmuir* **2009**, *25*, 825–31.
- (26) Zhao, Y.; Zhai, J.; He, J.; Chen, X.; Chen, L.; Zhang, L.; Tian, Y.; Jiang, L.; Zhu, D. *Chemistry of Materials* **2008**, *20*, 6022–6028.
- (27) Hu, H. Synthesis of Poly(Ionic Liquids) both in Solution and on Surface of Silica Nanoparticles as Novel Quasi-Solid State Electrolytes, 2013.
- (28) Zhang, Z.; Ito, S.; Moser, J.-E.; Zakeeruddin, S. M.; Grätzel, M. *ChemPhysChem : a European Journal of Chemical Physics and Physical Chemistry* **2009**, *10*, 1834–8.
- (29) Wang, M.; Chen, P.; Humphry-Baker, R.; Zakeeruddin, S. M.; Grätzel, M. *ChemPhysChem : a European Journal of Chemical Physics and Physical Chemistry* **2009**, *10*, 290–9.
- (30) Kim, J.-J.; Choi, H.; Lee, J.-W.; Kang, M.-S.; Song, K.; Kang, S. O.; Ko, J. *Journal of Materials Chemistry* **2008**, *18*, 5223–5229.

- (31) Houarner-Rassin, C.; Blart, E.; Buvat, P.; Odobel, F. *Journal of Photochemistry and Photobiology A: Chemistry* **2007**, *186*, 135–142.
- (32) Lei, B.-X.; Fang, W.-J.; Hou, Y.-F.; Liao, J.-Y.; Kuang, D.-B.; Su, C.-Y. *Journal of Photochemistry and Photobiology A: Chemistry* **2010**, *216*, 8–14.
- (33) Ahmad, I.; Khan, U.; Gun'ko, Y. K. *Journal of Materials Chemistry* **2011**, *21*, 16990.

Chapter 5. Platinum Nanoclusters Embedded on Graphene for Dye-Sensitized Solar Cells

5.1 Introduction

In the dye-sensitized solar cell, the counter electrode completes the circuit, making it a completely regenerative cell, by electrocatalyzing the reduction of the oxidized redox species. As previously mentioned, we use a ruthenium-based chromophore, N3, the most well-known dye in DSSC literature. When using this ruthenium dye, the iodide/triiodide redox couple is the most efficient for the re-reduction of the metal center after injection has occurred. Currently, the best catalyst for the reduction of triiodide couple is a platinum catalyst. Platinum is one of the rarest metals on earth, making it an extremely expensive aspect of the cell, a significant detriment given the global perspective of our research.

As stated previously, our goals in this research are to reduce the overall cost of the cell, making them a more viable option for scalability. Due to the nature of the platinum catalyst primarily used, discussed later, it must be deposited onto a conductive substrate. Transparent conductive oxide (TCO) substrates are another fairly expensive component of the cell because they are composed of other rare metals such as indium and tin, and are prepared via costly procedures such as chemical vapor deposition, laser deposition and magnetron sputtering. Two common examples of these conductive oxides are FTO, and indium tin oxide (ITO) glass, a conductive glass similar to FTO but with lower resistivity and higher cost. Due to this additional modular cost, in parallel to concentrating our efforts on lowering the platinum loading level, we are also doing research to replace the conductive oxide glass with a cheaper material.

The conventional electrocatalyst, thermalized platinum, was first prepared and optimized for the iodide/triiodide redox couple in 1997 by Papageorgiou et al.¹ The catalyst is prepared from hexachloroplatinic acid and it was drop-caste, sprayed or spin-coated onto different substrates, including ITO. Once applied, the catalyst is then baked at 385°C. The resulting platinum coating exists as discrete islands of nanoscale platinum clusters rather than a thin uniform layer, which is the reason the TCO is necessary for continuous conductivity needed to transport electrons to the external circuit. The electrode is chemically, electrochemically and mechanically stable.² The Pt loading is 5 $\mu\text{g}/\text{cm}^2$ and provides 0.35A/cm² exchange current density in acetonitrile with 0.5M I⁻ and 0.05M I₃⁻.¹ This value corresponds to R_{CT} equal to 0.04 Ω/cm^2 via $R_{CT} = RT/nFJ_0$ where $n = 2$ for the overall iodide/triiodide reaction: $\text{I}_3^- + 2e = 3\text{I}^-$. This corresponds to a loss of less than 2mV for champion cells that have a current close to 20mA/cm² or a loss less than 1mV for our standard cells with a current equal to 6mA/cm². The goal is to create new electrodes that give similar or better performance than this benchmark Pt electrode.

A multitude of research has been done on finding new counter electrodes for DSSCs. Metal oxides and sulfides,^{3–6} polymer materials,^{7–9} carbon-based electrodes,^{10–13} carbon/metal composites,^{14–16} and other metal catalysts^{16–19} electrodes have all been studied for use as counter electrodes.

In collaboration with a materials science group, as part of a multi-faceted research program funded by the National Science Foundation, novel counter electrodes that significantly reduce platinum loading were constructed and incorporated into the standard DSSC. The novel counter electrodes are composed of platinum nanoparticles that are

embedded on a conductive graphene template. The goal is to reduce the amount of platinum used for the electrode but increase the surface area by using discrete nanoparticles, effectively unaffected or possibly even improving the catalytic activity. The carbon-based backbone, provides the cost-effective conductivity that is desired, removing the need for TCO substrates.

The Drzal group at Michigan State University has developed a unique platinum nanoparticle synthesis that decorates exfoliated graphene nanoplatelets (Figure 5-1) designed for use in fuel cells and further application as a biosensor.^{20,21} The highly reproducible and controlled system has been thoroughly studied²⁰ and provides a convenient transition from the robust literature standard of thermalized platinum to an intricate system of nanoparticles anchored to an economical conductive substrate to be

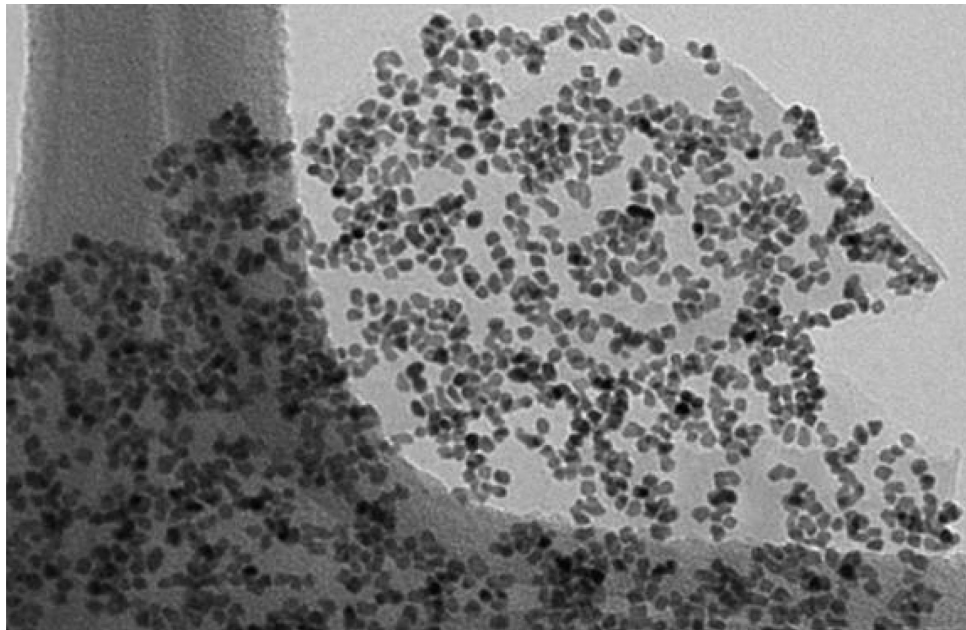


Figure 5-1. TEM images of 50 wt% platinum nanoparticles.²²

used as a counter electrode in DSSCs.

Metal nanoparticles have multiple advantages such as high surface area to volume ratio, catalytic activity, electrochemical enhancements, conductivity, magnetism and size-controllable synthesis. They have extensive uses in sensors, data storage, separation science, and biological delivery, also optical and electronic uses in energy-related applications, to name a few.

Graphene has a wide range of applications due to its conductivity, versatility, durability, malleability, and cost-effectiveness. Graphene can exist as fullerenes, nanodiamonds, nanofibers, nanotubes, nanosheets, nanocones, nanodisks and nanohorns and can easily be functionalized with polymers or metal oxide nanoparticles.²³ It has been researched for use in super-capacitors,²⁴ adhesives,²⁵ catalysts,²⁶ biological applications,²⁷ environmental pollutant adsorption²⁸ and used for cathodes in batteries, fuel cells and solar cells.^{5,13,14,24,29-34}

These counter electrodes that are formulated from new materials with distinct physical properties required modifications to the standard fabrication method. We extend the current standard fabrication method to integrate the new electrodes into the procedure. Numerous iterations of electrode design were required in order to achieve an electrode that could be incorporated in the DSSC reproducibly. Once the new materials are assimilated into the DSSC, their efficiencies were compared against the consistency of the standard DSSCs efficiency parameters.

5.2 Experimental

General. All chemicals were reagent grade and used without further modification

or purification unless otherwise noted. TEC-15 ($15 \text{ } \Omega/\text{mm}^2$) fluorine-doped tin oxide (FTO) coated glass was purchased from Hartford Glass Co. Transparent titania paste, Ti-Nanoxide HT/SP, was purchased from Solaronix. Hydrogen hexachloroplatinate (IV) hydrate (40% Pt) and iodine resublimed (99.5%) were purchased from Acros Organics. 4-*tert*-Butylpyridine from TCI America Inc. Anhydrous 2-propanol (99.5%), HPLC grade acetonitrile, lithium iodide was purchased from Sigma Aldrich. 3M Scotch 811 Tape. Silver conductive epoxy (8331G) was purchased from Fulton Radio Supply Co.

Slides were baked in an electrically heated furnace from Cress Manufacturing Co. Model C601/SD Ser. No. 0910. Perkin Elmer Lambda 1050 Spectrophotometer equipped with a 150 mm InGaAs Integrating Sphere performed all film %Transmittance measurements. 25 μm thick Surlyn from Solaronix was the sealant spacer in the DSSC. Voltage was applied by a Heathkit 30V 3A Power Supply during resistive heating. Corning Microscope cover glass thickness 0.14 mm covered the Surlyn to seal the injection holes, injection was facilitated by 0.5 mL and 1 mL syringes from BD Medical. ACCO 3/4" small nickel-plated binder clips were used in clamp cells. A glass cutter and 790 μm thick ethylene propylene diene monomer (EPDM) rubber sheet spacer was purchased from McMaster-Carr. Standard 'Plain' 1" x 3" x 1.2 mm microscope slides purchased from MSU Chemistry Stores were substrates for the graphene counter electrodes. Alconox Powder Detergent was used to clean slides.

The solar simulation setup consisted of a 450 W Xenon arc lamp, MicroHR dual turret monochromator equipped with a 600 g/mm 500 nm blaze diffraction grating and a mirror purchased from Horiba Jobin Yvon. The spectrum was shaped by AM0 and AM1.5 filter set purchased from Solar Light Co. Neutral Density filters were purchased

from Thorlabs, Inc. Electrochemical measurements were purposed by a CH Instruments Inc. 650D Potentiostat equipped with a Windows XP operating system Dell computer to run the software. Power was monitored by a 3A-SH-ROHS Power meter from Ophir Optics and a Uniblitz VCMD1 shutter and shutter driver from Vincent Associates Inc. control the on/off of the light.

cis-Bis(isothiocyanato)bis(2,2'-bipyridyl-4,4'-dicarboxylato) ruthenium(II) was synthesized and the DSSCs were fabricated as described in Chapter 2 unless otherwise noted. New platinum nanoparticles and their graphene substrates for the counter electrode materials were purposed by Dr. Patrick Aderhold.

X-ray Photoelectron Spectroscopy (XPS) measurements were made on a Perkin Elmer Phi 5400 ESCA system with a magnesium $K\alpha$ X-ray source. Samples were analyzed at pressures between 10^{-9} and 10^{-8} torr with a pass energy of 29.35 eV and a take-off angle of 45° . The spot size is roughly $250 \mu\text{m}^2$. Atomic concentrations were determined using previously determined sensitivity factors. All peaks were referenced to the signature C1s peak for adventitious carbon at 284.6 eV. Inductively Coupled Plasma Mass Spectrometry (ICP-MS) was implemented by Galbraith Laboratories, Inc.

Electrochemical measurements of the new GNP/PP/Pt system in solution were performed in a three-electrode configuration with a no-leak Ag/AgCl (CH Instruments Inc.) reference electrode, and Pt foil as the counter. The working electrode is a 5 mm x 5 mm cut section of a Pt/FTO or GNP/PP/Pt electrode which a copper tape is fastened to with Ag paste to function as the lead. The lead is reinforced with polystyrene strips and then wrapped in Teflon tape. The electrolyte consisted of 5 mM LiI, 0.5 mM I_2 , 0.1 M LiClO_4 in acetonitrile. CV scans were performed from -0.25 V to 1.25 V at a scan rate of

50 mV/s, the current was corrected for electrode area using reflected light microscopy.²²

5.3 Modification and Subsequent Counter Electrode Iterations

5.3.1 Platinum Nanoparticles on Graphene Nanoplatelets. The first type of electrode that was attempted as a counter electrode in a standard DSSC setup was platinum nanoclusters embedded on a thin layer of graphite nanoplatelets (GNP). The graphite layers were prepared by the precursor graphite-intercalated compound which is subjected to microwave radiation, mechanical exfoliation via sonication in chloroform, and extraction into a bilayer with the addition of water.²² The nanoplatelets were applied to a microscope glass slide by lifting a slide through the surface layer, then dried and annealed. Pt nanoclusters were embedded by submitting the graphene-coated slides to microwave radiation while submerged in a solution of chloroplatinic acid hexahydrate in ethylene glycol. The substrates were washed with DI water and dried under vacuum. SEM images of the nanoplatelets before and after decoration with Pt can be seen in Figure 5-2. Under inspection the layers appeared fractured and discontinuous. Fractures in the sheets expose the insulating glass beneath (Figure 5-3) disrupting conductivity, causing it to be extremely low. There was also difficulty with adhesion to the glass surface. Methods to improve this substrate were unsuccessful.

The conductivity of this prepared counter electrode was either low or discontinuous. We chose to further improve the design of the electrode instead of moving forward with incorporating it into a solar cell at this stage. Resistive losses would have

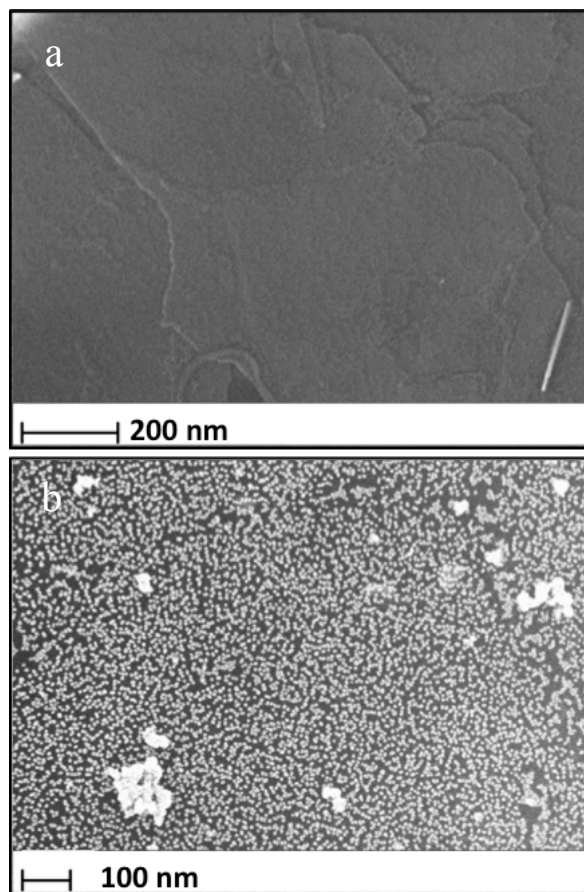


Figure 5-2. SEM Images of graphene nanoplatelets a) before and b) after decoration with Pt nanoclusters using microwave radiation.²²

been overwhelming if current was to be able to flow through the electrode at all. The layers could have been applied to an FTO slide which would've breached the gaps, maintaining conductivity, but replacing the costly FTO was one of the two goals. A uniform layer of stable conductive GNP is desired to provide the effective base for Pt ornament.

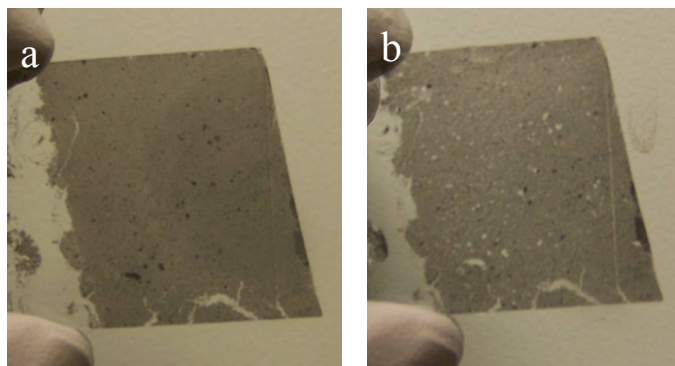


Figure 5-3. Photographs of graphene nanoplatelets on microscope glass a) before and b) after decoration with Pt nanoclusters using microwave radiation. Breaks in the graphene layer are apparent.²²

5.3.2 Platinum Nanoparticles on Pressed Graphene Nanoplatelet Papers. A new substrate consisting of pressed graphene nanoplatelet paper was prepared to serve as the basis for Pt enrichment.²² Graphene-intercalated compound was exfoliated by microwave heating, dispersed in aqueous polyethylenimine (PEI), ultrasonicated and then filtered. The filtrate was dried in air and then under vacuum and then heated to remove water and decompose the PEI. The papers were then pressed, before and after pressing is seen in Figure 5-4. The papers were 30-60 μm with a sheet resistance of 0.08 Ω/cm^2 , significantly lower compared to FTO (15 Ω/cm^2). Platinum nanocluster decoration was completed as before; the papers were microwave radiated in ethylene glycol in a solution of H_2PtCl_6 to embed the Pt, before and after is seen in Figure 5-5. This method creates the uniform conductive layer desired and discrete Pt nanoclusters formed as before. At

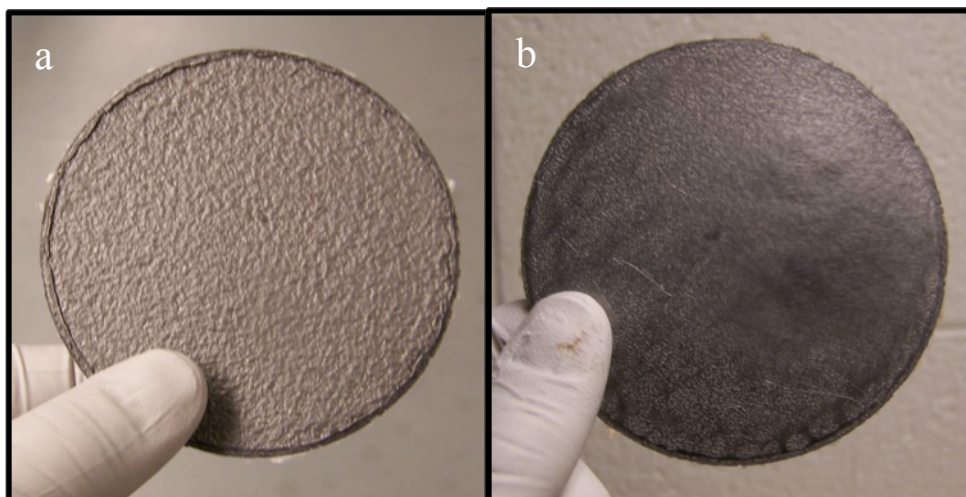


Figure 5-4. Photographs of graphene nanoplatelet paper before and after pressing.²²

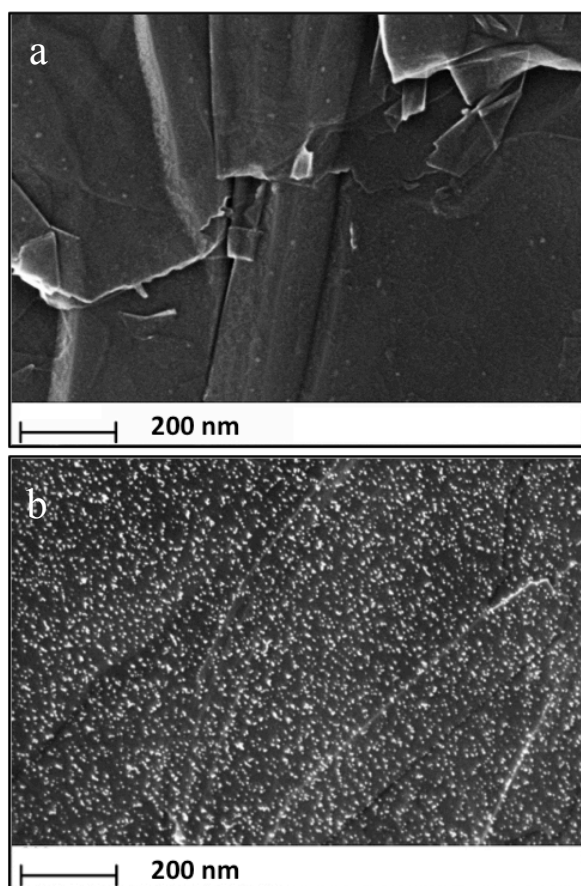


Figure 5-5. Photographs of graphene nanoplatelet paper before and after Pt enhancement.²²

inspection, it was noticed that the layers could have ridges in them. The Surlyn spacer is a mere 25 μm so any of the ridges that rise taller than that from the surface have the danger of reaching the photoanode, shorting out the cell.

With subsequent batches of GNP paper the papers were pressed further to help smooth the surface and areas of the paper that had the flattest, most uniform morphology were chosen for use. Next the flexible GNP paper needed a rigid backing for use in a fully functioning cell. A piece of Surlyn was melted onto a thin glass microscope slide, while still hot, the paper was pressed onto the Surlyn using a piece of Teflon film in front of the surface applying pressure. The Surlyn tended to bubble up when heated as a larger piece rather than as a simple frame as before for the seal, so a degassing step was necessary before heating the Surlyn on the glass to reduce the frequency of bubbles.

The Pt-GNP papers were checked after this process to ensure the integrity of the layers hadn't been affected; Teflon proved to unalter the surface, and the Pt remained. The Teflon film also helped to compress the paper onto the slide to smooth out any rough areas or bubbles that remained, decreasing the possibility of shorting. GNP papers were fabricated using 20 μM and 200 μM concentrations of H_2PtCl_6 precursor solution and they are shown in Figure 5-6. The process proved to be reproducible at different concentrations with Pt particles at an average size of 4nm.

These novel Pt-GNP paper electrodes were incorporated into the standard DSSC procedure standing in as the counter electrode, first without any modifications to the procedure. Once the new counter electrodes were sealed to the photoanode, the Surlyn, as it was only in contact with the first few layers of the pressed GNP paper, separated these

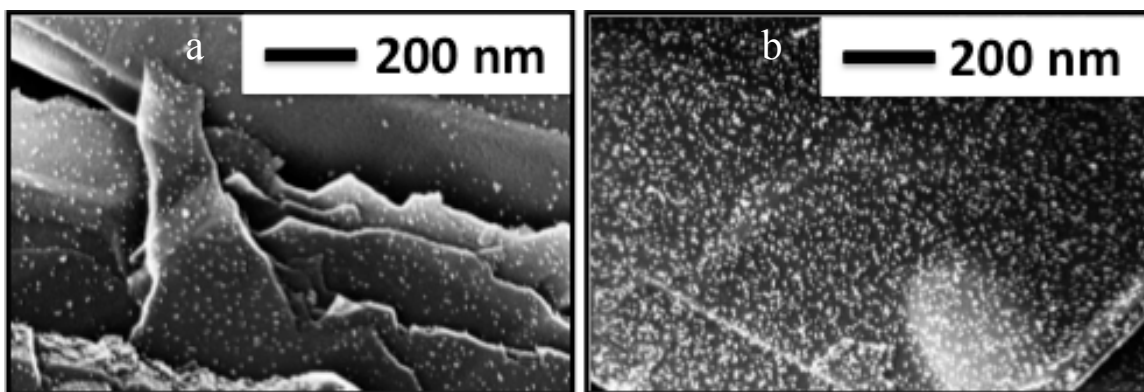


Figure 5-6. Photographs of graphene nanoplatelet pressed paper after Pt enhancement. a) 20 μM and b) 200 μM H_2PtCl_6 precursor concentrations.²²

layers from the rest of the electrode. It delaminated the first GNP layers it was bonded to and unsealed the cell, seen in Figure 5-7. So a new electrode that was more mechanically reliable was necessary. A composition was needed that could hold its nanoplatelet sheets

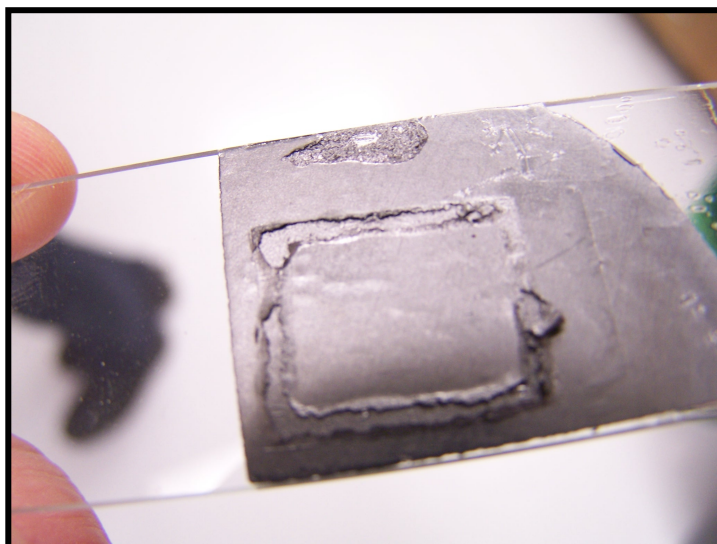


Figure 5-7. Photograph showing the delamination that occurs with GNP pressed paper when Surllyn is used to seal the counter electrode to the photoanode.²²

together while maintaining conductivity and providing a medium onto which the synthesis of the Pt nanoparticle could occur.

Another different issue also surfaced with these electrodes. When the voltage was applied to the new electrode to resistively heat the composite to seal to the photoanode sparking occurred. Small flashes of white sparks flashed periodically in the middle of the electrode during the heating process, but were concentrated at the edges where it was in contact with Surlyn, where the pressure was being applied. At first it was thought there was a contamination of the film, but successive papers produced the same sparking during the sealing process. We considered heating the electrode with the use of a hot plate in order to seal it to the photoanode but were reluctant to introduce additional heat to the Surlyn that held the paper to the microscope glass for fear that it would create bubbles inside the cell we would be unable to smooth out. Even though the sparks didn't seem to mar the surface of the Pt-GNP paper we were wary about the cause of them. Since new electrodes were needed due to delamination, we moved forward without locating the reason for the sparking anomaly.

5.3.3 Pt Nanoparticles on Pressed Graphene Nanoplatelets with a Polypropylene Binder. *Synthesis.* The new electrode architecture included polypropylene as a binder to give the GNP sheets more mechanical stability, hopefully hindering the delamination during the sealing process.²² Polypropylene (PP) was added during sonication of the water, GNP, and PEI mixture. The suspension was filtered to create the GNP papers and then dried in air and then under vacuum. The PEI was removed by leaching with water, since it could not be heated to decompose the PEI as PP

degrades at a similar temperature. The papers were again dried and then pressed using a new molding procedure²² that left the papers with a smooth flat finish seen in Figure 5-8.

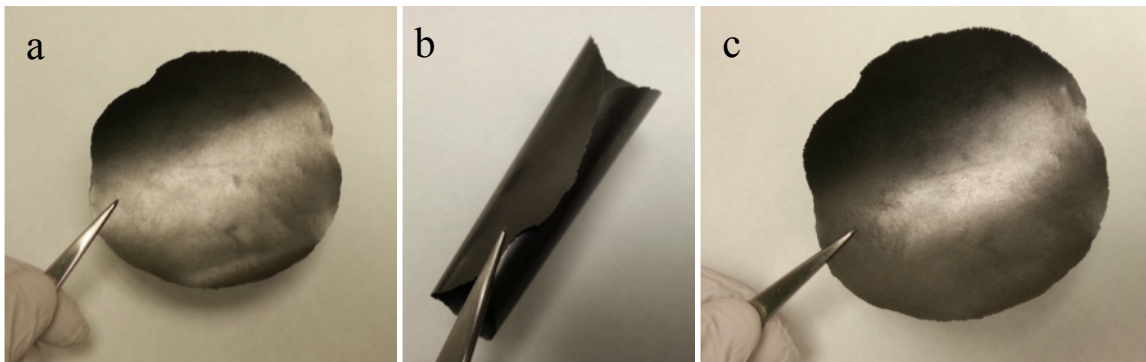


Figure 5-8. Graphene nanoplatelet with polypropylene paper after pressing using a molding procedure. a) Top side, b) rolled up, and c) unrolled again.²²

In order to be able to decorate the GNP/PP paper with platinum, the PP had to be removed with an oxygen plasma treatment. The Pt nanoparticle synthesis was performed as before²² and complete uniform coverage was obtained for each of the three concentrations, 20 μM , 200 μM and 1000 μM seen in Figure 5-9. The papers were attached to microscope slides with Surlyn as previously described.

Quantification. The next step is to quantify the platinum loading to ensure the platinum nanoparticles is indeed lower for the concentrations used to decorate the GNP/PP paper. The methods used were XPS and ICP-MS. XPS determines the elemental composition of the first few nanometers of a sample by irradiating with x-rays and detecting the kinetic energy of the resulting emitted electrons. Different concentrations of GNP/PP/Pt samples were prepared for XPS²² in ethylene glycol and a

standard Pt on FTO sample. As can be seen in Figure 5-10, the GNP/PP/Pt samples

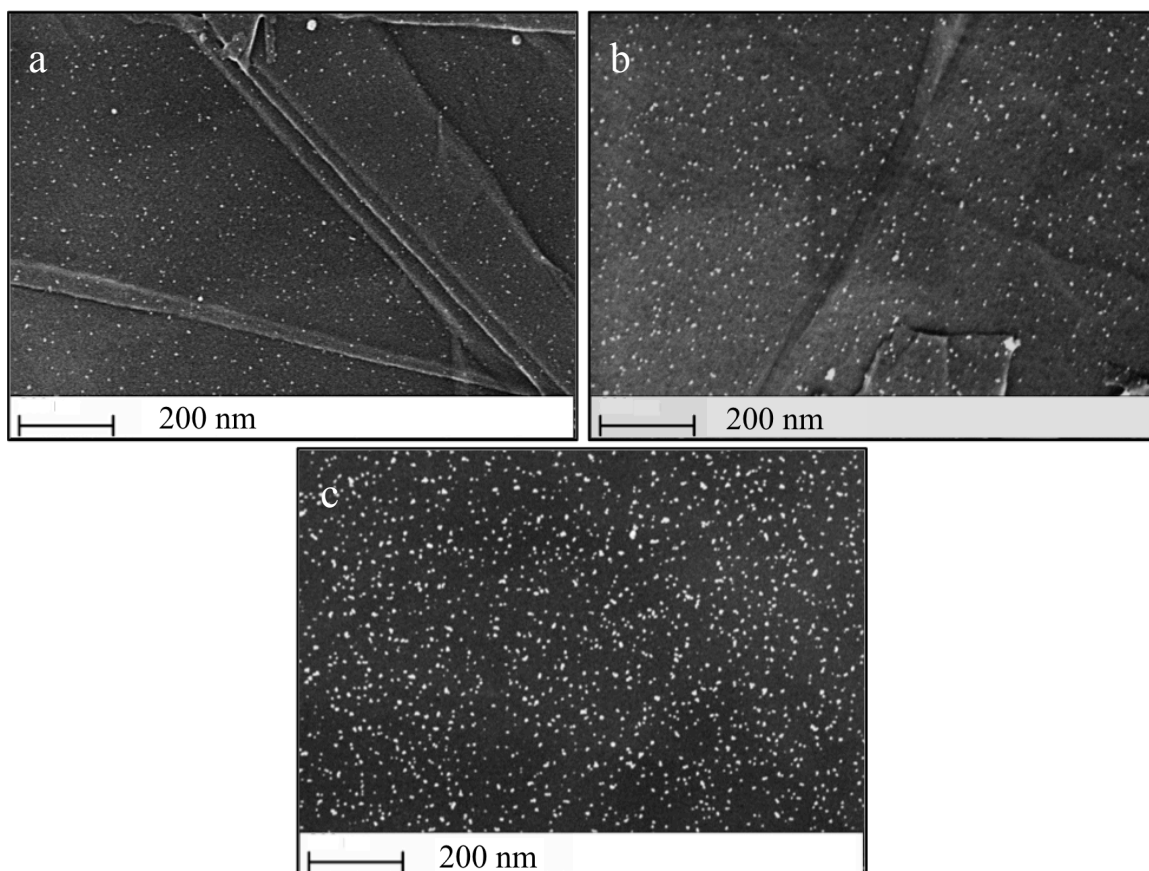


Figure 5-9. SEM images showing Pt nanoparticle coverage on plasma-treated GNP/PP surfaces from microwave heating in three concentrations of H_2PtCl_6 solutions: a) $20 \mu\text{M}$ b) $200 \mu\text{M}$ and c) $1000 \mu\text{M}$.²²

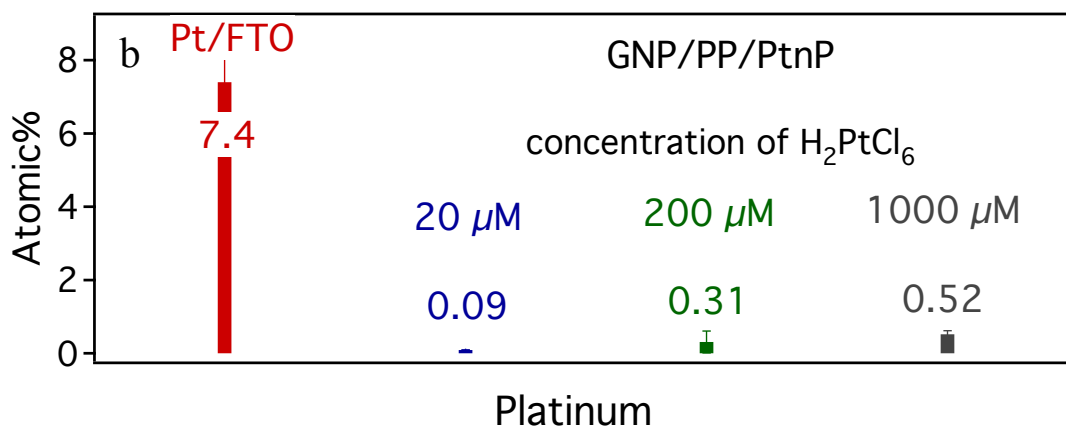
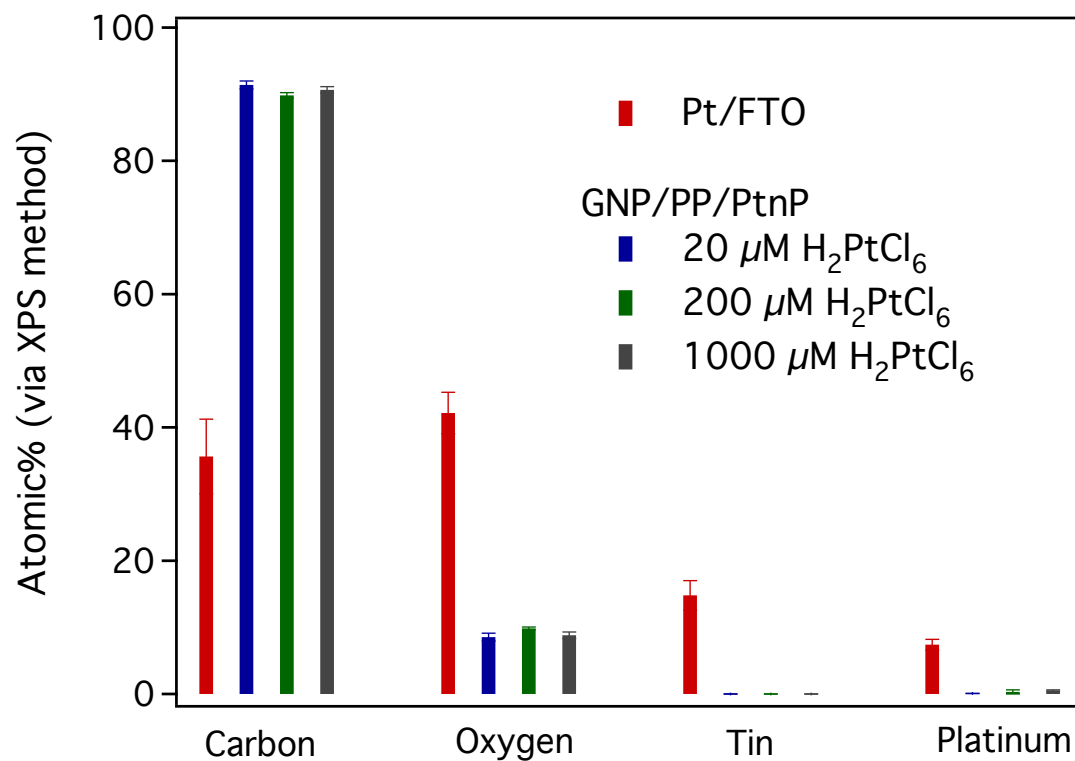


Figure 5-10. a) Elemental abundance and b) Pt loading at surface of GNP/PP/PtnP and FTO/Pt samples as measured by XPS. (adapted from ref 22)

exhibit a much weaker signal than the Pt/FTO sample for Pt; an order of magnitude less Pt is seen. XPS gives the surface composition but an absolute platinum loading is desired so a more in-depth analysis was performed using newly prepared²² samples that undergo acid digestion followed by ICP-MS. Its results compared to the XPS evaluation is seen in Figure 5-11. The ICP-MS method also shows a significant reduction in Pt loading for the

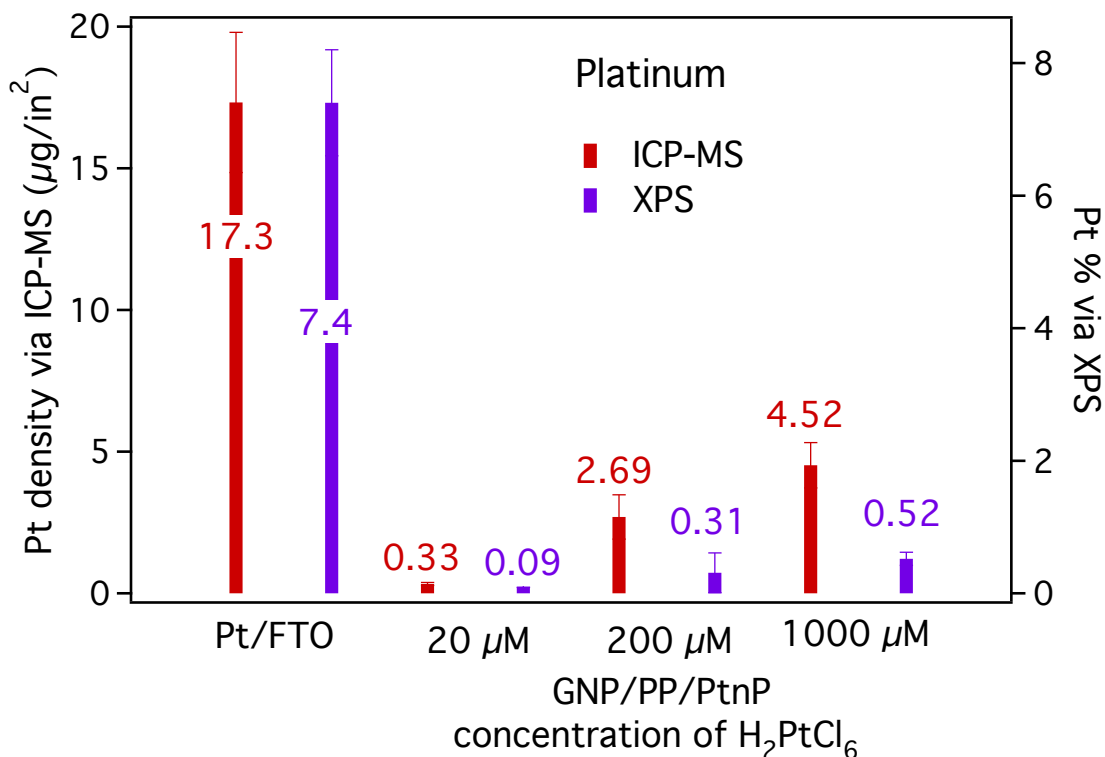


Figure 5-11. Quantification of Platinum loading by XPS and ICP-MS.²²

GNP/PP/Pt samples as compared to Pt/FTO. Also increased Pt loading is seen with increasing concentration of H₂PtCl₆, as is seen with XPS. Each data set was normalized to the lowest value. The XPS set gives a ratio of FTO/Pt: 20 μM : 200 μM : 1000 μM as 82 : 1 : 3.4 : 5.8 and for ICP-MS gives 52 : 1 : 8.2 : 13 showing a discrepancy between the relative ratios. The XPS ratios are smaller than ICP-MS data for both the 200 μM and

the 1000 μM but higher for the FTO/Pt value. This could indicate that the surface detection method, XPS is better suited for the FTO/Pt substrate than it is for the GNP/PP/PtNP materials. Yet after further analysis, the ICP-MS value for the Pt/FTO at 17.33 $\mu\text{g}/\text{in}^2$ appears to be an underestimate. During preparation that is described in Chapter 2, 31.55 μL of a 5 mM H_2PtCl_6 (409.8g/mol; Pt: 195.08g/mol) solution is applied to the 1" x 1" square FTO slide; this results in a value of 30.77 μg of Pt per in^2 , a little under 2 times the value that was found by the ICP-MS method. This could demonstrate that the acid digestion step did not fully dissolve the Pt from the FTO glass. A possibility of the discrepancy between methods is that Pt nanoparticles percolated beneath the first few nanometers of GNP/PP paper allowing detection by ICP-MS and not by XPS. It is suggested that this is not the case as PP fills the spaces that GNP leaves between platelets and delaminating layers of paper showed no Pt nanoparticles at further nanoplatelet depths.²² During the microwave irradiation the GNP/PP paper is suspended in the ethylene glycol solution of H_2PtCl_6 so possible decoration of the underside of the paper is possible. SEM imaging of the underside of the GNP/PP paper indeed shows nonuniform Pt nanoparticles decoration providing an explanation for the higher values seen for ICP-MS as compared to XPS. The quantification discrepancies reduce ability to directly compare loading levels, but the GNP/PP/Pt system provides a controlled, reliable system that could be used as a counter electrode in a novel DSSC.

Catalytic Activity. With all the physical properties in place, the system needs to be checked electrochemically to see how well it performs with the iodide/triiodide redox couple present. The working electrode is seen in Figure 5-12, it is constructed from a 5

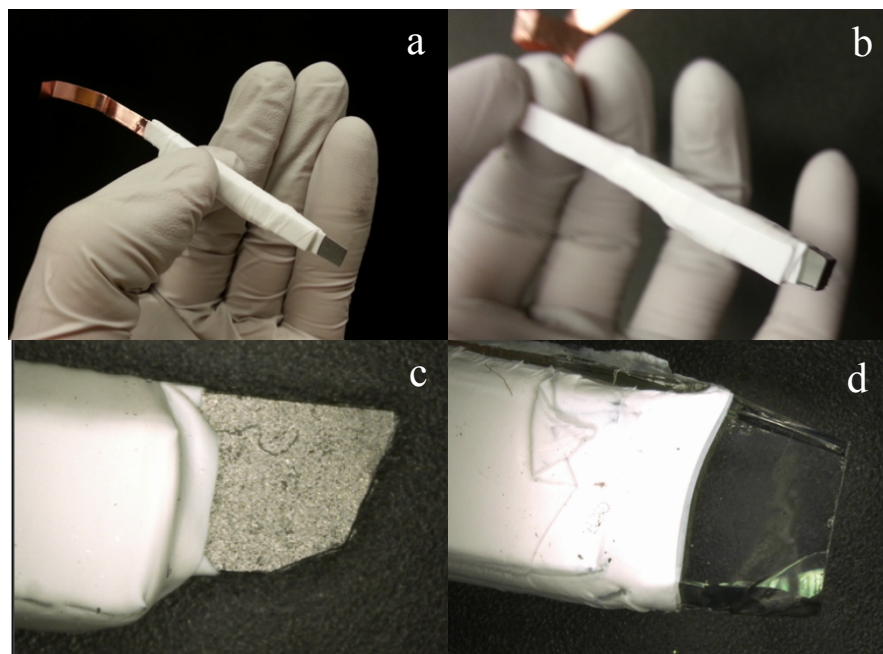


Figure 5-12. Working electrodes for cyclic voltammetry for a) GNP/PP/Pt and b) FTO/Pt. Close up of c) GNP/PP/Pt and d) FTO/Pt electrode area used for reflected light microscopy to normalize the current.²²

mm x 5 mm cut section of Pt/FTO or GNP/PP/Pt electrode. A piece of copper tape providing the lead is fastened with Ag conductive paste and is reinforced with polystyrene strips and wrapped in Teflon tape. The cyclic voltammograms of each GNP/PP/Pt sample at the three different concentrations, a GNP/PP control (no Pt) and the standard Pt/FTO electrode are seen in Figure 5-13, normalized for the imaged electrode area by reflected light microscopy. Each platinum functionalized electrode exhibits the signature waves for the iodide/triiodide species,³² where the control does not show a I_3^- wave ($\sim -0.1V$). Interestingly, the GNP/PP/Pt electrodes display a higher current than the Pt/FTO with a much lower Pt loading. The higher current for these samples is indicating

additional area at the electrode surface unaccounted for in the normalization in contact

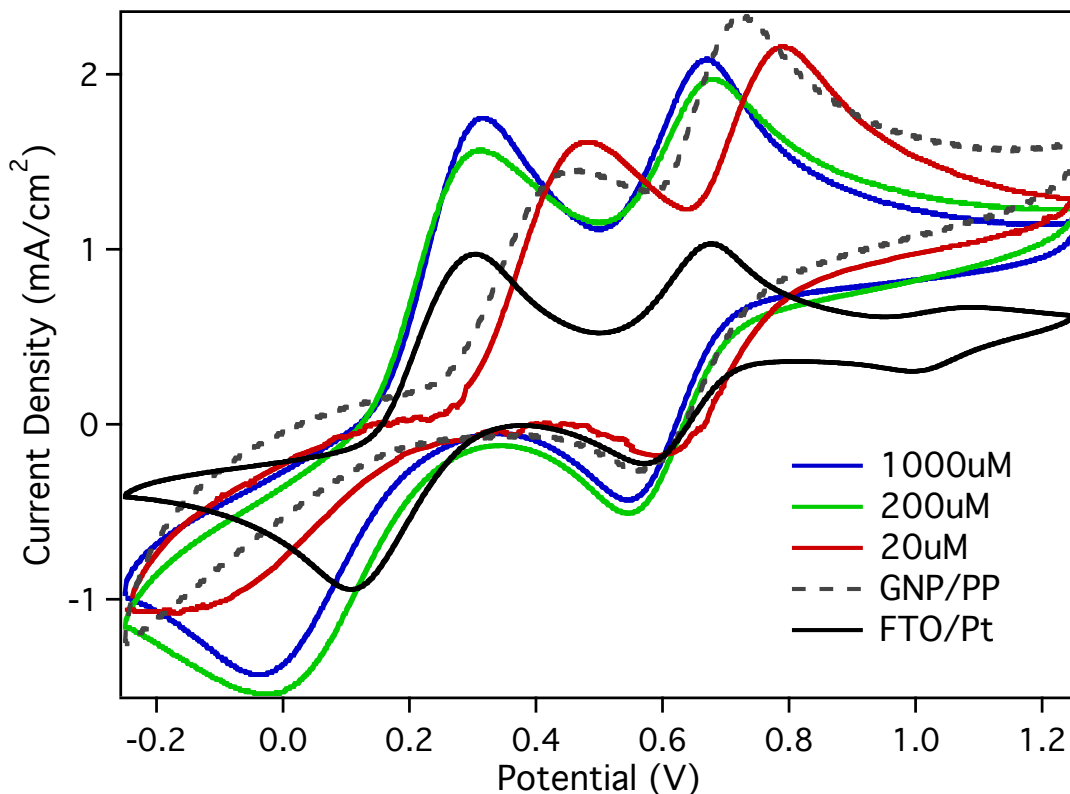


Figure 5-13. Cyclic voltammograms of GNP/PP/Pt and Pt/FTO samples in the electrolyte composed of 5 mM LiI, 0.5 mM I₂ and 0.1 M LiClO₄ in acetonitrile. Ag/AgCl reference. Scan rate was 50 mV/s. The current was corrected for electrode area using reflected light microscopy.²²

with solution, presumably the nanoparticle area. The 200 μM and 1000 μM samples display a higher, yet similar wave for the I₃⁻ wave at -0.1V than the 20 μM sample. The higher platinum loading of these samples would imply higher current, their similar currents can be explained by the inconsistency of coverage as is seen by the error bars in the quantification (Figure 5-11). With subsequent runs the I₃⁻ wave disappeared and peak heights changed. Surface examination with XPS shows that platinum nanoparticles remained but there were also adsorbed ClO₄⁻ ions, seemingly blocking normal electrode function and the cause of the decreased current.

Pt nanoparticles on pressed graphene nanoplatelets with a polypropylene binder seems to have all the qualities necessary for use in a dye-sensitized solar cell: mechanically stable with the use of PP and Surlyn attachment to glass substrates; smooth, flat surfaces to prevent shorting of the cell, and significantly reduced platinum loading on highly conductive carbon-based paper as compared to the standard thermalized platinum, and catalytic activity for the reduction of triiodide.

5.4 Dye-Sensitized Solar Cell Fabrication with Platinum Nanoparticles Embedded on Pressed Graphene Nanoplatelets with a Polypropylene Binder as the Counter Electrode. *DSSC Fabrication.* The photoanode was prepared as described in Chapter 2.

Difficulties arose when attempting to use the resistive heating method to seal the GNP/PP/Pt to the dyed photoanode. Care is always taken to limit the amount and time that the photoanode is exposed to heat as the dye desorbs at increased temperatures. As mentioned previously for the GNP/PP/PtNP electrodes, Surlyn attaches the paper to the glass substrate and when the electrode is heated, this section of Surlyn will also melt and can bubble, breaching the short distance to the photoanode causing shorts. It was discovered that the GNP/PP/Pt electrodes would not heat up as well as the FTO/Pt electrodes in order to melt the Surlyn for sealing. It is speculated that the polymer additive helped to dissipate the heat. We were hesitant to increase the voltage applied to increase the current and subsequently the resistance to be sure the surface wasn't being altered during this step. We also decided against heating using a hot plate, mentioned above, Surlyn that secures the graphene to the glass would also heat and could bubble. Instead we decided to institute a new type of electrode configuration, the clamp cell, one that would not need heat to seal. A rubber EPDM material was purchased to provide the

seal. For these cells, the counter electrode glass did not need to have sandblasted holes in them as the electrolyte was injected at the EPDM seal; the modified procedure follows.

Microscope glass slides (no holes) were cut to 1" x 1" pieces, along with pieces of Surlyn and the GNP/PP/Pt papers. The Surlyn was placed onto the glass, and then the paper was aligned atop. The layers were heated to ~100 °C and a Teflon sheet was used to protect the GNP/PP/Pt surface from the object that applied pressure, to attach the paper to the glass, the complete electrode (no leads) is seen in Figure 5-14. Wire leads are attached using silver conductive epoxy, curing 4 hours at room temp or 15 minutes at 65 °C.

The photoanode was prepared as described in Chapter 2; the lead was applied in

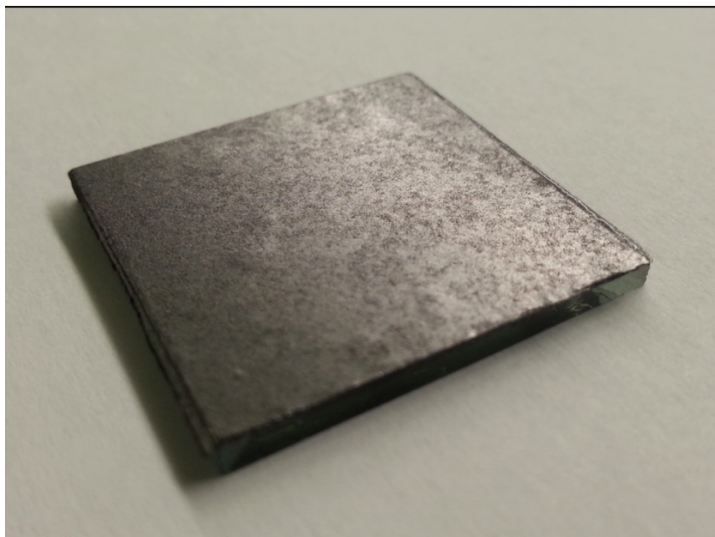


Figure 5-14. The complete GNP/PP/Pt electrode ready for DSSC assembly.²²

the dark directly after dyeing step. A square frame was cut from the EPDM sheet that would enclose the TiO_2 active area and it was placed on top of the counter electrode, which rested on the lab bench, then the photoanode was placed on the EPDM frame. The unsealed cell was carefully maneuvered to the edge of the bench and a small binder clip was placed on an edge that a lead was along. A 0.5 mL syringe full of electrolyte is placed at the counter electrode side of the EPDM, at the bottom corner on the edge opposite to the direction the leads point. Another syringe without a plunger is placed 'above' the electrolyte syringe to allow the internal air to escape, seen in Figure 5-15. The electrolyte is pushed into the cell while the cell is held upright, positioning the cell during injection to guide the air bubbles toward the exit syringe. Once electrolyte breaches the exit syringe the two syringes are removed and a third binder clip is put in

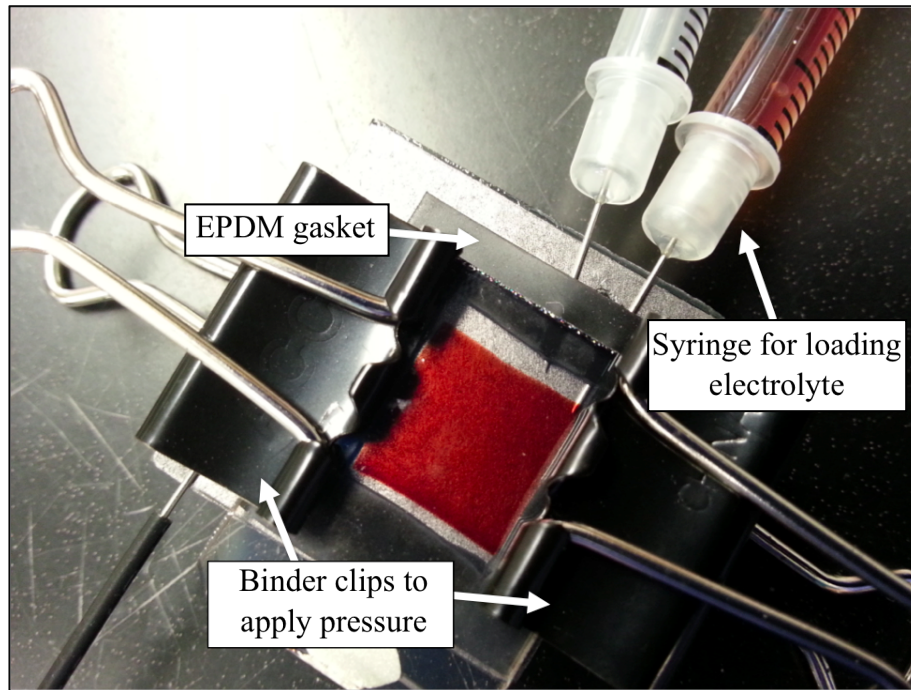


Figure 5-15. GNP/PP/Pt Clamp cell assembly at electrolyte injection step.²²

their place. Often electrolyte leaks a little around the EPDM at the syringes once the cell is close to full, excess electrolyte is wiped away so one can tell if leaking occurs later. Although the cells were tested and did not leak for up to a week with minimal loss of solvent. Once the cell was filled the completed cell was allowed to equilibrate for 5 to 10 minutes. A set of standard cells was also fabricated using the same method just described, for comparison. Four cells were constructed for each type of solar cell, FTO/Pt, control GNP/PP (same steps, no Pt precursor), 20 μM , 200 μM and 1000 μM H_2PtCl_6 precursor solution concentrations for GNP/PP/Pt electrodes.

DSSC Characterization. The DSSCs were tested as described in Chapter 2 in a two-electrode arrangement. The cell was attached to the post and masked to provide an illuminated area of 0.3167 cm^2 . Using the power meter a vertical and horizontal position was located for the maximum power density of 100 mW/cm^2 . Dark J-V curves were measured first, the light was turned on and vertical position was chosen based on the highest current produced by the cell since the maximum power density of 100 mW/cm^2 should also correspond to the highest cell current. Then the light J-V curves were taken; representative curves are seen in Figure 5-16 and the efficiency parameters are seen in Table 5-1. The 1000 μM cell average has the largest J_{SC} at 4.55 mA/cm^2 and the largest overall efficiency at 1.41%. The high performance indicates even though it has much lower Pt loading than the Pt/FTO standard, it is functioning better, producing higher current and similar V_{OC} and fill factor.

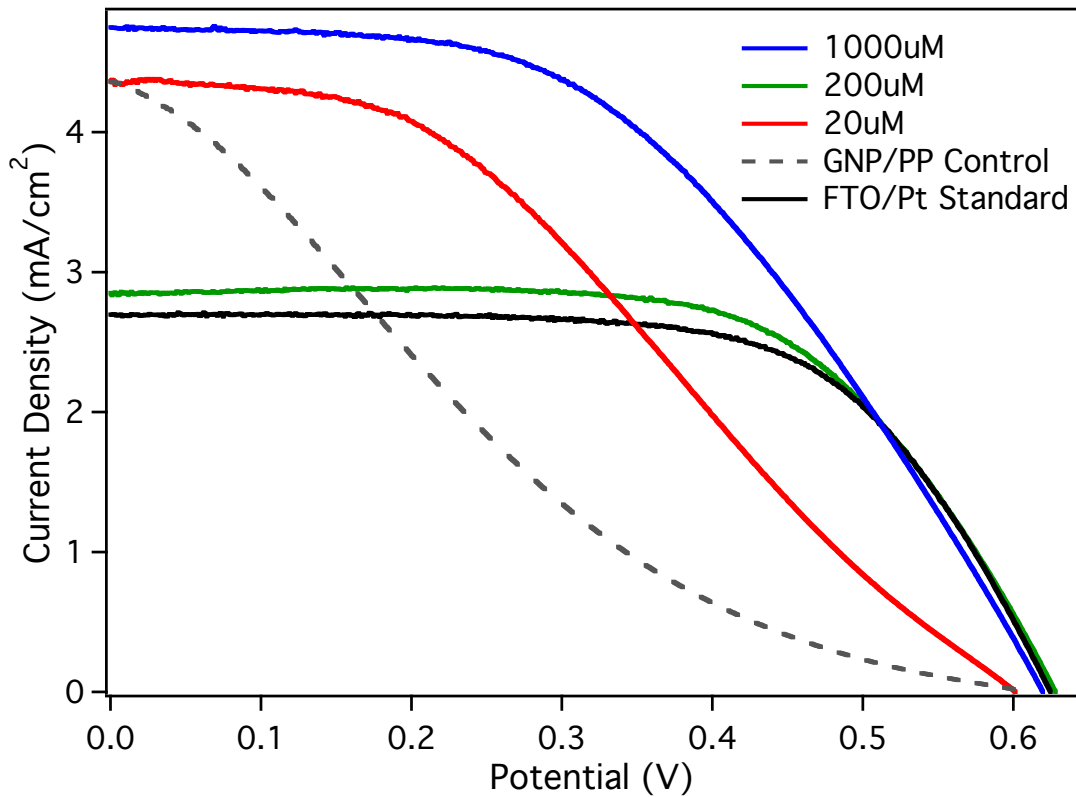


Figure 5-16. Representative J-V Curves for 20 μM , 200 μM and 1000 μM H_2PtCl_6 GNP/PP/Pt, control GNP/PP (no Pt), and FTO/Pt counter electrodes.²²

	Voc	Jsc	ff	η
1000 μM	0.63	4.55 mA/cm²	0.49	1.41%
200 μM	0.63	2.95 mA/cm²	0.61	1.13%
20 μM	0.59	4.22 mA/cm²	0.39	0.98%
GNP/PP Control	0.62	4.08 mA/cm²	0.20	0.49%
FTO/Pt	0.64	2.71 mA/cm²	0.64	1.08%

Table 5-1. Efficiency Parameters for 20 μM , 200 μM and 1000 μM H_2PtCl_6 GNP/PP/Pt, control GNP/PP (no Pt), and FTO/Pt counter electrodes. N3 dye, electrolyte: 0.3 M LiI, 0.03 M I_2 , 0.2 M TBP in acetonitrile.²²

The standard FTO and the 200 μM cells are approximately giving the same response for all parameters, this assumes that their Pt surface area is similar even though the GNP/PP/Pt electrode is ~ 6 times lower than the standard.

Surprisingly the 20 μM and the control are only $\sim 0.5\text{A}/\text{cm}^2$ below the 1000 μM in current density. The 20 μM , and especially the control, show significant S-shaped curves with incredibly low ff. S-shaped curves have been reported as result of a large internal series resistance.^{4,35-37} It seems this is indicating that there is not enough platinum at the electrode surface available to catalyze the reaction of the 20 μM concentration (and for the control) concentration. Inadequate reduction depletes the iodide species that is needed to reduce the oxidized dye. The ff increases as the resistance decreases at the higher Pt concentrations. The larger ff for the higher Pt precursor concentrations show minimal loss, enough catalyst is at the surface to keep up with the reduction reaction. Though the reaction is not being catalyzed efficiently, the short-circuit current density is higher for the 20 μM and the control, than it is for the FTO/Pt and 200 μM samples. This reveals that when there is no barrier opposing electron flow through the circuit, more current is produced by the 200 μM and the sample with no platinum. In order to better understand this concept, the average integrated current density was calculated for each set and a standard deviation was arrived at. This shows the total current passed by each cell, normalized to area, the plot is seen in Figure 5-17. The current passed by the 1000 μM is significantly greater than all others, and all other cells are approximately within error of each other with a slight exception being Pt standard being lower than the 20 μM data set. It is proposed that, with or without the Pt nanoparticles, the reaction is catalyzed by GNP/PP just as well as the standard until a coverage threshold of Pt nanoparticles is

reached. Once the threshold concentration is reached the reaction is catalyzed better as is seen with 1000 μM data. Further experiments to confirm this are needed.

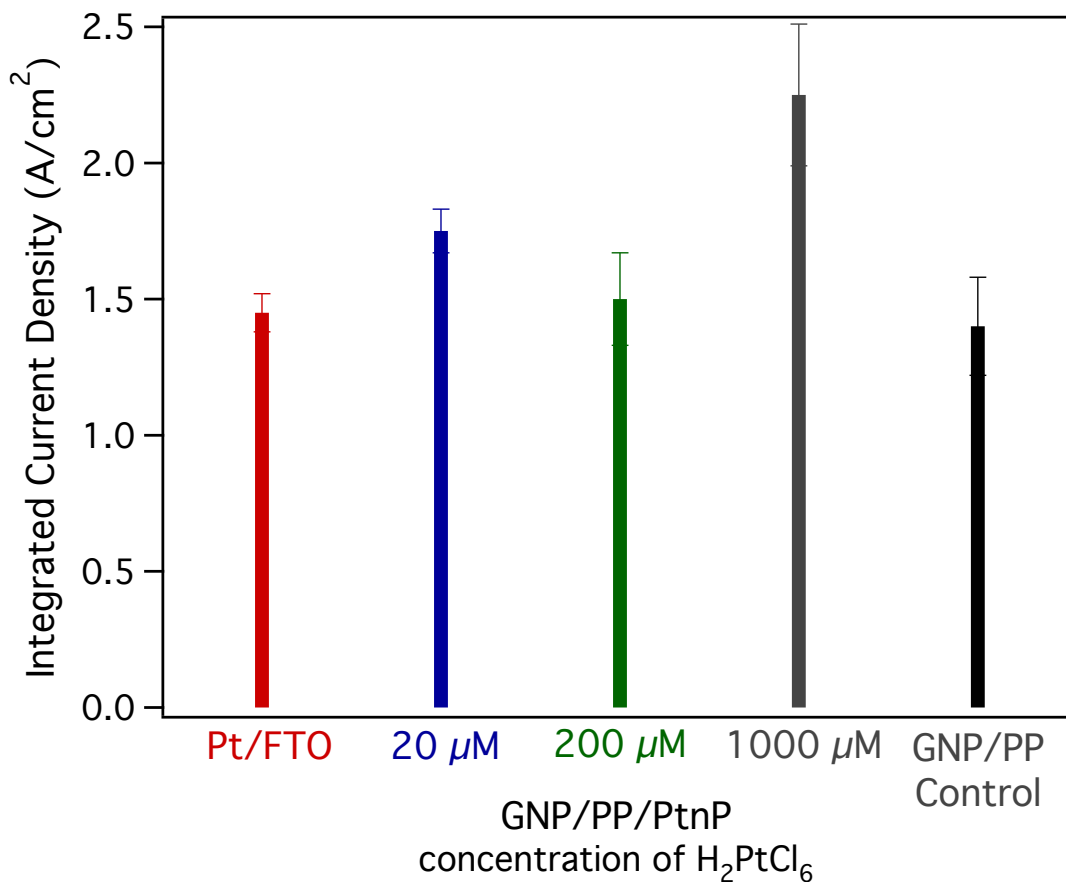


Figure 5-17. Integrated Current Density for 20 μM , 200 μM and 1000 μM H₂PtCl₆GNP/PP/Pt, control GNP/PP (no Pt), and FTO/Pt counter electrodes.²²

5.4 Concluding Comments

A novel counter electrode designed by Prof. Drzal's group has been assimilated into our standard method of fabrication of dye-sensitized solar cells. Electrode composition had to be modified in order to be able to introduce into a DSSC. Upon adjustment the electrode became a reproducible, sturdy, smooth and stable catalyst. One

change that was made was a thicker foundation of graphene in the form of pressed paper to increase reproducibility and maintain a conductive layer between nanoparticles of Pt. Second, a polypropylene binder was necessary to strengthen the graphene, to prohibit the delamination of layers of graphene during sealing. The pressed GNP/PP paper also required a different method of attachment to a glass substrate by means of Surlyn. Since resistive heating of the standard method was less effective for the graphene layer, an adaptation to the fabrication method was necessary. These cells were constructed as binder clip clamped cells with a rubber gasket as the spacer. The method of electrolyte injection now included a needled syringe for entrance of electrolyte and exit (no plunger) of air after clamped. The variation to the method was carefully implemented and reproducibility of the cells was maintained for all data sets with low relative error at 2 - 8%. The control had a larger relative error of ff and efficiency (~25%) due to variance in the strong S-shaped curves.

The new electrodes were successfully integrated into the procedure and through reproducibility of the electrodes we were able to determine that lower Pt loading levels still catalyze the triiodide reduction reaction at the counter electrode. The parameters proved to be significantly better for the 1000 μM precursor concentration. This novel electrode is a viable, cost-effective and consistent counter electrode for use in dye-sensitized solar cells that employ iodide/triiodide as a redox couple.

Further studies are needed to confirm the notion that the lower levels and electrodes without platinum have similar activity to the standard FTO/Pt substrate. Also conducting a study that includes a higher distribution of Pt precursor concentrations to investigate further the potential for a threshold Pt level that could exist. Once the threshold Pt level is exceeded, although lower than the standard Pt loading, performance

of the material tops the standard FTO/Pt. Optimization of the electrode would be beneficial, looking into other particle sizes, other binders, also developing a more effective fabrication method that would not decorate the underside of the paper. Another study would include testing the new electrode with other redox couples, opening up possibilities for different dyes, such as iron-based chromophores, discussed in Chapter 3.

APPENDIX

APPENDIX

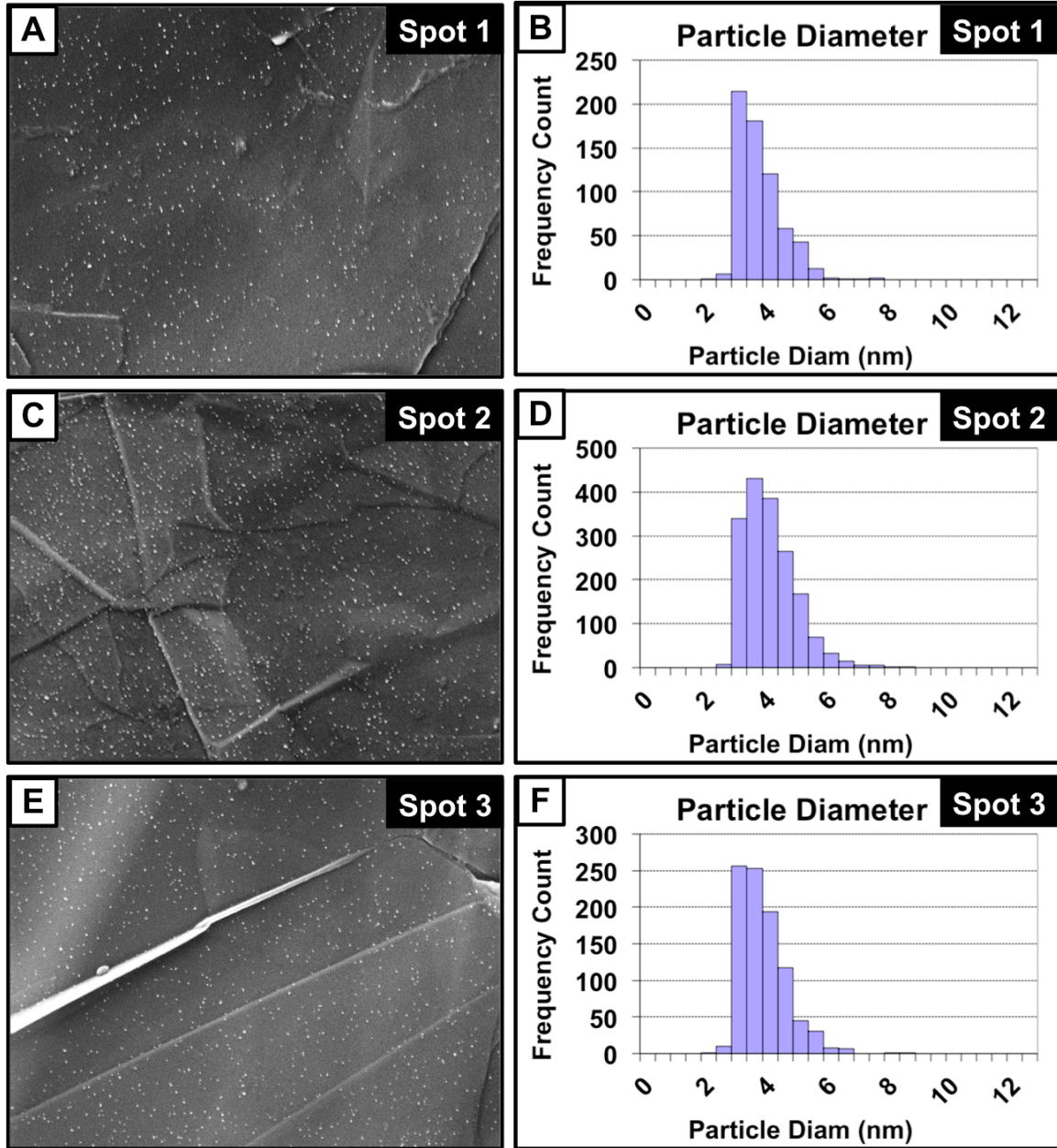


Figure 5-18. Particle distribution of 20 μM H_2PtCl_6 GNP paper in three different spots.²² a), c) and e) are SEM images of each spot. b), d) and f) are the size distribution of the nanoparticles.

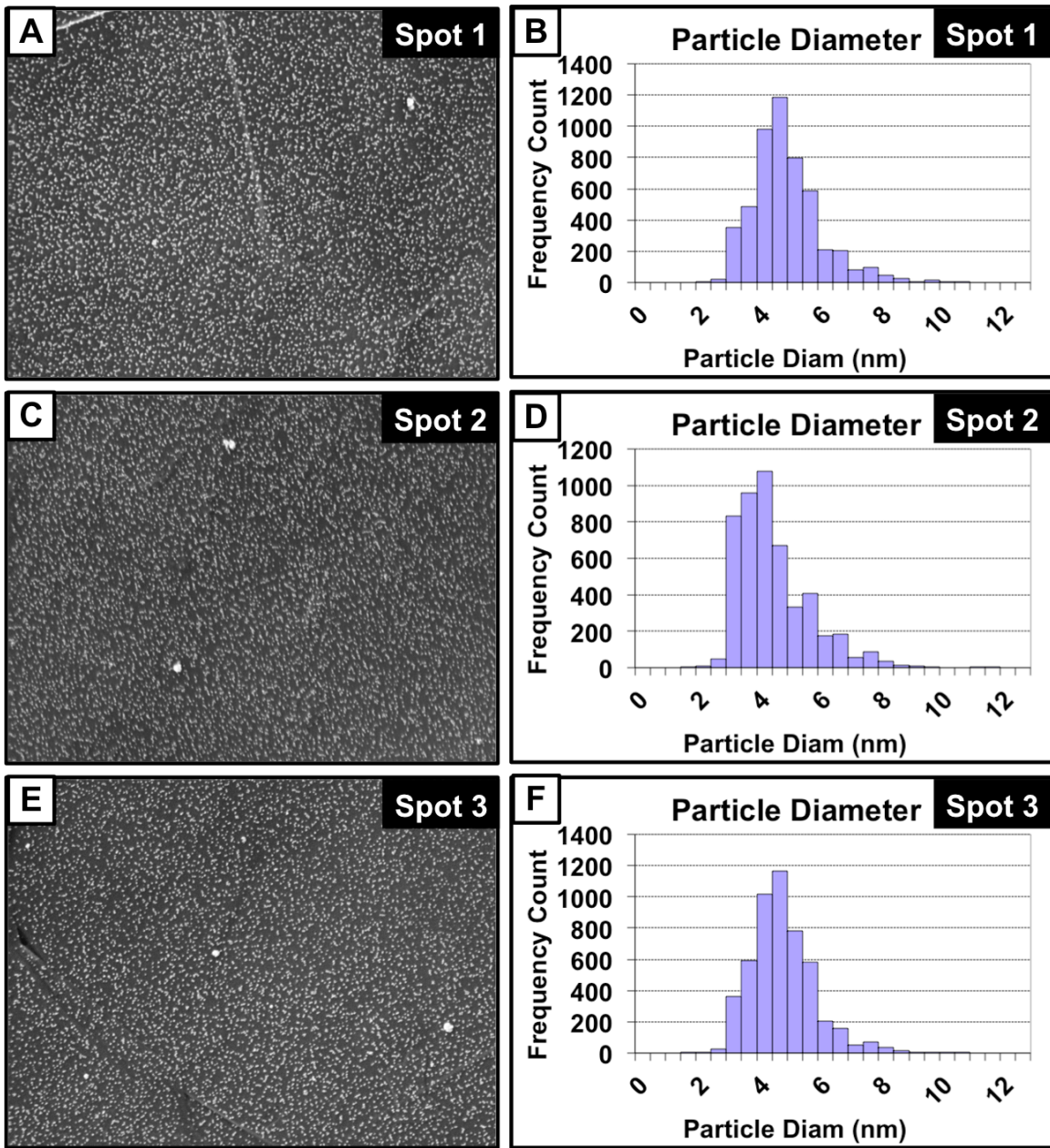


Figure 5-19. Particle distribution of 200 μM H_2PtCl_6 GNP paper in three different spots.²² a), c) and e) are SEM images of each spot. b), d) and f) are the size distribution of the nanoparticles.

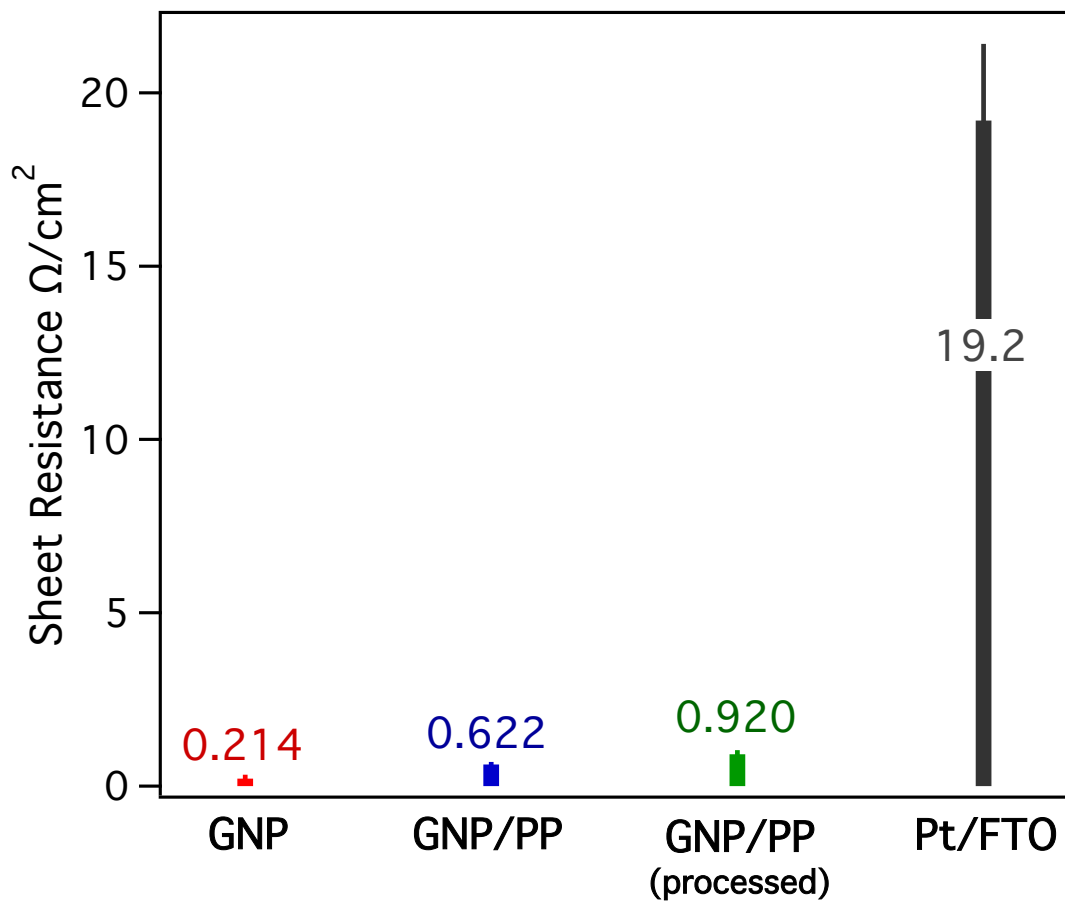


Figure 5-20. Sheet resistance of the different composites and treatments of GNP and GNP with polypropylene.²² Processed is microwave irradiated and plasma treated.

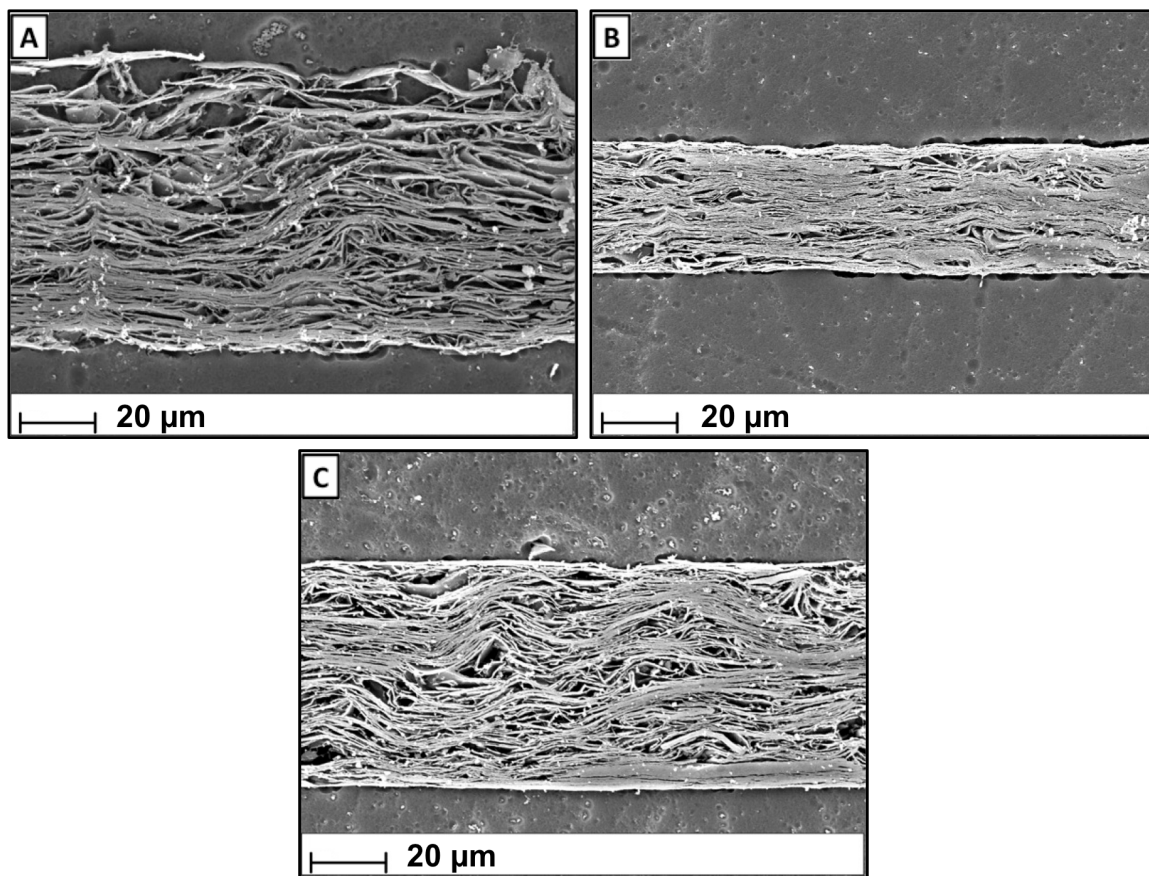


Figure 5-21. FESEM images of a) un-pressed GNP paper b) pressed GNP paper and c) pressed GNP with poly propylene paper.²²

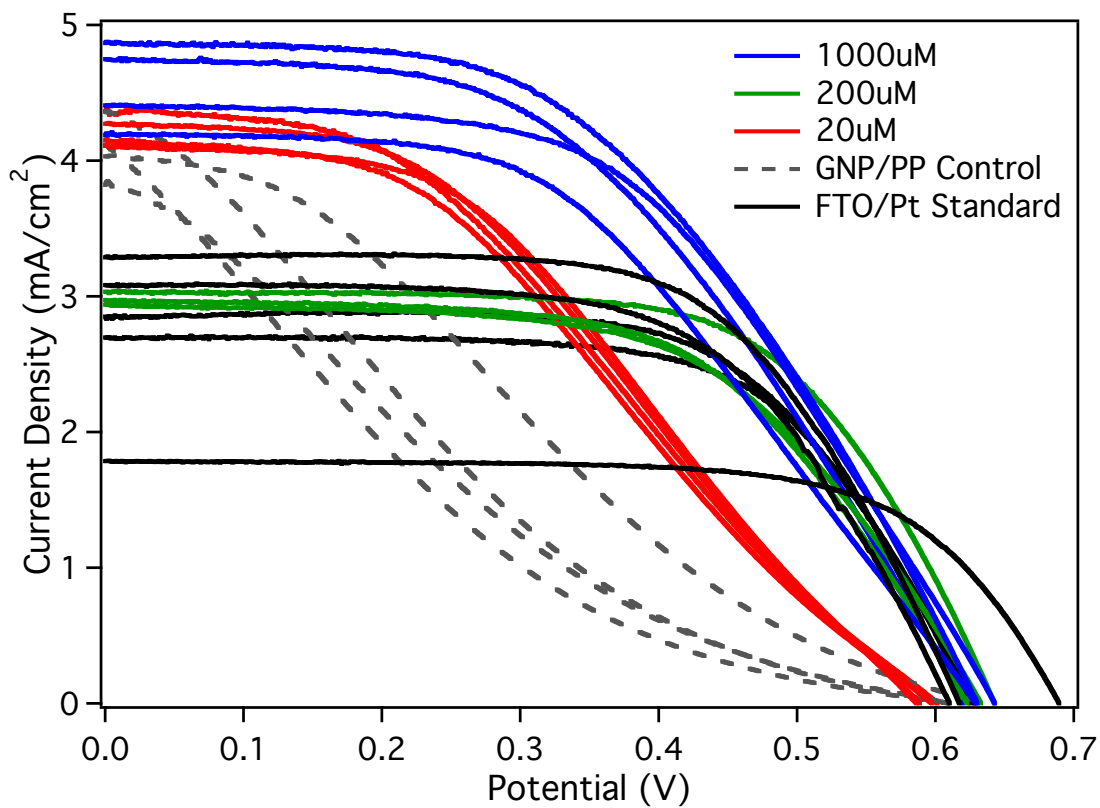


Figure 5-22. Each set of four J-V Curves for 20 μM , 200 μM and 1000 μM H_2PtCl_6 GNP/PP/Pt, control GNP/PP (no Pt), and FTO/Pt counter electrodes.²²

REFERENCES

REFERENCES

- (1) Papageorgiou, N.; Maier, W. F.; Gratzel, M. *Journal of The Electrochemical Society* **1997**, *144*, 876.
- (2) Papageorgiou, N. *Coordination Chemistry Reviews* **2004**, *248*, 1421–1446.
- (3) Zhao, W.; Zhu, X.; Bi, H.; Cui, H.; Sun, S.; Huang, F. *Journal of Power Sources* **2013**, *242*, 28–32.
- (4) Jeong, I.; Jo, C.; Anthonysamy, A.; Kim, J.-M.; Kang, E.; Hwang, J.; Ramasamy, E.; Rhee, S.-W.; Kim, J. K.; Ha, K.-S.; Jun, K.-W.; Lee, J. *ChemSusChem* **2013**, *6*, 299–307.
- (5) Khurana, G.; Sahoo, S.; Barik, S. K.; Katiyar, R. S. *Journal of Alloys and Compounds* **2013**, *578*, 257–260.
- (6) Wang, M.; Anghel, A. M.; Marsan, B.; Cevey Ha, N.-L.; Pootrakulchote, N.; Zakeeruddin, S. M.; Grätzel, M. *Journal of the American Chemical Society* **2009**, *131*, 15976–7.
- (7) Chen, J.; Wei, H.; Ho, K. *Solar Energy Materials and Solar Cells* **2007**, *91*, 1472–1477.
- (8) Tian, H.; Yu, Z.; Hagfeldt, A.; Kloo, L.; Sun, L. *Journal of the American Chemical Society* **2011**, *133*, 9413–22.
- (9) Saito, Y.; Kubo, W.; Kitamura, T.; Wada, Y.; Yanagida, S. *Journal of Photochemistry and Photobiology A: Chemistry* **2004**, *164*, 153–157.
- (10) Murakami, T. N.; Ito, S.; Wang, Q.; Nazeeruddin, M. K.; Bessho, T.; Cesar, I.; Liska, P.; Humphry-Baker, R.; Comte, P.; Péchy, P.; Gratzel, M. *Journal of The Electrochemical Society* **2006**, *153*, A2255.
- (11) Huang, Z.; Liu, X.; Li, K.; Li, D.; Luo, Y.; Li, H.; Song, W.; Chen, L.; Meng, Q. *Electrochemistry Communications* **2007**, *9*, 596–598.
- (12) Ramasamy, E.; Lee, W. J.; Lee, D. Y.; Song, J. S. *Applied Physics Letters* **2007**, *90*, 173103.
- (13) Kavan, L.; Yum, J. H.; Grätzel, M. *ACS Nano* **2011**, *5*, 165–72.
- (14) Kim, Y.-G.; Akbar, Z. A.; Kim, D. Y.; Jo, S. M.; Jang, S.-Y. *ACS Applied Materials & Interfaces* **2013**, *5*, 2053–61.

- (15) Han, H.; Bach, U.; Cheng, Y.-B.; Caruso, R. a.; MacRae, C. *Applied Physics Letters* **2009**, *94*, 103102.
- (16) Katsanaki, A. V.; Tsoukleris, D. S.; Falaras, P.; Karayianni, H. S.; Bernard, M.-C. *Journal of Solar Energy Engineering* **2008**, *130*, 041008.
- (17) Dao, V.-D.; Kim, S.-H.; Choi, H.-S.; Kim, J.-H.; Park, H.-O.; Lee, J.-K. *The Journal of Physical Chemistry C* **2011**, *115*, 25529–25534.
- (18) Kim, S.-S.; Nah, Y.-C.; Noh, Y.-Y.; Jo, J.; Kim, D.-Y. *Electrochimica Acta* **2006**, *51*, 3814–3819.
- (19) Kim, S.-S.; Park, K.-W.; Yum, J.-H.; Sung, Y.-E. *Journal of Photochemistry and Photobiology A: Chemistry* **2007**, *189*, 301–306.
- (20) Do, I.-H. Metal Decoration of Exfoliated Graphite Nanoplatelets (xGNP) for Fuel Cell Application, 2006.
- (21) Lu, J.; Do, I.; Drzal, L. T.; Worden, R. M.; Lee, I. *ACS Nano* **2008**, *2*, 1825–32.
- (22) Aderhold, P. Graphite Nanoplatelet Assemblies for Transarent and Catalytic Electrodes in Dye-Sensitized Solar Cells, 2013.
- (23) Zhang, B.-T.; Zheng, X.; Li, H.-F.; Lin, J.-M. *Analytica Chimica Acta* **2013**, *784*, 1–17.
- (24) Liang, M.; Luo, B.; Zhi, L. *International Journal of Energy Research* **2009**, *33*, 1161–1170.
- (25) Santamaria, A.; Muñoz, M. E.; Fernández, M.; Landa, M. *Journal of Applied Polymer Science* **2013**, *129*, 1643–1652.
- (26) Yang, X.-F.; Wang, A.; Qiao, B.; Li, J.; Liu, J.; Zhang, T. *Accounts of Chemical Research* **2013**, *46*, 1740–8.
- (27) Duan, X.; Fu, T.-M.; Liu, J.; Lieber, C. M. *Nano Today* **2013**, *8*, 351–373.
- (28) Wang, S.; Sun, H.; Ang, H. M.; Tadé, M. O. *Chemical Engineering Journal* **2013**, *226*, 336–347.
- (29) Hao, F.; Dong, P.; Luo, Q.; Li, J.; Lou, J.; Lin, H. *Energy & Environmental Science* **2013**, *6*, 2003.
- (30) Biswas, S.; Drzal, L. T. *Nano letters* **2009**, *9*, 167–72.

- (31) Yang, H.; Guo, C.; Guai, G. H.; Song, Q.; Jiang, S. P.; Li, C. M. *ACS Applied Materials & Interfaces* **2011**, *3*, 1940–5.
- (32) Bajpai, R.; Roy, S.; Kumar, P.; Bajpai, P.; Kulshrestha, N.; Rafiee, J.; Koratkar, N.; Misra, D. S. *ACS Applied Materials & Interfaces* **2011**, *3*, 3884–9.
- (33) Berry, V. *Carbon* **2013**, *62*, 1–10.
- (34) Kucinskis, G.; Bajars, G.; Kleperis, J. *Journal of Power Sources* **2013**, *240*, 66–79.
- (35) Burschka, J.; Brault, V.; Ahmad, S.; Breau, L.; Nazeeruddin, M. K.; Marsan, B.; Zakeeruddin, S. M.; Grätzel, M. *Energy & Environmental Science* **2012**, *5*, 6089.
- (36) Fan, S.-Q.; Fang, B.; Kim, J. H.; Jeong, B.; Kim, C.; Yu, J.-S.; Ko, J. *Langmuir : the ACS journal of surfaces and colloids* **2010**, *26*, 13644–9.
- (37) Wagenpfahl, A.; Rauh, D.; Binder, M.; Deibel, C.; Dyakonov, V. *Physical Review B* **2010**, *82*, 115306.

Chapter 6. Future Work and Direction

We have successfully made alterations to DSSCs by way of first-row transition metal-based chromophores, different electrolyte introducing new solid-state properties, and a novel counter electrode. Most of these changes were made one at a time, opening up the door to incorporate all of the components together into a much more cost-effective DSSC device.

We would like to build on our work with iron(II) polypyridyls to better gain a fundamental understanding of how their electronic structure changes their spectroscopic and electrochemical properties. We continue to study homo- and heteroleptic compounds in our group to guide their potential for use in DSSCs. In Chapter 3 we looked at an iron(II) heteroleptic bipyridyl compound previously studied. More research is needed to confirm its performance in our standard DSSC as compared to its ruthenium(II) analog. Future work on these two compounds is planned.

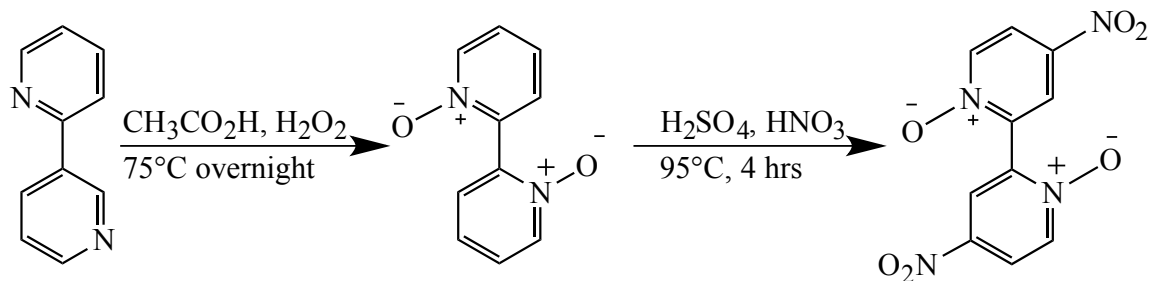
We would also like to evaluate DSSC performance and reaction rate changes for different anchoring groups. Our plan is to use tris bipyridyl compounds for ease of synthesis and to circumvent any electronic structure changes that are introduced with differing ligands. We want to focus solely on the change in the binding of the chromophore to the semiconductor, first looking at titanium dioxide, then move onto others, which are discussed later. The anchoring groups we would like to compare are the well-known carboxylic acid (dcbpy), the hydroxamic acid (hx) and the acetylacetonate (acac), all attached at the four-positions of tris bipyridyl iron(II) compounds. A recent collaboration with Prof. Jakubikova's theoretical group at North Carolina State University should provide further insight into these linkers. Calculations are in progress

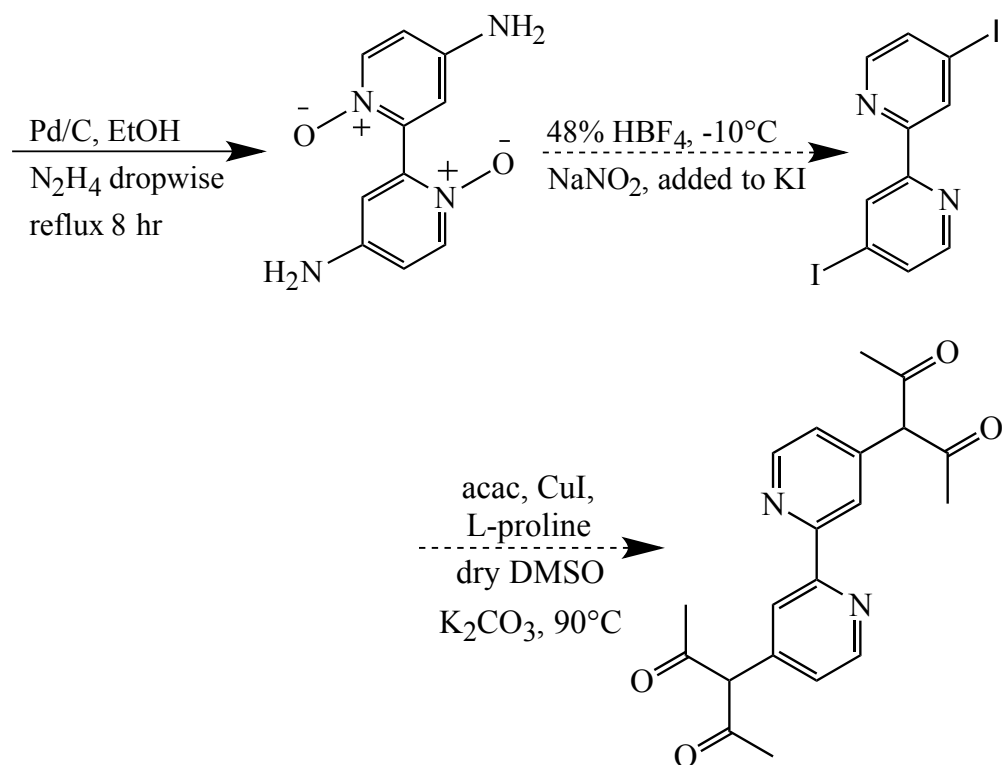
of the rates of injection of each of the iron complexes with the different linkers attached to TiO₂. We expect to have a successful future collaborating with this group, building on each other's findings, confirming calculation results with experiment.

The dcbpy ligand synthesis is described in Chapter 2. The associated iron complex, [Fe(dcbpy)₃](PF₆)₂, has been attained, the synthesis and characterization is shown in the Appendix. The complex is easily obtained by deprotonating the ligand to dissolve, simple addition of an iron salt, then minimal heating to complex, acidification yields the complex. The compound has been made numerous times, but the difficulty comes in purification. The reaction is performed in an excess of the iron salt, but the ligand remains as an impurity in the product. Acid-base recrystallization has been attempted as the complexed ligand should have different pK_as than the free ligand, which has pK_as at 3.7 and <2,¹ but a pH was not found that precipitated one and not the other. Dissolution in a basic methanol solution and then recrystallized with ether diffusion also did not yield the pure product. Column chromatography on Sephadex LH-20 or DEAE A-25 also did not effectively separate the ligand completely from the complex. It is believed with continued attempts a complete separation is attainable but we decided to use the complex in a trial-run DSSC as the free ligand should not interfere in the rates. The ligand could adsorb to the TiO₂ displacing the Fe dye and further as it is already considerably lower than RuCN or FeCN with dyed films having an absorbance of ~0.14. Preliminarily, the Fe(II) tris dcbpy complex produced a photocurrent similar to that of the Fe(dcbpy)₂(CN)₂ complex. Further cell batches are needed to confirm its performance. The ruthenium analog of this tris dcbpy complex has also been obtained. DSSC performance comparisons of the iron versus the ruthenium complexes will aid in the investigation that has been initiated by the FeCN and RuCN chromophores.

The tris(4,4'-diethylester-2,2'-bipyridine)iron(II) compound was also synthesized in anticipation of this compound would be easier to purify or that it would hydrolyze upon adsorption to TiO₂. It was found that it is much easier to purify, characterization is found in the Appendix. But it would not hydrolyze upon attempted adsorption onto TiO₂, and in fact would not adsorb at all. A method to convert Ru(deeb)₃²⁺ to the Ru(dcbpy)₃²⁺ by stirring the compound in ammonia² was attempted on pure [Fe(deeb)₃](PF₆)₂ and monitored by TLC. It was found to indeed convert the compound from the tris deeb complex to the tris dcbpy complex but at the same time it was converting the soluble pink iron(II) complex to the insoluble orange iron(III) complex, in effect unpurifying the complex at the same time. So this avenue was abandoned.

Acac-based linkers have been studied in recent years for application in DSSCs and photoactive systems.³⁻⁷ They are seen to be quite sturdy linkers that don't require the profound communication that has historically been known to be a requirement of ligand-TiO₂ linkers.⁵ A route for the synthesis of acac-bpy is shown in Scheme 6-1. The synthesis begins with the commercially available 2,2'-bipyridyl and proceeds through the widely known N,N'-oxide and nitrated versions. Synthesis has been successful through the amino-substituted version; characterization is in the Appendix. Work continues in the group to attain this ligand and the associated complex which should be easily attainable in the same manner that the tris dcbpy complex is achieved.





Scheme 6-1. Synthesis of 4,4'-acetylacetonate-2,2'-bipyridyl.^{3,6,8,9}

The 4,4'-hydroxamic acid-2,2'-bipyridine ligand is seen in Figure 6-1; it is obtained from the dcbpy precursor, proceeding through the diacyl dichloride which is reacted with hydroxylamine hydrochloride in the presence of triethylamine.^{10,11} The product was obtained and NMR characterization is in the Appendix. The ligand is known to have isomers that appear in NMR and the shifts obtained match the literature¹² but due

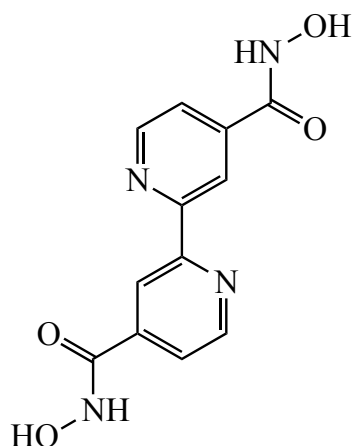


Figure 6-1. Structure of 4,4'-hydroxamic acid-2,2'-bipyridine.

to odd solubility, although obtained, the ligand is not thought to be completely pure. There is ongoing work in the group to obtain the pure ligand and the associated iron(II) complex.

Since new chromophores have been prepared in DSSCs and others are planned, electron transfer rates can be evaluated. Time-resolved spectroscopy can be utilized to determine species lifetimes and the corresponding rates for the processes that govern the efficiency of the solar cell. The ground state recovery of the chromophore can be evaluated. This experiment can be performed on films of both titanium dioxide, where hot injection is said to occur for iron molecules,¹³ and a semiconductor where no injection will occur. Some examples for 'reference' semiconductors are aluminum oxide,^{14,15} zinc oxide,¹⁶ and zirconium dioxide^{17,18} have all been investigated for use. Requirements of a non-quenching semiconductor are much the same as for a quenching semiconductor, transparency, nanocrystalline, dye binds similarly, etc., the only added requirement is that the conduction band be sufficiently negative so injection is not

possible, and the excited state of the dye is not quenched. The experiment can be done on a simple dyed film with a drop of a viscous electrolyte, such as propylene carbonate, that is secured with a cover slip. The rates can be compared of films that are exposed to electrolyte with and without the addition of a redox couple. Full cells can also be tested as our large cell area and configuration has included the necessary requirements that would allow laser spectroscopy, discussed in Chapter 2.

Other research in our group has been focused on the development of an octahedral compound that would in effect reduce the number of states induced by the ligand field.¹⁹ The lower number of states would hopefully slow the deactivation and extend the lifetime of the MLCT excited states, increasing the time to allow for injection into the semiconductor conduction band. This compound, bis(2,6-di(2-carboxypyridyl)pyridine)iron(II), $[\text{Fe}(\text{dcpp})_2](\text{PF}_6)_2$, exhibits a much more positive redox potential, 1.93 V, an entire volt more positive than the FeCN compound presented in Chapter 3. The $[\text{Fe}(\text{dcpp})_2](\text{PF}_6)_2$ compound has also been functionalized with carboxylic acid to allow its incorporation into a DSSC.

Ruthenium(II) bipyridyl compounds have historically been adsorbed to the semiconductor titanium dioxide for use in DSSCs. Among the reasons described in Chapter 2, the reason for using TiO_2 we would like to address is that the Ru(II) MLCT excited states, both long and short-lived, are higher in energy than the conduction band edge, making it a viable semiconductor for electron injection and subsequent charge separation. Although a current is seen from iron(II) compounds its electronic states are not suitable for the conduction band edge of titanium dioxide. We have begun an investigation of new semiconductors that have more positive band edges that could energetically allow injection to occur. Characteristics of a practicable semiconductor

were discussed in Chapter 2. We have begun looking into antimony oxides as a potential replacement to titanium dioxide. Antimony oxide exists in different forms, Sb_2O_3 , Sb_2O_4 , Sb_2O_5 , Sb_6O_{13} .^{20–24} Nanocrystalline Sb_2O_3 has a band gap that changes with thickness of the film, it has been shown to have a range of 3.1 eV to 3.9 eV.^{24,25} Sb_6O_{13} has a bandgap of 3.05 eV and a band edge at -0.16 eV²¹ vs. NHE. Another option is SnO_2 which has a band gap of 3.6 eV²⁶ and a conduction band edge at 0.05 V²⁷ compared to TiO_2 with a bandgap of 3.2 eV and a band edge of -0.5 V vs. NHE. SnO_2 can also be tuned by doping with antimony; increased doping shifts the Fermi level more negative.²⁷ $\text{Sb}:\text{SnO}_2$ could be useful in finding the optimal Fermi level position to allow injection yet have a maximum V_{OC} with respect to the potential of the chosen redox couple.

The iodide/triiodide has historically been the best redox shuttle for ruthenium based chromophores, and this is where our research has originated as we have investigated the potential use and success of iron chromophores in DSSCs. We have begun to investigate other redox shuttles that might reduce iron compounds faster and more effectively out-performing the backwards reaction rates, potentially increasing photocurrent and photovoltage for these cells. Recent reports on cobalt redox shuttles^{28–36} have sparked our interest and these are the first new compounds we have begun to study in our iron DSSCs. Photocurrents were observed from a FeCN -based DSSC employing $\text{Co}(\text{dtb-bpy})_3^{2+}$ as the redox couple. A large hysteresis was observed in the J-V curves; it is suspected that the slower diffusion of the cobalt compound is the source in coordination with the larger spacer that is used for iron DSSCs, causing them to be non-steady state.³⁷

Also with our more positive shift in potential for the $[\text{Fe}(\text{dcpp})_2](\text{PF}_6)_2$ compound we need to find new redox shuttles that also have more positive redox potentials, this can substantially increase our V_{OC} as it is the difference between the quasi Fermi level and the redox couple potential. Some examples of redox shuttles for this compound and others discussed are ferrocene, $(\text{SCN})_2/\text{SCN}^-$,³⁸ tetrathiafulvalene,³⁹ $[\text{Cu-bis}(2,9\text{-dimethyl-1,10-phenanthroline})_2](\text{CF}_3\text{SO}_3)_2$,⁴⁰ $[\text{Co}(1,10\text{-phenanthroline})_3](\text{CF}_3\text{SO}_3)_2$, $[\text{Co}(2,6\text{-bis}(1\text{-butylbenzimidazol-2-yl)pyridine})_2](\text{ClO}_4)_2$ ³⁶ and $\text{Br}^-/\text{Br}_3^-$.⁴¹ Solid state electrolytes are also a potential option once we understand more about the iron system and its applicability in DSSCs.

As discussed in Chapter 4, one of the significant issues with quasi solid-state electrolytes is its resistance to infiltration effectively into the pores of nanocrystalline titanium dioxide. There are methods in place such as using vacuum to induce pore-filling^{42,43} heating to decrease viscosity,⁴⁴ dissolving in a removable solvent,⁴⁵ and *in situ* polymerizing.^{46,47} Also in coordination with our NSF-Solar collaboration low glass transition polymerized ionic liquids were developed that can be incorporated into our DSSC configuration.⁴⁷

Development of a new photoanode with a 3-D network that would facilitate viscous electrolytes interaction within the photoanode would improve infiltration of the electrolyte. As part of our NSF-Solar collaboration, preliminary work by Prof. Drzal's research group on a novel photoelectrode incorporating a cellulose structure interdispersed in the TiO_2 that degrades when the film is sintered.⁴⁸⁻⁵⁰ There have been many studies on modifying the photoanode (nanowires, nanotubes, large pores etc.) to help incorporate the quasi solid-state electrolytes.⁵¹⁻⁵³

There is quite an extensive amount of opportunities for modifications to the DSSC since there are many integrated components, each with their own requirements. We have started a few avenues of this research and have made considerable progress on each of these facets of research. Our group will continue to delve into these issues, hopefully with continued understanding and advancement of the intricacies of the DSSC system.

APPENDIX

APPENDIX

Synthesis of Tetrakis (tetrabutylammonium) tris (4,4'-dicarboxylate-2,2'-bipyridine)iron(II) . $\text{TBA}_4\text{Fe}(\text{dcbpy})_3$ was synthesized according to a modified literature procedure.⁵⁴ 0.0713 g (0.292 mmol) of dcbpy was ground into a fine powder and added to 50 mL of methanol, 25 mL of acetone and 584 μL of tetrabutylammonium hydroxide in a 125 mL Erlenmeyer flask while vigorously stirring. The solution was heated to boiling and 0.0441 g of $(\text{NH}_4)_2\text{Fe}(\text{SO}_4)_2 \cdot 6\text{H}_2\text{O}$ was dissolved in 10 mL in water and added all at once; the solution immediately turned a bright medium pink. 20 mL more of water was added and the methanol and the acetone were boiled off. The water was removed using vacuum distillation, the solution was dissolved in methanol and the unreacted ligand was filtered off using a fine 0.22 mm filter paper. The solution was acidified when necessary for use but remained the TBA^+ salt until then so yield was not calculated. ^1H NMR (0.05 M NaOD in D_2O , 300 MHz), δ 7.35 (d, $J = 6$ Hz, 2H), 7.45 (dd, $J = 6$ Hz, 2H), 8.68 (s, 2H).

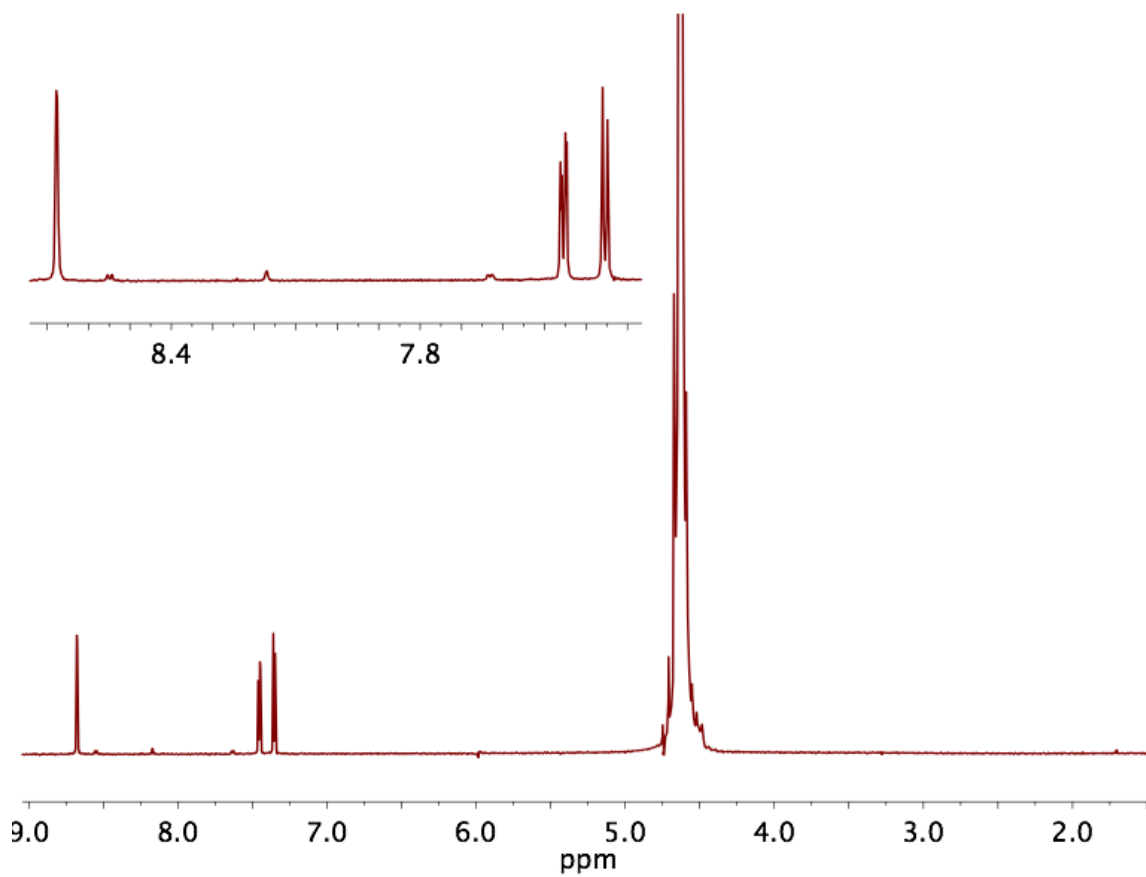


Figure 6-2. ^1H NMR Spectrum of tris(4,4'-dicarboxylic acid-2,2'-bipyridine)iron(II) in 0.05 M NaOD in D_2O .

Synthesis of 4,4'-Diethylester-2,2'-bipyridine (deeb). deeb was prepared via a modified version of a combination of literature procedures.⁵⁵⁻⁵⁷ 1.09 g (4.46 mmol) of dc bpy was ground into a fine powder and added to a 250 mL round bottom flask containing 26.1 mL (446 mmol) of ethanol, then 12 mL (223 mmol) of concentrated sulfuric acid was added while stirring. The mixture was heated to reflux and appeared completely solubilized in 30 minutes, and a light pink after 2 hours, a darker pink after 3 hours. The reaction was refluxed for 4 hours total, and let cool overnight. The unreacted dc bpy was filtered off through a medium glass frit. 5 M NaOH was added and a precipitate formed. Ice was added to cool and help precipitation. White microcrystalline solid was filtered on a medium frit and allowed to dry. More solid was obtained from the filtrate with more base added. The solid was recrystallized in a minimal amount of hot ethanol to create billowy needle-like crystals, letting the solution cool slowly without disturbance, cooling in the fridge, then blowing off some of the ethanol helps create more product. ¹H NMR (CDCl₃, 500 MHz): δ 1.43 (t, J = 7 Hz, 6H), 4.45 (q, J = 7 Hz, 4H), 7.89 (t, J = 7 Hz, 2H), 8.85 (dd, J = 5 Hz, 2H), 8.93 (qs, J = 1 Hz, 2H). ¹³C NMR (CDCl₃, 500 MHz): δ 14.25, 61.88, 120.56, 123.22, 138.98, 150.04, 156.48, 165.11.

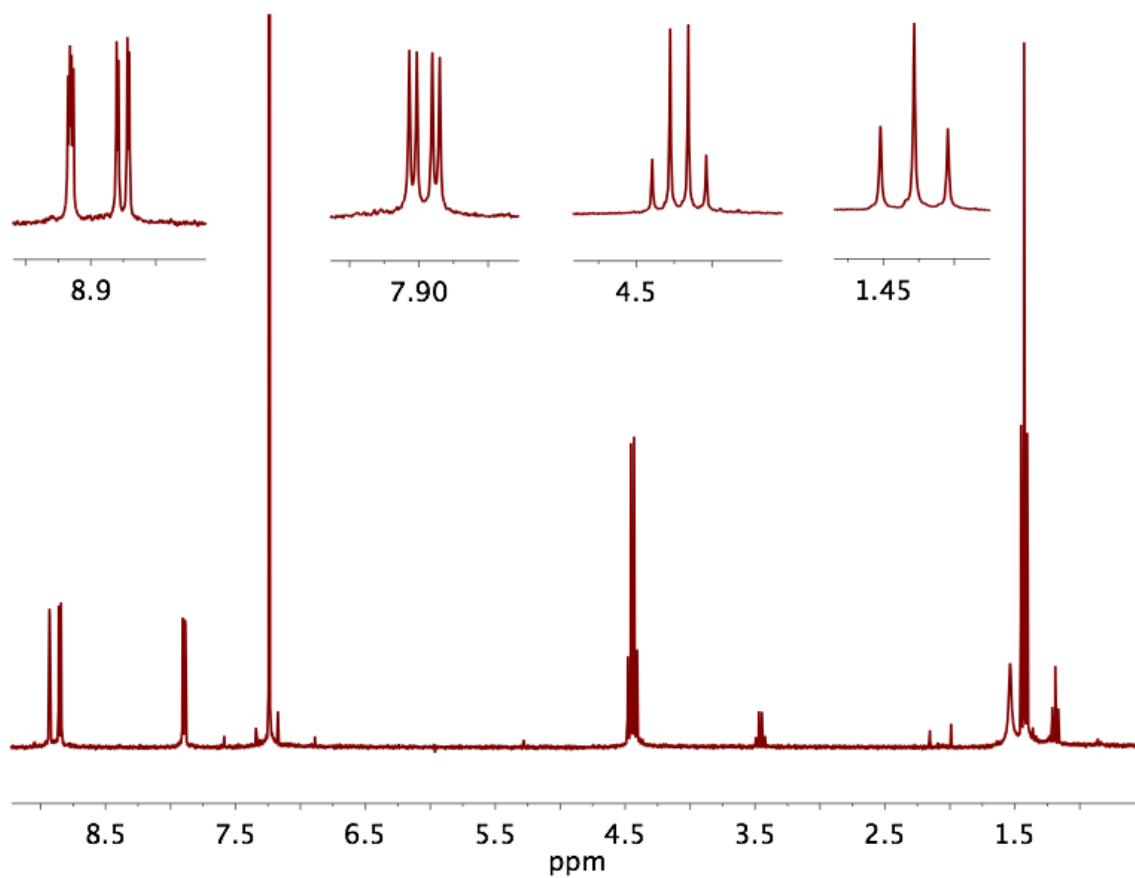


Figure 6-3. ¹H NMR spectrum of 4,4'-diethylester-2,2'-bipyridine in CDCl₃.

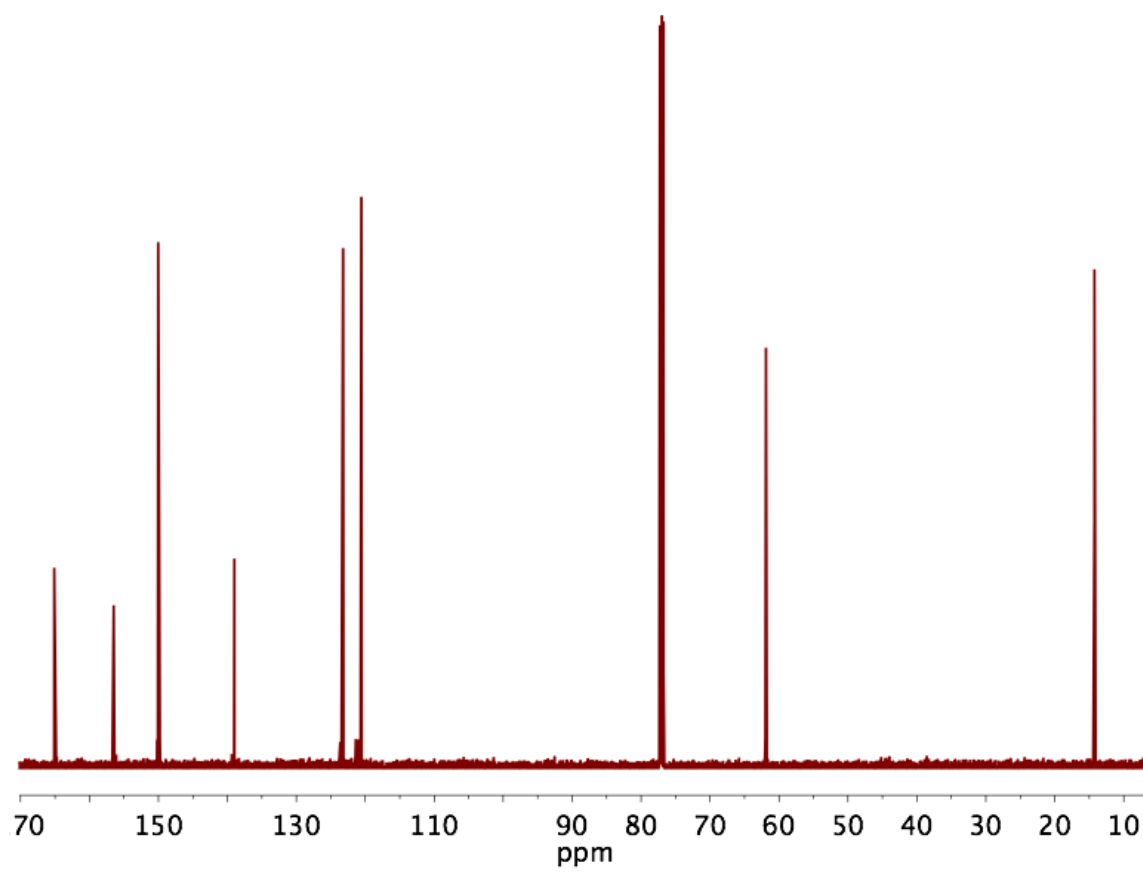


Figure 6-4. ^{13}C NMR Spectrum of 4,4'-diethylester-2,2'-bipyridine in CDCl_3 .

Synthesis of Tris(4,4'-diethylester-2,2'-bipyridine)iron(II) Hexafluorophosphate.

0.0875 g (0.291 mmol) of deeb was added to 25 mL of chloroform and 25 mL of ethanol, both bubble degassed, in a 250 mL round bottom flask. 0.022 g (0.135 mmol) of $\text{FeCl}_2 \cdot 2\text{H}_2\text{O}$ stored in an air- and water-free glovebox was removed via a 25 mL round bottom fit with a septum. 10 mL of degassed water was cannula-transferred into the $\text{FeCl}_2 \cdot 2\text{H}_2\text{O}$ and then the solution was cannula-transferred to the reaction flask. The reaction was heated, after 30 minutes the temperature was 40 °C, after 30 more minutes the temperature was 45 °C, after 15 more minutes the reaction reached 50 °C and then remained at this temperature for the next 2 hours and then the heat was removed and let stir overnight. Total heating time was 3 hours and 15 minutes. The ethanol was evaporated under nitrogen while stirring. The compound was partially precipitated with the addition of ammonium hexafluorophosphate, acetonitrile was added and let evaporate slowly and crystals formed. The red/purple compound was collected on a medium glass frit and washed with ether to dry, and further dried in a dessicator under vacuum. The pure product was obtained by recrystallization in acetonitrile via ether diffusion. ^1H NMR (CD_3CN , 300 MHz): δ 1.43 (t, $J = 7$ Hz, 6H), 4.49 (q, $J = 7$ Hz, 4H), 7.57 (t, $J = 6$ Hz, 2H), 7.82 (d, $J = 6$ Hz, 2H), 9.10 (s, 2H).

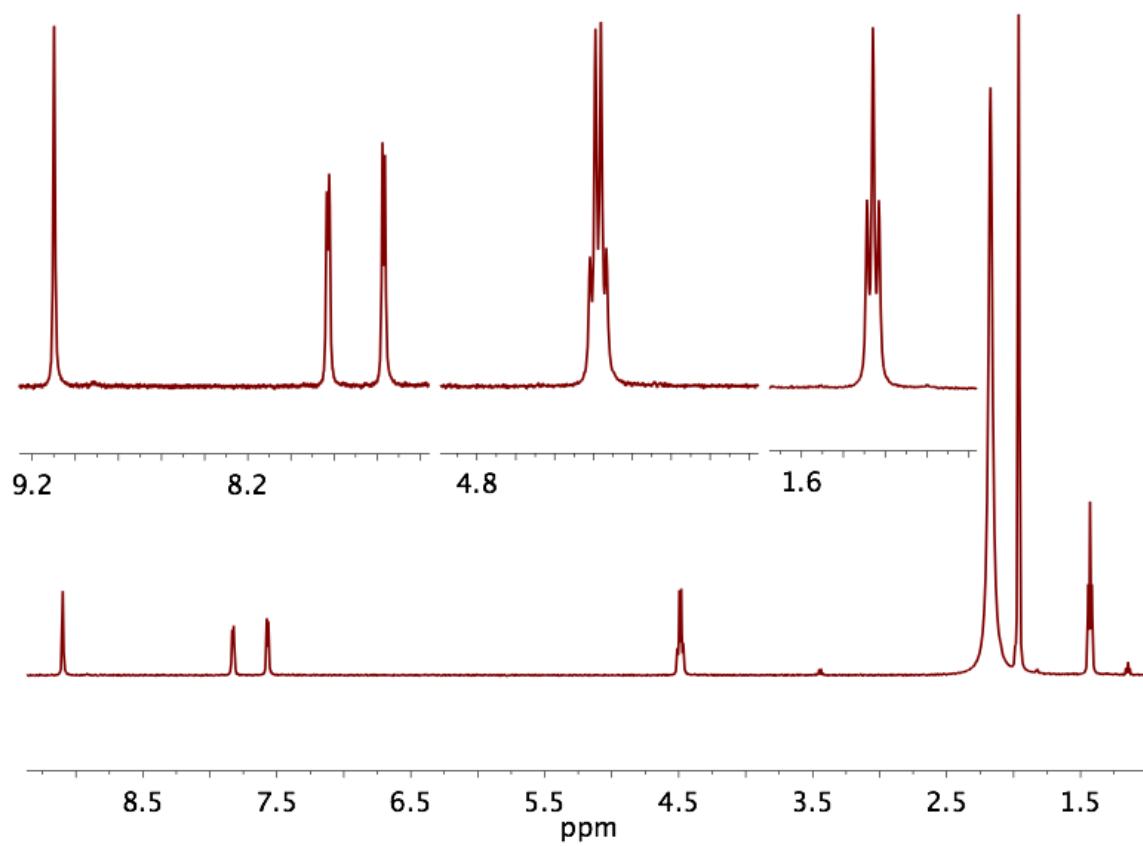


Figure 6-5. ¹H NMR Spectrum of tris(4,4'-diethylester-2,2'-bipyridine)iron(II) in CDCl₃.

Synthesis of 4,4'-Hydroxamic acid-2,2'-bipyridine (hx-bpy). hx-bpy was prepared via literature procedure¹⁰. 100mL of triethylamine was dried over potassium hydroxide and activated carbon, 50mL of benzene was dried over calcium hydride, and chloroform was dried over sodium sulfate for one week. All glassware was dried in the oven overnight. 0.37 g (1.5 mmol) of dcbpy was refluxed in 4.0 mL (54 mmol) of thionyl chloride, under nitrogen for 3 hours. The solid never completely dissolved, but the end solid was a fluffier solid of the diacylchloride compared to the hard crust of dcbpy. Using a side-arm condenser under positive nitrogen pressure, three 10 mL fractions of the dry benzene was added and to remove the thionyl chloride; the mixture forms an azeotrope and distills off with little heat at ~35-40°C. The diacylchloride solid was suspended in the dry chloroform and transferred into a dropping funnel equipped to attach to the next step of the reaction sequence, under positive nitrogen pressure. Under nitrogen, hydroxylamine hydrochloride was added to 3 mL of dry chloroform in a 3-neck round bottom flask that a condenser and a dropping funnel was also attached to. 1.0 mL (7.3 mmol) triethylamine was then added via syringe through a septum, a gas evolved at addition, and the solution remained a suspension. The diacyl chloride was added all at once via the dropping funnel and the mixture turned pink. The mixture was stirred for 2 days; no heat was added. The peach crude product was filtered on a medium glass frit. NMR shows numerous peaks, the compound is the major peaks, which are listed based on literature values.¹⁰ ¹H NMR (d₆-DMSO, 500 MHz): δ 7.75 (dd, J = 5 Hz, 2H), 8.70 (s, 2H), 8.78-8.83 (d, J = 5 Hz, 2H).

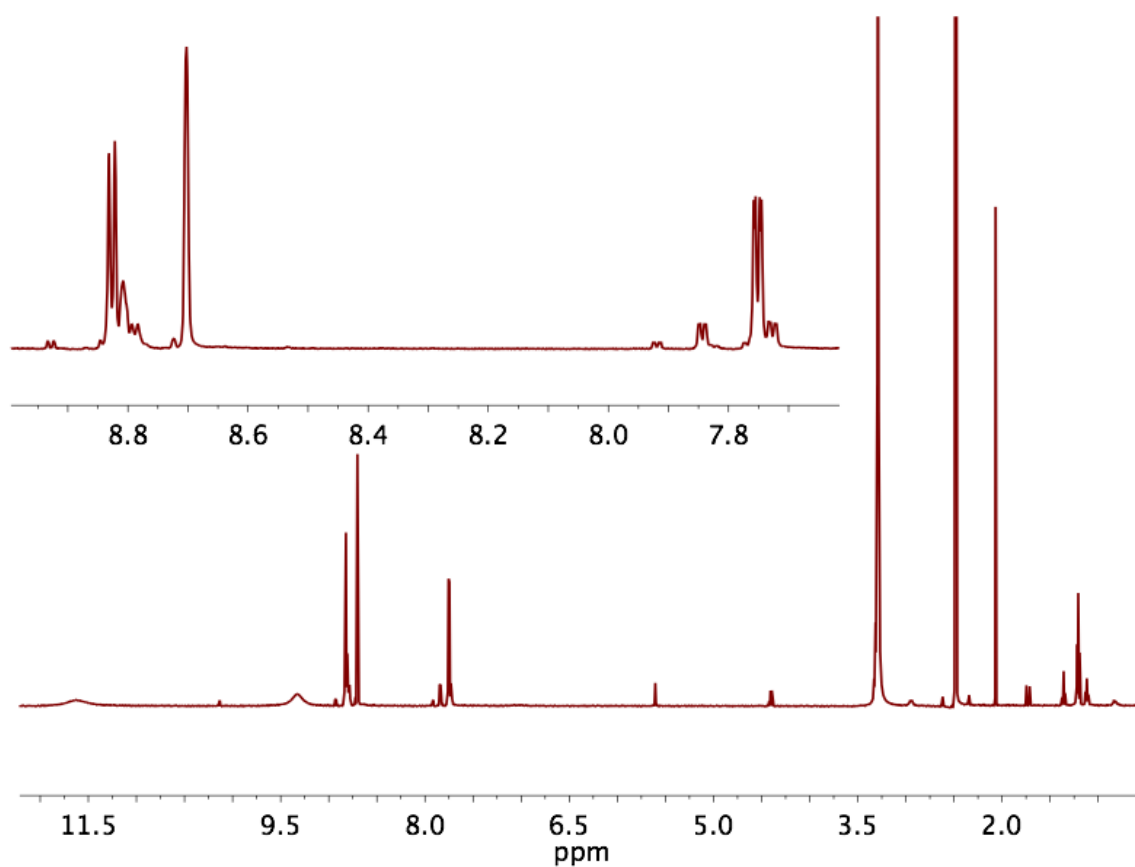


Figure 6-6. ¹H NMR Spectrum of 4,4'-hydroxamic acid-2,2'-bipyridine in d₆-DMSO.

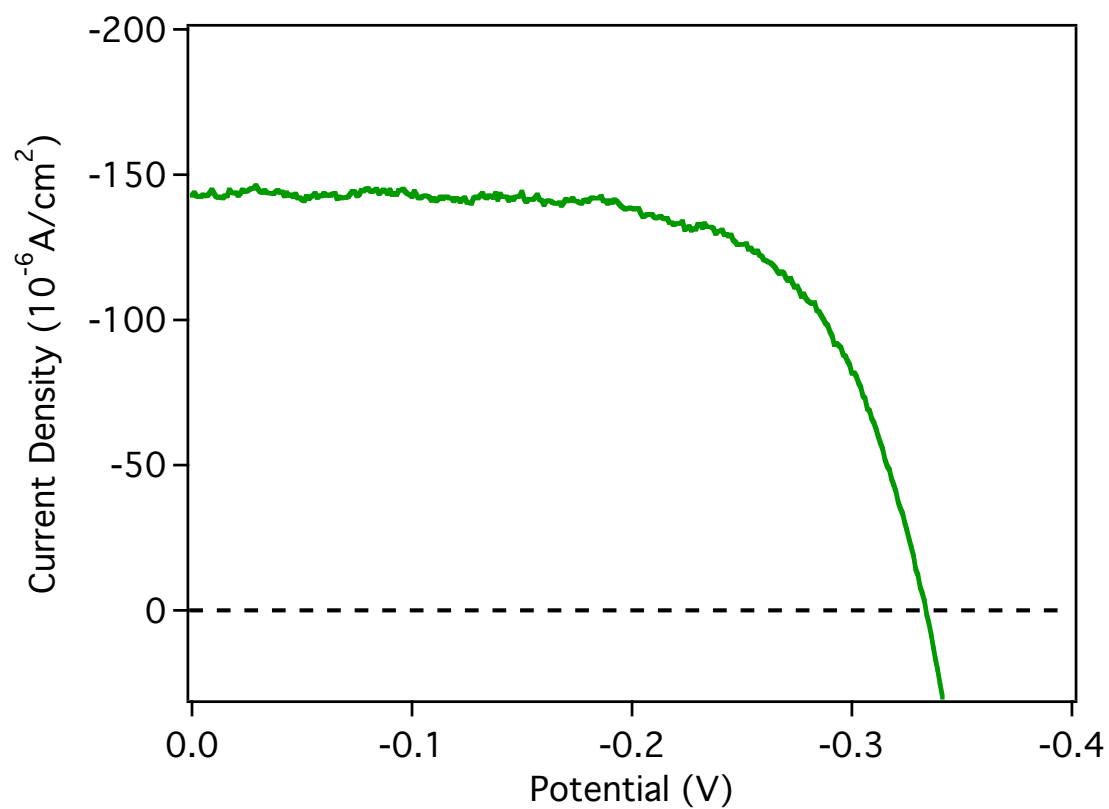


Figure 6-7. Representative J-V curve of $[\text{Fe}(\text{dcbpy})_3](\text{PF}_6)_2$ as a chromophore in DSSC. Electrolyte: 0.5 M LiI, 0.05 M I_2 , 0.2 M TBP in MeCN, thermalized Pt counter electrode.

Synthesis of Tris(2,2'-bipyridine)cobalt(II) Hexafluorophosphate. $[\text{Co}(\text{bpy})_3](\text{PF}_6)_2$ was synthesized according to modified literature procedures.^{29,30} 0.22 g (1.4 mmol) of bpy was dissolved in a minimal amount of methanol (~2-3 mL) in a small round bottom flask while stirring. 0.12 g (0.47 mmol) of $\text{Co}(\text{CH}_3\text{CO}_2)_2 \cdot 4\text{H}_2\text{O}$ was also dissolved in a minimal amount of methanol with sonication and then added all at once to the reaction flask. The solution immediately turned yellow but remained dissolved; the solution was let react at room temperature for 2 hours. An excess of ammonium hexafluorophosphate was added to crash out the yellow product. It was collected on a medium glass frit and washed with ether, dried in a vacuum dessicator. The pure product in yellow microcrystalline product was obtained via an acetonitrile/ether diffusion. Yield: 0.37 g (96%). ^1H NMR (d^6 -acetone, 500 MHz), δ 14.6 (s, 2H), 45.89 (s, 2H), 83.36 (s, 2H), 87.84 (s, 2H).

Synthesis of Tris(2,2'-bipyridine)cobalt(III) Hexafluorophosphate. $[\text{Co}(\text{bpy})_3](\text{PF}_6)_3$ was synthesized according to modified literature procedures.^{29,30,37} 0.10 g (0.13 mmol) of $[\text{Co}(\text{bpy})_3](\text{PF}_6)_2$ was dissolved in acetonitrile, excess NOPF_6 was added and stirred for 30 to 45 minutes. Some of the solution was evaporated and recrystallized by ether diffusion and the darker yellow powder was filtered on a medium frit and dried under vacuum. The pure microcrystalline solid was obtained after a slow ether diffusion from acetonitrile. Yield: 0.11 g (93%). ^1H NMR (CD_3CN , 500 MHz), 7.30 (d, $J = 6$ Hz, 2H), 7.76 (t, $J = 7$ Hz, 2H), 8.50 (t, $J = 8$ Hz, 2H), 8.71 (d, $J = 8$ Hz, 2H).

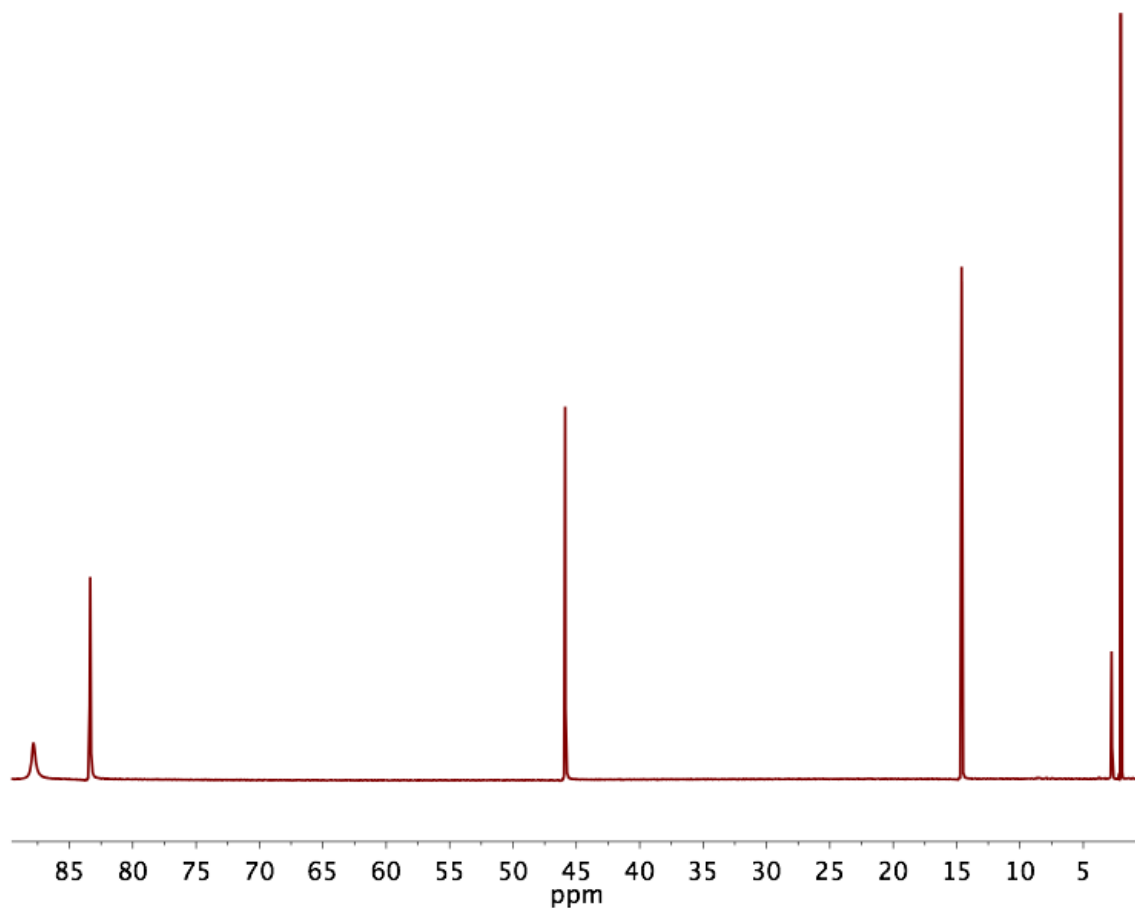


Figure 6-8. ^1H NMR Spectrum of Tris(2,2'-bipyridine)cobalt(II) Hexafluorophosphate in d_6 -acetone.

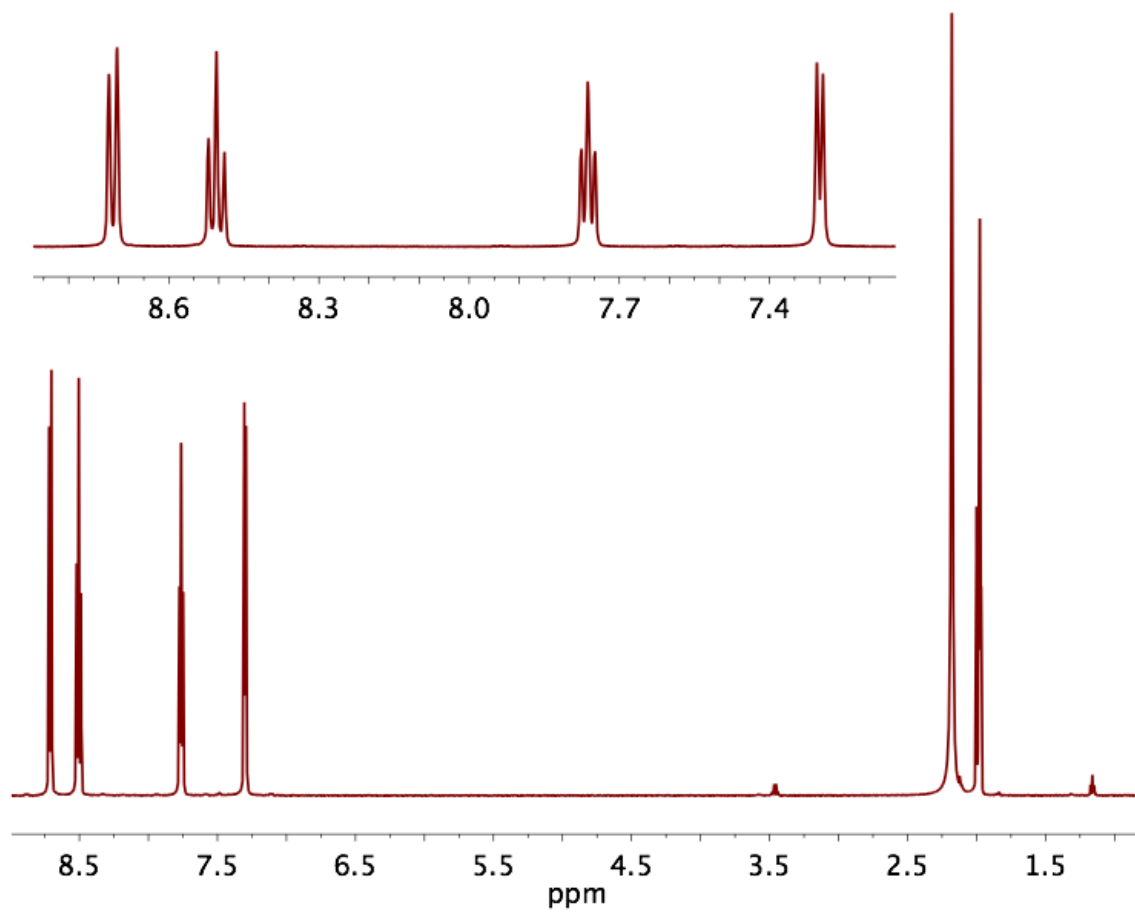


Figure 6-9. ¹H NMR Spectrum of Tris(2,2'-bipyridine)cobalt(III) Hexafluorophosphate in CD₃CN.

Synthesis of Tris(4,4'-di-*tert*-butyl-2,2'-bipyridine)cobalt(II) Hexafluorophosphate.

[Co(dtb-bpy)₃](PF₆)₂ was synthesized according to modified literature procedures.^{29,30} The reaction was performed as the [Co(bpy)₃](PF₆)₂ was synthesized in the same molar ratios. The pure product was an orange microcrystalline solid. Yield: 92%. ¹H NMR (d₆-acetone, 500 MHz), δ 3.39 (s, 6H), 42.71 (s, 2H), 79.79 (s, 2H), 90.96 (s, 2H).

Synthesis of Tris(4,4'-di-*tert*-butyl-2,2'-Bipyridine)cobalt(III) Hexafluorophosphate.

[Co(dtb-bpy)₃](PF₆)₃ was synthesized according to modified literature procedures.^{29,30,37} The reaction was performed as the [Co(bpy)₃](PF₆)₃ was synthesized in the same molar ratios. The pure product was a darker orange microcrystalline solid. Yield: 86%. ¹H NMR (D₃CN, 500 MHz), δ 1.47 (s, 6H), 7.10 (d, J = 6 Hz, 2H), 7.71 (dd, J = 6 Hz, 2H), 8.65 (ds, 2H).

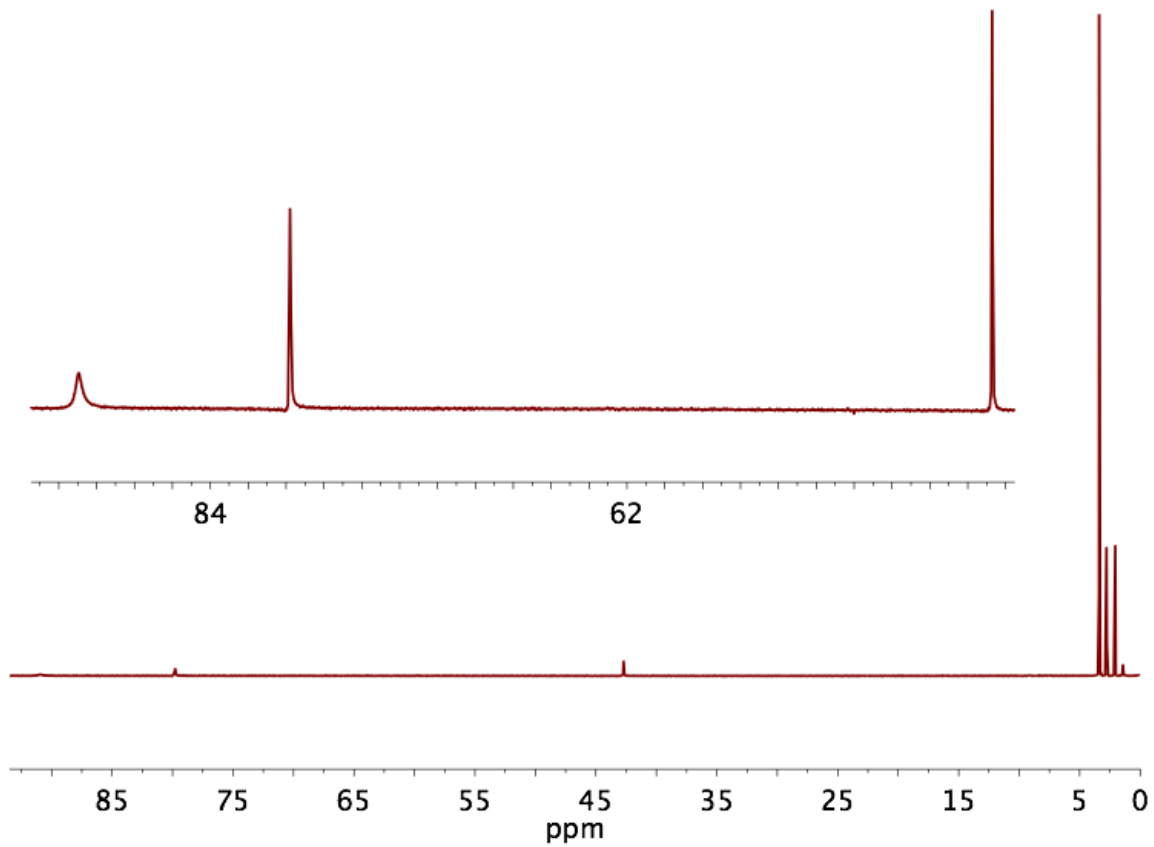


Figure 6-10. ¹H NMR Spectrum of Tris(4,4'-di-*tert*-butyl-2,2'-ipyridine)cobalt(II) Hexafluorophosphate in d⁶-acetone.

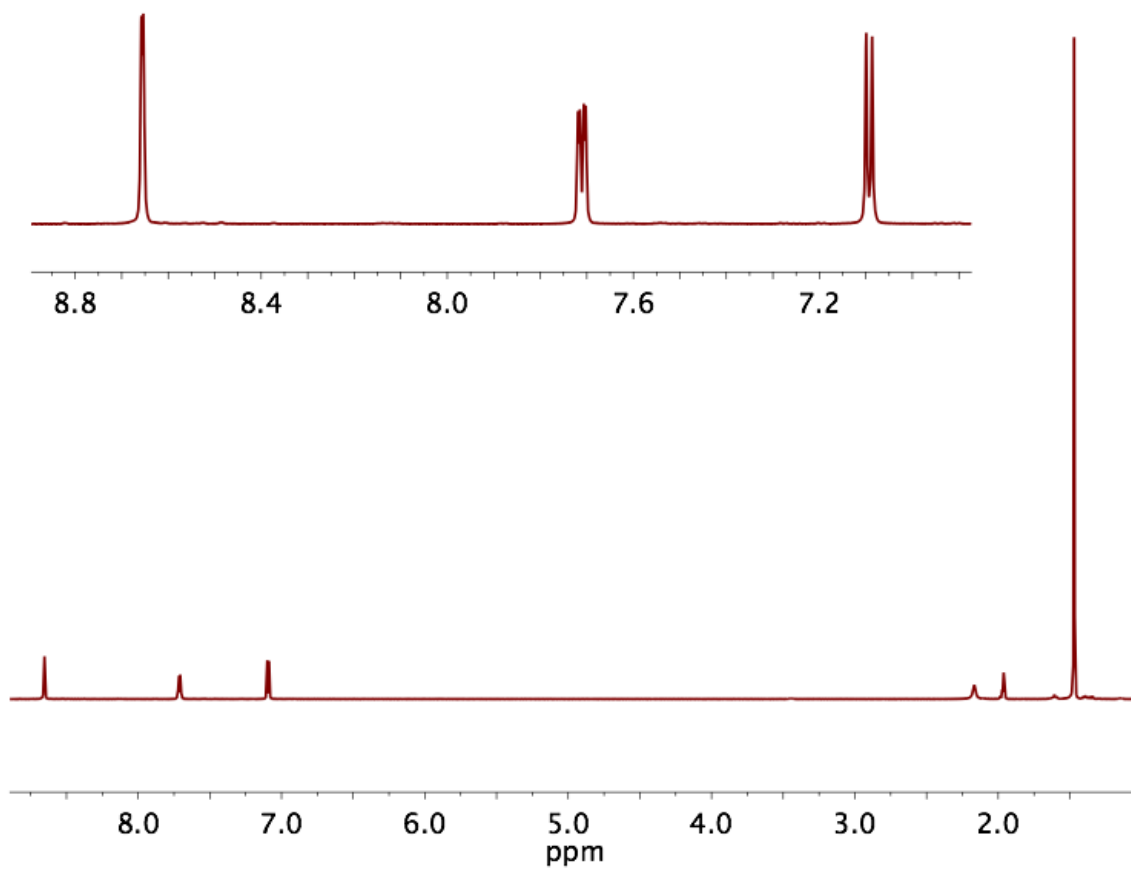


Figure 6-11. ¹H NMR Spectrum of Tris(4,4'-di-*tert*-butyl-2,2'-bipyridine)cobalt(III) Hexafluorophosphate in CD₃CN.

REFERENCES

REFERENCES

- (1) Shimidzu, T.; Iyoda, T.; Izaki, K. *The Journal of Physical Chemistry* **1985**, *89*, 642–645.
- (2) Hammarström, L.; Norrby, T.; Stenhagen, G.; Mårtensson, J.; Åkermark, B.; Almgren, M. *The Journal of Physical Chemistry B* **1997**, *101*, 7494–7504.
- (3) Xiao, D.; Martini, L. a; Snoeberger, R. C.; Crabtree, R. H.; Batista, V. S. *Journal of the American Chemical Society* **2011**, *133*, 9014–22.
- (4) Olivier, J.-H.; Harrowfield, J.; Ziessel, R. *Chemical Communications* **2011**, *47*, 11176–88.
- (5) Heimer, T. A.; D’Arcangelis, S. T.; Farzad, F.; Stipkala, J. M.; Meyer, G. J. *Inorganic Chemistry* **1996**, *35*, 5319–5324.
- (6) Olivier, J.-H.; Haefele, A.; Retailleau, P.; Ziessel, R. *Organic Letters* **2010**, *12*, 408–11.
- (7) Warnan, J.; Guerin, V.-M.; Anne, F. B.; Pellegrin, Y.; Blart, E.; Jacquemin, D.; Pauporté, T.; Odobel, F. *The Journal of Physical Chemistry C* **2013**, *117*, 8652–8660.
- (8) Liu, J.; Zeng, R.; Zhou, C.; Zou, J. *Chinese Journal of Chemistry* **2011**, *29*, 309–313.
- (9) McCusker, C. E. Probing Vibrational Relaxation Dynamics in Charge-Transfer Excited States: Synthesis, Physical, and Photophysical Characterization of Cyano-Substituted Polypyridyl Complexes of Ru(II), 2010.
- (10) Donnici, C. L.; Máximo Filho, D. H.; Moreira, L. L. C.; Reis, G. T. dos; Cordeiro, E. S.; Oliveira, I. M. F. de; Carvalho, S.; Paniago, E. B. *Journal of the Brazilian Chemical Society* **1998**, *9*, 455–460.
- (11) Tanaka, K.; Matsuo, K.; Nakanishi, A.; Hatano, T.; Izeki, H.; Ishida, Y.; Mori, W. *Chemical & Pharmaceutical Bulletin* **1983**, *31*, 2810–2819.
- (12) Brown, D. A.; Glass, W. K.; Mageswaran, R.; Mohammed, S. A. *Magnetic Resonance in Chemistry* **1991**, *29*, 40–45.
- (13) Asbury, J. B.; Wang, Y.-Q.; Hao, E.; Ghosh, H. N.; Lian, T. *Research on Chemical Intermediates* **2001**, *27*, 393–406.

- (14) Docampo, P.; Snaith, H. J. *Nanotechnology* **2011**, *22*, 225403.
- (15) Lee, M. M.; Teuscher, J.; Miyasaka, T.; Murakami, T. N.; Snaith, H. J. *Science* **2012**, *338*, 643–7.
- (16) Anderson, N. a; Ai, X.; Lian, T. *The Journal of Physical Chemistry B* **2003**, *107*, 14414–14421.
- (17) Kalyanasundaram, K.; Grätzel, M. *Coordination chemistry reviews* **1998**, *77*, 347–414.
- (18) Kay, A.; Humphry-Baker, R.; Gratzel, M. *The Journal of Physical Chemistry* **1994**, *98*, 952–959.
- (19) Jamula, L. L. Exploring Design Strategies to Tune the Electronic Structure and Ultrafast Dynamics of Iron(II) Polypyridyl Chromophores, 2013.
- (20) Xiong, H.-M.; Chen, J.-S.; Li, D.-M. *Journal of Materials Chemistry* **2003**, *13*, 1994.
- (21) Kim, J.-H.; Jang, J.-Y.; Kim, S.-C.; Han, C.-H.; Kim, S.-J. *Bulletin of the Korean Chemical Society* **2012**, *33*, 1204–1208.
- (22) Ouni, B.; Haj Lakhdar, M.; Boughalmi, R.; Larbi, T.; Boukhachem, A.; Madani, A.; Boubaker, K.; Amlouk, M. *Journal of Non-Crystalline Solids* **2013**, *367*, 1–7.
- (23) Li, B.; Xu, X.; Zhao, Y.; Zhang, Z. *Materials Research Bulletin* **2013**, *48*, 1281–1287.
- (24) Matsumoto, A.; Koyama, Y.; Togo, A.; Choi, M.; Tanaka, I. *Physical Review B* **2011**, *83*, 214110.
- (25) Tigau, N.; Ciupina, V.; Prodan, G. *Journal of Optoelectronics and Advanced Materials* **2006**, *8*, 37 – 42.
- (26) Robertson, J.; Falabretti, B. In *Handbook of Transparent Conductors*; Ginley, D. S., Ed.; Springer US: Boston, MA, 2011; pp. 27–50.
- (27) Guo, J.; She, C.; Lian, T. *The Journal of Physical Chemistry B* **2005**, *109*, 7095–102.
- (28) Cameron, P. J.; Peter, L. M.; Zakeeruddin, S. M.; Grätzel, M. *Coordination Chemistry Reviews* **2004**, *248*, 1447–1453.
- (29) Sapp, S. A.; Elliott, C. M.; Contado, C.; Caramori, S.; Bignozzi, C. A. *Journal of the American Chemical Society* **2002**, *124*, 11215–22.

- (30) Klahr, B. M.; Hamann, T. W. *The Journal of Physical Chemistry C* **2009**, *113*, 14040–14045.
- (31) Ondersma, J. W.; Hamann, T. W. *Journal of the American Chemical Society* **2011**, *133*, 8264–71.
- (32) Yella, A.; Lee, H.-W.; Tsao, H. N.; Yi, C.; Chandiran, A. K.; Nazeeruddin, M. K.; Diau, E. W.-G.; Yeh, C.-Y.; Zakeeruddin, S. M.; Grätzel, M. *Science* **2011**, *334*, 629–34.
- (33) Yum, J.-H.; Baranoff, E.; Kessler, F.; Moehl, T.; Ahmad, S.; Bessho, T.; Marchioro, A.; Ghadiri, E.; Moser, J.-E.; Yi, C.; Nazeeruddin, M. K.; Grätzel, M. *Nature Communications* **2012**, *3*, 631.
- (34) DeVries, M. J.; Pellin, M. J.; Hupp, J. T. *Langmuir* **2010**, *26*, 9082–7.
- (35) Xie, Y.; Hamann, T. W. *The Journal of Physical Chemistry Letters* **2013**, *4*, 328–332.
- (36) Nusbaumer, H.; Zakeeruddin, S. M.; Moser, J.-E.; Grätzel, M. *Chemistry (Weinheim an der Bergstrasse, Germany)* **2003**, *9*, 3756–63.
- (37) Personal Correspondence with Prof. Tom Hamann's group.
- (38) Oskam, G.; Bergeron, B. V.; Meyer, G. J.; Searson, P. C. *The Journal of Physical Chemistry B* **2001**, *105*, 6867–6873.
- (39) Yu, Z.; Tian, H.; Gabrielsson, E.; Boschloo, G.; Gorlov, M.; Sun, L.; Kloo, L. *RSC Advances* **2012**, *2*, 1083.
- (40) Hattori, S.; Wada, Y.; Yanagida, S.; Fukuzumi, S. *Journal of the American Chemical Society* **2005**, *127*, 9648–54.
- (41) Wang, Z.-S.; Sayama, K.; Sugihara, H. *The Journal of Physical Chemistry B* **2005**, *109*, 22449–55.
- (42) Han, H.; Bach, U.; Cheng, Y.-B.; Caruso, R. a. *Applied Physics Letters* **2007**, *90*, 213510.
- (43) Wang, B.; Chang, S.; Lee, L. T. L.; Zheng, S.; Wong, K. Y.; Li, Q.; Xiao, X.; Chen, T. *ACS applied materials & interfaces* **2013**, *5*, 8289–93.
- (44) Wang, P.; Zakeeruddin, S. M.; Moser, J. E.; Nazeeruddin, M. K.; Sekiguchi, T.; Grätzel, M. *Nature Materials* **2003**, *2*, 402–7.

- (45) Smestad, G. P.; Spiekermann, S.; Kowalik, J.; Grant, C. D.; Schwartzberg, A. M.; Zhang, J.; Tolbert, L. M.; Moons, E. *Solar Energy Materials and Solar Cells* **2003**, *76*, 85–105.
- (46) Kal, S. H.; Joseph, J.; Lee, J.; Kim, K.-J. *Journal of The Electrochemical Society* **2005**, *152*, A1378.
- (47) Hu, H. Synthesis of Poly(Ionic Liquids) both in Solution and on Surface of Silica Nanoparticles as Novel Quasi-Solid State Electrolytes, 2013.
- (48) Ghadiri, E.; Taghavinia, N.; Zakeeruddin, S. M.; Grätzel, M.; Moser, J.-E. *Nano letters* **2010**, *10*, 1632–8.
- (49) Imai, H.; Matsuta, M.; Shimizu, K.; Hirashima, H.; Negishi, N. *Journal of Materials Chemistry* **2000**, *10*, 2005–2006.
- (50) Shimizu, K.; Imai, H.; Hirashima, H.; Tsukuma, K. *Thin solid films* **1999**, *351*, 220–224.
- (51) Tétreault, N.; Horváth, E.; Moehl, T.; Brillet, J.; Smajda, R.; Bungener, S.; Cai, N.; Wang, P.; Zakeeruddin, S. M.; Forró, L.; Magrez, A.; Grätzel, M. *ACS Nano* **2010**, *4*, 7644–50.
- (52) Yang, L.; Leung, W. W.-F. *Advanced Materials* **2011**, *23*, 4559–62.
- (53) Zhang, J.; Deng, Y.; Gu, D.; Wang, S.; She, L.; Che, R.; Wang, Z.-S.; Tu, B.; Xie, S.; Zhao, D. *Advanced Energy Materials* **2011**, *1*, 241–248.
- (54) Ferrere, S. *Chemistry of Materials* **2000**, *12*, 1083–1089.
- (55) Elliott, C. M.; Hershenhart, E. J. *Journal of the American Chemical Society* **1982**, *104*, 7519–7526.
- (56) Maerker, G.; Case, F. *Journal of the American Chemical Society* **1958**, *80*, 2745–2748.
- (57) Garelli, N.; Vierling, P. *The Journal of Organic Chemistry* **1992**, *57*, 3046–3051.